The Mineralogy of Dust Around Evolved Stars

A Thesis submitted for the Degree

of

Doctor of Philosophy of the University of London

by

Angela Karen Speck

Department of Physics & Astronomy

University College London

University of London

September 1998

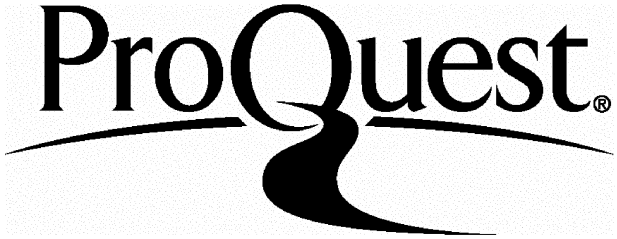

to my Granddad,

Alec Buta,

"Guardian of the Potatoes",

5th March 1923 - 2nd August 1998

Abstract

Infrared (IR) observations of evolved red giant stars (AGB stars) have shown that many are surrounded by dust envelopes, which are ejected into the interstellar medium and seed the next generation of stars and planets. By studying these one can understand the origins of interstellar and solar system materials. AGB stars fall into two main categories: oxygen-rich and carbon-rich. The prominent features of the IR spectra of AGB stars are: the 11.3μm feature of C-stars, attributed to silicon carbide (SiC); and the 9.7μm feature of O-rich stars, attributed to silicates. There are also various minor features with less secure identifications. Identifying dust around stars requires the use of laboratory spectra of dust species analogous to those one expects to observe. I have compiled a database of such spectra, and thereby constrained the identifications of circumstellar dust, which I have also tried to ensure are compatible with data from meteoritic presolar grains. Some laboratory spectra need to be modified before they are relevant to the problem in hand, i.e. stardust. The techniques used for such modifications are outlined in the thesis. In order to fully comprehend the problems that can arise from using laboratory spectra, the way in which light interacts with matter must be understood. To this end the optical properties of matter are discussed.

While the mineral constituents of the Earth have been reprocessed so extensively that they no longer contain any evidence of their stellar origins, the same is not true of primitive meteorites which contain "presolar" dust grains with isotopic fingerprints identifying their stellar sources. By comparing these presolar grains with nucleosynthesis models, grains expected to form around various stars and observational evidence of dust, we can gain a better picture of the formation mechanisms and sites of the various dust grains.

I have investigated the mineralogy of SiC of 32 C-stars and its relationship to meteoritic dust by using a χ^2-minimisation routine to fit the observed SiC features, using laboratory optical constants that have been published for a variety of SiC samples. In addition to the extreme carbon star AFGL 3068, the only C-star previously known to show the 11.3μm SiC feature in absorption, I have discovered three further examples of sources that show SiC in net absorption. Previous attempts to identify the type of SiC present around carbon stars have all identified it with α-SiC. However, I have found that the previous work is

based on flawed laboratory data and that a better fit is achieved using β-SiC, which agrees with meteoritic data.

I have also used the same techniques to investigate the mineralogy of 80 O-rich stars. Dust mineralogy around O-rich stars is considerably more complicated. The 9.7μm feature attributed to silicates varies greatly in shape and intensity as well as exact peak position from star to star, and the number of possible laboratory analogues is much greater than for SiC. Most of these spectra have been fitted using some form of forsterite (Mg_2SiO_4) and/or enstatite ($MgSiO_3$), although constraining the mineralogy further was not possible. There is little evidence of Al_2O_3 around these stars, contrary to theoretical predictions and previous radiative transfer models. Relating the O-rich dust species to meteoritic data is also more complicated, as most of the silicate material was reprocessed in the early solar system, although data on a small number of O-rich presolar grains have been used for this purpose. I have also discovered a previously unrecognized feature in the spectra of O-rich stars at 9.25μm. This feature, and the 12.5-13.0μm feature previously attributed to Al_2O_3, have been attributed to SiO_2.

Implications of the new attributions for both C- and O-rich stars are discussed

Acknowledgements

I am very grateful to many people who have contributed directly and indirectly to the completion of this thesis. First, I would like to thank my supervisor Mike Barlow, who not only took me on in a less than perfect physical state, but has also provided guidance and support throughout and has put up with various strops, bouts of PMT, family crises, Hall crises, my jaunts to Paris and having a bar manager as a student. I would also like to thank Roger Sylvester for being very helpful, understanding and explaining science in words of one syllable when necessary, and for putting up with me on two observing trips to UKIRT. Thanks also go to Chris Skinner who, although I did not have much contact with, was very helpful on chapter 6 and also put up with me at UKIRT. Sarah Dunkin is thanked for putting up with my neuroses and generally rants in the office, along with everyone else in the department who has had to deal with me. Other science honours go to Anne Hofmeister who helped to solve the silicon carbide problem and managed to play host to me in St Louis even with three (other) kids to deal with. Tom Bernatowicz is thanked for arranging the collaboration with Anne Hofmeister and for inviting me to the meeting in St Louis (October 1996). Thanks also to David Williams for chats, Molap and believing in meteorites. Special sciencey thanks go to Anja Andersen for being a kindred spirit.

I am grateful to PPARC for letting me start a new PhD with Mike and funding it for nearly two and a half years, to the Department of Physic and Astronomy, UCL, for an extra six months funding, and to the staff at UKIRT for their assistance on observing trips.

I have to thank (just about) everyone in International Hall - without whom my PhD would have been finished earlier, but I'd've had a lot less fun. Special thanks go to Kaelyn McGregor and Deborah Parsons for "girlie nights" and general best friend type things, Stuart Graham, for being the best deputy bar manager anyone could ask for and preventing the nervous breakdown that should've happened this summer, the other DBMs, Dave, Thomas and Charlie, and David Hart for signing the cheques. Bernadette Dunne is thanked for always being ready for a good, healthy bitch about whatever happened to be on our minds.

I thank my sister for not distracting me too often and for making me realise things could always be worse. And my parents, for continuous support and moving to the middle of nowhere just so I'd have a place to run away to and do work without distractions.

Finally, big snogs to Elric for so many things I can't possibly list them all here, but especially for much needed stress relief, putting up with bad tempers, neuroses and an extra two stone in weight, and for proof-reading more of this thesis than anyone could reasonably expect.

Contents

List of Tables

List of Figures

Chapter 1

Introduction

"...come to model heaven,
And calculate the stars, how they will wield
The mighty frame, how build, unbuild, contrive..."
Paradise Lost, Milton (1667)

Where do we come from? One of the fundamental goals in all science is to understand the origins of life on Earth. The basic particles that make up life on Earth, as well as the Earth itself, the other planets and the sun, were created at the beginning of the universe, but how did they become what they are today? With the exception of hydrogen, some helium and some lithium, all the atoms in the universe were created by stars, through nucleosynthesis, where hydrogen atoms are processed to make other elements. These elements are then ejected from the stars in various ways, either through relatively gentle mass-loss in the case of low mass stars or explosively in the case of high mass stars. These new atoms form dust and molecules in space and are then incorporated into new stellar systems, planets and life. Hence, we are all made of stardust.

One of the sites of dust formation is in the atmospheres of asymptotic giant branch (AGB) stars (other sources include novae and supernovae). The aim of this work is to investigate the nature of the dust forming in these circumstellar regions, and in particular the mineralogical composition of the dust. This involves an understanding of the nucleosynthetic processes that create the elements from which the dust forms, and of the chemistry

that determines the specific type of dust that forms. The method of observing these dust grains uses spectroscopy[1], which enables their identification through the recognition of the spectroscopic signature of a specific mineral. We can use spectroscopy of terrestrial samples in the laboratory to identify these signatures for individual minerals, but we must also understand the way in which electromagnetic radiation (light) from the star interacts with surrounding dust to produce the observed stellar spectra.

The study of meteorites has provided useful information on the nature of the dust and molecules forming in the circumstellar regions around AGB stars. Isotopic studies have shown that meteorites contain *presolar* grains that have survived intact since their formation around such stars. The results of the spectroscopic studies of stardust should be be related to, or even constrained by, presolar grains in meteorites

Most stars whose main-sequence mass is less than about $8M_{\odot}$ evolve into a phase known as the Asymptotic Giant Branch or AGB. These stars have low effective temperatures ($\leq$3000K) and high luminosity ($\geq 3000L_{\odot}$). These "low-to-intermediate mass" stars build a core of degenerate electron gas, with a helium-burning shell around it and surrounding that, a mantle of hydrogen[2]. It is the hydrogen-burning shell that is responsible for their high luminosity. During the AGB phase stars begin to expel matter. This matter ejection process leads to the formation of a circumstellar envelope around the star. It is this circumstellar envelope that is of interest in a discussion about stardust.

The basic scenario is this: an AGB star has a spherically symmetric gas outflow. Dust particles form in the circumstellar envelope at some distance from the star. The precise nature of the circumstellar dust grains varies from star to star. The dust's evolution and physical properties are dominated by the star. For example, the temperature of the dust grains is dependent on the nature of the grains and the central star. The chemical composition of the grains depends on the nature of the gas being ejected from the star. In turn the chemical composition of the ejected gas is controlled by the nucleosynthesis within the star. The chemistry around a star is usually either dominated by carbon or by oxygen. The reason for this is the remarkable stability of the carbon monoxide (CO) molecule.

[1] The study of objects by analysing the way they reflect, transmit and absorb electromagnetic radiation

[2] The exact structure of the interior of the star depends on the initial mass and the metallicity. This is discussed in more detail chapter 2

The molecule forms very easily and is very stable. Therefore, depending on the ratio of carbon-to-oxygen atoms around a star, one of the species will be completely locked into CO molecules, leaving the other to form dust and molecules. If the carbon-to-oxygen ratio (C/O) is less than unity, all the carbon atoms will be locked into CO, leaving the excess oxygen atoms to dominate the chemistry. Similarly, if C/O>1, there will be an excess of carbon dominating the chemistry. The rare exception to this is when C/O=1 and the carbon and oxygen atoms are equally depleted, leaving other atoms (e.g. nitrogen, sulphur) to form the majority of the dust and molecules.

The dust grains around a central star absorb light from the star and re-emit this light in the infrared region. The exact nature of the re-emitted light depends on the nature of the incident light as well as the chemical and physical composition of the dust and molecules. Therefore, we can use this infrared emission to detect and investigate circumstellar dust shells. The infrared emission from the dust is detected in the form of both continuum emission (infrared excess) and discrete spectral features due to individual dust species. These spectral features have been investigated by many people (e.g. see reviews by Woolf 1973, Woolf & Ney 1969, Bode 1988 and also sections 6.1, 6.2, 7.1, 8.1). The quest to more accurately identify these features incorporates the use of many laboratory mineral spectra, an understanding of how these minerals interact with the incident light, and models of the condensation sequences of dust expected in these regions.

The widely observed 9.7 μm feature is generally accepted to be due to Si-O bond stretching in silicate dust (assumed to be mostly iron and magnesium silicates). The profile of the feature varies from star to star and is thought to be due to variations in the exact nature of the silicates (e.g. whether crystalline or amorphous, which cations are present, what impurities are present, etc.). Silicates also have a feature at about 18 μm due to the O-Si-O bond bending.

There is another relatively common spectral feature at about 11.3 μm seen in carbon-rich AGB star spectra, which has been attributed to silicon carbide (SiC). The silicon carbide feature has been the subject of some debate (Friedemann *et al.* 1981, Borghesi *et al.* 1985, Pégourié 1988, Groenewegen 1995, Speck *et al.* 1997a,b, Papoular *et al.* 1998), not least because presolar SiC grains have been found in meteorites with isotopic

compositions suggestive of AGB star origins. The data from these meteoritic grains has disagreed with the astronomical observations of the 11.3 μm feature, and this problem is further addressed in this thesis.

Another set of features seen in the spectra of many astronomical objects are the so-called unidentified infrared (UIR) bands. These are a set of narrow features found in the infrared region of the spectrum. Their relative strengths vary from source to source. These bands have been attributed to some form of hydrogenated carbon, although whether it is in the form of molecules or dust grains is still under debate. Given that they would need a carbon-rich environment in which to form, carbon stars have been suggested as a possible source of such species. Unfortunately the UIR bands need a source of ultraviolet (UV) radiation to be produced, which is something carbon-rich AGB stars have a distinct lack of, and therefore these dust grains/molecules would not be seen even if they were present around such stars. However, some carbons stars can be found in binary systems with hot companion stars which can provide the UV radiation needed to produce the UIR bands. Therefore, these bands may be observable in the spectra of these carbon stars.

The work presented in this thesis is broadly split into two sections based on the chemistry: carbon-rich and oxygen-rich. In chapter 2, the basic evolution and nucleosynthesis of AGB stars is discussed. How these objects evolve from stars with oxygen-rich atmospheres to stars with carbon-rich atmospheres is outlined. Chapter 3 gives an introduction to meteorites and in particular presolar grains. The aim of the chapter is to help the reader understand how the isotopic analysis of presolar grains has lead to a better knowledge of their supposed origins, and how this relates to observational spectroscopy[3].

As discussed above, the use of spectroscopy requires an intimate knowledge of how matter interacts with light. Chapter 4 contains a basic discussion of the principles of the optical properties of matter. During this work, an error in previous laboratory spectra was uncovered. This is discussed and has implications for chapter 6. Following on from the discussion of optical properties of matter, essential to the astronomical spectroscopist is a good selection of laboratory spectra with which to compare observations. Therefore, chapter 5 contains a catalogue of mineral spectra of use to astronomers, with a discussion

[3] Whilst tryingto explain that I study dust around stars, an archaeologist friend asked "But how do you get the dust down?". The answer is *in meteorites*.

of the similarities and differences between the spectra and how they relate to the theoretical dust condensation sequences around AGB stars.

Chapter 6 covers the interpretation of the 11.3μm feature in the spectra of carbon-rich AGB stars. The implications of the findings in chapter 4 regarding errors in laboratory spectra are also discussed and how they lead to the reconciliation of astronomical and meteoritic data on silicon carbide. This is followed in chapter 7 by further studies of carbon-rich AGB star spectra, with respect to UIR bands. The observation of a UIR band in the spectra of two carbon-rich stars with hot star companions is discussed. There is also a brief discussion of the possibility of diamond dust forming around these stars, prompted by the presolar diamonds found in meteorites.

Chapter 8 investigates the spectra of oxygen-rich AGB stars. These stars present a much wider range of spectral features and theoretical condensation models suggest there are many possible minerals forming in the circumstellar regions around these stars. Oxygen-rich AGB stars present a much more complicated situation than the carbon-rich stars. The basic interpretation of the 9.7μm feature as a silicate is investigated and an attempt is made to constrain the identification further. The discovery of a new feature at 9.25μm, attributed to SiO_2 dust is discussed. Some forms of SiO_2 also have a spectral feature at 12.5-13.0μm. A similar feature in the O-rich AGB star spectra, previously identified as an Al_2O_3 feature, may also be attributable to SiO_2.

Finally, chapter 9 summarises the results from the previous chapters and discusses future research that should be undertaken to benefit from the advances made in this work.

Chapter 2

Element/Isotope Production in AGB stars

"It is a riddle wrapped in a mystery inside an enigma"

Winston Churchill

2.1 Introduction

It is now appropriate to discuss nucleosynthetic processes in the interiors of stars as this is where the constituents of dust particles originate. This chapter will provide a basic introduction to the relevant nucleosyntheses and how they apply to low- to intermediate-mass stars (the precursors of AGB stars) at their various stages of evolution. This chapter is based upon the works of Iben & Renzini (1983), Frost & Lattanzio (1992), Lattanzio & Frost (1998) and Mowlavi (1998a,b)[1].

2.1.1 The Hertzsprung-Russell (H-R) diagram

As a star evolves, different mechanisms of element production, i.e. nucleosynthetic processes, are brought into play. The evolution of a star may be shown as a path on a Hertzsprung-Russell diagram[2]. The basic route for an approximately solar mass star is shown schematically in Fig. 2.1. As a star grows older it will run through the H-R diagram on an evolutionary track fixed from the beginning by its basic characteristics, mass and composition. Since, for the purposes of this thesis, we are interested only in the post-main

[1] For the nuclear reactions presented here, $X + a \rightarrow Y + b$ is represented by X(a,b)Y.

[2] A Hertzsprung-Russell diagram (or H-R diagram) is a graph of luminosity versus effective temperature

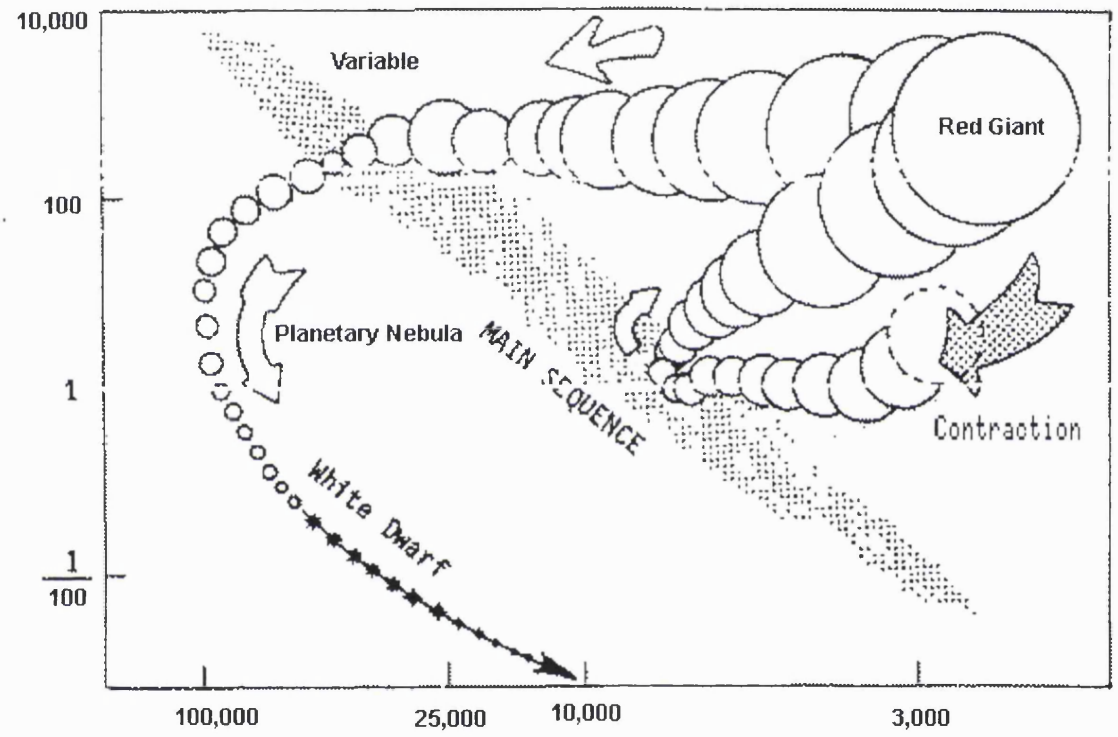

Figure 2.1: A basic schematic representation of the evolution of a $\sim 1 M_{\odot}$ star on a Hertzsprung-Russell diagram. The x-axis is temperature in kelvin, the y-axis is luminosity in units of solar luminosity (i.e. $1=1 L_{\odot}$)

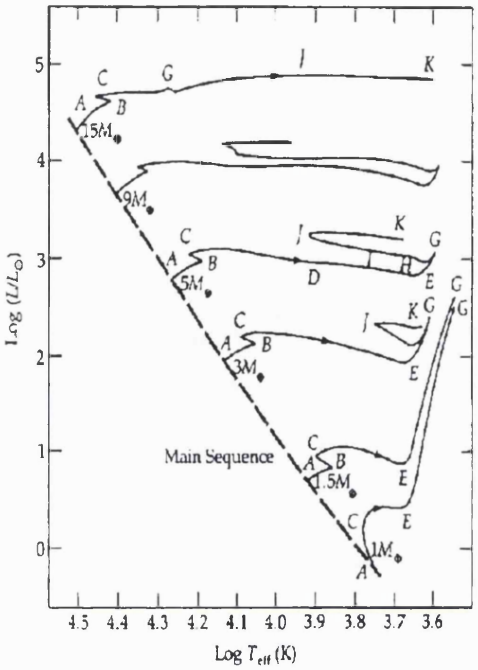

Figure 2.2: The Hertzsprung-Russell diagram of the post-main-sequence evolution of stars with different initial masses (from Zeilek & Smith 1987).

sequence evolution, Fig. 2.2 shows the evolutionary track of stars of various initial masses from the main sequence to the top of the asymptotic giant branch[3]. It is easily seen that the initial mass has an effect on the precise evolutionary track.

2.1.2 Nucleosynthetic processes

There are four major processes by which elements are manufactured at various stages of a low- or intermediate-mass (LIM) star's evolution, which will be discussed later in this chapter: 1) the proton-proton chains; 2) the CNO cycles; 3) helium burning; and 4) the *s-process*. The first three are energy generating reactions which release energy as the nuclei fuse and attain higher binding energies per nucleon. This is the case for the production of elements up to ^{56}Fe, which has the maximum binding energy per nucleon. The fourth nucleosynthetic process we discuss, the *s-process*, manufactures elements beyond the "iron peak", i.e. those elements and isotopes heavier than ^{56}Fe, which is the most energetically stable isotopic composition.

[3]the $9M_\odot$ and $15M_\odot$ initial masses are shown for completeness. These stars do not have AGB phases since they do not develop degenerate cores

From the point of view of dust forming species and interstellar chemical enrichment, nucleosynthesis involves only hydrogen burning during the main sequence and up to the top of the first assent of the red giant branch, where core helium burning begins. The two nucleosynthetic processes relevant to H-burning, i.e. the p-p chains and the CNO cycles, are discussed in the next section. At core temperatures $T_{core} \leq\sim 2 \times 10^7 K$ (i.e. stars with main sequence masses $M_\star \leq\sim 1.2 M_\odot$) the p-p chains are the dominant energy producers. For stars with main sequence masses $M_\star \geq\sim 1.2 M_\odot$, and therefore higher core temperatures, the CNO cycle dominates. As the star evolves other nucleosynthetic processes come into play. Eventually helium-burning and the s-process produce more varied, heavier elements and affect the chemical and isotopic evolution of the star.

2.1.3 Chemical evolution

Once stars reaches the AGB phase, strong convection currents dredge up the newly synthesized elements to the surface. This has a profound effect on the chemistry occurring in the atmospheres of the stars and their grain forming potentials. On reaching the AGB phase, a star has an oxygen rich atmosphere. In the helium-burning regions inside the star the triple-α process is manufacturing ^{12}C (see section 2.2.1.4). This carbon is dredged up to the surface by the convection currents and thus changes the chemical composition of the stellar atmosphere. This is due to the remarkable stability of the carbon monoxide (CO) molecule, which is very stable and forms very easily. Therefore, the relative abundances of carbon and oxygen are crucial to the chemistry in the star's atmosphere (Salpeter 1977). If the carbon-to-oxygen ratio (C/O) is less than unity all the carbon atoms will be locked into CO and not available for formation of molecule and grains around these stars and hence the chemistry is oxygen-rich. Similarly, if C/O>1, all the oxygen atoms are trapped in CO and the chemistry is dominated by the carbon atoms. The dredge-up of carbon from the helium-burning regions slowly changes the surface of the stars from oxygen-rich (C/O<1) to carbon-rich (C/O>1). Some of the effects on the chemistry and the grains forming around these stars are discussed in chapters 6 & 7 (carbon-rich chemistry) and chapter 8 (oxygen-rich).

2.2 Evolution of LIM stars: pre-main sequence to the AGB phase

Low- and intermediate mass (LIM) stars are those which end their lives without proceeding through carbon- and heavier-element burning. Within this group of stars, there is still a difference in the exact evolutionary path taken, depending on their initial masses. Stars with initial mass $M_\star \leq 0.08 M_\odot$ never reach central temperatures high enough to ignite hydrogen and become brown dwarfs. Those stars with initial masses of $\sim 0.08 M_\odot \leq M_\star \leq\sim 0.5 M_\odot$ only experience core hydrogen burning to produce helium and end their lives as He-white dwarfs. However stars with initial masses of $\sim 0.5 M_\odot \leq M_\star \leq\sim 8 M_\odot$ experience both hydrogen and helium burning and eventually become C-O white dwarfs. Stars with $M_\star >\sim 10 M_\odot$ do not develop degenerate C-O cores and will burn hydrogen, helium, carbon and heavier elements, to finally explode as a supernova. Such massive stars are beyond the scope of this work.

2.2.1 Structural evolution of LIM stars

There are five different phases in the evolution of LIM stars: pre-main sequence, main sequence, red giant branch, core helium burning and the asymptotic giant branch.

2.2.1.1 The pre-main sequence (PMS) phase

During this phase the young proto-star contracts until the core temperature is high enough to ignite hydrogen. The energy released prior to this phase is gravitational.

2.2.1.2 The main sequence (MS) phase

The main sequence is represented in Fig. 2.2 by a dashed line. Once the core temperature of the star reaches $1.2 \times 10^7 K \leq T_{core} \leq 2.5 \times 10^7 K$, hydrogen ignites and starts to manufacture helium through the p-p chain and CN-cycle starts, this marks the transition from the PMS to the MS. Hydrogen-burning characterizes the main sequence.

The p-p chains basically convert hydrogen into helium by the following three reaction routes:

$$\text{a)}\,^1H(p,\beta^+\nu)^2D(p,\gamma)^3He(^3He,pp)^4He$$

b)$^3He(\alpha,\gamma)^7Be(\beta^-,n)^7Li(p,\alpha)^4He$

c)$^7Be(p,\gamma)^8B(\quad,\beta^+\nu)^8Be(\quad,\alpha)^4He$

The p-p chain reactions dominate nucleosynthesis in low-mass ($<\sim 1.2M_\odot$) main-sequence stars.

Fig. 2.3 is a schematic representation of the CNO cycles. The left-hand cycle in Fig. 2.3 is known as the CN cycle. This is the important part of the cycle with respect to low- and intermediate-mass stars, since the temperatures required to allow the ON part of the cycle to operate are only expected for quite massive stars. By far the slowest reaction in the CN-cycle, under conditions relevant to those stars in which the CN cycle is expected to operate, is the $^{14}N(p,\gamma)^{15}O$ reaction. Therefore we should expect a buildup of ^{14}N. If the CN cycle operates for a sufficient time practically all of the C and N isotopes will be transformed into ^{14}N. This is one of the characteristics of the CN cycles. Another important signature of CNO processed material is the isotopic ratio of $^{12}C/^{13}C$. The solar value for this ratio is $\sim$89, while the value for CN-processed material should be $\sim$4. The CN cycle dominates in stars with main-sequence masses $>\sim 1.2M_\odot$. The full CNO cycle can come into operation for sufficiently high masses (leading to the eventual conversion of oxygen into nitrogen) but is not usually relevant to the low and intermediate mass stars considered here.

The main sequence is the longest phase of a star's life (the actual time a star spends on the main sequence depends on the initial mass of the star).

2.2.1.3 The red giant branch (RGB) phase

The transit of a star from its main sequence position on the H-R diagram to the red giant region is so rapid that stars are rarely observed between these two regions. The evolution to the red giant phase is indicated on the H-R diagram (Fig. 2.2) as point C. At this stage, the stellar core is exhausted of hydrogen and the star has to rearrange its structure. The helium core contracts rapidly and heats up, while hydrogen in a shell surrounding the core continues to burn. For low-mass stars, the core becomes so dense that it becomes

Figure 2.3: The CNO cycles with an additional reaction to ^{19}F.

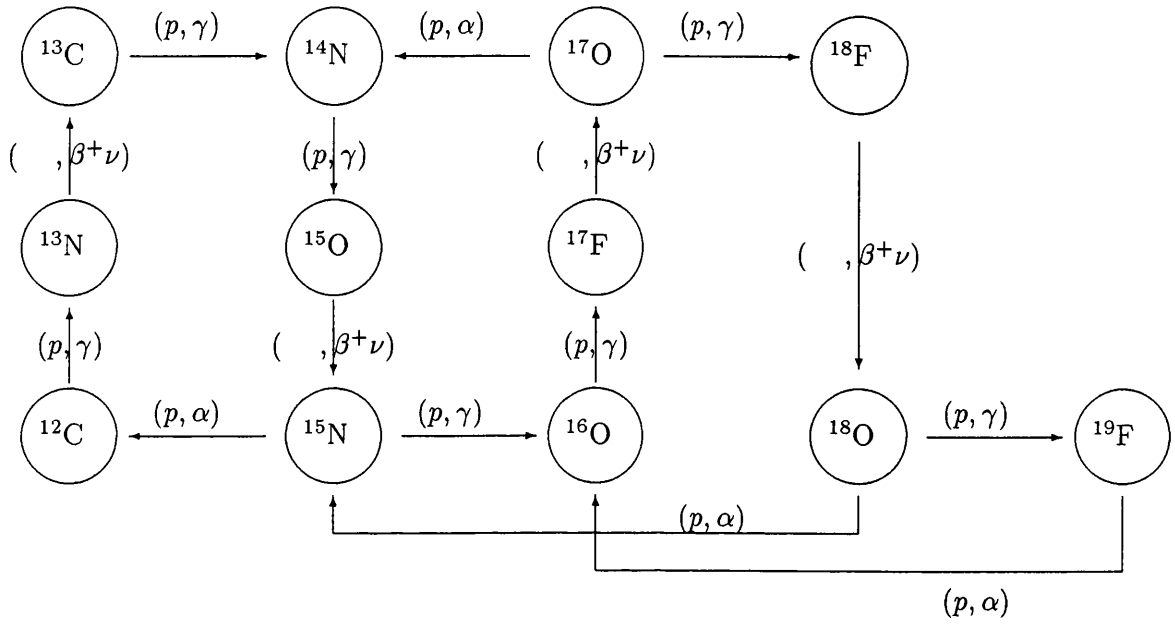

degenerate[4]. In this state, the core has a degenerate gas pressure which depends only density, not temperature. This enables the core to attain a pressure sufficient to support the weight of the upper layers of gas, even though no fusion reactions are taking place in the core. For intermediate-mass stars, the helium core does not become degenerate, but burns the helium to create a carbon-oxygen core (which does become degenerate). As the core contracts, the outer layers expand and cool and the star swells to become a red giant. Low mass stars ($M_\star \leq\sim 2M_\odot$) may spend up to ~20% of their lives as red giants, whereas intermediate mass stars ($\sim 2M_\odot \leq M_\star \leq \sim 8M_\odot$) have much shorter red giant phases (<7% of their MS lifetime). During the RGB phase there is a deep convective outer envelope, which penetrates the deep layers containing the remnants of hydrogen burning. Thus, newly synthesized nuclei are mixed and transported to the surface. This process is called the "*first dredge-up*". As this name implies, there are further "*dredge-up*" scenarios, and thus the red giant branch is only the first time the star travels up the giant branch of the H-R diagram. This has lead to the red giant branch also being called the "first ascent

[4]According to the *Pauli Exclusion Principle* only two electrons with opposite spins can have a given energy in a given volume at one time. Consequently in a very dense gas, the atoms are so tightly packed that they are only held apart by the fact that the electrons cannot exist in the same space. This creates the degenerate gas pressure that prevents further contraction.

of the giant branch".

2.2.1.4 The core helium burning (CHeB) phase

At this stage the helium core contracts and therefore heats up. Eventually the temperature needed to ignite the helium is reached ($\sim 10^8$K) and the triple-α process begins. This causes the *helium flash* which occurs because the helium core is degenerate and the triple-α process is very sensitive to temperature. Instead of expanding as the temperature increases (as we expect for an ordinary gas), a degenerate gas conducts[5] the energy produced to other parts of the core and thus the onset of helium-burning in a small part of the core quickly spreads to throughout the whole core. This is the *helium flash.* Eventually the core temperature reaches $\sim 350 \times 10^6$K causing the gas to become non-degenerate, expand and cool. The *helium flash* marks the end of the RGB phase. This is represented on the H-R diagram (Fig. 2.2) as point E.

During the core helium burning phase, helium is fused to produce carbon and oxygen in a convective core within a thin hydrogen burning shell. Helium burning includes the triple α-process, which is the mechanism by which ^{12}C is produced from three ^{4}He nuclei by the reaction:

$$^4He(\alpha,\ )^8Be(\alpha,\ )^{12}C^*(\ ,\gamma\gamma)^{12}C$$

where the '$*$' indicates an excited state of the ^{12}C nucleus. The third α must be added faster than ^8Be can decay. Since the half-life of ^8Be is $\sim 7 \times 10^{-16}$seconds, it is clear that the equilibrium abundance of ^{8}Be is very small. Helium burning can also lead to the α-rich nuclides ^{16}O, ^{20}Ne and ^{24}Mg by (α,γ) addition reactions starting from ^{12}C. Furthermore, α-addition to the ^{14}N seed (abundant following the CN cycle) can follow this chain:

$$^{14}N(\alpha,\gamma)^{18}F(\ ,\beta^+\nu)^{18}O(\alpha,\gamma)^{22}Ne$$

[5] In a degenerate gas, the electrons are distributed more or less uniformly throughout the medium, surrounding the nuclei. The nuclei themselves are regularly spaced and become more tightly constrained as the pressures increase, until they are so fixed with respect to each other that they resemble a crystal lattice. Under such conditions, the material more closely resembles a solid than a gas. The degenerate gas is, therefore, a very good energy conductor

The end member, ^{22}Ne, may be of importance in interpreting meteoritic data (see chapter 3). It may also be important in the *s-process*.

2.2.1.5 The asymptotic giant branch (AGB) phase

When the core is exhausted of helium the star enters the AGB phase and becomes a red giant again (Fig. 2.2 point E-G). This is called the second ascent of the giant branch. At this stage the degenerate core is made of carbon and oxygen, and there is now a thin helium-burning shell, at the base of the helium-shell, surrounding the C-O core and above the He-shell, a thin hydrogen-burning shell, at the base of the outer hydrogen-rich shell. The outer hydrogen zone contains a deep convective envelope which, in stars with $M_\star >\sim 4M_\odot$, transports the products of hydrogen-burning to the surface when the star reaches the base of the AGB ("*second dredge-up*"). The energy-producing nucleosynthetic processes are confined to two regions (the He-burning shell and the H-burning shell) containing less than 3% of the total stellar mass. One of the characteristics of the AGB phase is the thermally unstable He-burning shell. This shell periodically produces a hundred to a million times the energy produced by the H-burning shell on a time-scale of several tens of years. These energy bursts manifest themselves as thermal pulses and hence this phase is known as the thermally pulsing-AGB or TP-AGB phase. These pulses typically happen every 10^4years or so for a C-O core mass of $\sim$0.6-0.8$M_\odot$, during which time the star is quiescent (the "interpulse" phase; Mowlavi 1998). The pulses create convective zones in the He-burning shell. The consequences of the pulses are important to both the chemistry and the structure of the stars. The material manufactured in the He-burning shell is convectively mixed and transported to close to the base of the H-burning shell, where the products of these two shells can be involved in further nucleosynthesis. Furthermore, after the extinction of the He-burning thermal pulse, the outer convective zone then penetrates deep into the hydrogen and helium burning shells where, eventually, it can transport carbon to the surface. This is called the "*third dredge-up*". It is clear that, since the thermal pulses are repeated periodically, the third dredge-up event can happen many times. Eventually, enough carbon can be transported to the surface that the initial cosmic C/O ratio of $\sim$0.4 is raised to $>$1 and a carbon star is formed due to the transformation of the surface chemistry.

2.3 AGB phase nucleosynthesis

There are four sites of nucleosynthesis identifiable in AGB stars: the hydrogen burning shell; the helium burning shell; sites of extra ^{13}C production; and hot bottom burning[6]

1) **The H-burning shell:**
During the interpulse phase the H-burning shell synthesizes helium and some heavier elements through the p-p chains and the CN-cycle. These elements are brought to the stellar surface continuously by the deep convective envelope.

There are two nuclides, ^{13}C and ^{17}O, produced by the CNO cycles which are important for testing stellar models using observations. As discussed in section 2.2.1, all paths in the CNO cycle lead to the overproduction of ^{14}N. Consider the production of ^{13}C by the reaction $^{12}C(p,\gamma)^{13}N(\ ,\beta^+)^{13}C$. The ^{13}C is then destroyed by the reaction $^{13}C(p,\gamma)^{14}N$. A similar situation occurs for ^{17}O which is created by $^{16}O(p,\gamma)^{17}F(\ ,\beta^+)^{17}O$, but destroyed by $^{17}O(p,\alpha)^{14}N$. As a result of these mechanisms, ^{13}C and ^{17}O are overabundant in the less proton-dense intermediate layers of LIM stars, but destroyed in the proton-dense deeper regions. The first dredge-up transports ^{13}C and ^{17}O to the surface. This is observed in the drastic decrease in the $^{12}C/^{13}C$ and $^{16}O/^{17}O$ ratios of red giant stars (El Eid 1994).

2) **The He-burning shell:**
Remnants of the H-burning shell injected into the He-burning shell also cause it to produce *s-process* elements/isotopes. For instance, the injection of ^{13}C into the He-burning shell leads to the production of neutrons by the reaction $^{13}C(\alpha,n)^{16}O$. The neutrons are then used in the slow neutron addition - the *s-process*. As mentioned above, once the fusion of nuclei has reached ^{56}Fe, fusion no longer takes place and the heavier elements are made by neutron addition. There are two distinct paths this process can take: rapid neutron addition (the *r-process*), in which the neutron additions occur before any nuclei have time to β-decay. In this process neutrons must be added in a fraction of a second, correspond-

[6] Hot bottom burning occurs in the H-burning shell and is, therefore, not strictly a separate site, however it requires high temperatures and core mass to operate and therefore will be regarded as separate here

ing to neutron densities of $\sim 10^{23}\mathrm{cm}^{-3}$. This sort of neutron addition is expected to occur in supernovae rather than AGB stars and will not be discussed further here. The alternative is slow neutron addition or *s-process*, in which any β-decay that can happen, will happen before the addition of another neutron. For all β-decays to occur, the time interval between neutron captures must be $\sim 10^4$years, corresponding to neutron densities of only $\sim 10^5\mathrm{cm}^{-3}$. This process is pertinent to AGB stars. In order for the *s-process* to operate there must be a source of neutrons. Sources of neutrons include: ^{22}Ne nuclei which produce neutrons by the reaction: $^{22}Ne(\alpha,n)^{25}Mg$; and also ^{13}C nuclei produced earlier by the CN-cycle which produce neutrons by the reaction $^{13}C(\alpha,n)^{16}O$.

3) **Extra ^{13}C production**:

The quantity of neutrons required to account for the *s-process* products cannot solely come from the above ^{13}C from the H-burning shell (Mowlavi 1998a). This can be compensated for by the injection of protons into the C-rich areas. During the interpulse phases, when the temperature increases, the following reaction can occur: $^{12}C(p,\gamma)^{13}N(\ ,\beta^+\nu)^{13}C$, providing another source of ^{13}C and thus another source of neutrons for the *s-process*. There are other sources of neutrons for the *s-process*, including ^{22}Ne in the higher mass stars.

4) **Hot bottom burning**:

This occurs in stars with masses $M_\star \gtrsim 4M_\odot$, in which the bottom of the convective envelope can reach temperatures $T \gtrsim 5\times10^7$K. This initiates H-burning within the convective envelope, which is known as envelope-burning or hot bottom burning. This process destroys ^{12}C by the reaction $^{12}C(p,\gamma)^{13}N(\ ,\beta^+\nu)^{13}C$ and ^{18}O by the reaction $^{18}O(p,\alpha)^{15}N(p,\alpha)^{12}C(p,\gamma)^{13}N(\ ,\beta^+\nu)^{13}C$ through the CNO cycle (Boothroyd *et al.* 1993), which adds to the apparent high abundance of ^{13}C around some AGB stars and yields nitrogen-rich Type I planetary nebulae (Kingsburgh & Barlow 1994).

We now have the broad outline of which elements and isotopes are expected to be produced by AGB stars, and so we can discuss the dust species expected to form in their atmospheres (chapter 5).

Chapter 3

Meteorites & Cosmic Chemical Memory

"On earth there is no heaven, but there are pieces of it."

Jules Renard

3.1 An introduction to meteorites

The term meteorite is derived from the Greek. It means *that which originates in the atmosphere.* Today, we define a **meteoroid** as a small object travelling through space; a **meteor** as its luminous trail in the sky; and **meteorites** are the fragments of the meteoroid that collide with the Earth and survive to reach the surface.

Meteoritic materials are constantly reaching the Earth. Several falls are observed and recovered every year. Most of these are stones or metallic masses of only a few kilograms, small enough to be held in your hand. The rarer, larger falls are produced when a mass of hundreds or thousands of kilograms strikes the atmosphere, often breaking up to scatter fragments over a large area. Even larger projectiles can also strike at intervals of thousands of years, producing impact craters when they crash into the surface.

A surprising variety of rocks are in the Earth's meteorite collections. The traditional description of these meteorites are based on their appearance and bulk composition. There are three classes of meteorite: iron, stony and the rarer stony-iron types. **Iron** meteorites are nearly pure metallic nickel-iron. Their extraterrestrial origin is obvious when we bear

in mind that iron and most other metals naturally occur on the earth in the form of oxides rather than in the pure metallic state. The **stony** meteorites more closely resemble terrestrial rocks, and they are not generally recognized as extraterrestrial in origin unless their fall was witnessed. The **stony-irons** contain a mixture of stone and metallic iron, as suggested by their name.

A more useful categorization, rather than one dependent on appearance and bulk composition of the meteorites, is based on their history or that of their parent bodies (the asteroids and/or comets of which the meteorites are fragments). Some meteorites have a chemistry indicative of little alteration since their formation (and probably since the formation of the solar system). These are known as **primitive meteorites**. All primitive meteorites are stony, although not all stony meteorites are primitive. Primitive meteoritic material remains largely unaltered by its violent arrival at the Earth's surface. Those meteorites that have experienced major chemical or physical changes since their formation are known as **differentiated meteorites**. Like igneous rocks on Earth, these rocks solidified out of a molten state. Differentiated meteorites appear to be fragments of differentiated parent bodies that had experienced major episodes of heating, along with the loss of volatile materials. All of the iron and stony-iron meteorites (and many of the stony meteorites) are instances of differentiated meteorites.

Primitive meteorites have chemical compositions that are relatively unchanged since they formed in the cooling solar nebula $\sim$4.5billion years ago. Except for a shortage of gaseous and other volatile constituents such as hydrogen, helium, argon, carbon and oxygen, the composition of the primitive meteorites is thought to be the same as that of the sun.

The *most* primitive meteorites are a special group, called the **carbonaceous meteorites**. These are relatively rich in carbon and also in volatile compounds such as water. From their composition we conclude that they were formed in a cooler region of the solar nebula from the other primitive meteorites.

3.2 Cosmic chemical memory

There has long been a consensus that the solar system was formed from part of an interstellar cloud containing dust grains from a variety of stellar sources. However, in the 1960's and early 1970's the most popular theory for the formation of the solar system was that the material in the proto-solar system (the solar nebula) was completely vaporized and mixed so that it became isotopically and chemically homogeneous and thus lost any evidence of its previous history. The first evidence that the solar nebula was not homogeneous came from oxygen isotope studies which revealed an excess of ^{16}O in the calcium-aluminium-rich inclusions in meteorites (Clayton *et al.* 1977). This was closely followed by the detection of other isotopic anomalies for Mg, Si, Ca, Ti, etc. (e.g. Lorin & Michel-Levy 1978; McCulloch & Wasserburg 1978; Lee *et al.* 1978). These anomalies are very small and are believed to imply severe reprocessing and dilution of the carrier grains in the solar nebula. These were not pristine interstellar grains. In the late 1980's, however, small refractory grains were found in the most primitive meteorites, which have isotopic anomalies orders of magnitude larger than those in the calcium-aluminium-rich inclusions. These anomalies are indicative of an unaltered presolar origin. The isotopic anomalies have become collectively known as the *cosmic chemical memory* of the grains (Clayton 1978). Since their discovery, a great deal of laboratory investigation of presolar grains has been undertaken and has produced much data of interest regarding interstellar and circumstellar grain nucleation, growth and composition as well as models of stellar nucleosynthesis.

In the next few paragraphs there will be a brief outline of the presolar grains found in meteorites, followed by a discussion of the information available from isotopic analyses of presolar grains concerning their history and origin.

3.2.1 Using isotopes

Six types of presolar material have been isolated from meteorites (Alexander 1997) - silicon carbide (SiC), silicon nitride (Si_3N_4), graphite, the refractory oxides corundum (Al_2O_3) and spinel ($MgAl_2O_4$), nanodiamonds and organic material. The organic material is probably of interstellar origin (Sandford 1996). Since we are interested in species formed in circumstellar regions, the organic material will not be discussed further here. The re-

maining five materials are believed to be of circumstellar origin and with the exception of diamond have had single grains isotopically analysed. Due to their small grain sizes, the diamonds have proved impossible to separate into individual grains. Hence, the isotopic analyses have been performed on aggregates of many grains, and have, therefore, provided less obvious evidence of their origins than the other presolar grains. This will be discussed further later.

Presolar grains were discovered through the search for the carriers of isotopically anomalous noble gas components in bulk analyses. This led to the isolation of the carbon bearing presolar grains. They have since been extensively analysed for anomalies in the isotopic compositions of the major elements as well as trace elements and noble gases trapped inside the grains. These isotopic investigations have led to the inferred origins of the grains (e.g. Bernatowicz 1987, Virag 1992) as well as to the reformulation of some nucleosynthesis models (e.g. Gallino *et al.* 1993, 1994).

In order to understand the vast amount of complex data available from these presolar grains, I will set down a few examples of how isotopic compositions put constraints on the sources of the elemental constituents of the grains.

Silicon carbide from meteorites is probably the best understood of the presolar grains available in the laboratory. Presolar SiC contains the major elements silicon and carbon, both of which have non-solar isotopic compositions; trace elements including nitrogen, magnesium, calcium, titanium, barium, strontium, neodymium and samarium, also with non-solar isotopic compositions; and isotopically non-solar noble gases. By comparing the isotopic compositions of all these constituents with nucleosynthesis models, most presolar SiC grains have been attributed to carbon-rich AGB star sources, with a few ($\sim$1%) attributed to novae and supernovae sources. Closer investigations of certain elements have constrained the stellar sources still further (Anders & Zinner 1993).

For example, the isotopes of krypton, ^{80}Kr and ^{86}Kr, can be used to discriminate among various stellar sources. ^{86}Kr can act as a chronometer of the s-process. Its precursor ^{85}Kr has a half-life of only 10.8 years and thus decays before capturing a neutron if the mean neutron capture time is much longer than 10 years. The other isotope, ^{80}Kr, is a stellar

thermometer. Its precursor ^{79}Se has a long-lived ground state ($t_{\frac{1}{2}} = 6.4 \times 10^4 years$), but a short-lived excited state ($t_{\frac{1}{2}} = 3.92 mins$), so that at low temperatures it mainly capture neutrons and bypasses ^{80}Kr, but at high temperatures the following chain takes place:

$$^{79}Se(\beta, 3.9mins)^{79}Br(n,\gamma)^{80}Br(\beta, 18mins)^{80}Kr.$$

For low mass AGB stars (1-3$M_\odot$) the process is the low temperature one and therefore the ^{80}Kr production is low. In intermediate mass stars (4-8$M_\odot$) the temperature is high enough but the neutron density is so high that ^{80}Kr production is still low, whereas stars of more than $\sim 10M_\odot$ have the necessary combination of high temperature and low neutron density to produce copious amounts of ^{80}Kr. Therefore, presolar grains with an excess of ^{80}Kr can be attributed to stars of mass $>10M_\odot$.

The isotopic composition of barium can also put constraints on the stellar source. The isotope ^{138}Ba has an extremely small neutron capture cross-section, and consequently the ratio ^{138}Ba/^{136}Ba is a sensitive measure of the neutron exposure experienced by the seed nuclei (Gallino *et al.* 1993).

Some presolar carbonaceous materials found in meteorites have anomalous neon isotopic compositions. These grains have been found to be extremely ^{22}Ne-rich, ^{22}Ne/^{20}Ne $\geq$ 100 (almost a thousand times the solar ratio). One explanation for this high abundance of ^{22}Ne is that it is the daughter product of ^{22}Na which was trapped during condensation from a hot gas during a rapid cooling. Nucleosynthesis arguments point to novae as the probable source (Leising & Clayton 1987). Another possible source of ^{22}Ne was mentioned in chapter 2, where I discussed the production of ^{22}Ne through helium burning starting with the abundant ^{14}N isotope produced by the CNO cycle:

$$^{14}N(\alpha,\gamma)^{18}F(\ \ ,\beta^+\nu)^{18}O(\alpha,\gamma)^{22}Ne$$

This is expected to occur in AGB stars. It is interesting to note that the ^{22}Ne/^{20}Ne ratio is similarly high in cosmic rays and has been attributed to an origin from high and intermediate mass stars (Lukasiak *et al.* 1994)

By studying the nature of meteoritic presolar grains we can learn about grain formation

processes. It is also important to make models of circumstellar grain growth consistent with the samples of these grains available in the laboratory.

As indicated above, silicon carbide is probably the best studied of the meteoritic presolar grains. It can also be studied through infrared observations of circumstellar dust. It is therefore germane to discuss the nature of meteoritic SiC in detail.

3.2.2 Presolar silicon carbide

For detailed reviews of SiC in meteorites see Ander & Zinner (1993), Ott (1993) and Hoppe & Ott (1997).

The first unambiguous identification of SiC in meteorites was by Bernatowicz *et al.* (1987). The SiC they found was of the β-SiC form and the crystal grains were 0.1-1 μm in size. Bernatowicz *et al.* (1987) concluded that the SiC was probably formed in the atmospheres of late-type carbon stars. Since then, there have been many papers on the origin of SiC grains in meteorites based on isotopic measurements (e.g. Tang *et al.* 1989; Virag *et al.* 1992; Hoppe *et al. 1994*; Amari *et al. 1994*, etc.) There has also been some discussion about grain sizes and the amounts of SiC found in meteorites. All SiC recovered from meteorites has turned out to be of the β-SiC polytype (Bernatowicz 1997). Tang *et al.* (1989) looked at SiC found in carbonaceous chondrites. They found single grains up to 12 μm in diameter. This is much larger than the grain sizes predicted by circumstellar grain condensation models (e.g. Kosaza *et al.* 1996) or by radiative transfer fits to the overall energy distribution (e.g. Griffin 1990). Tang *et al.* (1989) found that most of the carbon and nitrogen isotope ratios were indicative of nucleosynthetic processes believed to occur in carbon-rich AGB stars, whilst a few indicated possible nova sources. Based on this and the silicon isotopic composition, they concluded that the meteoritic SiC in their sample came from at least four separate types of stars, including novae. They also pointed out the surprising rarity of SiC in meteorites. Carbon stars are though to contribute approximately a third of the total mass ejected into the interstellar medium by stars (Tielens 1990), and yet even the most primitive chondrites contain only 6 p.p.m. of their silicon in SiC, the rest being in the form of silicates (Anders & Zinner 1993). There is also as yet no firm evidence of any SiC in the interstellar medium, which implies an observational

upper limit to the SiC abundance of 5% of the interstellar medium dust mass (Whittet *et al.* 1990). To address this problem, Tang *et al.* 1989 suggested several destruction mechanisms for SiC, none of which satisfactorily explain the observational and laboratory data.

Virag *et al.* (1992) investigated the "large" meteoritic SiC grains of 1.5-26 μm effective diameter. The first problem with such large grains is, in fact, their size. As mentioned above, conventional theories cannot grow such large grains. Analysis of the infrared emission from AGB stars (believed to be the source of much of the SiC in meteorites), with mass-loss rates of typically $<10^{-5}M_{\odot}yr^{-1}$, give an upper size limit for the grain radii of a few hundred angstroms (Virag *et al.* 1992). Optical constraints require that for effective emission at wavelength λ by grains of radius a, $2\pi a$ should be $\ll \lambda$, implying that most of the observed emitting grains are of a size $\leq$0.1 μm (Jura 1990). Constraints on grain size were also discussed by Martin & Rogers (1987), who found a grain size limit of 0.1 μm based on polarization measurements. However, Jura (1994) found that for amorphous carbon grains around the carbon star IRC+10216, about 1% of the dust mass must contain particles that are larger than 1 μm in diameter in order to explain the observed circumstellar polarisation. He suggested that if the SiC grains have a similar size distribution, then large SiC grains found in meteorites could originate in the outflows of such stars. Jura, Turner & Balm (1997) have suggested that some AGB/post-AGB stars have long-lived discs rather than simple outflows. For their example of the Red Rectangle (a post-AGB object), millimetre and submillimetre observations are consistent with orbiting particles of diameter $\geq$ 0.04cm (400 μm) at temperatures of about 50K. This may also explain the meteoritic grain-size problem. However, Griffin (1990) found that his SED (spectral energy distribution) modelling required the size of the particles around IRC+10216 to be limited to the range 0.005 μm$\leq$ *radius* $\leq$ 0.05 μm. Bagnulo, Doyle & Griffin (1995) also used radiative transfer modelling to fit the spectrum of IRC+10216. They found that their best fit to the observed IRAS LRS spectrum was achieved using only amorphous carbon and no SiC, which is surprising since this star has an obvious infrared feature attributed to SiC (Treffers & Cohen 1974; Speck *et al.* 1997). However, their fit also required the carbon grains to have a radius of $\leq$ 0.05 μm. Such small grains obviously cannot account for the large-grained meteoritic samples of SiC believed to originate in the outflows of carbon stars. Groenewegen (1997) also performed radiative transfer modelling on the spectrum

of IRC+10216. He found that, rather than using a range of grain sizes, the spectrum was best fitted by assuming a single dominant grain size of ~0.16 μm, and that this seemed to be independent of the exact optical constants used. He also found that grains of 0.1 μm and 0.35 μm size are needed to explain the polarization observations. He suggested that very small grains ($\leq$0.08 μm) may not exist around late-type stars. Thus the astronomical evidence to which the meteoritic work is compared is somewhat contradictory. We note that larger grains might be present in carbon star outflows and yet not contribute to the observed infrared feature. However, half the mass of the SiC isolated from the Murchison meteorite is in grains of dimension $\geq$0.6 μm. Anders & Zinner (1993) argued that the low abundance of small grains (diameter $\leq$0.4 μm) was not experimental, although they did not suggest any other reason for the lack of small grains. It has since been pointed out (Alexander 1997) that Murchison SiC grains appear to be unusually large compared to the other meteoritic samples. It has been suggested that Murchison may be missing 50-80% by mass of its SiC, most of which would have been <0.4 μm in diameter, which was probably lost during extraction from the meteorite. Alexander (1997) also pointed out that 1.5-35nm diameter SiC grains are present in and amongst the meteoritic nanodiamonds. So it seems that there are small enough grains in meteorites to account for astronomical observations, but that models to fit astronomical observations cannot account for the large SiC grains found in meteorites. The models are somewhat conflicting and it is conceivable that they are based on erroneous optical constants (See chapter 4). It is also possible that the larger grains do not contribute to the spectral regions being analysed. These models need to be re-evaluated in order to accommodate the meteoritic data.

Alexander (1993) set out to determine how many stellar sources are needed to explain the isotopic compositions of SiC grains found in meteorites, and whether the isotopic data can be explained by a single AGB star. He argued that either most of the grains come from separate sources, or that there are relatively few sources, with varying isotopic compositions. If each individual source has a fixed isotopic ratio, more than 75 sources would be needed to explain all the isotopic data from the grains in this study. He concluded that between 10 and 100 AGB stars contributed to the SiC in the solar system. He did not discuss any contribution from novae or supernovae. One of the problems of assigning the production of the meteoritic SiC to individual AGB stars seems to be that the silicon isotope ratios do not correlate with the carbon and nitrogen isotope ratios (Alexander 1993),

implying that the silicon and carbon come from different sources. A possible explanation for this discrepancy between nucleosynthetic predictions of Si isotopic composition for SiC grains from a single AGB star and the actual isotopic composition of meteoritic SiC grains is touched on by Timmes & Clayton (1996), who suggested that the silicon isotopic ratios of the whole galaxy change as a function of time. This is because the production rates of different silicon isotopes in supernovae change with time. Early Type II supernovae produce only ^{28}Si, whereas the later supernovae (Type I and Type II) also manufacture ^{29}Si and ^{30}Si. Therefore, low- and intermediate-mass stars born at different times incorporate silicon with different isotopic ratios. When these stars reach the AGB phase and produce carbonaceous dust grains, the silicon isotopic ratios of these grains reflect the original silicon composition. Since the time taken to evolve to the AGB phase depends on the mass of the star, the SiC released from AGB stars of different initial mass at the same time may have different silicon isotopic compositions. Therefore, more detailed analyses of the evolution of galactic silicon isotopic compositions are desirable.

A small fraction (<1%) of SiC grains from meteorites have isotopic signatures consistent with an origin in supernovae. Amari *et al.* (1992) studied five meteoritic SiC grains with peculiar isotopic ratios not attributable to AGB star origins. They concluded that these grains could be attributed to a supernova if a satisfactory mechanism for mixing between different nucleosynthetic production layers could be brought into play. There have been other papers on supernova origins for some SiC grains (e.g. Nittler et al 1995a,b), however, it is beyond the scope of the present work to go into this subject in detail.

It is clear from the discussion above that there are details obtained from meteoritic SiC that need to be incorporated into our models of dust for both circumstellar and interstellar space. The most striking data that should be incorporated are: (a) the SiC grains originate from around carbon-rich AGB stars; (b) the grains range from as small as 1.5nm to as large as 26μm in size; and (c) they are all of a single polytype (β-SiC).

3.2.3 Other presolar grains

Diamonds: The least well understood of the presolar grains in meteorites are the diamonds (also known as nanodiamonds due to their small size). Diamonds in the interstellar medium were first expounded in 1969 by Saslaw & Gaustad (1969). They argued that.

although graphite is the thermodynamically stable form of carbon in dust-forming regions and in interstellar space, it should be possible for diamond to form as a metastable product. They argued that carbon atoms impinging on graphite have a low sticking probability, which can be explained on the basis that new carbon atoms can attach themselves strongly only at the edges of the graphite sheet, which constitutes a very small fraction of the total area. Carbon atoms which land at an arbitrary site are more likely to be removed by collision than to migrate to the edge of the sheet and stick there. The more isotropic diamond crystal is not limited in this way, and one might expect diamonds would grow more rapidly than graphite particles from a supersaturated carbon vapour. It has since been shown that diamonds do form by chemical vapour deposition (Daulton *et al.* 1996). Under these conditions diamond is only metastable by 2kJ/mol, therefore the kinetics can be fine-tuned to favour diamond formation. Following this theoretical work, interest in diamond lay dormant until, in 1987, interstellar diamonds were found in meteorites (Lewis *et al.* 1987). Diamonds are the most abundant presolar grains found in meteorites, at 400 p.p.m. (c.f. 6 p.p.m for SiC and 2 p.p.m. for graphite). These interstellar diamonds have the following properties:

1) They have a mass-weighted mean crystallite size of $\sim 16\mathring{A}$

2) Correspondingly, the median size is only $\sim 10\mathring{A}$

3) These small sizes correspond to only ~60-110 atoms

4) Their size distribution is log-normal rather than power law, usually indicative of grain growth rather than grain shattering

5) Their bulk density is only 2.22-2.33g/cm^3 (compared with 3.52g/cm^3 for normal diamond; 2.25g/cm^3 for graphite)

At these small sizes many of the atoms are on the surface. Indeed, the meteoritic diamonds seems to have an interior to surface atom ratio of 3:1. This gives these diamonds some unusual characteristics.

The isotopic complexity of the noble gas component in meteoritic diamonds indicates that it comes from several sources. Other isotopically anomalous elements have also been found, including barium and strontium, which are slightly enriched in r-process isotopes. Nitrogen is also isotopically anomalous. Carbon falls within the isotopic range exhibited by terrestrial carbon, providing an excellent reminder that, while anomalous isotopic compositions are useful for identifying material formed outside the solar system, it is not

required that such material have anomalous isotopic compositions. Many models of the formation of diamonds in space that would correlate with the detailed information from meteoritic diamonds have been constructed (see chapter 7). However, as yet, there are no models that satisfactorily explain all the isotopic features.

The concept of interstellar or circumstellar diamonds has largely been ignored by the astronomical community (With the notable exception of Allamandola *et al.* 1992, discussed in chapter 7). This point will be elaborated on further after the discussion of meteoritic graphite grains.

Graphite: Graphite grains are the scarcest carbonaceous presolar grain type found in meteorites (2 p.p.m.). Presolar graphite from meteorites lies at the graphitic end of the continuum between kerogen, amorphous carbon and graphite. The grains range in size from 0.8-28 μm in diameter and have a range of densities from 1.6g/cm^3 to 2.2g/cm^3. The density of "normal" crystalline graphite is 2.25g/cm^3. All the presolar graphite grains from meteorites are in the form of spherules (Zinner 1991). Transmission electron microscopy has revealed a concentric shell structure within the spherules (Bernatowicz *et al.* 1991). The isotopic analyses of these grains, as with other presolar grains, suggest a number of stellar sources including several different AGB stars. novae, supernovae and possibly Wolf Rayet stars and planetary nebulae (Anders & Zinner 1993 and refs therein).

Again it is interesting to note that these findings have largely been ignored by astronomers, who insist on looking for amorphous carbon. Amorphous carbon is not found in meteorites. Carbon in meteorites is found in the forms mentioned above, i.e. diamond, graphite and organic molecules. However, observational studies of dust shells around carbon stars have suggested that the carbon grains are predominantly amorphous (Jura 1986; Le Bertre 1987; Volk, Kwok & Langill 1992; Lorenz-Martins & Lefevre 1993; Lorenz-Matin 1996; Le Bertre 1997). This constitutes a disparity between observational and meteoritic data that should be investigated further (c.f. Section 4.4).

There are possible explanations for this discrepancy: the fact that amorphous carbon consists of randomly oriented graphite microcrystals may be the key, but this would require a mechanism by which the microcrystals became re-oriented. The high reactivity of

amorphous carbon may cause these grains to be preferentially destroyed/transformed into organic carbon (c.f. argument for diamond stability; section 3.2.3). A better definition of similarities and differences between graphite and amorphous carbon may be helpful Unfortunately, such research is beyond the scope of the present thesis.

Refractory oxides: There are very small quantities of presolar refractory oxides (even less than graphite) found in meteorites (Huss *et al.* 1995; Nittler *et al.* 1994a,b; 1997). Most of these grains are corundum (Al_2O_3) with a small amount ($\sim$2%) in the form of spinel ($MgAl_2O_4$). On the basis of oxygen isotope analyses these grains have been divided into four groups (Nittler *et al.* 1994a,b; 1997) and the probable stellar sources were determined. The most likely stellar sources of these grains are AGB stars, although the different groups of grains are attributed to AGB stars with different initial masses or metallicities or to different evolutionary stages.

Chapter 4

Optical Properties of Solids

"The light in dust lies dead,
When the cloud is scattered
The rainbow's glory shed"

Shelley (1824)

4.1 Introduction

A particle placed in a beam of light will scatter some of the light incident on it (i.e. the light will change direction) and absorb some of the light (i.e. the electromagnetic energy is transformed into other forms of energy by the particle). The light we then receive has been attenuated or, to put it another way, suffered *extinction.* The amount of light scattered and/or absorbed by the particle depends, in an intricately involved way, on the exact nature of the particle, and also the nature of the incident light. Consequently the extinction is dependent on the chemical composition of the particle and its size, shape and orientation, together with the wavelength and polarization state of the light. Therefore, we must include all these factors in our interpretations of spectra.

Identification of astronomical dust is usually achieved by comparing the observed spectral data with a catalogue of laboratory spectra of materials considered to be similar to those found in the astronomical dust (see chapter 5). A computer program can be used to make correlations between the reference spectra and the observed spectra, however there are limitations to this technique. In order to compare the laboratory and observed spectra they need to be of similar type, i.e. transmission spectra of very fine particulate materials. Many of the available spectra are obtained from samples for which no attempt has been

made to simulate the possible conditions in the observed astronomical dust. One of the reasons for this is that the laboratories want to optimize the surface conditions of the sample to yield the maximum amount of spectral information. Also, the applications to which infrared spectra are put are diverse and therefore the collection of such spectra uses many different techniques, producing different types of spectra, according to the application. A complete understanding of the transmission and reflection properties of both particulate and bulk media is imperative for the correct interpretation of the spectral data.

In this chapter a basic classical model for absorption/emission of electromagnetic radiation by material media is outlined. The correlations and differences between the various spectroscopic types and methods for standardizing these spectra to a single type (i.e. very fine particulate transmission) are discussed.

4.2 Physical optics

Absorption, reflection, scattering, polarization and dispersion of light by a material medium can all be explained in terms of the atoms, molecules and lattice structures which make up the medium. This section will concentrate on the mechanisms by which electromagnetic radiation is absorbed by matter, and is based on work by van de Hulst (1957), Abelès (1972), Wooten (1972), Bohren & Huffman (1983), Parker (1988) and Evans (1994).

Absorption of radiation by matter always involves the loss of energy by the radiation and a gain in energy by the atoms or molecules of the medium. The energy of an assembly of atoms consists partly of thermal energy and partly of internal energy associated with the binding of the extra-nuclear electrons to the nucleus and with the binding of the particles within the nucleus itself. Molecules have, in addition, energy associated with the oscillations of the atoms within the molecule with respect to one another, and solids have energy associated with intermolecular bonds. The energy absorbed from radiation appears as increased internal energy or as increased vibrational energy of interatomic or intermolecular bonds.

4.2.1 Classical electromagnetic theory

In classical electromagnetic theory, atoms and molecules are considered to contain electrical charges (i.e. electrons, ions) which are regarded as oscillating about positions of

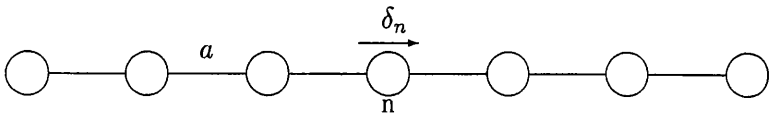

Figure 4.1: A simple chain lattice of identical atoms

equilibrium, each with its appropriate natural frequency, ν_o. When placed in a radiation field of frequency ν, each oscillator in the atom or molecule is set into forced vibration with the same frequency as that of the radiation. If $\nu \ll \nu_o$ or $\nu \gg \nu_o$, the amplitude of the forced vibration is small, but as ν approaches ν_o, the amplitude of the forced vibration increases rapidly.

To account for the absorption of energy from the radiation field, it is necessary to assume that the oscillator in the atom or molecule must overcome some frictional force proportional to its velocity during its forced motion. For small amplitudes of forced oscillation, when ν is very different from ν_o, the frictional force, and therefore the absorption of energy, is negligible. Near resonance ($\nu \approx \nu_o$), the amplitude of oscillation becomes large, with a correspondingly large absorption of energy to overcome the frictional force. Therefore, the radiation of frequencies near the natural frequency of the oscillator corresponds to an absorption band.

4.2.2 Acoustic and optical modes

Now, let us examine the allowed vibration modes in a lattice. The most rudimentary lattice we can consider is a linear chain of identical atoms shown in Fig. 4.1.

If we displace the n^{th} atom from its equilibrium position by a small amount δ_n parallel to the chain, the neighbouring atoms ($(n\text{-}1)^{th}$ and $(n+1)^{th}$) will also be displaced by δ_{n-1} and δ_{n+1} respectively. Therefore the n^{th} atom is actually displaced by an amount $\delta_n - \delta_{n-1}$ with respect to the $(n\text{-}1)^{th}$ atom, and by $\delta_n - \delta_{n+1}$ with respect to the $(n+1)^{th}$ atom. According to the Lorentz model, these atoms can be considered to be connected by springs. Therefore the n^{th} atom will experience a restoring force F equivalent to that of Hooke's Law. Because the n^{th} atom is connected to two springs (one to each neighbouring

atom) there will be two contributions to this force, which is given by:

$$F = -\eta[(\delta_n - \delta_{n-1}) - (\delta_{n+1} - \delta_n)]$$

where η is the spring constant. Applying Newton's second law we also get:

$$F = m\frac{d^2\delta_n}{dt^2}$$

where m is the mass of the oscillator. Thus,

$$\frac{d^2\delta_n}{dt^2} = (\frac{\eta}{m})[(\delta_n - \delta_{n-1}) - (\delta_{n+1} - \delta_n)] \tag{4.1}$$

Solutions to equation (4.1) have the form:

$$\delta_n = \delta_0 e^{i(kna-\omega t)} \tag{4.2}$$

where ω is the angular frequency of the wave, k is the wavenumber and δ_0 is the amplitude of oscillation. If we now substitute equation (4.2) into equation (4.1) we get:

$$\omega^2 = 2\frac{\eta}{m}[(1 - cos(ka)]$$

$$\omega^2 = 4\frac{\eta}{m}sin^2(ka/2)$$

$$\omega = \pm 2\left(\frac{\eta}{m}\right)^{\frac{1}{2}} sin(ka/2) \tag{4.3}$$

This equation gives the allowed vibration modes in this simple lattice. From equation (4.3) it is obvious that $\omega > 2\sqrt{(\frac{\eta}{m})}$ is not possible. Frequencies above $\omega = 2\sqrt{(\frac{\eta}{m})}$ cannot propagate through the lattice. In this model the displacement of the oscillator is along the chain, therefore the wave motion is longitudinal. This is the longitudinal acoustic mode.

Now consider a chain in which there are two different atoms of type X and Y, with masses m_X and m_Y respectively ($m_X > m_Y$), placed alternately along the chain. Again we displace the n^{th} atom, of type X, by a small amount δ_n. The nearest neighbouring atoms, both of type Y, are displaced by δ_{n-1} and δ_{n+1} as before; the next nearest atoms, both of type X, are displaced by δ_{n-2} and δ_{n+2} and so on. We have two different atom types in the chain, so we require two equations for the restoring force: one for the n^{th} atom of type X and one for the $(n+1)^{th}$ atom of type Y. Hence we get:

$$F_X = -\eta_X[(\delta_n - \delta_{n-1}) - (\delta_{n+1} - \delta_n)]$$

$$F_Y = -\eta_Y[(\delta_n - \delta_{n+1}) - (\delta_{n+1} - \delta_{n+2})]$$

For simplicity, let $\eta_X = \eta_Y = \eta$. Again we can use Newton's second law and get:

$$F_X = m_X \frac{d^2\delta_n}{dt^2}$$

$$F_Y = m_Y \frac{d^2\delta_{n+1}}{dt^2}$$

And again, analogous to the monatomic chain we get solutions of the form:

$$\delta_n = \delta_X e^{i(kna-\omega t)}$$

$$\delta_n = \delta_Y e^{i(k(n+1)a-\omega t)}$$

From which we get:

$$\omega^2 = \eta\left(\frac{1}{m_X} + \frac{1}{m_Y}\right) \pm \eta\left(\left[\frac{1}{m_X} + \frac{1}{m_Y}\right]^2 - \frac{4sin^2(ka)}{m_X m_Y}\right)^{\frac{1}{2}} \tag{4.4}$$

If we take the negative sign in equation (4.4), we get the acoustic mode already encountered, with the maximum allowed frequency at $\omega = 2\sqrt{(\frac{\eta}{m_X})}$ again. However, if we take the positive sign in equation (4.4), we get the optical mode, so called because this mode is easily excited by radiation of the appropriate frequency in ionic solids. In this case we find that there is a range of permitted frequencies with both a maximum and a minimum which correspond to the longitudinal and transverse optical (LO and TO) modes. The minimum frequency (TO) is given by:

$$\omega_{TO} = 2\left(\frac{\eta}{m_Y}\right)^{\frac{1}{2}}$$

The maximum frequency (LO) is given by:

$$\omega_{LO} = 2\left[\frac{\eta}{\left(\frac{1}{m_X} + \frac{1}{m_Y}\right)}\right]^{\frac{1}{2}}$$

The transverse and longitudinal optical modes represent the onset and cutoff of an absorption band.

It is generally thought that absorptivity measurements only involve the TO component,

however, in reality the LO component can play an important role (Berreman 1963). The contribution from the LO mode depends on the constituents of the molecule/solid under consideration as well as the crystal structure, grain size/sample thickness etc. The conditions under which the spectrum is taken and the nature of the spectrometer also affect the relative contributions from the TO and LO modes. It is therefore necessary to understand the contributions from all these factors in order to interpret spectra correctly.

4.2.3 Electrical properties of matter

At the beginning of this section the mechanism by which electromagnetic radiation loses energy to material media was outlined. We have just concluded a simple discussion of the permitted frequencies in a material medium. Now we need to combine these two: we have a system in which atoms or molecules are connected by "springs" and that are forced to oscillate in an electric field. The motion is affected by friction in the guise of a damping force. If the oscillator has mass m and charge q, we can expect an equation of motion of the form:

$$m\ddot{\delta} + b\dot{\delta} + \eta\delta = q\mathbf{E} \tag{4.5}$$

where δ is the displacement of the oscillator, b is the damping force, η is the spring constant and $\mathbf{E}$ electric field of the electromagnetic radiation incident on the material. The electric field is assumed to be time harmonic with frequency ω. From equation (4.3) we can see that $\eta \approx m\omega_o^2$ (where ω_o^2 is the natural frequency of the medium); the damping force can be written as $b = \gamma m$, where γ is the damping coefficient. Thus, equation (4.5) becomes:

$$\ddot{\delta} + \gamma\dot{\delta} + \omega_o^2\delta = \frac{q\mathbf{E}}{m} \tag{4.6}$$

The solution of equation (4.6) is:

$$\delta = \frac{-q\mathbf{E}}{m} \cdot \frac{1}{(\omega_o^2 - \omega^2) - i\gamma\omega}$$

which gives us an induced dipole moment, $\hat{\mathbf{p}}$, of:

$$\hat{\mathbf{p}} = \frac{-q^2\mathbf{E}}{m} \cdot \frac{1}{(\omega_o^2 - \omega^2) - i\gamma\omega} \tag{4.7}$$

If we assume that the displacement δ is small we can also assume that there is a linear relationship between the induced dipole moment and the electric field, which gives:

$$\hat{\mathbf{p}} = \hat{\alpha}(\omega)\mathbf{E} \tag{4.8}$$

where $\hat{\alpha}(\omega)$ is the frequency dependent polarizability of the atom or molecule. Combining equations (4.7) and (4.8), we can see that:

$$\hat{\alpha}(\omega) = \frac{-q^2}{m} \cdot \frac{1}{(\omega_o^2 - \omega^2) - i\gamma\omega} \tag{4.9}$$

Because of the inclusion of the damping term, the polarizability is a complex quantity. If there are N oscillators per unit volume, the macroscopic polarizability, $\mathbf{P}$, is given by:

$$\mathbf{P} = N < \hat{\mathbf{p}} >= N\hat{\alpha}\mathbf{E} \tag{4.10}$$

From Maxwell's equations we can get a complex displacement $\hat{\mathbf{D}}$, given by:

$$\hat{\mathbf{D}} = \hat{\epsilon}\mathbf{E} = \mathbf{E} + 4\pi\mathbf{P} \tag{4.11}$$

where $\hat{\epsilon}$ is the complex dielectric function. Substituting for $\mathbf{P}$ from equation (4.10) into equation (4.11) we get:

$$\hat{\epsilon}\mathbf{E} = \mathbf{E} + 4\pi N\hat{\alpha}\mathbf{E}$$

$$\hat{\epsilon} = 1 + 4\pi N\hat{\alpha}$$

now substituting from equation (4.9) we get:

$$\hat{\epsilon} = 1 + \frac{4\pi N q^2}{m} \cdot \frac{1}{(\omega_o^2 - \omega^2) - i\gamma\omega} \tag{4.12}$$

The dielectric function is complex and can, therefore, be written as:

$$\hat{\epsilon} = \epsilon' + i\epsilon''$$

From equation (4.12) we get:

$$\epsilon' = 1 + \frac{4\pi N q^2}{m} \cdot \frac{(\omega_o^2 - \omega^2)}{(\omega_o^2 - \omega^2)^2 + \gamma^2\omega^2} \tag{4.13}$$

$$\epsilon'' = \frac{4\pi N q^2}{m} \cdot \frac{\gamma\omega}{(\omega_o^2 - \omega^2)^2 + \gamma^2\omega^2} \tag{4.14}$$

We have expressions for the real and imaginary parts of the complex dielectric function (ϵ' and ϵ''). What do these expressions tell us about the response of a material to electromagnetic radiation? Let us consider the frequency dependence of ϵ' and ϵ''. The frequency

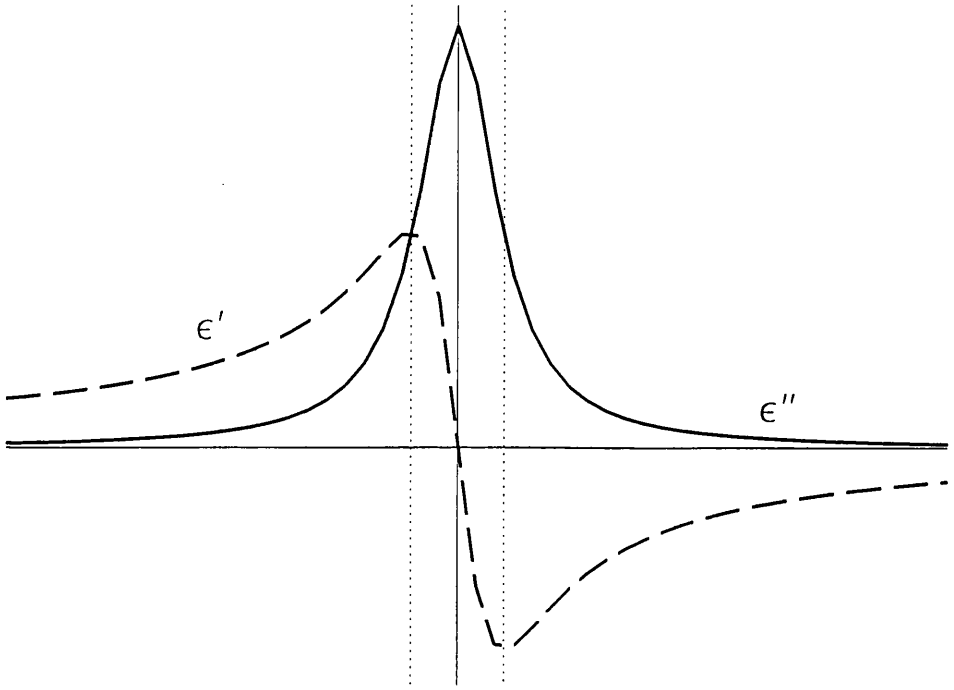

Figure 4.2: The variation of the real and imaginary parts of the dielectric function (ϵ' and ϵ'') with respect to frequency ω

dependences given by equations (4.13) and (4.14) are shown in Fig. 4.2, which shows that, for most of the spectrum, ϵ' increases with increasing frequency ω. This is known as *normal dispersion.* However, for a small section close to the resonance frequency of the oscillator, ω_o (the portion of Fig. 4.2 between the dotted vertical lines), the value of ϵ' decreases with increasing ω. This is known as *anomalous dispersion.* The width of the region of anomalous dispersion is determined by the strength of the damping coefficient, γ. For small values of γ, the region of anomalous dispersion is narrow. However, for large values of γ, the anomalous dispersion covers a broader range of frequencies, and hence the region over which absorption by the medium extends is broader. Inspection of equations (4.13) and (4.14) also shows us that, for small values of γ, the value of ϵ'' remains small and the peak of ϵ'' is very close to the resonance frequency of the medium, ω_o. Likewise, ϵ' has its anomalous region centred at about ω_o. However, for large values of γ, the situation is quite different. With increasing γ, the height of the peak of ϵ'' becomes much larger and the peak position moves away from the resonance frequency, as does the position of the anomalous region in ϵ'. Since γ is the measure of the damping within a medium, i.e. the mechanism by which the medium absorbs energy from electromagnetic radiation, large values of γ correspond to highly absorbing media. Similarly, low values of γ correspond to

relatively transparent media. Therefore, for relatively non-absorbing materials, a region of anomalous dispersion, and therefore an absorption feature, coincides approximately with the resonance frequency of the oscillators. Furthermore, for highly opaque, absorbing materials, the anomalous dispersion and the absorption feature will be shifted away from the resonance frequency of the oscillators.

As can easily be seen from equation (4.11) the physical property of a solid that determines its dielectric function is its electric polarizability, which, in turn, consists of contributions from the individual dipole moments of the oscillators within the solid. It is therefore useful to consider what actually constitutes these dipole moments. There are three possible sources of individual dipole moments in solids to examine: (i) the dipole moments due to the orientation of polar molecules in the solid; (ii) ionic polarisation due to the relative movement of the ions in the solid; and (iii) electronic polarisation due to the displacement of atomic electrons relative to the nuclei. Depending on the nature of the solid, the first two considerations may not be applicable (i.e. the solid may not contain polar molecules or ions), however all solids contain electrons and nuclei and therefore electronic polarisation is found in all solids. The contributions to the dielectric function from these three types of "oscillators" lead to features in three separate regions of the spectrum. The dipole moments of polar molecules are expected to give rise to features in the $\sim 10^{11}$Hz ($\sim$3mm) region of the spectrum; likewise the ionic polarisation affects the spectrum in the $\sim 10^{13}$Hz (30μm) region (the infrared); and the electronic polarisation will make contributions at $\sim 10^{15}$Hz (0.3μm; UV). Therefore we expect some solids to exhibit spectral features in all these regions.

4.3 The complex refractive indices of material media

There are two sets of optical constants that are closely interrelated. These are: 1) the real and imaginary parts of the complex refractive index $\mathbf{n} = n - ik$; and 2) the real and imaginary parts of the complex dielectric function (relative permittivity). $\epsilon = \epsilon' - i\epsilon''$. They are related by:

$$\epsilon' = \frac{\varepsilon'}{\varepsilon_o} = n^2 - k^2 = \Re[\mathbf{n}^2]$$

$$\epsilon'' = \frac{\varepsilon''}{\varepsilon_o} = 2nk = \Im[\mathbf{n}^2]$$

$$n = \sqrt{\left(\frac{\sqrt{(\epsilon'^2 + \epsilon''^2)} + \epsilon'}{2}\right)}$$

$$k = \sqrt{\left(\frac{\sqrt{(\epsilon'^2 + \epsilon''^2)} - \epsilon'}{2}\right)}$$

Which of these two sets of constants are most applicable depends on the material under investigation. Reflection and transmission by bulk media are best described using the complex refractive index $(n - ik)$, whereas absorption and scattering by particles which are small compared with the wavelength are best described by the complex dielectric function $(\epsilon' + i\epsilon'')$, however, they remain interchangeable. The media with which we are concerned have complex refractive indices that depend on wavelength and are complex. We can write the refractive index, $\mathbf{n}$, of a medium as:

$$\mathbf{n} = n - ik$$

To simplify the problem we assume that we have radiation incident on our medium in the form of an idealised, sinusoidal wave. The incident radiation can be written as:

$$A = A_o e^{i(\omega t - \frac{2\pi}{\lambda}x)}$$

where A is the amplitude, ω is the angular frequency and the wave is propagating in the positive x-direction.

Once the radiation enters the medium, the velocity of light becomes $\frac{c}{\mathbf{n}}$, so that:

$$A = A_o e^{i(\omega t - \frac{2\pi}{\lambda}\mathbf{n}x)}$$

$$A = A_o e^{i\omega t - i\frac{2\pi}{\lambda}(n-ik)x}$$

$$A = A_o e^{i(\omega t - \frac{2\pi}{\lambda}nx)} e^{-\frac{2\pi}{\lambda}kx}$$

From this we can see that the intensity of the wave (which is proportional to A^2) will decrease exponentially with decay constant of $\frac{4\pi}{\lambda}k$. Therefore the imaginary part of the refractive index, k, is directly responsible for the absorption of the light in the medium.

4.3.1 Scattering

Another consideration in the spectra of small particles is scattering. Consider a small particle placed in a beam of light. The intensity of the electromagnetic radiation incident on the particle is I_o; at a point a large distance r from the particle, the intensity of the scattered light is I. The scattered intensity I must be proportional to the incident intensity I_o, and the inverse square of the distance $\frac{1}{r^2}$, hence we can say that:

$$I = \frac{I_o F(\theta, \phi)}{k^2 r^2}$$

where $k = \frac{2\pi}{\lambda}$ is the wavenumber, and $F(\theta, \phi)$ is an orientation dependent, dimensionless function of the direction but not distance from the particle.

The total energy scattered by the particle in all directions is defined as being equal to the energy of the incident light falling on the cross-sectional area C_{sca}, where C_{sca} is the scattering cross section.

If the function $F(\theta, \phi)$ is divided by $k^2 C_{sca}$ the phase function is obtained, which has no dimensions and whose integral over all directions is 1. Therefore:

$$C_{sca} = \frac{1}{k^2} \int F(\theta, \phi) d\omega$$

where $d\omega = sin\theta d\theta d\phi$ is the element of solid angle and the integral is taken over all directions.

In a similar way to the scattering cross-section case, the energy absorbed by the particle can be put equal to the energy incident on the area C_{abs} (the absorption cross-section). Likewise the total energy depleted from the original beam can be put equal to the incident energy on the area C_{ext}, the extinction cross-section. The law of conservation of energy requires that:

$$C_{ext} = C_{abs} + C_{sca}$$

.

The efficiency of a particle to absorb, scatter and extinguish are given by the Q factors. where:

$$C_{ext} = Q_{ext} \times area$$

$$C_{abs} = Q_{abs} \times area$$

$$C_{sca} = Q_{sca} \times area$$

Therefore:

$$Q_{ext} = Q_{abs} + Q_{sca}$$

.

The Q-factors can be calculated from the complex refractive index (or complex dielectric function) using Mie Theory

4.3.2 Simulating the Particulate Spectra: Mie Theory

Mie theory describes the way in which spherical, homogeneous particles interact with electromagnetic radiation. Certain assumptions are made about these particles in order to simplify the situation. These assumptions are:

1) Only the interactions of a single particle with light of arbitrary wavelength are considered.

2) The optical properties of the particle are completely described by frequency-dependent optical constants (i.e. the complex refractive index or the complex dielectric function).

3) Scattering is elastic, i.e. the frequency of the scattered light is identical to that of the incident light.

4) Only *single-scattering* occurs. That is, each individual particle is acted on by an external field (due to the incident radiation) in isolation from the other particles. The total scattered field is merely the sum of the fields scattered by each particle (i.e. the particles do not affect each other).

5) For a collection of particles, the number of particles is large and their separations are random, so that the waves scattered by the individual particles have no systematic phase relation.

6) The medium in which the particles are embedded is considered to be: a) linear, b) homogeneous and c) isotropic.

The theory used to find the transmission spectra of small particles from the optical constants is known as Mie Theory. This calculates the Q-factors, which are the efficiency factors for extinction, scattering and absorption. There is no simple explicit formula for the Q-factors, however if $\frac{2\pi a}{\lambda} \ll 1$, (where a is the radius of a spherical particle and λ is the wavelength of the incident light), then for a spherical particle:

$$Q_{sca} = \frac{8}{3}\left(\frac{2\pi a}{\lambda}\right)^4 \Re\left[\left(\frac{\mathbf{n}^2-1}{\mathbf{n}^2+2}\right)^2\right] \tag{4.15}$$

$$Q_{abs} = \frac{8\pi a}{\lambda} \Im\left[\frac{\mathbf{n}^2-1}{\mathbf{n}^2+2}\right] \tag{4.16}$$

where $\mathbf{n} = n - ik$ (Bohren & Huffman 1983).
Given the close relation between the complex refractive index and the complex dielectric function, we can also write these equations in terms of the dielectric function:

$$Q_{sca} = \frac{8}{3}\left(\frac{2\pi a}{\lambda}\right)^4 \Re\left[\frac{\hat{\epsilon}-1}{\hat{\epsilon}+2}\right]$$

$$Q_{abs} = \frac{8\pi a}{\lambda} \Im\left[\frac{\hat{\epsilon}-1}{\hat{\epsilon}+2}\right]$$

where $\hat{\epsilon} = \epsilon' - i\epsilon''$.
There are computer programs that use Mie Theory to evaluate the Q-factors and thus produce the relevant spectra. These programs require the input of:
1) A dimensionless length $\frac{2\pi a}{\lambda}$
2) The real and imaginary parts of the refractive index of the materials $\mathbf{n}(\lambda) = n - ik$, or the real and imaginary parts of the dielectric function of the material $\hat{\epsilon}(\lambda) = \epsilon' - i\epsilon''$.

4.3.3 Experimental Determination of Optical Constants

It is assumed that the optical properties of a particle are completely specified by frequency-dependent optical constants (assumption 2 in section 4.3.2). The optical constants of minerals of astronomical significance must, therefore, be determined. This is most easily done

using bulk materials, as opposed to particles, but either can be used. The data accumulated from published sources include both bulk and particulate samples and transmission, absorption and reflection spectra. It is not very useful to compare spectra measured by different techniques, especially since the appearance of the spectra depends on the measurement conditions. The transmission spectrum of a bulk medium is often very different from its particulate counterpart. The chemical composition remains the same, but the state of aggregation, and hence scattering properties, differ. The homogeneous bulk does not scatter light, however the particulate material has a transmission spectrum that may be primarily the result of scattering. Gross optical properties of a given material differ appreciably depending on its state of aggregation. Optical theory was therefore used to normalize the data by finding the intrinsic optical constants and calculating the spectra. Since most of the astronomical spectra will be particulate, either emissive or absorptive in nature, the data can be used to calculate the spectra of such systems. There are various methods, each of which has its advantages and limitations, depending on the form of the material we are interested in, are outlined here:

1) Measurement of refractive angles. The real part of the refractive index, n, can be obtained using Snell's Law. This requires the sample to be of high transparency (i.e. $k \approx 0$).

2) Measurement of transmittance and reflectance of a slab for light at near-normal incidence. Again, the sample needs to be transparent in order to have a measurable transmission, but the transparency required is not as high as method 1.

3) Measurement of reflectance at near-normal incidence over a wide range of frequencies. This involves using a Kramers-Kronig relation to obtain the phase shift of the reflected light (see section 4.5). The sample must be highly opaque and the method requires measurements over an extended wavelength region and usually extrapolation into unmeasured regions.

4) Ellipsometric techniques. These measure the amplitude ratios and phase shifts directly. They are difficult to use over large wavelength regions due to instrument limitations.

5) Measurements of reflectance for incident light of various polarisation states and two oblique angles of incidence. This method generally requires large sample surfaces, although the use of this method with small surfaces has been achieve by utilising cryogenic detectors (Hofmeister *pers. comm.*).

Many spectra have been obtained for use with astronomical observations and are therefore already the absorption/emission spectra for particulate material. However, the exact nature of the spectrum must be taken into account. While they already represent spectra of particulate material, the spectrum plot may be of percentage transmission, percentage absorption or absorption/extinction efficiency. Astronomical spectra are of the latter type, and therefore it is necessary to normalise all other spectra to this type. So, the question is, how do we generate the extinction efficiency, Q_{ext}, from the percentage absorption or transmission? Since the absorption is the inverse of the transmission, the method is essentially the same for either type of spectrum.

Suppose we have a ray which passes through an infinitesimally thin region of thickness dx which causes extinction. Let the intensity of the ray entering the extinguishing region be I_ν. The radiation will lose intensity through interaction between the radiation and the matter in the extinguishing region, so that the intensity of radiation emerging from the extinguishing region is $I_\nu + dI_\nu$. The *extinction coefficient*, κ is defined by:

$$dI_\nu = -\kappa_\nu I_\nu dx$$

We can also define the optical depth, τ, as:

$$\tau_\nu = \int_{pathlength} \kappa_\nu dx$$

The attenuation of radiation by the effects of extinction is given by $e^{-\tau_\nu}$. This is essentially the absorption of the radiation. Therefore:

$$A = e^{-\tau_\nu}$$

and,

$$lnA = -\tau_\nu$$

where A is the absorption. Since transmission is the inverse of absorption, $T = 1/A$, we also have:

$$lnT = \tau_\nu$$

So the optical depth, τ, can be obtained from the absorption or transmission. This must then be related to the extinction efficiency, Q_{ext}

The optical depth has been defined as:

$$\tau_\nu = \int_{pathlength} \kappa_\nu dx$$

For a homogeneous extinguishing medium this gives:

$$\tau_\nu = D\kappa_\nu$$

,

where D is the path-length, and κ_ν is defined as:

$$\kappa_\nu = nC_\nu$$

where n is the number of particles per unit volume and C_ν is the extinction cross-section for each particle.

$$C_\nu = Q_{ext}\pi a^2$$

Hence,

$$\tau_\nu = DnQ_{ext}\pi a^2$$

and,

$$\tau_\nu \propto Q_{ext}$$

Therefore the shape of the extinction efficiency spectrum is identical to the shape of the optical depth spectrum, and:

$$lnT \propto Q_{ext}$$

From the transmission (or absorption) spectra we can find the shape and positions of spectral feature, however this is not a quantitative method unless the pathlength is known and the medium is homogenous.

4.4 A problem with the laboratory spectra

A problem has arisen regarding the laboratory spectra of some particulate materials which seems to have come about as a result of a misunderstanding of the optical properties of solids. The usual method for obtaining spectra from a particulate sample is to disperse the sample in a pellet of a substance which is transparent to light in the wavelength range of interest. This is typically potassium bromide (KBr) for mid-infrared measurements. In 1978, Dorschner *et al.* (1978) undertook a study comparing the spectra of silicate samples produced using the KBr-dispersion method with spectra produced by extracting the optical constants from bulk samples. This resulted in a mismatch between the spectra, which they took to imply that the KBr embedding created a shift in the peaks of spectral features to longer wavelength. Since then the use of this correction of spectra for KBr-dispersion has been widespread, although not universal. The most prevalent use of this correction factor has been with respect to silicon carbide (SiC) spectra. Silicon carbide was theoretically predicted to form around carbon-rich AGB stars in 1969 (Gilman 1969; Friedmann 1969) and it was suggested that the $\sim$11.5μm feature seen in the spectra of these stars may be due to silicon carbide dust (Gilra & Code 1971; Hackwell 1972; Treffers & Cohen 1974). This prompted various laboratory investigations of this solid (e.g. Friedemann *et al.* 1981; Borghesi *et al.* 1985; Pégourié 1988). Following the work of Dorschner *et al.* (1978), Friedemann *et al.* (1981) used the same procedures to investigate the differences between a KBr-dispersed particulate SiC spectrum and the spectrum derived from the bulk SiC sample. They found a shift in the peak wavelength analogous to that found by Dorschner *et al.* (1978), from which they surmised that a spectrum of SiC obtained from a KBr-dispersion sample must be corrected by shifting the peak of the feature by 0.4μm to shorter wavelengths. The result of applying this correction factor was to give their α-SiC sample a feature with a peak at 11.4μm rather than the 11.8μm peak before correction. The SiC spectra published by Borghesi *et al.* (1985) were again obtained using the KBr-dispersion method. Their published spectra are not corrected for the method, but it is explicitly declared that the correction factor should be applied before the spectra could be used. Again it is found that the α-SiC sample has a peak position which is shifted from 11.8μm to 11.4μm by correction. Borghesi *et al.* (1985) also presented a β-SiC sample which has a peak position shifted from 11.4μm to 11.0μm by this correction. Pégourié (1988) used various existing KBr-corrected laboratory spectra to derive a complete spectrum for α-SiC. The use of these various sources of laboratory spectra by

astronomers led to the identification of the ~11.5μm feature in carbon star spectra with α-SiC (Groenewegen 1995; Speck *et al.* 1997). However, as discussed in Chapter 3, there are samples of SiC available in meteorites which are believed to have been formed around such stars, and all these grains are of the β-SiC form. It is difficult to find a mechanism by which α-SiC could be transformed into β-SiC, and thus it is assumed that the meteoritic grains were formed as β-SiC. This constitutes a discrepancy between the astronomical and meteoritic results. However, if the KBr-correction factor is not applied to the laboratory data, the silicon carbide type which best fits the astronomical observations switches from α-SiC to β-SiC, removing the discrepancy between the astronomical and meteoritic data. The change in the attribution of the ~11.5μm feature in carbon star spectra is discussed further in Chapter 6. The effect of the correction factor has been to cause the misidentification of a dust species in space, therefore, it is necessary to understand how this correction factor arose and why it is not valid.

The original work which proposed the KBr-correction (Dorschner *et al.* 1978) used Mie theory, which is not ideal since it assumes that the particles in the sample are spherical. It has since been shown that, for crystalline olivine, a similar method for deriving a spectrum from bulk optical constants using a continuous distribution of ellipsoids rather than spheres produces a spectrum that is almost identical to the KBr-dispersion spectrum (Molster *pers. comm.*).

Another problem with the KBr dispersion spectra of SiC arises from the high opacity of this compound. For any sample, overloading the KBr pellet with the sample causes the pellet to become opaque. The effect of this is that the zero-transmission point is incorrectly defined. In these cases the spectrum obtained is worthless. This problem is particularly important when the sample is SiC. Silicon carbide is a very efficient absorber, therefore the amount of SiC needed to cause the KBr pellet to become opaque is quite small (i.e. less than needed for other minerals). This is compounded by particle size considerations. Due to their great affinity for absorbing electromagnetic radiation, SiC particles do not have to be very large before they appear to be opaque. For very fine-sized particle dispersions, in reasonably low concentrations, this effect is negligible, allowing the acquisition of spectra that are apposite. A good example of the effect of overloading the KBr pellet with sample can be seen in Papoular *et al.* (1998), who presented two spectra of β-SiC consisting of

broad overlapping peaks at 10.9 and 12.2 μm, unlike any other reported spectra. These positions are close to the TO and LO components. The very high absorbance units of 1 and 2.5 for these samples indicate overloaded pellets. For extreme concentrations of SiC (or large thicknesses), light is reflected between the TO and LO modes: the scattering in the pellet produces the dip in absorption. Problems occur at high absorption because the partial opacity induces a frequency dependent baseline. Papoular *et al.* (1998) were attempting a reassessment of the KBr correction factor, however the use of overloaded KBr pellets means that their results are erroneous.

4.4.1 Thin film vs. KBr-dispersion spectra

The problems incurred by the use of the KBr-dispersion technique has prompted the hunt for an alternative source of applicable spectra. New infrared (IR) absorption spectra of thin films of α- and β-SiC created by compression in a diamond anvil cell (DAC) will be presented here. Unlike the KBr-dispersion method, a dispersive medium is not used. This relatively new approach is quantitative (if sufficient care is taken to produce an appropriately thin and uniform film) as shown by comparison of thin film spectra of olivines, garnets, wadsleyite, $MgAl_2O_4$ spinel, and $CaGeO_3$ perovskite to reflectivity data from the same samples (Hofmeister *et al.* 1989; Chopelas and Hofmeister, 1991; Lu and Hofmeister, 1994; Cynn and Hofmeister, 1994; Hofmeister, 1995; 1997). Furthermore, measurements of thin film spectra of garnets are nearly identical to single-crystal absorption data (McAloon and Hofmeister, 1993; Hofmeister, 1995). Moreover, spectra of thin films of AlN (aluminium nitride) are identical to the spectra of nanometre-sized particles obtained using the KBr technique. Therefore, thin film spectra are equivalent to the collection of spectra of small particles in a vacuum, and can therefore be applied to astronomical data without further manipulation.

4.4.1.1 Laboratory techniques and results for thin-film samples

Single-crystals of α-SiC were purchased by A.M. Hofmeister from Alpha/Aesar (catalog no. 36224). This specimen is 99.8% SiC, consisting of hexagonal platelets of 50 to 250 μm in diameter and 5 to 15 μm thick. Less than 1% of the platelets had an amber color, the remainder were pale grey. All were transparent in the visible with smooth, highly reflective surfaces. Polycrystals of β-SiC were donated by Superior Graphite. The purity of this

sample is also 99.8%. One batch consisted of 1 μm powder, the other was a conglomerate of equant crystallites of up to 25 μm in size. For this study, only the gray crystals of α-SiC were examined. Mid-IR spectra were obtained from 450 to 4000 cm^{-1} (2.5-22.2 μm) at 2 cm^{-1} ($\sim$ 0.01 μm) resolution using a liquid-nitrogen cooled HgCdTe detector, a KBr beam splitter and an evacuated Bomem DA 3.02 Fourier transform interferometer by A.M. Hofmeister at Washington University, St. Louis. Thin films were created through compression in a diamond anvil cell which was interfaced with the spectrometer using a beam condenser. Type II diamonds were used. Film thickness was estimated from the initial grain size, by the relative relief and color seen among the various films, and by the increase in grain diameter from the initial size during compression. Efforts were made to cover the entire diamond tip (0.6 mm diameter) with an even layer of sample, but slight irregularities in the thickness were inevitable. Reference spectra were collected from the empty DAC. Uncertainties in peak positions are related to peak widths because the accuracy of the FTIR spectrometer is high, $\pm$0.01 cm^{-1}. For procedural details see Hofmeister (1997).

Spectra obtained from α-SiC (Fig. 4.3a,b) have an intense, broad band near 11.8 μm. The peak position lies between the longitudinal optic mode (LO) and transverse optic mode (TO) components observed by Spitzer *et al.* (1959a,b) and a shoulder is seen at the LO position. A shoulder also occurs at 12.2 μm. The sample thickness could not be precisely determined, but was estimated to be sub-micron. Spectra obtained from β-SiC (Fig. 4.3c-g) depend somewhat on thickness. For the thinnest films, of sub-micron thickness (Fig. 4.3c,d), a fairly symmetric peak is found at 11.3 to 11.4 μm, and a weak shoulder exists at 10.7 μm, consistent with excitation of the LO component. Spectra from thicker film samples, $\sim$ 1 μm in thickness from visual inspection (Fig. 4.3e,f), have a peak at a similar position, with an asymmetric increase in intensity on the short-wavelength side, and display additional weak features. The 12.7 μm band is due to the TO feature. The weak, broad band at 13.4 microns is not an absorbance feature but is due to the Christiansen effect which gives a minimum when the real part of the index of refraction is unity (Hapke 1993). The asymmetry of the main peak is due to the baseline rising towards the visible, probably a scattering effect from the grain boundaries. A spectrum from the thickest sample examined ($\sim$ 1 μm). had high absorbance values overall, with the Si-C stretching peak superimposed (Fig. 4.3g). The appearance of the peak is in-

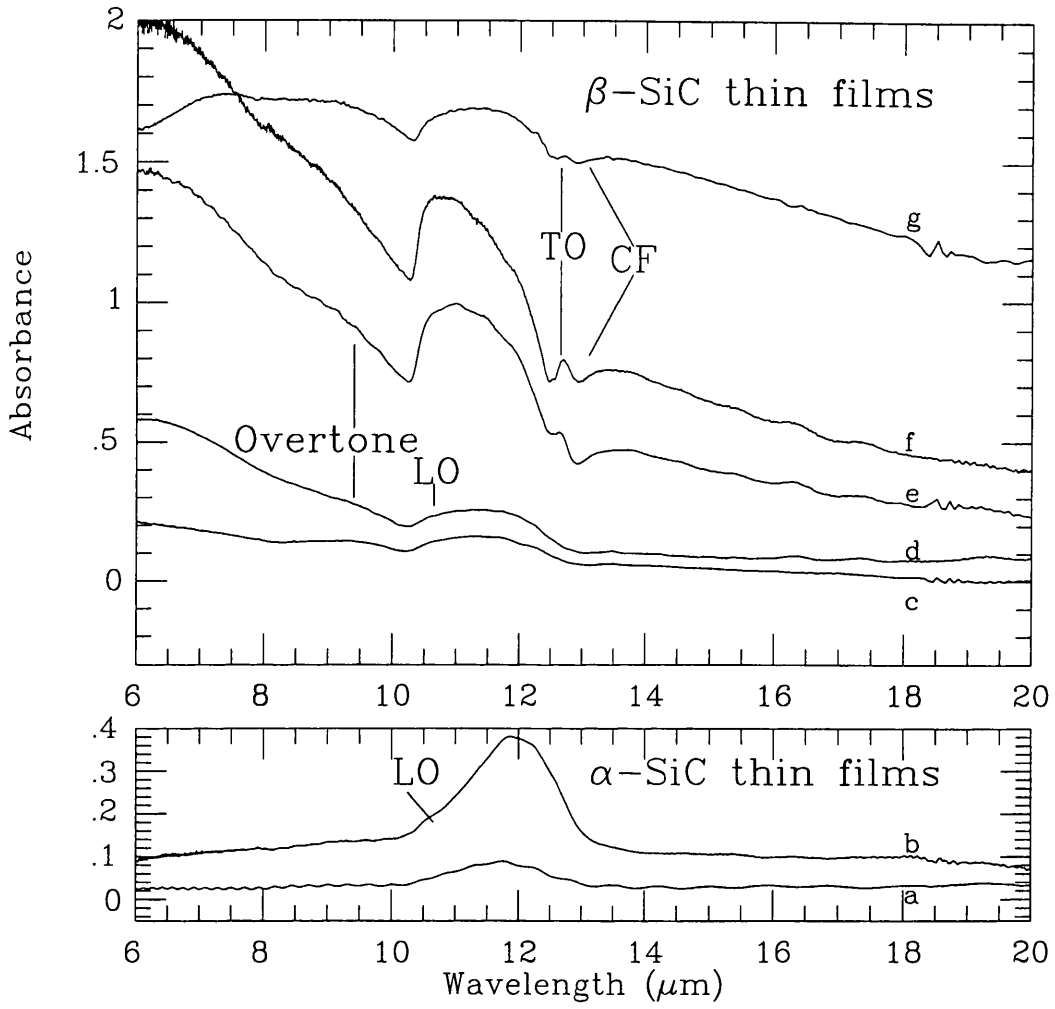

Figure 4.3: Representative thin-film IR spectra. (a-b) (lower): sub-micron films of α-SiC, which have an intense broad band at 11.70 μm (a) and 11.87 μm (b). (c-g) (upper): β-SiC spectra acquired from films increasing in thickness from <0.1 μm to ~1 μm. For clarity, plot (d) was offset by +0.2 absorbance units, and plot (b) by +0.1 absorbance units. Absorbance clearly increases with thickness for β-SiC. The positions of the longitudinal optic (LO) and transverse optic (TO) modes of SiC are shown, as well as those of the overtone and Christiansen feature (CF).

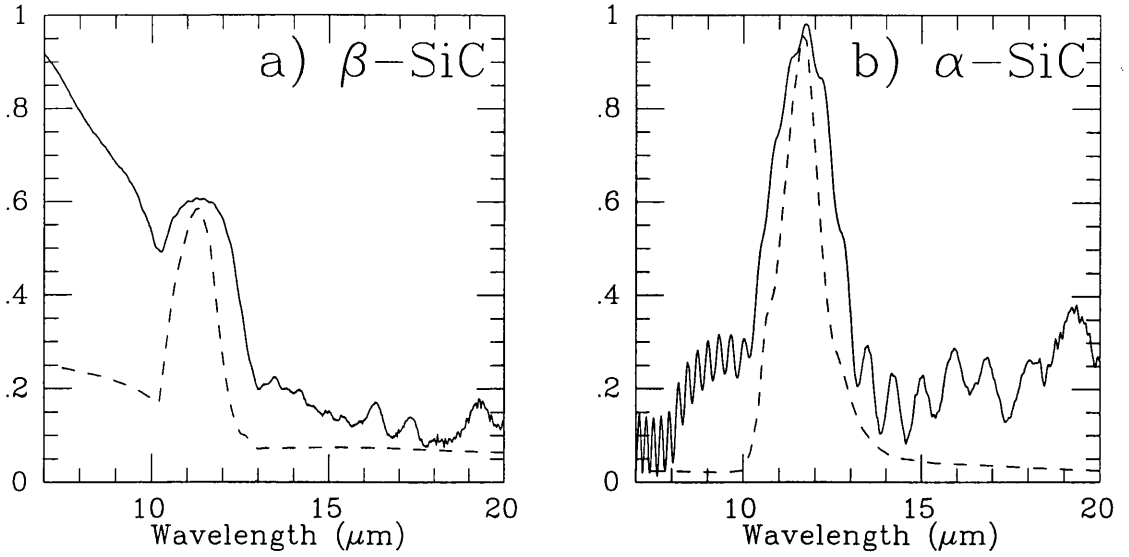

Figure 4.4: Thin film spectra (solid lines) and the uncorrected Borghesi *et al.* (1985) KBr dispersion data (dashed lines).

termediate between the peaks observed from the thin (Fig. 4.3d) and moderately thick samples (Fig. 4.3e), in that the main peak is symmetric but that a weak subsidiary feature exists at 12.7 μm. Below 8 μm, the absorbance in Fig. 4.3e drops, rather than increasing as in the other spectra, because of interference fringes in the near-IR (not shown). These interference fringes indicate a distance of 5 μm, inferred to be the separation of the diamond anvils. The peak positions of the β-SiC samples are relatively independent of the thickness. No difference can be discerned between the two samples of β-SiC (fine grain size vs. mixed grain sizes). Fig. 4.3c,g were made from a mixture of grain sizes and Fig. 4.3d,e,f are from the 1 μm powder fraction. Additional spectra from both β-samples resembled those shown. The appearance of the spectra are consistent with being due to pure absorption for the thinnest samples (Fig. 4.3c,d) and absorption with minor reflection for the thicker samples (Fig. 4.3e-g), given that the LO-TO coupling is stronger in β-SiC than in α-SiC (Hofmeister & Speck 1998).

4.4.1.2 Comparison with dispersed-sample results

KBr matrix spectra of β-SiC obtained by Borghesi *et al.* (1985) for a fine grain size sample (mean diameter modeled by them as 0.02 μm, average diameter observed in TEM as 0.12 μm) closely match our own thin-film data, particularly the spectrum in Fig. 4.3e (shown in Fig. 4.4a). The greatest difference is that the TO mode appears as a shoulder,

rather than a separate peak. This difference is obviously due to sample thickness, because the thinner film of Fig. 4.3d has a barely discernable shoulder at the TO position. The LO mode occurs as a weak shoulder in their dispersion data, but this was not noted by them. Their peak barycenter was at 11.4 μm, which equals the results from our thin films. The match of Borghesi *et al.* (1985)'s dispersion data with Fig. 4.3e is consistent with an estimated film thickness <0.1 μm. The β-SiC spectrum of Papoular *et al.* (1998), that has maximum absorbance of 0.4 (i.e. the pellet is not overloaded), has a peak at 11.5 μm, in agreement with previous results and Fig. 4.3. For α-SiC, the KBr-dispersion spectrum of Borghesi *et al.* (1985)'s smallest-grained (mean diameter modeled by them as 0.04 μm, average diameter observed in TEM as 0.16 μm) and purest sample (SiC-600) closely matches the spectrum of our thinnest film (Fig. 4.3a; comparison shown in Fig. 4.4b). Its peak position of 11.6 μm equals our result, given the experimental uncertainties. The positions of the shoulders are comparable to the LO and TO positions (Spitzer *et al.* 1959a). Their sample N is compromised by $\sim$ 10% impurities (C and SiO_2). Their SiC-1200 sample was 3-10 times larger grained, even for the ground and sedimented fraction, and is inappropriate for comparison. The study by Friedemann *et al.* (1981) involved larger grain sizes, but yielded similar spectral profiles, with a slight shift of the peak position to 11.8 μm. It is clear that the application of a KBr matrix wavelength correction (e.g. Pégourié 1988) is incorrect, since the barycenter peak for KBr dispersions with fine grain sizes and reasonably low concentrations equals that of corresponding thin films, while the peak shapes are in excellent agreement. For these (<0.1 μm) grain sizes or film thicknesses, bulk absorption rather than surface effects dominates in the vicinity of the intense peak. Further, Bohren and Huffman (1983, p.329) incorrectly assumed that absorption peaks occur at the maximum in the dielectric function ϵ'', which is neither expected from theory nor observed experimentally (Wooten, 1972). Also, the width in epsilon double prime was assumed to be zero, which is particularly inappropriate for intense IR modes as seen in SiC. The maximum in ϵ'' defines the TO position, whereas the bulk absorption peak is shifted towards the LO position. The shift correlates with the strength of the mode: for SiC, the effect is pronounced, with the absorption lying roughly midway between the TO and LO modes (Fig. 4.3). Only for extremely thick or large grain samples, $\sim$ 1 μm, do the parameters of the dispersions (Borghesi *et al.* 1985) differ from those of a bulk sample but the differences are due to internal scattering among the particulates and sampling effects due to incorrect assumptions for zero transmission. Similarly, the application of a KBr

correction for silicates (Dorschner *et al.* 1978) is also problematic. Recent measurements by Colangeli *et al.* (1993, 1995) indicate minimal matrix effects for various silicates. The application of a KBr correction of silicates has never been universally accepted in the way it has for SiC. The 11.3 μm narrow feature often attributed to crystalline olivine would appear at 11.0 μm if the corrected spectrum were to be believed. Finally, for virtually all spectra obtained from dispersions, the derived mass extinction coefficients may be incorrect, due to the majority of the particles in the dispersions being "opaque". Thin film data on the other hand do not suffer from this problem.

The new thin-film spectra and the uncorrected KBr-dispersion spectra are used in chapter 6 to re-identify to 11.4 μm feature seen in the spectra of carbon-rich AGB stars.

4.5 Kramers-Kronig dispersion relations

There is also a vast collection of mineral spectra available to geologists, which are all reflectance spectra of bulk materials. Therefore, in order to make use of these spectra we must use the third option (section 4.3.3) for extracting the optical constants n and k.

In this case we need to understand the Kramers-Kronig dispersion relation. Kramers (1956) and Kronig (1926) introduced the concept of dispersion into optics, where dispersion of light occurs as a consequence of the dependence of the refractive index on wavelength or frequency. As previously discussed, the refractive index $\mathbf{n}$ has a real part n, determined by the phase velocity, and an imaginary part k, determined by the absorption. Kramers and Kronig showed that the real part of the refractive index could be expressed as an integral of the imaginary part. To demonstrate this theory it is convenient to consider a complex function $f(z)$ that is analytic in the upper half of the complex plane and on the real axis. It is required that

$$\lim_{|z|\to\infty} |f(z)| = 0$$

for $0 \leq arg(z) \leq \pi$

so that the integral over an infinite semicircle will vanish. The point of these conditions is that $f(z)$ may be expressed by the Cauchy integral formula

$$f(z_o) = \frac{1}{2\pi i} \oint \frac{f(z)}{z - z_o} dz$$

The integral over the upper semicircle vanishes, so that

$$f(z_o) = \frac{1}{2\pi i}\int_{-\infty}^{\infty} \frac{f(x)}{x - z_o}dx$$

Now, if we let z_o approach the real axis from above ($z_o \rightarrow x_o$):

$$f(x_o) = \frac{1}{\pi i}P\int_{-\infty}^{\infty} \frac{f(x)}{x - x_o}dx$$

where P indicates the Cauchy principle value.

Splitting the function, $f(x_o)$, into real and imaginary parts we obtain

$$f(x_o) = u(x_o) + iv(x_o) \tag{4.17}$$

$$f(x_o) = \frac{P}{\pi}\int_{-\infty}^{\infty} \frac{v(x)}{x - x_o}dx - \frac{iP'}{\pi}\int_{-\infty}^{\infty} \frac{u(x)}{x - x_o}dx \tag{4.18}$$

Finally, equating the real parts of equations (4.17) and (4.18):

$$u(x_o) = \frac{P}{\pi}\int_{-\infty}^{\infty} \frac{v(x)}{x - x_o}dx$$

and equating the imaginary parts of equations (4.17) and (4.18):

$$v(x_o) = \frac{P'}{\pi}\int_{-\infty}^{\infty} \frac{u(x)}{x - x_o}dx$$

These are the Kramers-Kronig dispersion relations. Note that these relations are only meaningful when $f(x)$ is a complex function of the real variable (x).

Application of the Kramers-Kronig dispersion relation to normal incidence reflectance or reflectivity data permits the determination of the complex refractive index, $\mathbf{n} = n - ik$, and hence a large number of associated optical and dielectric parameters, including the absorption spectrum of the same material.

Reflectivity is a complex physical quantity which connects the amplitude of the electric field of a reflected electromagnetic wave, to that of the incident wave:

$$E_{reflected} = r(\omega)E_{incident}$$

since r(ω) is complex it can be expressed as:

$$r(\omega) = \rho(\omega)e^{i\theta(\omega)}$$

$$r(\omega) = \frac{1-\mathbf{n}}{1+\mathbf{n}}$$

Therefore,

$$\frac{1-n+ik}{1+n-ik} = \rho cos(\theta) + i\rho sin(\theta)$$

where $\rho(\omega)$ is the magnitude of the reflectivity and $\theta(\omega)$ is the phase difference between the electric fields of the reflected and incident waves.

The quantity measured in reflection spectra is the *reflectance power*, R(ω), which connects the intensity of a reflected wave, to that of the incident wave:

$$I_{reflected} = R(\omega)I_{incident}$$

$$R(\omega) = r(\omega)r^*(\omega) = \rho^2(\omega)$$

$$\sqrt{R} = \left|\frac{1-\mathbf{n}}{1+\mathbf{n}}\right|$$

$$\sqrt{R} = \frac{1-n^2-k^2}{(n+1)^2+k^2} - i\frac{2k}{(n+1)^2+k^2}$$

From this it follows that:

$$n = \frac{1-R}{1+R-2\sqrt{R}\cos\theta}$$

$$k = \frac{-2\sqrt{R}\sin\theta}{1+R-2\sqrt{R}\cos\theta}$$

The reflectance R can be measured directly and the phase shift θ can be calculated using the Kramers-Kronig dispersion relation. The dispersion between the phase-shift and the reflectance at a given frequency can be expressed as:

$$\theta(\omega_0) = \frac{1}{\pi}\int_0^\infty ln\left|\frac{\omega+\omega_0}{\omega-\omega_0}\right| \frac{dln\sqrt{R(\omega)}}{d\omega} d\omega.$$

This equation is valid for any region of the spectrum. The spectrum can therefore split over the whole range into three parts. The wavelength range of experimental data will make up the middle part, with the other two sections extending from zero to the experimental region, and from the experimental region to infinity. This can be expressed as:

$$\theta(\omega_0) = \frac{1}{\pi}\int_0^a f(R,\omega_0)d\omega - \frac{1}{\pi}\int_a^b f(R,\omega_0)d\omega - \frac{1}{\pi}\int_b^\infty f(R,\omega_0)d\omega$$

where:

$$f(R,\omega_0) = ln\left|\frac{\omega+\omega_0}{\omega-\omega_0}\right| \frac{dln\sqrt{R(\omega)}}{d\omega}d\omega.$$

and therefore:

$$\theta(\omega_0) = \alpha(\omega_0) + \phi(\omega_0) + \beta(\omega_0)$$

If these three functions can be evaluated, the complex refractive index, $\mathbf{n} = n - ik$ can be calculated.

Outside the measured region (a, b) the reflectance is assumed to be low and very slowly varying. Therefore, the term;

$$\frac{dln\sqrt{R(\omega)}}{d\omega}$$

is effectively zero, and,

$$\alpha(\omega_0) = 0$$

$$\beta(\omega_0) = 0$$

The weighting term $ln \mid \frac{\omega+\omega_0}{\omega-\omega_0} \mid$ also allows us to disregard contributions to the phase angle due to reflection at wavelengths far from the central waveband region. This term tends to zero as $\omega \ll \omega_0$ and $\omega \gg \omega_0$. The validity of disregarding the very long and very short wavelength regions in Kramers-Kronig analysis was also investigated by Abdullah & Sherman (1997), who found that they could obtain accurate optical constants using only a limited spectral range.

And so, now we have:

$$\theta(\omega_0) = \phi(\omega_0)$$

.

$$\phi(\omega_0) = \frac{1}{\pi}\int_a^b ln\left|\frac{\omega+\omega_0}{\omega-\omega_0}\right| \frac{dln\sqrt{R(\omega)}}{d\omega}d\omega$$

The integrand of this equation has a singularity at $\omega = \omega_0$. Therefore it cannot be solved for this value of ω. It can be shown, however, that the expression for the phase angle can be reformulated as:

$$\theta(\omega_0) = \frac{-\omega}{\pi} P \int_0^\infty \frac{lnR(\omega) - lnR(\omega_0)}{\omega^2 - \omega_0^2} d\omega$$

It can also be shown that, at $\omega = \omega_0$ this has a limiting form of:

$$\frac{1}{2\omega} \frac{dlnR(\omega_0)}{d\omega_0} \mid_{\omega_0=\omega}$$

When we have calculated ϕ, and hence θ, we can use the reflectance R, and the phase shift θ, to calculate the complex refractive index, $\mathbf{n} = n + ik$. Once the complex refractive index has been obtained, the absorption and transmission spectra of the material can be simulated using Mie theory. This is the method used by the Jena group to calculate optical constants of various silicates and oxides. Spectra calculated from their optical constants using Mie theory can be seen in the catalogue of laboratory spectra in Chapter 5. The optical constants are available from the Jena group website[1].

Having discussed the optical properties of solids and the methods by which we can extract them, it is now expedient to examine some of these spectra. This is done in chapter 5.

[1] http://www.astro.uni-jena.de/Group/Subgroups/Labor/Labor/odata.html

Chapter 5

Catalogue of mineral spectra

"Sometimes, there just aren't enough rocks"

Forrest Gump

5.1 Introduction

One of the aims of this thesis was to compile a database of mineral spectra relevant to stardust. These spectra come from a variety of sources and have been adjusted so that they are equivalent to extinction coefficient spectra, κ. The minerals of interest can be divided into two groups, like the stars that produce them, carbon- and oxygen- rich. The carbon-rich species are mostly organic molecules and inorganic carbides. The most important species are amorphous carbon, graphite and SiC and are discussed in both section 3.2 and chapter 6. The oxygen rich minerals, discussed here, are far more varied. The types of minerals expected to form around oxygen-rich stars can be divided roughly into oxides and silicates. Silicates can be further divided into olivines, pyroxenes and miscellaneous silicates for the purposes of this study.

The laboratory spectra of oxygen-rich minerals in this catalogue have been divided into three groups: olivines, pyroxenes, and oxides. The miscellaneous silicates were deemed to be of little use in the identification of circumstellar dust as many were hydrated or were minerals expected due to terrestrial metamorphism. Olivines and pyroxenes are the principal forms of silicates. The fundamental unit in the construction of a silicate is the SiO_4-tetrahedron in which the silicon atom (or more strictly, ion) is situated at the centre of a tetrahedron whose corners are occupied by four oxygen atoms. Classification of sili-

cates is based on the different ways in which the SiO_4-tetrahedra occur, either separately or linked together.

From the work of Gilman (1969), Hackwell (1971), Tielens (1990) and Pégourié & Papoular (1985) the expected condensation sequence of dust around oxygen-rich AGB stars is approximately:

$$
\begin{array}{cc}
Al_2O_3, Corundum & \\
\Downarrow & \\
Ca_2Al_2SiO_7, Augite & \\
\Downarrow & \\
CaMgSi_2O_6, Diopside & Mg_2SiO_4, Forsterite \\
\Downarrow & \Downarrow \\
MgAl_2O_4, Spinel & MgSiO_3, Enstatite \\
\Downarrow & \Downarrow \\
CaAl_2Si_2O_8, Anorthite & (Mg, Fe)_2SiO_4, Olivine
\end{array}
$$

Anorthite is not expected to form in circumstellar shells due to the unlikelihood of the required density and temperature conditions being met. Forsterite is expected to use corundum and augite as nucleation centres as the high density, low temperature conditions required for forsterite nucleation are improbable. Whether the transformation of forsterite into enstatite by gas-grain reactions occurs depends on the ambient conditions, i.e. whether there is enough time for the reactions to take place and a solid-gas interface for the reactions to take place on. (Grossman 1972; Larimer 1979).

Given that we have theoretical models for the dust types we expect to find around oxygen-rich M stars, it seems judicious to look at the laboratory spectra of these minerals. One of the problems in identifying which minerals are contributing to the astronomical spectra is that we cannot be sure of the crystalline/amorphous state of the dust grains. A "smooth" 10μm feature was discovered in the spectra of oxygen-rich stars and was attributed to amorphous silicate dust around those stars (e.g. Woolf & Ney 1969; see Chapter 8). Likewise, more recently evidence has been found for crystalline silicates around such stars in

ISO-SWS spectra (e.g. Waters *et al.* 1996; Waelkens *et al.* 1996). The current discussion of laboratory spectra therefore includes both crystalline and amorphous samples. There have been various published laboratory spectra of the relevant materials. Lists of the laboratory spectra we have collated can be found in Tables 5.1, 5.2 & 5.3. Spectra for the 7.5-13.5μ region (except Figs. 5.10 and 5.11 which cover the 7.5-24.5μ region) are shown in figs. 5.1 to 5.13

5.2 Olivines

The olivines have been further divided into into four subgroups: forsterite, ferromagnesian olivines, 92% forsterite (chosen to illustrate the differences even within samples of the same bulk composition; this particular composition was chosen due to the availability of good laboratory spectra) and nesosilicates. In order to understand these groups it is necessary to understand the geological vocabulary. The term "olivine" covers a wide compositional range. I have used the term olivines for this first group of minerals, however they would be more accurately described as nesosilicates, to which classification the olivine group is a specific subset. In nesosilicates, the SiO_4 tetrahedra are in separate units (i.e. not linked together). Strictly, olivines are nesosilicates which show a continuous sequence of compositions between pure magnesium olivine, forsterite (Mg_2SiO_4) and pure iron olivine, fayalite (Fe_2SiO_4) and between fayalite and pure manganese olivine, tephroite (Mn_2SiO_4). Other members of the olivine group are monticellite ($CaMgSiO_4$) and kirschsteinite ($CaFeSiO_4$). Pure calcium silicate of the same form (i.e.Ca_2SiO_4) is not an olivine. The mineral structure of olivine is usually written as $[Mg_xFe_{2-x}]SiO_4$ or in terms of percentage of an end-member, for example $[Mg_{1.5}Fe_{0.5}]SiO_4$ can be written as Fo75, denoting 75% forsterite; or it could be written as Fa25, denoting 25% fayalite. The nesosilicates presented here are not strictly olivines, but (as stated above) have olivine-like structure and are most appropriately included in this group. Table 5.1 lists the samples in this group.

According to condensation models for dust production around oxygen-rich stars (see section 5.5), the olivine most likely to be found in circumstellar environments is the pure magnesium olivine, forsterite. In fact, it is believed that the silicates in these regions should contain no more than 20% iron (Saxena & Eriksson 1983). This means that the

Table 5.1: Olivine minerals in laboratory spectral database

Mineral	Composition	Crystalline or Amorphous	Figure Figure	Ref.	Source Material
Forsterite	Mg_2SiO_4	Amorphous	5.1a	(1)	Bulk
Forsterite	Mg_2SiO_4	Crystal	5.1b	(3)	Particulate
Forsterite	$Mg_2SiO_4(.xH_2O)$ +imp.	Crystal	5.1c	(4)	Particulate
Forsterite	Mg_2SiO_4	Crystal	5.1d	(5)	Particulate
Forsterite	Mg_2SiO_4	Amorphous	5.1e	(6)	Bulk
Olivine	$[Mg,Fe]_2SiO_4$	Amorphous	5.2a	(1)	Bulk
Olivine	$Mg_{0.8}Fe_{1.2}SiO_4$	Amorphous	5.2b	(1)	Bulk
Olivine	$Mg_{0.8}Fe_{1.2}SiO_4$	Crystal	5.2c	(3)	Particulate
Olivine	$Mg_{1.2}Fe_{0.8}SiO_4$	Crystal	5.2d	(3)	Particulate
Olivine	$Mg_{1.6}Fe_{0.4}SiO_4$	Crystal	5.2e	(3)	Particulate
Olivine	$Mg_{0.22}Fe_{1.78}SiO_4$	Crystal	5.2f	(7)	Particulate
Olivine	$Mg_{0.36}Fe_{1.64}SiO_4$	Crystal	5.2g	(7)	Particulate
Olivine	$Mg_{0.58}Fe_{1.42}SiO_4$	Crystal	5.2h	(7)	Particulate
Olivine	$Mg_{0.82}Fe_{1.18}SiO_4$	Crystal	5.2i	(7)	Particulate
Olivine	$Mg_{1.02}Fe_{0.98}SiO_4$	Crystal	5.2j	(7)	Particulate
Olivine	$Mg_{1.2}Fe_{0.8}SiO_4$	Crystal	5.2k	(7)	Particulate
Olivine	$Mg_{1.32}Fe_{0.68}SiO_4$	Crystal	5.2l	(7)	Particulate
Olivine	$Mg_{1.76}Fe_{0.24}SiO_4$	Crystal	5.2m	(7)	Particulate
Olivine	$Mg_{1.76}Fe_{0.24}SiO_4$	Crystal	5.2n	(7)	Particulate
Olivine	$Mg_{1.84}Fe_{0.16}SiO_4$	Crystal	5.3a	(7)	Particulate
Olivine	$Mg_{1.84}Fe_{0.16}SiO_4$	Crystal	5.3b	(7)	Particulate
Olivine	$Mg_{1.84}Fe_{0.16}SiO_4$	Crystal	5.3c	(7)	Particulate
Olivine	$Mg_{1.84}Fe_{0.16}SiO_4$	Crystal	5.3d	(7)	Particulate
Monticellite	$CaMgSiO_4$	Crystal	5.2o	(7)	Particulate
Copper Silicate*	$Cu(II)SiO_4(.xH_2O)$	Crystal	5.4a	(4)	Particulate
Zinc Silicate*	$ZnSiO_4(.xH_2O$ or wet)	Crystal	5.4b	(4)	Particulate
Almandite*	$Fe_2^{3+}Al_2(SiO_4)_3$	Crystal	5.4c	(7)	Particulate
Andradite*	$Ca_3Fe_3^{2+}(SiO_4)_3$	Crystal	5.4d	(7)	Particulate
Grossular*	$Ca_3Al_2(Si0_4)_3$	Crystal	5.4e	(7)	Particulate
Pyrope*	$Mg_3Al_2(SiO_4)_3$	Crystal	5.4f	(7)	Particulate
Spessartine*	$Mn_3Al_2(SiO_4)_3$	Crystal	5.4g	(7)	Particulate

(1) Jena Group web site (http://www.astro.uni-jena.de/Group/Subgroups/Labor/Labor/odata.html)

(2) K.L. Day, 1979, *Astrophys. J.*, **234**, 158-161.

(3) Mukai & Koike, 1990, *Icarus*, **87**, 180-187.

(4) R.A. Nyquist, 1971, *Infrared Spectra of Inorganic Compounds.*

(5) P.J. Launer, 1952, *American Mineralogist*, **37** , 764-784.

(6) Kratschmer & Huffman, 1979, *Astrophys. Sp. Sci.*, **61**, 195.

(7) Salisbury, J.W., *Pers. Comm.*, FTP site - rocky.eps.jhu.edu.

(8) Koike *et al.*, 1995a, *Icarus*, **114**, 203-214

(9) Hofmeister, A.M., *Pers. Comm.*

* These minerals are not strictly olivine but have olivine-like structure

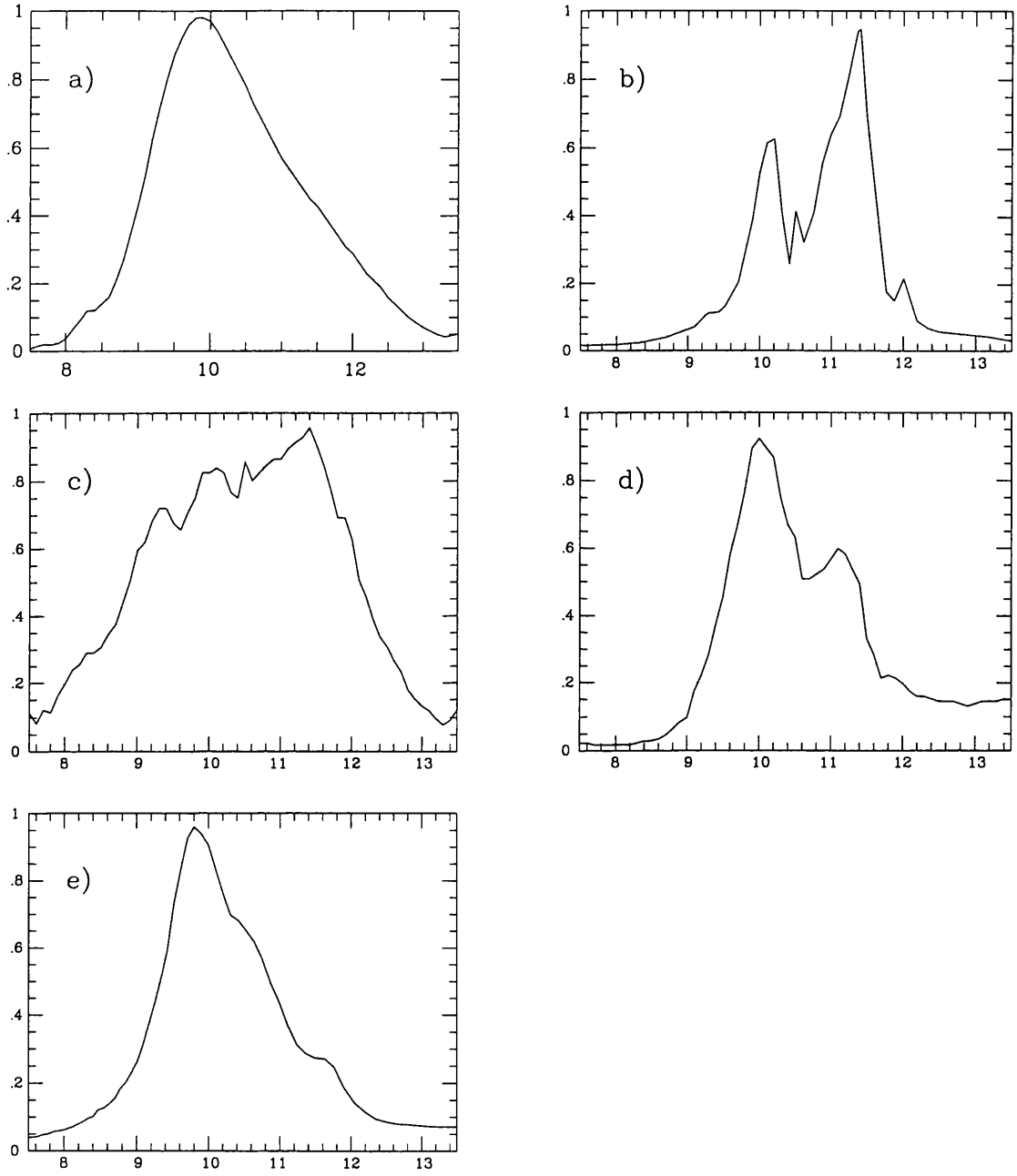

a) From Jena Group

b) From Koike *et al.* 1990

c) From Nyquist 1971

d) From Launer 1952

e) From Kratschmer and Huffman 1979

Figure 5.1: Laboratory spectra of forsterites; the x-axis is wavelength in μm, the y-axis is the normalised extinction κ.

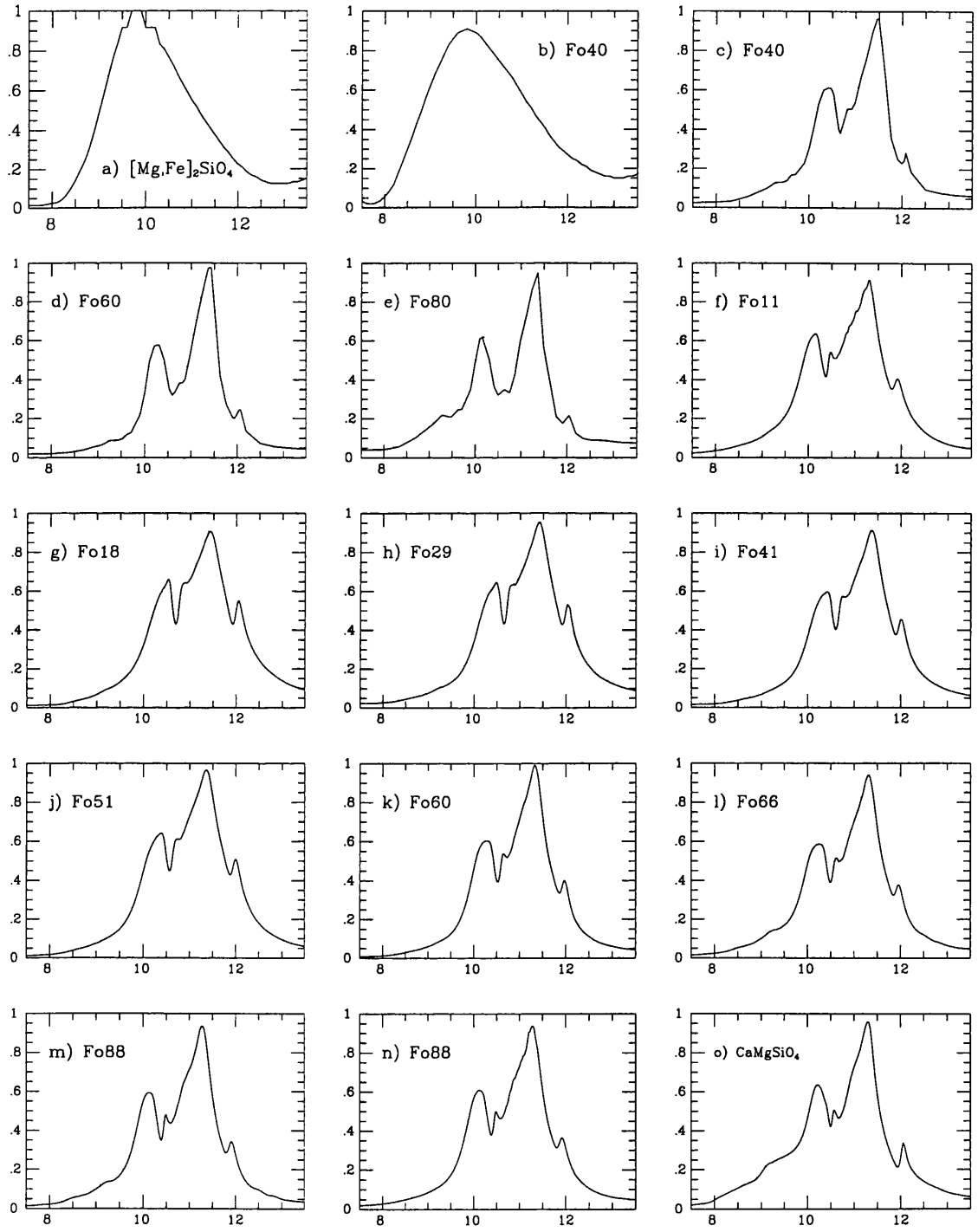

Figure 5.2: Laboratory spectra of ferromagnesian olivines; the x-axis is wavelength in μm, the y-axis is the normalised extinction κ.

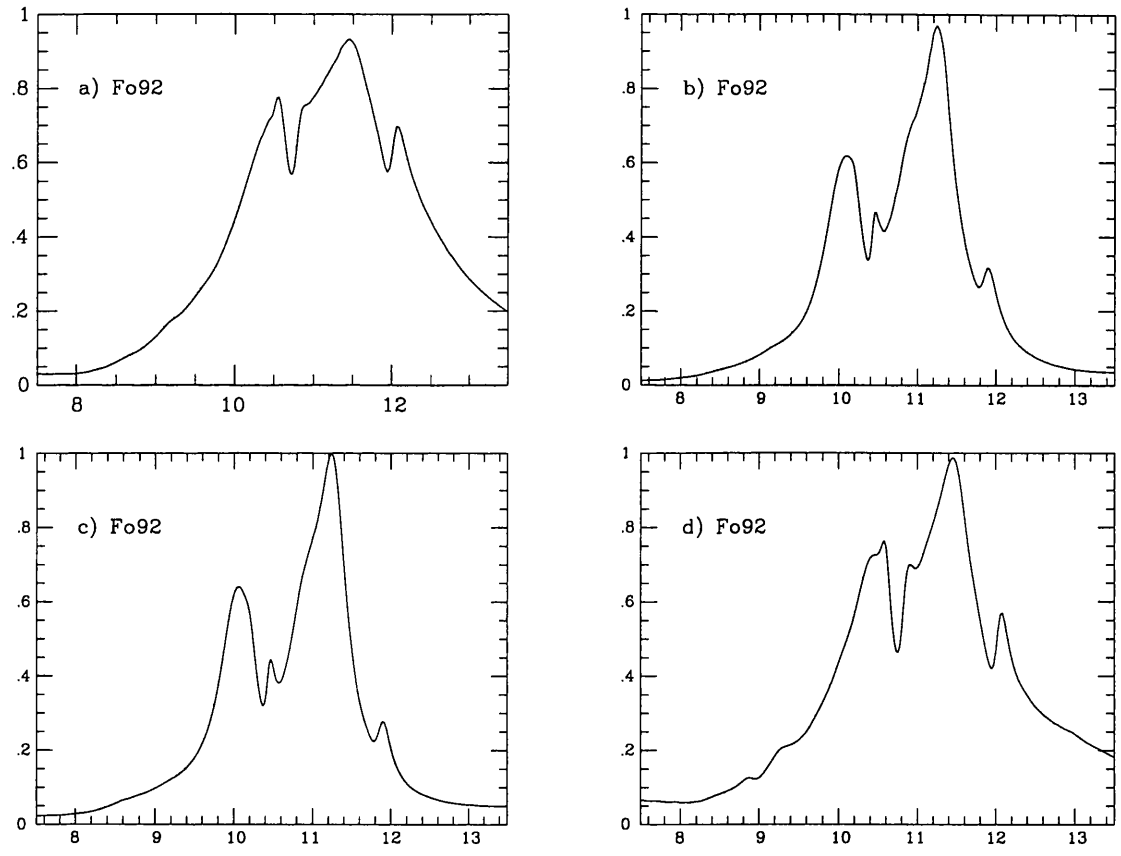

Figure 5.3: Laboratory spectra of 92% Forsterite ferromagnesian olivines; the x-axis is wavelength in μm, the y-axis is the normalised extinction κ.

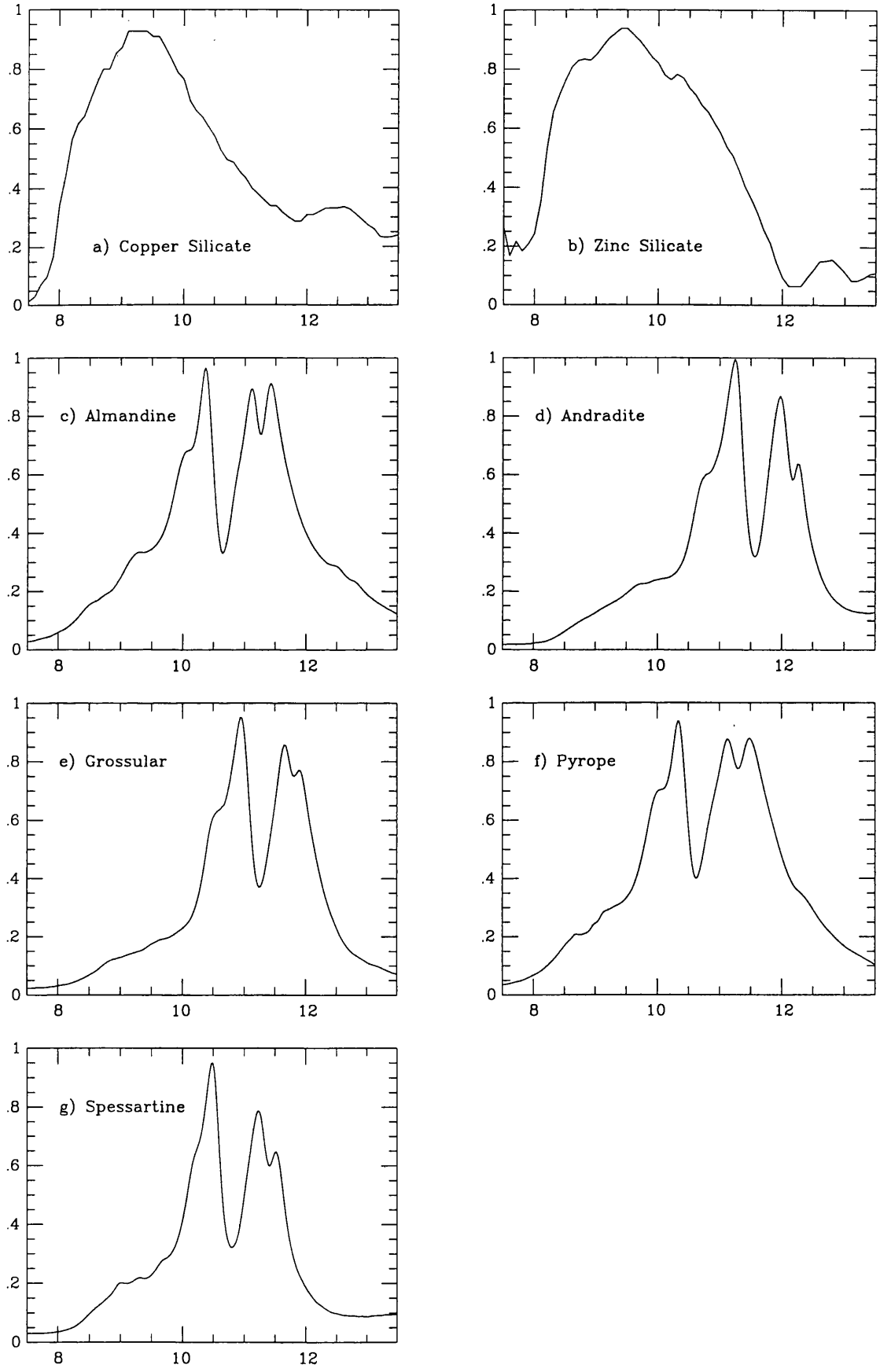

Figure 5.4: Laboratory spectra of nesosilicates; the x-axis is wavelength in μm, the y-axis is the normalised extinction κ.

ferromagnesian olivines of most interest range from Fo80 to Fo100 (80-100% forsterite). Forsterite melts at 1890°C and fayalite at 1205°C. These olivines demonstrate the effect of replacing an ion of smaller radius (Mg^{2+}, r=0.66Å) with a larger one (Fe^{2+}, r=0.74Å) on the melting point/formation temperature of a mineral. The cation-oxygen bonds are weaker for the larger cations, thus, as more of the larger cations enter the olivine the melting point/formation temperature drops. Fig. 5.1 shows the spectra of five forsterite samples. All five spectra are noticeably different, illustrating the difficulty in using such laboratory spectra to identify observed astronomical spectra features.

The five laboratory samples of forsterite have all been obtained using diverse techniques and samples of differing natures, explaining the differences in their spectra. The first sample spectrum, shown in Fig. 5.1a comes from a study by the Jena group and is available on their web-site[1]. The data is in the form of the complex refractive index (n and k) which I have used in conjunction with a Mie theory program using 0.1μm grain size in order to obtain the extinction efficiency. The complex refractive index was obtained by the Jena group using a Kramers-Kronig analysis of reflectance measurements from the polished surface of a bulk sample of forsterite glass, i.e. amorphous forsterite. The second spectrum, shown in Fig. 5.1b, from Mukai & Koike (1990), was collected using the KBr matrix method, discussed in Chapter 4. The sample itself, regardless of being dispersed in the KBr pellet, consisted of crystalline grains with an average size <0.4μm. The spectrum was not corrected for the KBr matrix. Comparing just these two samples we can see the enormous difference between amorphous and crystalline samples. The third forsterite spectrum, seen in Fig. 5.1c was taken from "Infrared Spectra of Inorganic Compounds" by Nyquist (1971). This sample contains water and impurities which may explain the unusual shape of the spectrum, which is unlike either the amorphous or the crystalline spectra in the sample. The fourth spectrum (Fig. 5.1d) was obtained from Launer (1952). This is the transmission spectrum of a thin film of powdered crystalline forsterite in which the powder grains have diameters <2μm. This spectrum appears to be a intermediate between the amorphous and crystalline samples. The final forsterite spectrum, shown in Fig. 5.1e was taken from Kratschmer and Huffman (1979). Like the work of the Jena group, this spectrum was obtained by using reflectance measurements of a disordered forsterite, however, in this case, the dielectric constants (ϵ' and ϵ'') were derived using classical dispersion

[1] http://www.astro.uni-jena.de/Group/Subgroups/Labor/Labor/odata.html

theory. The extinction efficiencies were calculated using Mie theory by the authors. The first and fifth spectra are similar, but with definite differences. These differences may have arisen through the use of differing techniques to extract the optical constants, differences in the Mie programs used or differences in the sample.

Fig. 5.2 shows the spectra of a collection of ferromagnesian olivines. As the name suggests, ferromagnesian olivines are olivines with iron and/or magnesium cations. These minerals represent the majority of olivines, although others exist, for example, with calcium and/or manganese cations. The first two spectra, shown in Fig. 5.2a & b, were obtained from amorphous (glassy) olivine by the Jena Group. These two spectra are clearly different from the remaining spectra all obtained from crystalline samples. Again the difference between the crystalline and amorphous samples is indisputable. Within the set of crystalline olivine spectra, there is a general similarity amongst all the spectra, with small changes in the detailed shape of the features as the relative amounts of magnesium and iron vary. However, even samples with the same ratio of magnesium to iron show differences in their spectra. This is better demonstrated in Fig. 5.3 where four spectra of Fo92 (92% forsterite) are plotted, each broadly the same but with definite differences. To explain these variations we need to look at the detailed descriptions of the four samples. All four spectra were taken from the same source, i.e. the FTP site of John Salisbury (rocky.eps.jhu.edu); came from naturally occurring forsterites from different geographical sites; were obtained by the same method, i.e. transmission spectrometry of KBr-dispersed powdered samples; and were all ground to the same particle size ($<2\mu$m). The only difference between members of this sample is in the nature and abundance of impurities. The third Fo92 (Fig. 5.3c) is apparently pure, whereas the other three sample have differing amounts of different impurities such as pyroxene, spinel, and ilmenite in sample 1 (Fig. 5.3a); limonite[2] in sample 2 (Fig. 5.3b); and serpentine[3] and iron in sample 4 (Fig. 5.3d). It is clear that small amount of impurities have a noticeable effect on the spectra of crystalline olivine.

The spectra of seven nesosilicates are shown in Fig. 5.4. As discussed at the beginning of this section, nesosilicates are silicate in which the SiO_4 tetrahedra are in separate units (i.e. not linked together). The nesosilicates presented here are not strictly olivines, but

[2]Limonite is the term used for a range of mixtures of hydrated iron oxides and iron hydroxides

[3]Serpentine is the main alteration product of olivine and pyroxene and has the chemical composition: $Mg_6Si_{10}(OH)_8$

(as stated above) have olivine-like structure with non-olivine cations. The copper and zinc silicates (Fig. 5.4a & b) have spectra very similar to those of the silicon dioxide samples discussed in section 5.4. The five remaining samples have similar crystal structure with differing cations (see Fig. 5.4c-g and Table 5.1). Their spectra are almost identical.

All the crystalline olivines have similar enough spectra, as do the amorphous olivines, that it is difficult to see how these laboratory spectra can be used to differentiate between olivines of different compositions in the spectra of oxygen-rich stars. One suggested identification technique for crystalline olivines relies on a longer wavelength infrared feature, in the region of 70μm, where a small change in the iron content produces a discernable shift in the peak wavelength of the features (Waters *et al.* 1996)

5.3 Pyroxenes

Once again, this group has been separated further into four subdivisions here: enstatites, ferromagnesian pyroxenes, augite pyroxenes and miscellaneous other pyroxenes. The general formula for a pyroxene can be written as $R_2^{2+}Si_2O_6$ or sometimes more simply as $R^{2+}SiO_3$. Pyroxenes are inosilicates, i.e. silicates which consist of a chain structure made of a linkage of SiO_4 tetrahedra each sharing two oxygen atoms. The common pyroxenes divide into two series based on their crystallographic structure: the clinopyroxenes with monoclinic[4] structure and the orthopyroxenes with orthorhombic[5] structure. The orthorhombic sub-group consists essentially of the compositional series $MgSiO_3$–$FeSiO_3$, while the monoclinic sub-group includes minerals having a wide range of chemical compositions. In a similar way to the olivines, ferromagnesian pyroxenes (or orthopyroxenes) form a continuous series between pure magnesium pyroxene, enstatite ($MgSiO_3$) and pure iron pyroxene, ferrosilite ($FeSiO_3$) end-members. Furthermore, in an analogous way to the ferromagnesian olivines, we expect the pyroxenes in circumstellar dust to contain $\leq$10% iron (Saxena & Eriksson 1983). Table 5.2 lists the samples available for this group.

Fig. 5.5 shows the spectra of six enstatite samples: three amorphous and three crystalline. The three amorphous enstatite spectra are almost identical. The three crystalline

[4] monoclinic crystals have three edges of unequal length with two axes that are mutually perpendicular and one inclined axis

[5] orthorhombic crystals have three axes which are mutually perpendicular

Table 5.2: Pyroxene minerals in laboratory spectral database

Mineral	Composition	Crystalline or Amorphous	Figure No.	Ref.*	Source Material
Enstatite	$MgSiO_3$	Amorphous	5.5a	(1)	Bulk
Enstatite	$Mg_{0.95}Fe_{0.05}SiO_3$	Amorphous	5.5b	(1)	Bulk
Enstatite	$MgSiO_3$	Crystalline	5.5d	(7)	Particulate
Enstatite	$MgSiO_3$	Amorphous	5.5c	(2)	Film
Enstatite	$MgSiO_3$	Powder	5.5e	(5)	Particulate
Enstatite	$MgSiO_3$	Powder	5.5f	(5)	Particulate
Bronzite	$Mg_{0.8}Fe_{0.2}SiO_3$	Amorphous	5.6a	(1)	Bulk
Bronzite	$Mg_{0.7}Fe_{0.3}SiO_3$	Amorphous	5.6b	(1)	Bulk
Hypersthene	$Mg_{0.6}Fe_{0.4}SiO_3$	Amorphous	5.6c	(1)	Bulk
Hypersthene	$Mg_{0.5}Fe_{0.5}SiO_3$	Amorphous	5.6d	(1)	Bulk
Hypersthene	$(Mg,Fe^{2+})SiO_3$	Crystalline	5.6e	(7)	Particulate
Ferrohypersthene	$Mg_{0.4}Fe_{0.6}SiO_3$	Amorphous	5.6f	(1)	Bulk
Ferromagnesian Pyroxene†	$(Mg,Fe^{2+})SiO_3$	Crystalline	5.6g	(7)	Particulate
Ferromagnesian Pyroxene‡	$(Mg,Fe^{2+})SiO_3$	Crystalline	5.6h	(7)	Particulate
Ferromagnesian Pyroxene	$(Mg,Fe^{2+})SiO_3$	Powder	5.6i	(5)	Particulate
Augite	$Mg_{0.5}Fe_{0.43}Ca_{0.03}Al_{0.04}SiO_3$	Amorphous	5.7a	(1)	Bulk
Augite	$(Ca,Na)(Mg,Fe,Al,Ti)(Si,Al)_2O_6$	Crystalline	5.7b	(7)	Particulate
Augite	$(Ca,Na)(Mg,Fe,Al,Ti)(Si,Al)_2O_6$	Crystalline	5.7c	(7)	Particulate
Diopside(Augite)	$CaMgSi_2O_6$	Crystalline	5.7d	(7)	Particulate
Diopside(Augite)	$CaMgSi_2O_6$	Crystalline	5.7e	(7)	Particulate
Hedenbergite(Augite)	$CaFe^{+2}Si_2O_6$	Crystalline	5.7f	(7)	Particulate
Aegerine(Augite)	$NaFe^{3+}(Si_2O_6$	Powder	5.7g	(5)	Particulate
Jadeite	$NaAlSi_2O_6$	Powder	5.8a	(5)	Particulate
Jadeite	$NaAlSi_2O_6$	Crystalline	5.8b	(7)	Particulate
Spodumene	$LiAlSi_2O_6$	Powder	5.8c	(5)	Particulate
Lithium Silicate	Li_2SiO_3	Crystal	5.8d	(4)	Particulate
Bustamite	$(Mn,Ca)_3Si_3O_9$	Crystal	5.8e	(7)	Particulate
Rhodonite	$(Mn^{2+},Fe^{2+},Mg,Ca)SiO_3$	Crystal	5.8f	(7)	Particulate

* see footnotes to Table 5.1

† sample has monoclinic crystal structure

‡ sample has orthorhombic crystal structure

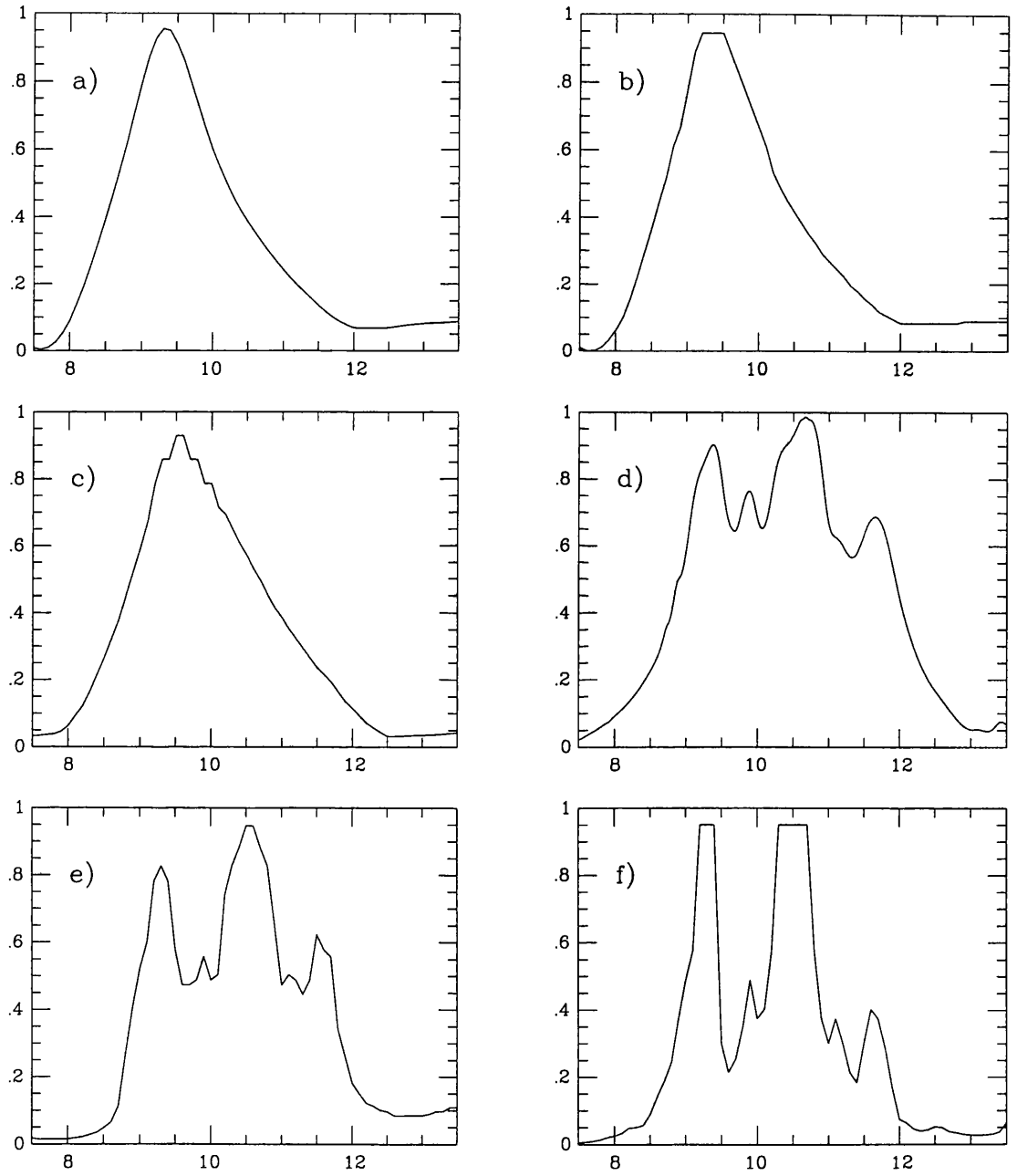

Figure 5.5: Laboratory spectra of enstatites; the x-axis is wavelength in μm, the y-axis is the normalised extinction κ.

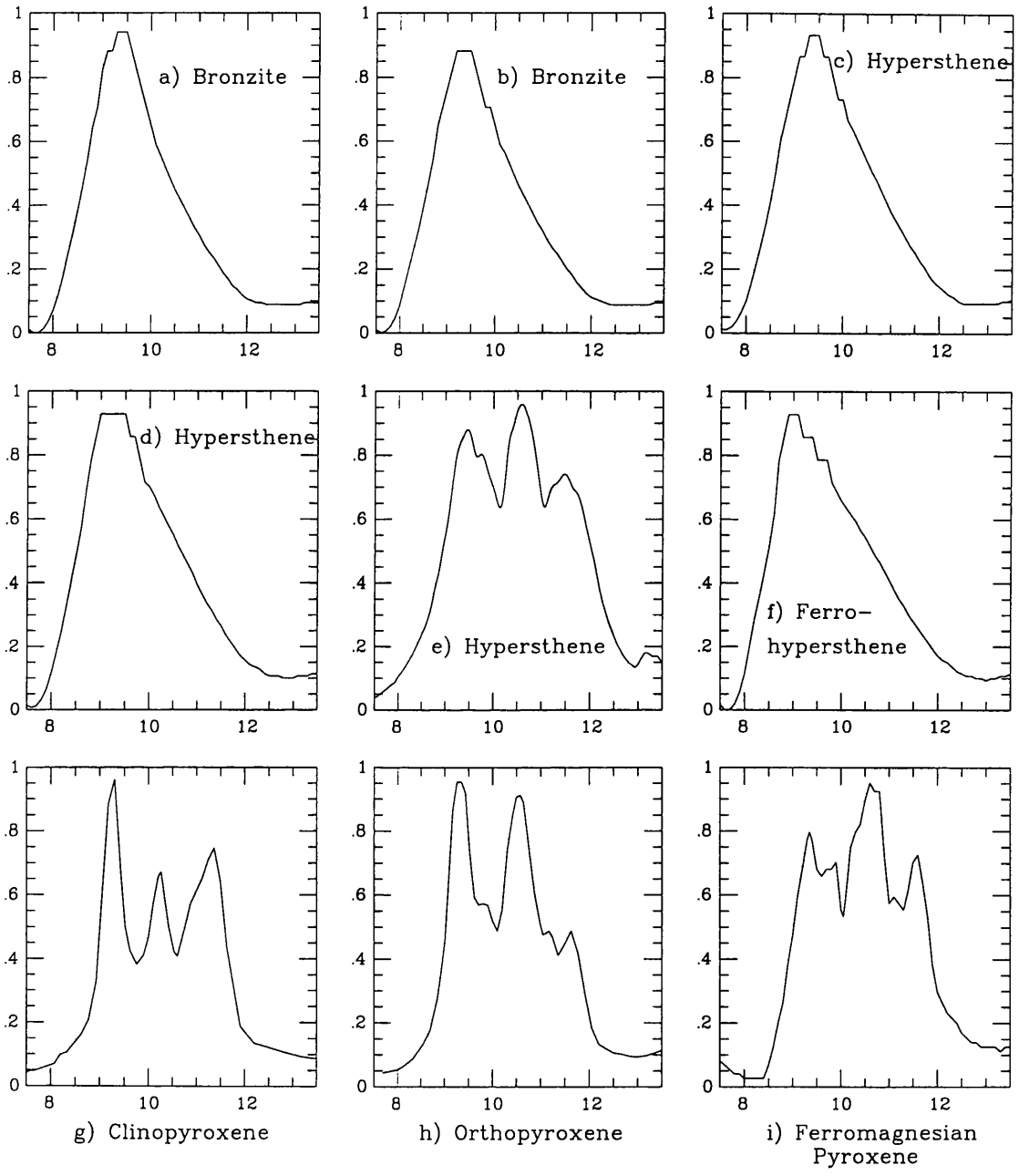

Figure 5.6: Laboratory spectra of ferromagnesian pyroxenes; the x-axis is wavelength in μm, the y-axis is the normalised extinction κ.

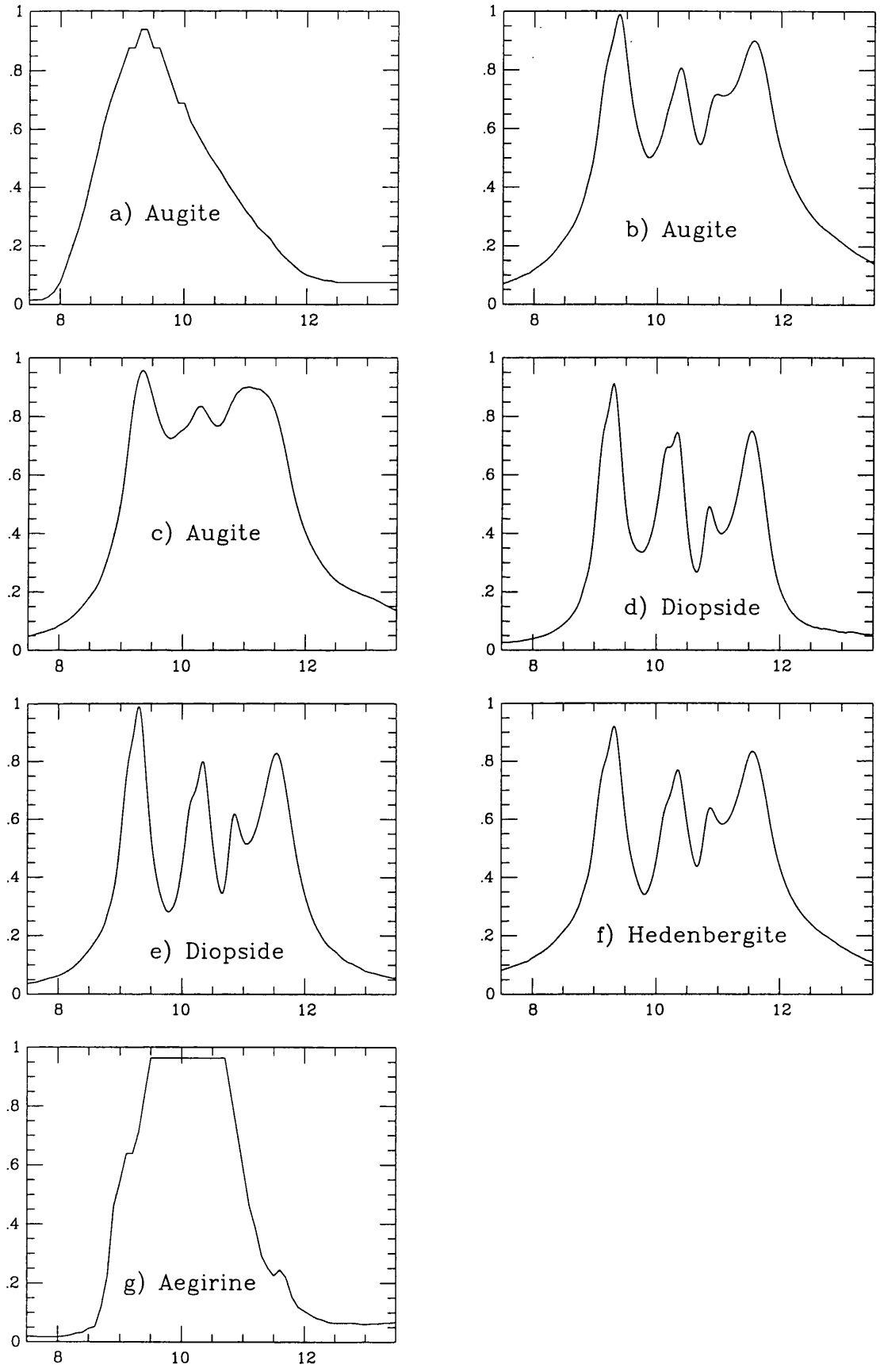

Figure 5.7: Laboratory spectra of augite pyroxenes; the x-axis is wavelength in μm, the y-axis is the normalised extinction κ.

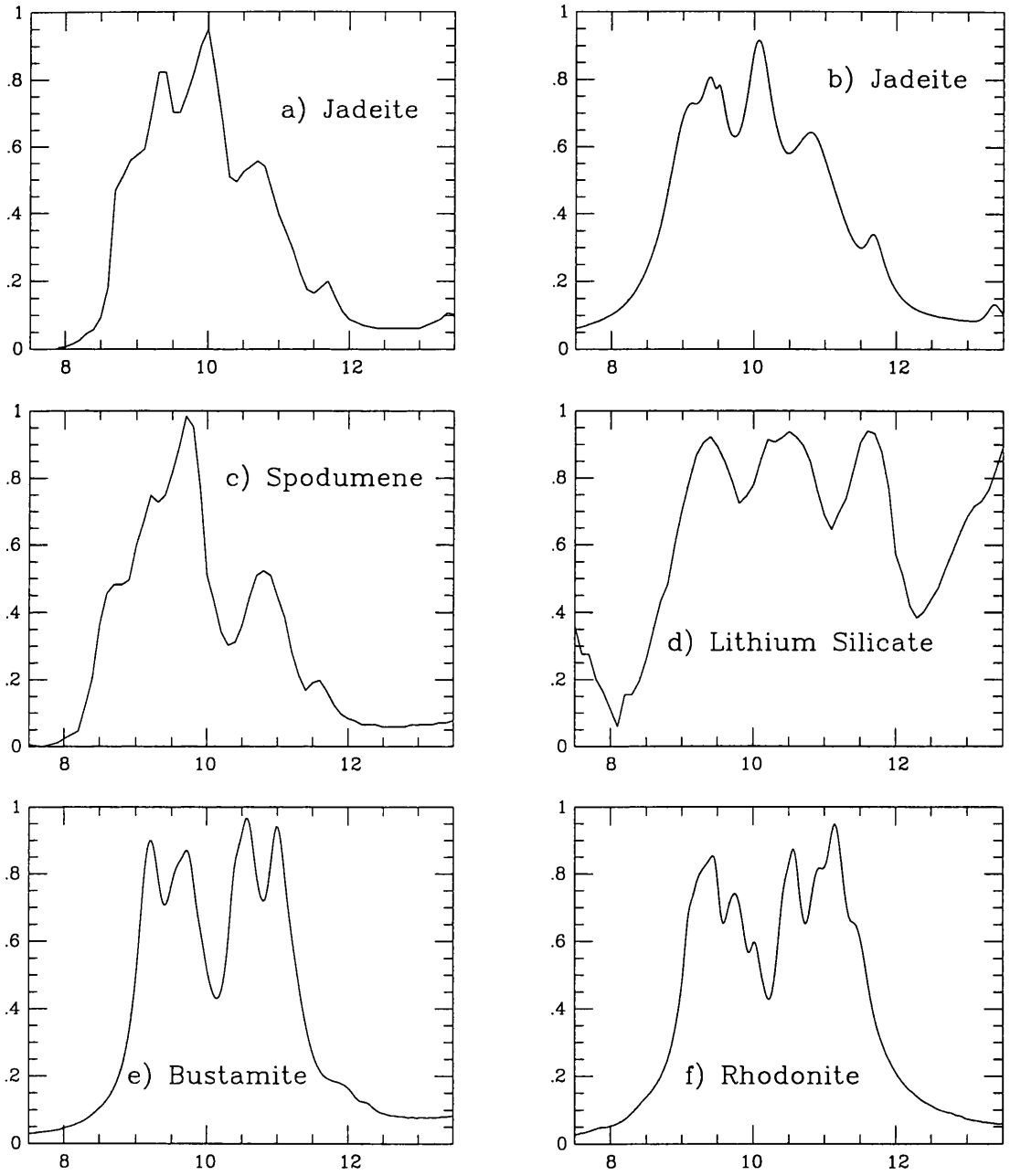

Figure 5.8: Laboratory spectra of other pyroxenes; the x-axis is wavelength in μm, the y-axis is the normalised extinction κ.

enstatite spectra have peaks in the same positions, but there are variations in the exact shapes of the features.

The ferromagnesian pyroxene spectra shown in Fig. 5.6 vary from 80% to 40% magnesium for the amorphous samples. The crystalline samples all contain about 50% magnesium. For the amorphous samples, the shapes and peak position of the features seem to remain fairly constant as the percentage of magnesium decreases down to about 50% (Fig. 5.6a-d). However, for the sample with 40% magnesium (Fig. 5.6f), the peak position of the spectral feature shifts slightly to a shorter wavelength. The spectra of the crystalline samples vary quite drastically. The effect of the crystal structure on the spectra becomes apparent when we compare the clino- and ortho-pyroxenes ((Fig. 5.6g & h). While the features peaks at the same wavelengths, the relative strengths of the features differ. The only difference between these two samples is in the crystal structure.

The augite pyroxenes (Fig. 5.7a-g) are a series of minerals with monoclinic crystals and the general composition: $(Ca,Mg,Fe,Al)_2(Al,Si)_2O_6$. The ferromagnesian orthopyroxene contained only iron and magnesium cations (as the name suggests), whereas the augite pyroxenes also contain other cations. In the expected condensation sequence (section 5.5) pyroxenes containing calcium and aluminium cations play an important role. These dust species are expected to form before, and are expected to act as nucleation centres for, the ferromagnesian silicates. This group comprises two amorphous (Fig. 5.7a & g) and five crystalline (Fig. 5.7b-f) samples. The spectrum of amorphous aegirine (Fig. 5.7g) is saturated and therefore of little use. The spectrum of amorphous augite ($Mg_{0.5}Fe_{0.43}Ca_{0.03}Al_{0.04}SiO_3$;Fig. 5.7a) is very similar to those of the amorphous ferromagnesian pyroxenes (Fig. 5.6a-d) and the amorphous enstatites (Fig. 5.5a-c), which is not unexpected given the small amounts of calcium and aluminium present in the amorphous augite sample relative to the amounts of magnesium and iron. Once more we see that small changes in the cation composition have little effect on the shapes or peak positions of the features in amorphous pyroxene spectra (see Fig. 5.7a, Fig. 5.6a-d and Fig. 5.5a-c). The shapes of the crystalline sample spectra do change considerably but the peak position remains reasonably constant (Fig. 5.7d-f).

Fig. 5.8 shows the spectra of the other pyroxenes with cations which are less likely to

be important in circumstellar environments. Bustamite and rhodonite are not true pyroxenes, but have pyroxene-like structure. These spectra show that the change in the cations has had a much larger effect on the shapes and peak positions of the spectral features than was evident in the spectra of the earlier pyroxene groups (Fig. 5.6 & Fig. 5.7).

5.4 Oxides

The minerals discussed in this section are divided into five parts: corundum (aluminium oxide), iron oxides, magnesium iron oxides, other metal oxides and silicon dioxide. The samples from which these spectra were taken are listed in Table 5.3. Aluminium oxide is important in the condensation models for dust formation around oxygen rich stars (see section 5.5) and silicon dioxide is peculiar because it behaves more like a silicate than an oxide. These two sub-groups will be discussed in detail; the other groups will not be dealt with in any depth.

Although I refer to aluminium oxide as corundum, corundum is strictly one specific form of Al_2O_3 which is actually found in several different forms. Corundum is Al_2O_3 with rhombohedral[6] crystal structure and is otherwise known as α-Al_2O_3. Other forms of aluminium oxide include sapphires (terrestrial gems) and γ-Al_2O_3, an artificially produced form of aluminium oxide with cubic crystal structure. Amorphous Al_2O_3 can also be produced. In Fig. 5.9 we can see that the shape of the spectra vary from sample to sample, however, the peak position remains more or less constant in the 11.5–12μm range.

The first two spectra in Fig. 5.9 (a & b) come from the Jena group web-site. As with the forsterite samples, these spectra were derived from reflectance spectra of amorphous bulk samples using Kramers-Kronig analyses and Mie theory. The difference between these two samples is that the first sample (Fig 5.9a) was porous in nature and the second (Fig 5.9b) was compact. The middle two spectra were taken from Koike *et al.* (1995a; Fig 5.9c & d), having been obtained using the KBr dispersion method. The transmission spectra were then used by the authors to derive the complex refractive index (n and k) through a classical dispersion analysis, so that the spectra presented here have been derived from the refractive index using 0.1μm grains in Mie theory. The first spectrum (Fig 5.9c) was

[6]The rhombohedral crystal structure (also known as trigonal crystal structure) has three non-orthogonal axes which are parallel to three edge-directions of a rhombohedron.

Table 5.3: Oxide minerals in laboratory spectral database

Mineral	Composition	Crystalline or Amorphous	Figure No.	Ref.	Source Material
Corundum	Al_2O_3	Amorphous	5.9a	1)	Bulk
Corundum	Al_2O_3	Amorphous	5.9b	1)	Bulk
Corundum	Al_2O_3	Crystal	5.9c	(8)	Particulate
Corundum	Al_2O_3	Crystal	5.9d	(8)	Particulate
Corundum	Al_2O_3	Crystal	5.9e	(4)	Particulate
Iron Oxide	FeO		5.10a	(1)	Bulk
Hematite	Fe_2O_3	Crystal	5.10b	(7)	Particulate
Magnetite	$Fe^{2+}Fe_2^{3+}O_4$	Crystal	5.10c	(7)	Particulate
Magnesium Iron Oxide	$Mg_{0.6}Fe_{0.4}O$		5.11a	(1)	Bulk
Magnesium Iron Oxide	$Mg_{0.5}Fe_{0.5}O$		5.11b	(1)	Bulk
Magnesium Iron Oxide	$Mg_{0.3}Fe_{0.7}O$		5.11c	(1)	Bulk
Magnesium Iron Oxide	$Mg_{0.2}Fe_{0.8}O$		5.11d	(1)	Bulk
Magnesium Iron Oxide	$Mg_{0.1}Fe_{0.9}O$		5.11e	(1)	Bulk
Magnesium Oxide	MgO	Crystal	5.12a	(4)	Particulate
Dilithium Oxide	Li_2O	Crystal	5.12b	(4)	Particulate
Titanium Dioxide	TiO_2	Crystal	5.12c	(4)	Particulate
Rutile	TiO_2	Crystal	5.12d	(7)	Particulate
Ilmenite	$Fe^{2+}TiO_3$	Crystal	5.12e	(7)	Particulate
Chromite	$Fe^{2+}Cr_2O_4$	Crystal	5.12f	(7)	Particulate
SiO_2^*					
Obsidian	SiO_2	Crystal	5.13a	(7)	Particulate
Quartz	SiO_2	Crystal	5.13b	(7)	Particulate
Silicon Dioxide	SiO_2	Crystal	5.13c	(4)	Particulate
Cristobalite	SiO_2	Crystal	5.13d	(4)	Particulate
Silica Glass	$(SiO_2)_n.xH_2O$	Crystal	5.13e	(4)	Particulate
Tridymite	SiO_2	Crystal	5.13f	(9)	Particulate

$*$ - silicon dioxide is more like a silicate than an oxide.

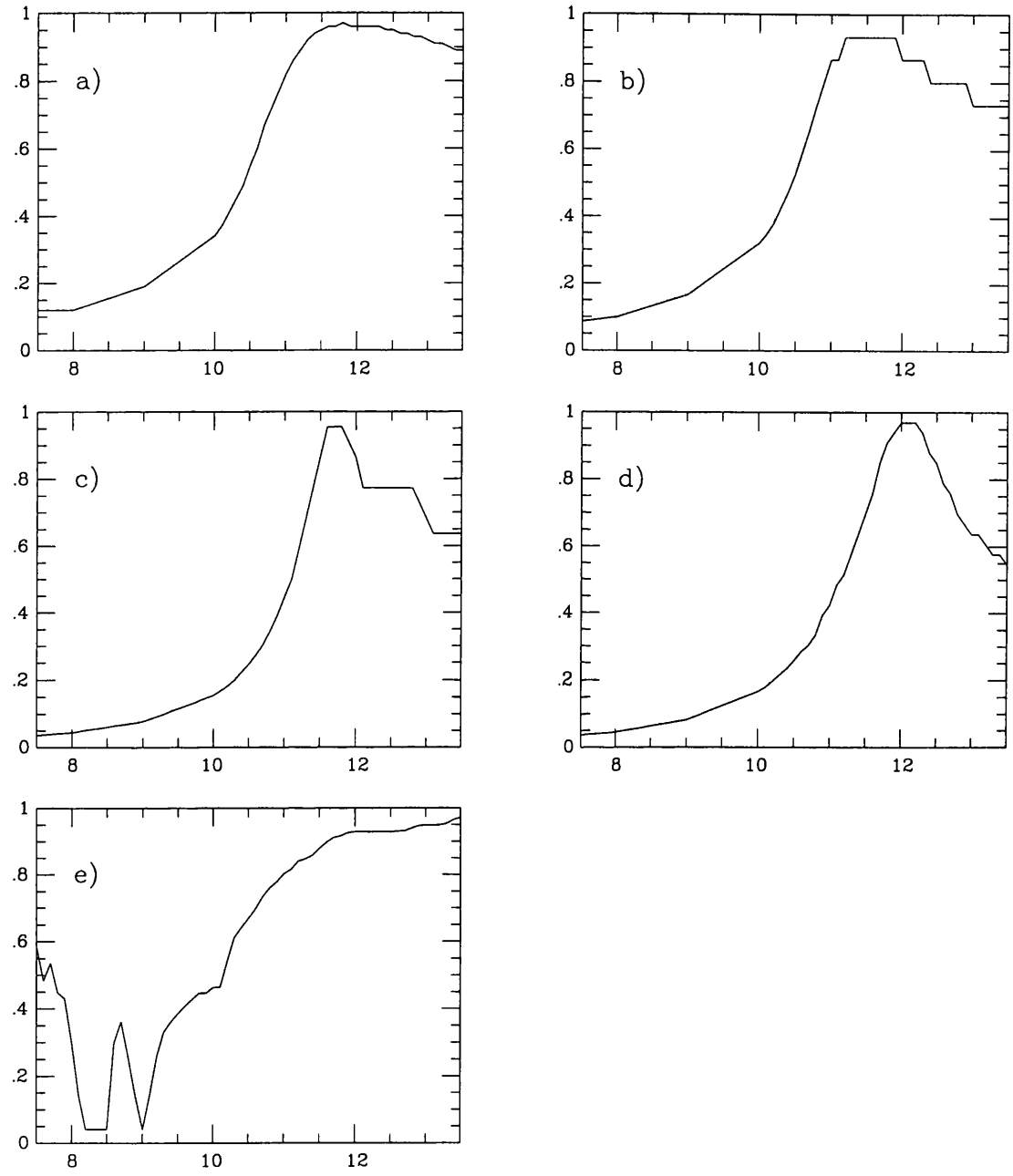

Figure 5.9: Laboratory spectra of corundum (Al_2O_3); the x-axis is wavelength in μm, the y-axis is the normalised extinction κ.

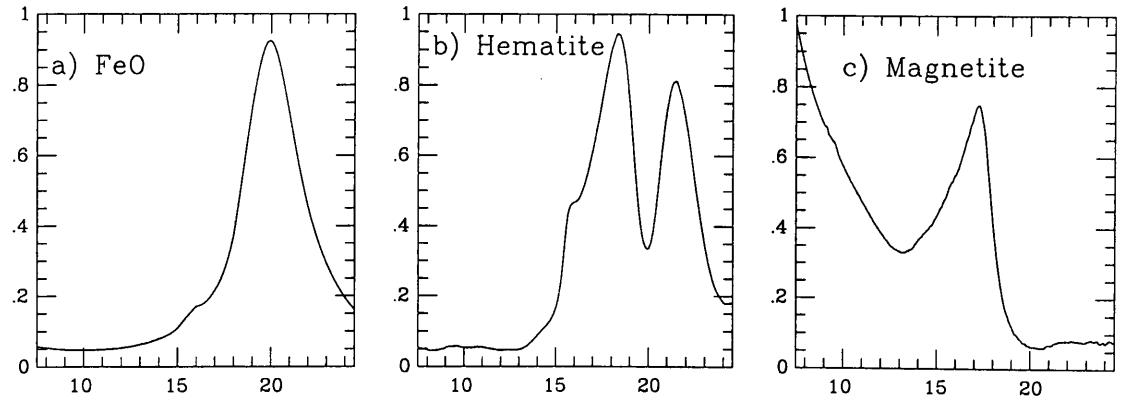

Figure 5.10: Laboratory spectra of iron oxides; the x-axis is wavelength in μm, the y-axis is the normalised extinction κ.

taken using a commercially available corundum with an average particle size of 200Å and was composed predominantly of γ-Al_2O_3 crystals with a small amount of α-Al_2O_3. The sample for the second spectrum from Koike *et al.* (1995a; Fig 5.9d) was obtained by combustion methods. This sample had grains with a mean size of 0.3μm and consisted of γ-Al_2O_3 crystals. In fact, the main difference between the four spectra in Fig 5.9 (a-d) is in the sharpness of the peak at 11.5–12μm; the two crystalline samples (Fig 5.9c & d) have marginally sharper features than the amorphous samples(Fig 5.9a & b). The second sample from Koike *et al.* (1995a) peaks at a slightly longer wavelength, closer to 12μm than 11.5μm. The final corundum spectrum comes from Nyquist's "Infrared Spectra of Inorganic Compounds". The difference in shape with respect to the other spectra is probably due to water and other impurities.

Fig. 5.10 shows the spectra of three oxides: FeO, Fe_2O_3 (hematite) and $Fe^{2+}Fe^{3+}{}_2O_4$ (Fe_3O_4; magnetite). They are all markedly different. All three are featureless in the 8-13μm region, however, FeO has a single peak at 20μm; hematite has a double feature with peaks at 18.2 and 21.2μm; and magnetite has a generally decreasing absorption moving from shorter to longer wavelengths with a single feature peaking at 17.1μm. Fig. 5.11 shows the spectra of five magnesium iron oxides. All these spectra peak between 15 and 20μm, with the peak position moving to longer wavelengths as the iron to magnesium ratio increases.

The miscellaneous metal oxide spectra shown in Fig. 5.12 are of little interest because the

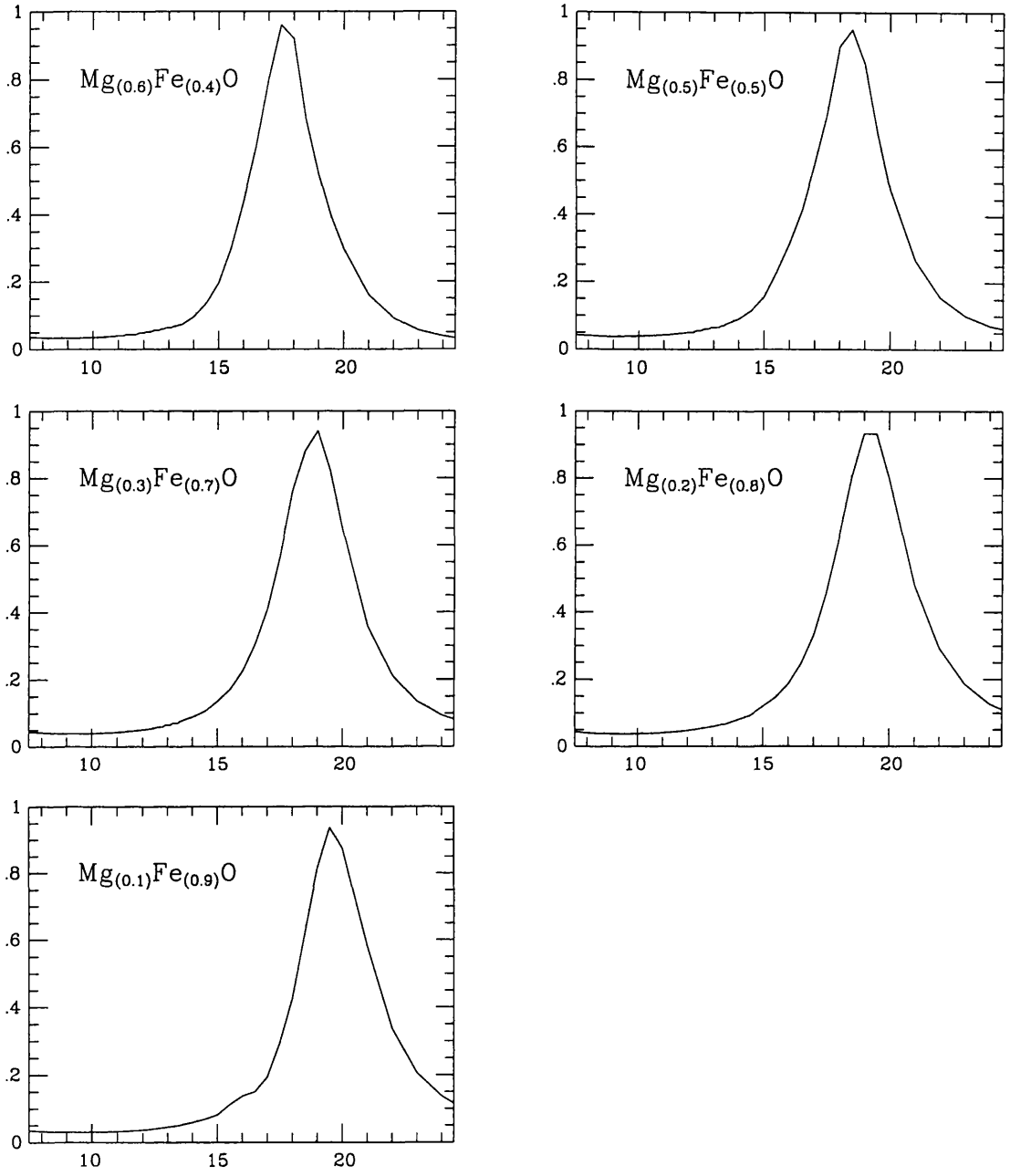

Figure 5.11: Laboratory spectra of magnesium iron oxides; the x-axis is wavelength in μm, the y-axis is the normalised extinction κ.

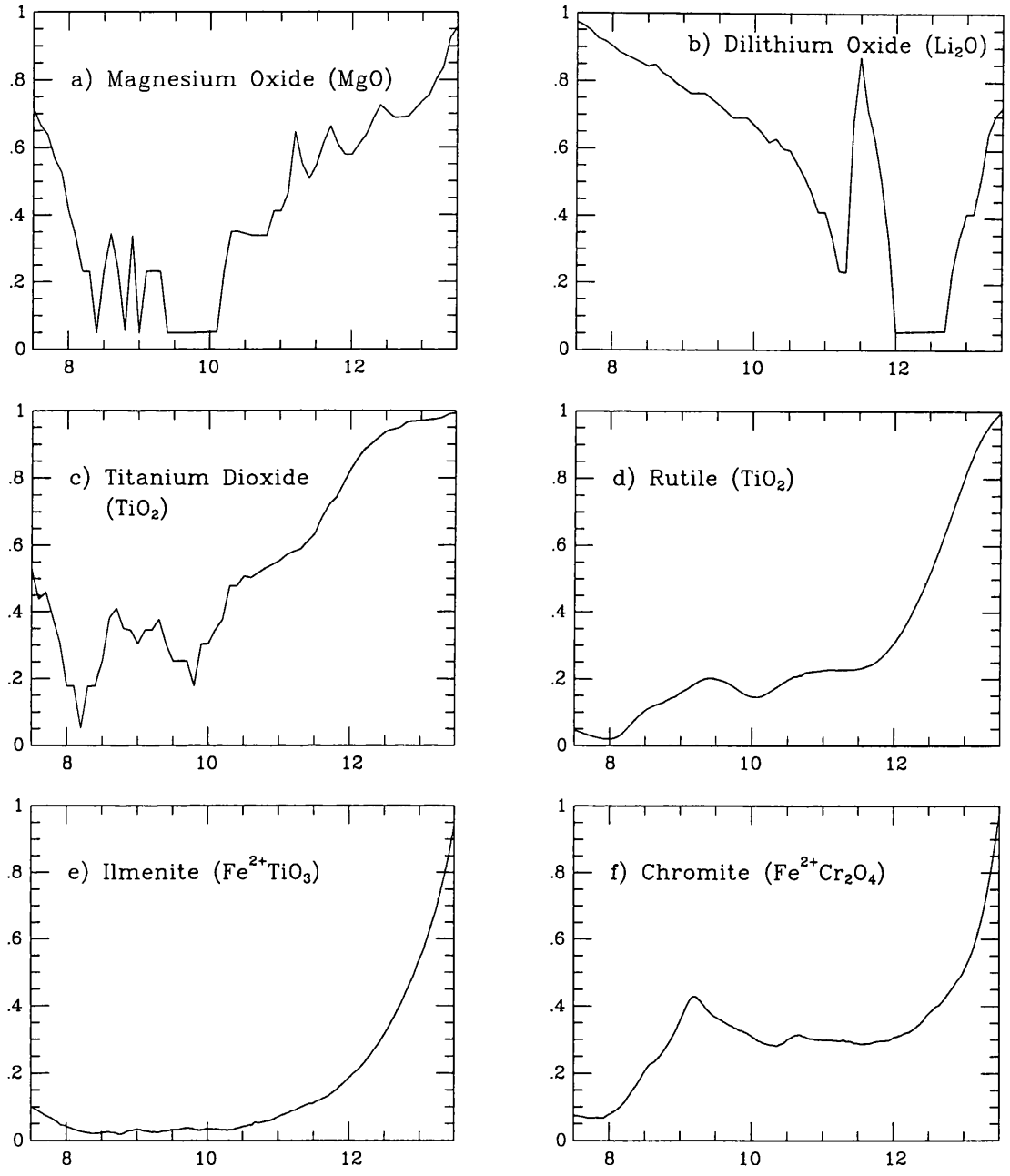

Figure 5.12: Laboratory spectra of other oxides; the x-axis is wavelength in μm, the y-axis is the normalised extinction κ.

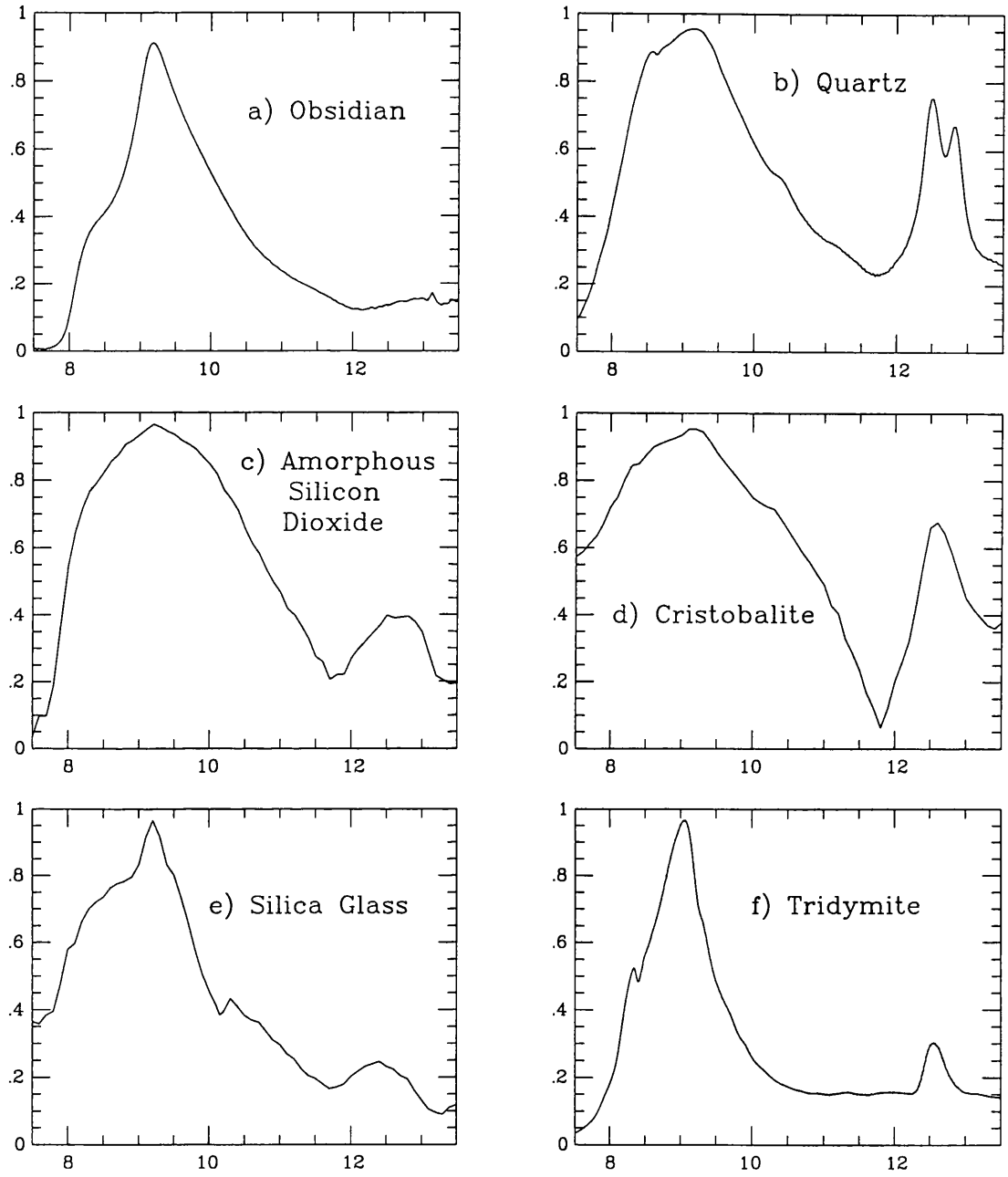

Figure 5.13: Laboratory spectra of silicon dioxides (SiO_2); the x-axis is wavelength in μm, the y-axis is the normalised extinction κ.

majority of the elements comprising the cation constituents are believed to have such low abundances around oxygen-rich stars that even if these oxides were formed, there would be little of them to be detectable in the observed spectra. These spectra are included for completeness. Magnesium oxide may be of interest from a detectability point of view, but the spectrum is very poor quality. Chromite ($Fe^{2+}Cr_2O_4$; Fig. 5.12f) is interesting because it is very similar structurally to magnetite ($Fe^{2+}Fe_2^{3+}O_4$; Fig. 5.10c). Chromite is just magnetite with the Fe^{3+} cations replaced with Cr cations. The change has produced a huge effect on the spectrum which can be seen if one compares Fig. 5.12f with Fig. 5.10c.

The final oxygen-rich mineral group in this catalogue comprises the silica minerals. Silicon dioxide is an anomaly amongst the oxides. Although SiO_2 is chemically an oxide, the structures and properties of the silica minerals are more closely allied to those of silicates. It is therefore not surprising that they should be included in a discussion of dust species around oxygen-rich stars. Silicon dioxide can be either crystalline or amorphous. In the crystalline case, the structure consists of 3-dimensional lattices of SiO_4 tetrahedra, in which all four oxygen atoms of each tetrahedron are shared by adjoining tetrahedra. There are three main forms or polymorphs of crystalline SiO_2: quartz, tridymite and cristobalite. These forms may be seen as a progression in the temperature of formation, but are also unstable outside the temperature range of formation (Deer, Howie & Zussman 1966). Quartz, itself, is also split into two types: α- and β-quartz. α-quartz is stable up to a temperature of 846K and is trigonal trapezoidal in crystal structure. At 846K, α-quartz converts into β-quartz, which has hexagonal trapezoidal crystals. β-quartz is stable between 846K and 1143K. At 1143K the β-quartz is transformed into tridymite which has hexagonal holohedral structure. At 1743K tridymite converts into cristobalite which is cubic in structure and melts at 1986K. Silicon dioxide can also exist in amorphous forms such as lechaterlierite, obsidian and silica glass. These glasses can exist up to about 1300K, at which temperature the rate of crystallization increases rapidly and the SiO_2 will tend to be annealed to a crystalline form. The different forms of silicon dioxide and their stable temperatures are summarised in Table 5.4. Fig. 5.13 shows the spectra of six forms of silicon dioxide. These spectra vary in shape but all have major features at $\sim$9.2μm and, with the exception of obsidian, minor features with peaks at $\sim$12.5μm.

Table 5.4: Stable temperatures of silica minerals

SiO_2 type	stable/formation temperature in K	Crystal Structure
α-quartz	$\leq$846	trigonal trapezoidal
β-quartz	846–1143	hexagonal trapezoidal
tridymite	1143–1743	hexagonal holohedral
cristobalite	1743–1986	cubic
silica glass	$\leq\sim$ 1300	amorphous
obsidian	$\leq\sim$ 1300	amorphous
lechaterlierite	$\leq\sim$ 1300	amorphous

5.5 Condensation sequences - expected minerals

The minerals expected to form around oxygen-rich stars are listed in sequence in Table 5.5. The first dust types expected to form are the most refractory (highest melting point) grains. The refractory grain most frequently discussed in this context is corundum (Al_2O_3; e.g. Tielens 1990; Begemann *et al.* 1997; Patzer *et al.* 1998), although there has also been mention of titanium dioxide (TiO_2; Sedlmayr 1998) and magnetite ($Fe^{2+}Fe_2^{3+}O_4$; Knacke 1978). Amorphous Al_2O_3 has a peak at $\sim$11.5–12.0 μm, while crystalline Al_2O_3 has a main peak at 11.7 μm with bumps at 12.4, 13.6 and 16.4 μm. TiO_2 has a small peak at about 9-9.5 μm and rises longwards of $\sim$11 μm. Magnetite has a featureless spectrum in the 7-14 μm region. Therefore, if these are the grains that are forming in the outflows around O-rich stars, we should expect to see spectra with features in the 11.5-12.0 μm region, possible with some smaller bumps and wings. Whether this dust forms around O-rich stars is dependent on the density structure of the stellar atmosphere, however, if they do not form, then no further evolved dust grains are expected to form. Given that we see evidence of dust around these stars, there ought to be some evidence of these refractory oxides.

The next dust type expected to form as the Al_2O_3 grains react with the gas in the atmosphere is a pyroxene, augite ($Ca_2Al_2SiO_7$), followed by another pyroxene in the same series, diopside ($CaMgSi_2O_6$). Amorphous augite has an absorption peak at about 9.4 μm. Crystalline augite and diopside have a main peak at 9.4 μm, and subsidiary peaks at 10.3

Table 5.5: Laboratory spectra of condensation sequence minerals

Mineral name	Chemical composition	Amorphous or Crystalline	Main Peak μm	Minor Peaks μm	Figure No.
Corundum	Al_2O_3	Amorphous	11.8		5.9a
Corundum	Al_2O_3	Amorphous	11.6		5.9b
Corundum	Al_2O_3	Crystalline	11.7	12.4, 13.6, 16.4	5.9c
Corundum	Al_2O_3	Crystalline	12.1		5.9d
Titanium Dioxide	TiO_2	Crystalline	~9	rise longwards of 9.8	5.12c
Rutile	TiO_2	Crystalline	—	rise longwards of 11.5	5.12d
Augite	$Mg_{0.5}Fe_{0.43}Ca_{0.03}Al_{0.04}SiO_3$	Amorphous	9.35		5.7a
Augite	$(Ca,Na)(Mg,Fe,Al,Ti)(Si,Al)_2O_6$	Crystalline	9.4,10.3,11.6		5.7b
Augite	$(Ca,Na)(Mg,Fe,Al,Ti)(Si,Al)_2O_6$	Crystalline	9.4, 10.4, 11.1		5.7c
Diopside	$CaMgSi_2O_6$	Crystalline	9.3, 11.5	10.2, 10.9,	5.7d & e
Hedenbergite	$CaFe^{2+}Si_2O_6$	Crystalline	9.3, 11.6	10.4, 10.9	5.7f
Spinel	$MgAl_2O_4$	Crystalline	14.5, 17.2,	19.2, 32.4	–
Anorthite	$CaAl_2Si_2O_8$	Crystalline	10.8	8.7, 9.1, 9.8, 13.2	–
Forsterite	Mg_2SiO_4	Amorphous	9.8		5.1a
Forsterite	Mg_2SiO_4	Crystalline	11.4	10.2, 12.0	5.1b
Forsterite	Mg_2SiO_4	Crystalline	9.8	11.1, 11.8	5.1d
Forsterite	Mg_2SiO_4	Amorphous	9.8	10.5, 11.7	5.1e
Enstatite	$MgSiO_3$	Amorphous	9.3		5.5a
Enstatite	$MgSiO_3$	Amorphous	9.55		5.5c
Enstatite	$MgSiO_3$	Crystalline	10.7	9.4, 11.7	5.5d
Enstatite	$MgSiO_3$	Crystalline	10.6	9.3, 11.5	5.5e
Enstatite	$MgSiO_3$	Crystalline	10.5	9.3, 11.6	5.5f
Olivine	$MgFeSiO_4$	Amorphous	9.8		5.2a
Olivine	$Mg_{0.8}Fe_{1.2}SiO_4$	Amorphous	9.8		5.2b
Olivine	$Mg_{0.8}Fe_{1.2}SiO_4$	Crystalline	11.5	10.4, 12.1	5.2c
Olivine	$Mg_{1.2}Fe_{0.8}SiO_4$	Crystalline	11.4	10.3, 12.1	5.2d
Olivine	$Mg_{1.6}Fe_{0.4}SiO_4$	Crystalline	11.4	10.2, 12.1	5.2e
Olivine	$Mg_{0.22}Fe_{1.78}SiO_4$	Crystalline	11.3	10.2, 11.9	5.2f
Olivine	$Mg_{0.36}Fe_{1.64}SiO_4$	Crystalline	11.4	10.5, 12.1	5.2g
Olivine	$Mg_{0.58}Fe_{1.42}SiO_4$	Crystalline	11.4	10.5, 12.1	5.2h
Olivine	$Mg_{0.82}Fe_{1.18}SiO_4$	Crystalline	11.4	10.4, 12.0	5.2i
Olivine	$Mg_{1.02}Fe_{0.98}SiO_4$	Crystalline	11.4	10.4, 12.0	5.2j
Olivine	$Mg_{1.2}Fe_{0.8}SiO_4$	Crystalline	11.3	10.3, 12.0	5.2k
Olivine	$Mg_{1.32}Fe_{0.68}SiO_4$	Crystalline	11.3	10.3, 12.0	5.2l
Olivine	$Mg_{1.76}Fe_{0.24}SiO_4$	Crystalline	11.3	10.1, 11.9	5.2m-n
Olivine	$Mg_{1.84}Fe_{0.16}SiO_4$	Crystalline	11.3	10.1, 11.9	5.3a-d

and ~11.1-11.6 μm. Therefore, for those stars in which the atmospheric density structure is such that the dust is cool enough and the density high enough for gas-solid reactions to take place, we should expect a change in spectral features so that a peak at 9.4 μm becomes evident and possible weaker features at 10.3 and ~11-11.5 μm. If there is still some corundum there may be a broad feature at about 11-12 μm.

As the augite is transformed into diopside by reaction with gaseous magnesium, it releases aluminium. This aluminium, together with the remaining corundum, is also predicted to undergo a gas-solid reaction with gaseous magnesium, to form spinel ($MgAl_2O_4$). Spectra of spinel (Preudhomme & Tarte 1971; White & DeAngelis 1967; not shown) exhibit peak absorption at 14.5 μm, 17.2 μm,19.2 μm and 32.4 μm. Unfortunately this is outside the scope of our ground-based 7.5-13.5 μm observations. Within our spectral range spinel is featureless with a rise in absorption longwards of ~11 μm. ISO-SWS spectra of O-rich stars do cover the wavelength region in which spinel has features and therefore may be able to provide constraints on the abundance of spinel around such stars. This would be doubly interesting since presolar spinel grains have been found in meteorites (see chapter 3).

Further cooling causes spinel to react with diopside to form $CaAl_2Si_2O_8$ (anorthite). Anorthite has a major feature which peaks at 10.8 μm, with a wing to the short wavelength side and minor peaks at 8.7, 9.1 and 9.8 μm and a bump at 13.2 μm[7] . If the conditions in the stellar atmosphere are appropriate for the spinel-diopside reaction to take place, we should at least see the emergence of a spectral feature at 10.8 μm, and possibly also weaker features at 8.7, 9.1, 9.8 μm and 13.2 μm.

At about the same temperature at which diopside is forming from a gas-solid reaction of augite grains with magnesium gas, forsterite (Mg_2SiO_4) is expected to form direct from the gas. It is expected that it will use the already formed corundum and augite grains as nucleation centres and form as a mantle on these grains (Tielens 1990). Magnesium is far more abundant than aluminium or calcium and we therefore expect to see far stronger features due to dust species comprising magnesium rather than those dominated by aluminium or calcium. Spectral features due to forsterite should dominate the spectrum of

[7]from a spectrum of anorthite form J.W. Salisbury's FTP site - rocky.eps.jhu.edu, not shown

those stars whose stellar atmospheres have the appropriate density structure for forsterite formation. In the laboratory, amorphous forsterite has a single, slightly asymmetric peak at ~9.8 μm. Crystalline forsterite has a main peak at 11.3 μm with other peaks at ~10-10.5 μm and ~12μm.

Forsterite should be transformed into enstatite ($MgSiO_3$) by reaction with gaseous SiO (Pégourié & Papoular 1985). Amorphous enstatite has a single peak at about 9.4μm. Crystalline enstatite has peaks at 9.3-9.4, 10.5-10.7 and 11.5-11.7μm. As the forsterite is transformed into enstatite we should see a shift in the main spectral feature from about 9.8μm to about 9.4μm, as well as shifts in the minor peaks (see Fig. 5.1a&e and 5.5a-c).

If the density structure of the stellar atmosphere is such that there is a high density region at a sufficient distance from the star for it to be cool enough for the enstatite to react with gaseous iron, various ferro-magnesian olivines should form (Tielens 1990). Amorphous [Mg,Fe] olivines have a single peak at about 9.8μm. Crystalline [Mg,Fe] olivines have a main peaks at 11.3-11.5μm, with a secondary peak at ~10.1-10.5μm and a bump at about 12μm. Therefore, evolved dust shells, with the required density structure, should show a strong spectral feature at 9.8μm and possibly weaker features at 11.3-11.5μm and ~12μm. This would be virtually indistinguishable from the spectrum of shells containing forsterite only.

The possible presence of SiO_2 dust around oxygen-rich stars has been generally ignored. It is discussed briefly by Pégourié & Papoular (1985) as being predicted by disequilibrium condensation calculations of Lattimer (1982) and also by Tielens (1990). There has been some work on the condensation/nucleation of SiO_2 dust (Morioka *et al.* 1998). As will be discussed in chapter 8, it is felt that the presence of SiO_2 in the dust around these stars should be taken more seriously.

Chapter 6

Carbon Stars I - the nature of the silicon carbide around C-rich AGB stars

"Whether we are based on carbon or silicon makes no fundamental difference.
We should each be treated with appropriate respect."
Chandra, 2010 (1984)

6.1 Introduction

It has been known for more than two decades that dust particles form in the atmospheres of cool stars and are ejected into the interstellar medium c.f. Gilra (1971), Woolf (1973), Stephens (1980), Mathis (1990) and Evans (1994). In this context there has been a great deal of work published on silicon carbide (SiC). From equilibrium condensation models, Friedemann (1969) and Gilman (1969) showed that silicon carbide should condense in the atmospheres of carbon stars. Following the work of Gilra & Code (1971), Hackwell (1972) and Treffers & Cohen (1974), a broad infrared emission feature seen in the spectra of many carbon stars, peaking between about 11.0 and 11.5 μm, has been attributed to solid SiC particles. SiC is therefore believed to be a significant constituent of the dust around carbon stars. There are in fact about 70 different forms of silicon carbide, known as polytypes, and a large number of papers have been published discussing which form most closely fits the observed feature near 11 μm. All these polytypes are variants of the same basic structure, based on a tetrahedral group of silicon and carbon atoms (Taylor & Jones, 1960). These

seventy different forms of silicon carbide can be divided into 2 basic groups - α and β silicon carbide (Bechstedt *et al.* 1997). The α-SiC form has a hexagonal or rhombohedric crystal structure and is very stable up to approximately 2700°C. The β-SiC form has a cubic structure and, at T < 2100°C is the favoured type when condensation takes place in a vacuum. β-SiC will transform into α-SiC at temperatures above about 2100°C but it is thermodynamically unlikely that this process will work in reverse. Very little (a few percent at best) α-SiC will transform into β-SiC (I.P.Parkin; private communication). The difference between these two forms is small, both structurally and thermodynamically (below 2100°C), but they can be distinguished by crystallographic techniques and by their infrared spectra (See chapter 4). One of the aims of the current work was to determine whether either type predominates in the circumstellar outflows around carbon stars, via observations of the 11 μm spectra of a significant sample of carbon stars.

6.2 Background

6.2.1 α-SiC vs β-SiC in astronomical environments

In the literature concerning the 11 μm SiC feature in carbon star spectra, much of the work already published is somewhat contradictory, and certainly needs some introduction. In order to address this problem, I therefore begin with a review of some of the existing work on this topic.

Gilman (1969) and Friedemann (1969) predicted that SiC could condense in the atmospheres of cool carbon stars. Gilra & Code (1971) used this information, together with calculations published by Gilra (1972), to predict that SiC should re-emit absorbed visible radiation as a feature in the 10-13 μm region. Hackwell (1972) found an emission feature in two carbon stars in this spectral region that was quite similar to Gilra's calculated emission feature. Treffers & Cohen (1974) published high resolution spectra of the SiC feature in several carbon stars and made use of unpublished calculations by Gilra, based on α-SiC optical constants, to interpret these spectra. It was shown that small particles of a single shape produce several narrow emission features situated between the longitudinal and transverse vibrational wavelengths of α-SiC at 10.2 μm and 12.8 μm and that particles of different shapes would produce features at different wavelengths between these limits (see also Kozasa *et al.* 1996). It was also shown that a continuous distribution of shapes

should give a smooth feature with cut-on and cut-off wavelengths corresponding to the longitudinal and transverse vibrational modes of SiC.

Stephens (1980) investigated various dust species (silicates, carbon and SiC) with a view to explaining the visible and ultraviolet extinction in the interstellar medium (ISM). He chose to use β-SiC for his experiments, as it is the most stable structural form of SiC below about 2000 K. He found that in order to fit the interstellar extinction curve, the SiC particles needed to be very much smaller (radius <0.005 μm) than the particles he used to produce spectra. He also used the fact that no 11.5 μm SiC feature is seen in the extinction curve of the ISM to constrain the SiC abundance. He concluded that "SiC is probably not the major contributor to the observed visible and ultraviolet extinction", contradicting the conclusion of Gilra (1971) that SiC was one of the constituents needed to explain the entire extinction curve of the ISM.

Whittet, Duley & Martin (1990) also investigated the presence of SiC in the ISM. They concurred with Stephens (1980) that SiC is not a major contributor to the ISM extinction curve, estimating that less than 5% of silicon atoms in the ISM can reside in SiC dust. To reconcile this lack of interstellar SiC with the fact that SiC is found in the circumstellar shells of carbon stars, they suggested that SiC is rare in carbon stars, citing the lack of SiC absorption in stars with optically thick circumstellar shells as evidence. However, as will be seen in section 6.7, SiC has now been seen in absorption in the spectra of several carbon stars. Another explanation for the lack of observed SiC in the ISM is the grain size. Many of the presolar SiC grains found in meteorites are large ($> 1\mu$m) and may not be observable by their IR spectrum (see section 3.2.2)

6.2.2 Laboratory spectra

Several papers have used laboratory analyses of SiC samples to simulate the SiC emission feature at 11-13 μm, with a view to identifying observed astronomical features. Friedemann *et al.* (1981) used two forms of commercially available α-SiC. They used five samples with various size distributions, made up of measured mixtures of the two types of α-SiC. They found that the bandwidth of the absorption feature was not affected by the size distribution or by impurities, but that the absorption peak (i.e. where the ratio of the feature intensity to the continuum intensity reaches a minimum) was affected, so that

when comparing different grain-size distributions, the larger grain-sizes give rise to reduced absorption peaks. They found a peak wavelength of 11.8 μm before correcting for their experimental substrate, and a wavelength peak of 11.4 μm after correction. Use of the correction factor is discussed in chapter 4. They also fitted one of their sample spectra to the spectrum of Y CVn. Goebel *et al.* (1995) describe the unusual J-type carbon star Y CVn as having a "somewhat different SiC band profile than normally found in other visible carbon stars". However, our CGS3 spectrum of Y CVn is not particularly unusual in the shape and peak wavelength of its SiC feature (see Fig. 6.1 and Table 6.2 below).

Borghesi *et al.* (1985) performed a comparative laboratory study of several samples of both α- and β-SiC. Their samples were ground and sedimented to various degrees in order to determine the effects of the size distribution. They found the feature to peak in wavelength at about 11.8 μm for α-SiC, and at about 11.4 μm for β-SiC, before correction for the KBr-dispersion technique, and at 11.4 μm and 11.0 μm after correction. This agrees well with the results of Friedemann *et al.* (1981). Borghesi *et al.* (1985) also found that, for their less pure α-SiC samples (i.e. 89% SiC rather than 99% SiC, with carbon, silicon, metallic iron and SiO_2 impurities), the peak wavelength shifted towards longer wavelengths as the particle size increased. This did not occur for their purest α-SiC nor for their β-SiC samples. Comparing this with the results of Friedemann *et al.* (1981), there are some obvious discrepancies as Friedemann *et al.* found no changes in the emission feature due to impurities. The data published by Borghesi *et al.* (1985) is not corrected for the use of the KBr matrix method, although they did state that it was necessary to apply a correction factor to their data. As discussed in chapter 4, the KBr correction is unnecessary. The result of applying the correction is to shift the peak wavelength of the feature. How this affects the attribution of the 11.3 μm feature to a certain type of SiC is discussed later in this chapter.

Pégourié (1988) set out to derive a synthetic dielectric function for SiC, from which spectral features could be predicted. He argued that the work of Baron *et al.* (1987) showed α-SiC to be the best candidate to reproduce the 11-11.5 μm feature in the IRAS LRS spectra of carbon stars. However, what Baron *et al.* (1987) actually concluded was that "The shape of the strongest feature is quite similar to the mass absorption of α-SiC"[1].

[1] whether this was KBr-corrected or uncorrected data is unclear

Taken together with their statement that "the feature becomes stronger and narrower as the temperature of the underlying continuum increases", this implies that their α-SiC spectrum probably gives a good fit to features in the spectra of the carbon stars with the most optically thin dust shells. However, the same conclusion might not necessarily be applicable to cooler stars and to features produced by optically thick shells. Having decided to use α-SiC, Pégourié (1988) derived a comprehensive dielectric function by compiling partial data from a number of different authors and using a Kramers-Kronig analysis. He found that slight changes in impurities or morphology have a huge impact on the shape of the feature. This is consistent with the findings of Borghesi *et al.* (1985) and contradicts the work of Friedemann *et al.* (1981) discussed above. This conclusion that morphology has a big influence is also consistent with the work of Gilra presented by Treffers & Cohen (1974), regarding the sensitivity of the feature wavelength to particle shape for single-shape particles. Pégourié (1988) found that the 'synthetic' α-SiC feature he had created had a peak wavelength of 11.33±0.5 μm. This is quite similar to the results of both Friedemann *et al.* (1981) and Borghesi *et al.* (1985; after KBr-correction). However, Pégourié (1988) used the KBr-corrected data of Borghesi *et al.* (1985). Following the finding in chapter 4, it is my belief that the use of KBr-corrected optical constants has given rise to a synthetic spectrum with an unnecessarily shifted absorption peak.

6.2.3 Previous studies of the mid-infrared spectra of carbon stars

Hackwell (1972) presented spectra and photometry of eleven M-, S- and C- type stars, only two of which are classed as carbon stars: V Hya and CIT 6. The spectra of both these stars showed a broad feature between 10 and 12 μm, similar to the emission feature calculated by Gilra (1972). This is one of the first published observations of the 11 μm feature, although it was not attributed to SiC by Hackwell (1972). Earlier, however, Hackwell (1971) had concluded on the grounds of condensation sequence studies that SiC was likely to be a major contributor to the circumstellar dust around carbon stars.

In 1974, Treffers & Cohen published the mid-infrared spectra of two carbon stars - IRC+10216 and CIT 6. They found that both stars showed a broad emission band peaking at about 11.5 μm which could be fitted very well using model spectra calculated by Gilra for small α-SiC particles having a distribution of shapes. Forrest, Gillett & Stein's (1975) sample of 8–13 μm spectra of cool stars included seven carbon stars, four of which overlap

with the present sample. They noted that the SiC feature in the spectra of the carbon stars varied in morphology from star to star. Merrill & Stein (1976) investigated the evolution of the infrared spectra of late-type stars. Their sample consisted of 23 oxygen-rich stars and 9 carbon-rich stars (four of which are also included in the present sample). They discussed the 11.5 μm emission feature, attributed to SiC, which had been seen in the spectra of all carbon stars surveyed at that time and noted that it was unique to carbon stars.

Jones *et al.* (1978) investigated the infrared source AFGL 3068, which had been suggested by Lebofsky & Rieke (1977) to be the most heavily obscured carbon star known at that time. From its infrared spectrum from 2 to 4 μm and 8 to 13 μm, Jones *et al.* (1978) found that: 1) there was an absorption feature at 3.1 μm; 2) there was an absence of a silicate feature at 9.7 μm; 3) there was a spectral break near 10.5 μm. The first two findings confirmed that AFGL 3068 is indeed a heavily dust-enshrouded carbon star. The third discovery was attributed to absorption by SiC grains, the first time that this had been observed. The large optical depth indicated by this implies a large mass-loss rate. Jones *et al.* (1978) therefore suggested that if there are many sources like AFGL 3068, they could be major contributors of material to the ISM.

Cohen (1984) presented the mid-IR spectra of 10 carbon stars. He divided the spectra by appropriate blackbodies to normalise them, in order to see the SiC features more clearly. By doing this he found that there appeared to be two types of features: triangular (narrow and peaked) and rectangular (broader and flatter-topped). The triangular feature could be fitted by a laboratory spectrum of α-SiC from Friedemann *et al.* (1981). The rectangular feature could not be fitted by any of Friedemann *et al.* (1981)'s laboratory spectra. He suggested that these two distinct features were indicative of different mechanisms of grain formation in different stars, controlled by the mass-loss rates. Alternatively, he suggested that the different feature shapes could arise as a result of different SiC optical depths.

Baron *et al.* (1987) studied the IRAS Low Resolution Spectrometer (LRS) spectra of 542 carbon stars and came to the following conclusions: 1) The strength of the circumstellar SiC feature is positively correlated with the temperature characterising the underlying

continuum; 2) The shape of the feature varies regularly with its strength and becomes narrower as the strength increases; 3) Weak SiC features are accompanied by an additional bump which peaks at about 8.75 μm. The strongest SiC features are accompanied by a steep rise in the continuum towards 8 μm.

Papoular (1988) studied the IRAS LRS spectra of about 3000 carbon stars. Using various smoothing and averaging techniques he found that the 11 μm features can be divided into three types, which he denoted - SiC(a), (b), and (c). Comparing these separate groups of features to laboratory spectra taken from Borghesi *et al.* (1985), he found that the different types could be attributed to different laboratory samples. SiC(a) could be fitted by the purest α-SiC with the smallest grains, while SiC(c) was fitted by the least pure α-SiC with the largest grains.

Skinner & Whitmore (1988b) discussed the mass-loss rates of carbon stars. They had previously shown that the mass-loss rates of oxygen-rich stars can be determined using the strength of the 9.7 μm silicate dust emission feature (Skinner & Whitmore 1988a). They attempted to use the same method for carbon stars, using the 11 μm SiC feature, and concluded that the method is reliable. From a sample of 29 carbon stars, they suggested that it is likely that the mass-loss rates increase with the carbon star's age. They also suggested that the amorphous carbon to SiC grain abundance ratio increases with mass-loss rate.

In 1988 Willems published two papers on the IRAS LRS spectra of carbon stars (Willems 1988a & b). He found that, for 72 relatively hot carbon stars ($T_{NIR} > 2000K$), the SiC feature peaked near 11.7 μm in most cases and was accompanied by an unidentified 8.6 μm emission feature, possibly similar to the feature seen by Baron *et al.* (1987). For 15 cooler carbon stars ($T_{NIR} < 2000K$) he found that the SiC feature peaked near to 11.3 μm, and concluded that, for these cooler stars, amorphous carbon dust is the main constituent of the circumstellar dust shells.

Goebel *et al.* (1995) have used SiC and other dust species to create a new classification system for carbon stars. Like Chan & Kwok (1990), they proposed a model explaining the variations in dust types as related to the evolutionary status of the star. They chose to

use the α-SiC data of Pégourié (1988) for their model. They proposed that SiC is the first species to condense (because it is very refractory). So, when the star is still relatively hot the contrast of the SiC feature should be very strong. Then, as the star cools and evolves to higher mass-loss rates, newly-formed SiC particles form nucleation sites for amorphous hydrogenated carbon (α:C-H). As the star evolves still further and more SiC grains are coated with α:C-H, the SiC feature weakens and a feature appears at about 8.5 μm due to α:C-H. Features in circumstellar spectra due to α:C-H have been discussed before (Baron *et al.* 1987, Skinner & Whitmore 1988, Puget *et al.* 1985). Baron *et al.* (1987) suggested that, together with the 8.5 μm feature, there is a feature at 11.7 μm also attributable to α:C-H. If this is true both features should appear in spectra when α:C-H is present.

6.2.4 Meteoritic SiC

Silicon carbide grains are also found in meteorites. From isotopic studies, many of these grains are believed to have formed around carbon-rich AGB stars. Meteoritic SiC and its implications are discussed in chapter 3 (section 3.2.2). The most notable information from meteoritic work is that *all* meteoritic SiC is of the β-SiC polymorph, whereas nearly all previous work based on astronomical observations, discussed in section 6.2.3, finds that all carbon star spectra with the 11.3 μm feature are best fitted by laboratory α-SiC.

6.3 Target Selection

We selected our carbon star targets from a number of source lists. Groenewegen *et al.* (1992) extended the carbon star infrared classification scheme of Willems & de Jong (1988) by defining five groups of carbon stars. Group I consisted of a small number of J-type carbon stars that exhibit a silicate emission feature. These are not considered further here. Group II sources are those with near-IR colour temperatures, $T_{\rm NIR}$, exceeding 2000 K, while Group III sources have $T_{\rm NIR}$ between 1000 K and 2000 K. Group II and III sources have optical counterparts. Group IV sources have $T_{\rm NIR}$ values below 1000 K. Group V sources have the reddest IR colour temperatures. This sequence was interpreted as one of increasing dust mass loss rate. Twenty-five of the objects in our sample were amongst the carbon stars having 12 μm *IRAS* fluxes larger than 100 Jy that were classified into these groups by Groenewegen *et al.* (1992), while Groenewegen (1995) classified another star in our sample AFGL 5076 (IRAS 02345+5422) as a Group V source. The Group classifications of the sources are listed in column 5 of Table 6.1.

Jura and Kleinmann (1989, 1990) tabulated sources which they classified as very dusty asymptotic giant branch stars. Nine stars in our sample were included in their 1989 listing of sources estimated to be nearer than 1 kpc to the Sun, while eight of our sources were included in their 1990 listing of very dusty carbon-rich sources estimated to be between 1 and 2.5 kpc from the Sun.

Volk, Kwok & Langill (1990) used the IRAS LRS database to identify a group of 32 known or candidate extreme carbon stars. They asserted that these extreme carbon stars have very weak or no SiC features and have a relatively low temperature blackbody-like continuum and so can be distinguished from 'normal' carbon stars. Ten stars from their sample are included in the present survey. IRAS 02408+5458 was selected from Volk, Kwok and Woodsworth's (1993) list of candidate carbon-rich AGB and post-AGB stars. OH maser emission has been searched for from this source, but not detected (e.g. Blommaert, Van Der Veen & Habing 1993, Wouterloot, Brand & Fiegle 1993). Our 8-13 μm spectrum of it exhibits an 11 μm SiC feature in absorption (see section 6.7), confirming its carbon-rich nature.

6.4 Observations

Most of the stars in this sample were observed on the nights of October 30 – November 2 1993. The sources CIT 6, V Hya, Y Cvn, AFGL 2155, AFGL 2233 and AFGL 2368 were observed on the nights of May 23–31 1991 while AFGL 3068, whose CGS3 spectrum has also been presented by Justtanont *et al.* (1996), was observed on the night of October 4 1990. The spectrum of IRC+10216 was obtained on the night of March 17 1995 and was kindly made available to us by Dr. T.R. Geballe. Table 1 provides some details of the observations. All observations were made using the 3.8m United Kingdom Infrared Telescope (UKIRT) with the common-user spectrometer CGS3, a liquid helium cooled, 10– and 20– μm grating spectrometer built at University College London. CGS3 contains an array of 32 discrete As:Si photoconductive detectors, and three interchangeable, permanently mounted gratings covering the 7.5–13.5 and 16.0–24.5 μm wavebands. Two settings of a grating give a fully sampled 64-point spectrum of the chosen waveband (in the case of IRC+10216, three setting of the grating gave a 96-point spectrum). We obtained

Table 6.1: Sources Observed

Source	IRAS names	Other names	Spec. Type*	Group†	Observation Date	Calibrator
IRAS 02152+2822	02152+2822			IV	2/11/93	β Peg
R For	02270–2619	AFGL 337	C3,4e	III	1/11/93	α Lyr
AFGL 341	02293+5748			IV	1&2/11/93	β Peg
AFGL 5076	02345+5422			V	1/11/93	α Tau
IRAS 02408+5458	02408+5458				1/11/93	α Tau
IRC+50096	03229+4721	V384 Per/AFGL 489		III	30/10/93	α Tau
AFGL 5102	03448+4432			IV	1&2/11/93	α Tau
V414 Per	03488+3943	AFGL 527		III	1/11/93	β Peg
R Lep	04573–1452	AFGL 667	C7,4e	III	30/10/93	α Tau
UV Aur	05185+3227	AFGL 735			31/10/93	α Tau
TU Tau	05421+2424	AFGL 812	C5,4		31/10/93	α Tau
UU Aur	06331+3829	AFGL 966	C6,4	II	31/10/93	α Tau
CS 776	07270–1921	AFGL 1131	C8,1e		1/11/93	α CMa
IRC+10216	09452+1330	CW Leo/AFGL 1381	C	IV	17/3/95	β Gem
CIT 6	10131+3049	RW LMi/AFGL 1403	C4,3	III	23/5/91	α Boo
V Hya	10491–2059	AFGL 1439	C7,5e	III	25/5/91	α Boo
Y CVn	12427+4542	AFGL 1576	C7,1e	II	23/5/91	α Boo
AFGL 2155	18240+2326		C	IV	23/5/91	α Boo
IRC+00365	18398–0220	AFGL 2233		III	31/5/91	α Boo
V Aql	19017–0545	AFGL 2314	C5,4	II	1/11/93	α Lyr
AFGL 2333	19075+0921			V	1/11/93	α Lyr
AFGL 2368	19175–0807		C5,4	III	31/5/91	α Lyr
AFGL 2477	19548+3035				31/10/93	α Tau
AFGL 2494	19594+4047			IV	31/11/93	α Lyr
V Cyg	20396+4757	AFGL 2632	C7,4e	III	30/10/93	α Lyr
AFGL 2699	21027+5309	V1899 Cyg	C8,3		30/10/93	β Peg
AFGL 5625	21318+5631			V	2/11/93	α Tau
IRAS 21489+5301	21489+5301			IV	2/11/93	α Lyr
AFGL 3068	23166+1655			V	4/10/90	β Peg
AFGL 3099	23257+1038	IZ Peg	C	IV	1/11/93	β Peg
IRC+40540	23320+4316	LP And/AFGL 3116	C8,3.4	III	30/10 & 2/11/93	β Peg
TX Psc	23438+0312	AFGL 3147	C		1/11/93	β Peg

* from Willems (1988a&b), Lorenz-Martin & Lefèvre (1993 & 1994), Blanco *et al.* (1994), Cohen (1979)

† from Groenewegen *et al.* (1992) and Groenewegen (1995)

7.4–13.5 μm spectra with a 5.5-arcsec circular beam, and a spectral resolution of 0.17 μm. Further details about CGS3 can be found in Cohen & Davies (1995). Six stars, α Boo, α CMa, α Tau, α Lyr, β Peg and β Gem, were used as flux standards. Table 6.1 lists the calibrator used for each source. The spectra of sources taken using α Tau as the standard star were flux-calibrated using the absolutely calibrated spectrum of α Tau constructed by Cohen *et al.* (1992a), whilst several sources were calibrated using a similarly constructed spectrum of β Peg provided by Dr. M. Cohen (see Cohen and Davies 1995). A number of sources were calibrated with respect to the A-type stars α Lyr and α CMa, for which Kurucz model atmosphere calibrations, described by Cohen *et al.* (1992a), were adopted. Several spectra were calibrated with respect to β Gem and α Boo, which were assumed to emit as blackbodies in the 10 μm region (see Cohen and Davies 1995), with effective temperatures of 4750K and 4450K respectively. The deep telluric ozone feature at 9.7 μm could not always be completely cancelled, hence in some cases spurious spectral structure could be present in the 9.3–9.8-μm region. The flux-calibrated spectra of all the sources are shown in Fig. 6.1. The error bars represent 1 σ standard errors on the fluxes.
The most prominent characteristic of the flux-calibrated spectra shown in Figs. 6.1 is the silicon carbide feature, which typically extends from just shortwards of 10 μm to about 12.5 μm. For 26 of the sources the SiC feature is in emission but for four sources the SiC feature appears to be in absorption. One of these, AFGL 3068, was the only source previously known to exhibit the SiC feature in absorption (Jones *et al.* 1978), while the other three sources were found to exhibit SiC absorption during the current survey, namely IRAS 02408+5458, AFGL 2477 and AFGL 5625. All four of these sources are discussed in more detail in section 6.7.

About half of the spectra plotted in Fig. 6.1 show a marked downturn shortward of 8 μm. This effect was first noticed by Forrest *et al.* (1975) and, making use of complete spectrophotometry from 0.75-13 μm for the carbon star V CrB, Goebel *et al.* (1981) were able to attribute this turndown to the long wavelength C_2H_2 wing of a band centred at 7.1 μm due to HCN and C_2H_2. Note that the carbon stars in our sample with optical counterparts tend not to exhibit a downturn shortwards of 8 μm, whereas the sources lacking optical counterparts do tend to exhibit the downturn. Since the latter sources are likely to correspond to those with higher mass loss rates, this indicates that the HCN and C_2H_2 molecules apparently responsible for the downturn reside in the outflows.

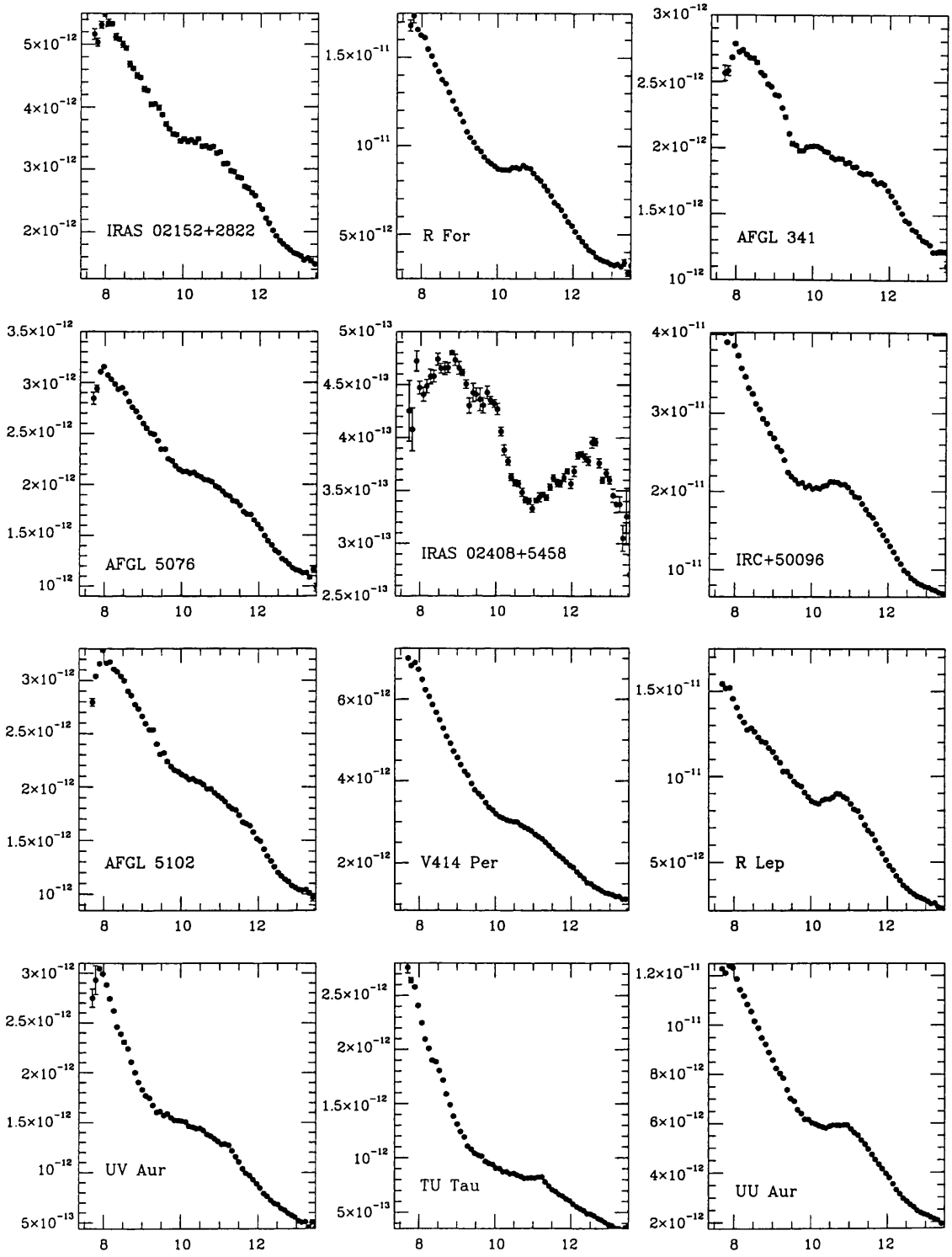

Figure 6.1: 8-13 μm flux-calibrated spectra of carbon stars (x-axis: wavelength in μm; y-axis: flux in $\mathrm{Wm^{-2}\mu m^{-1}}$)

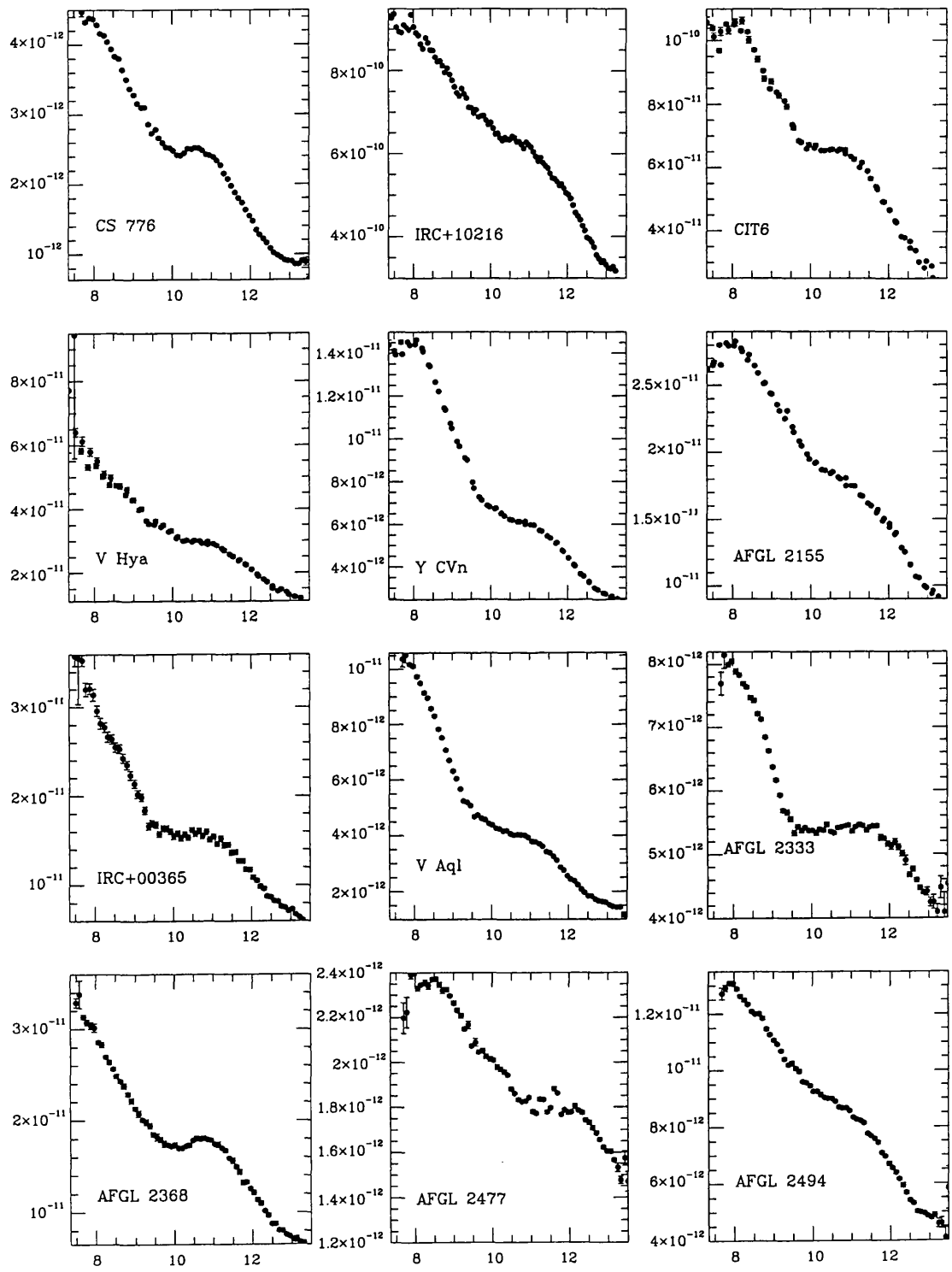

Figure 6.1: (cont.)

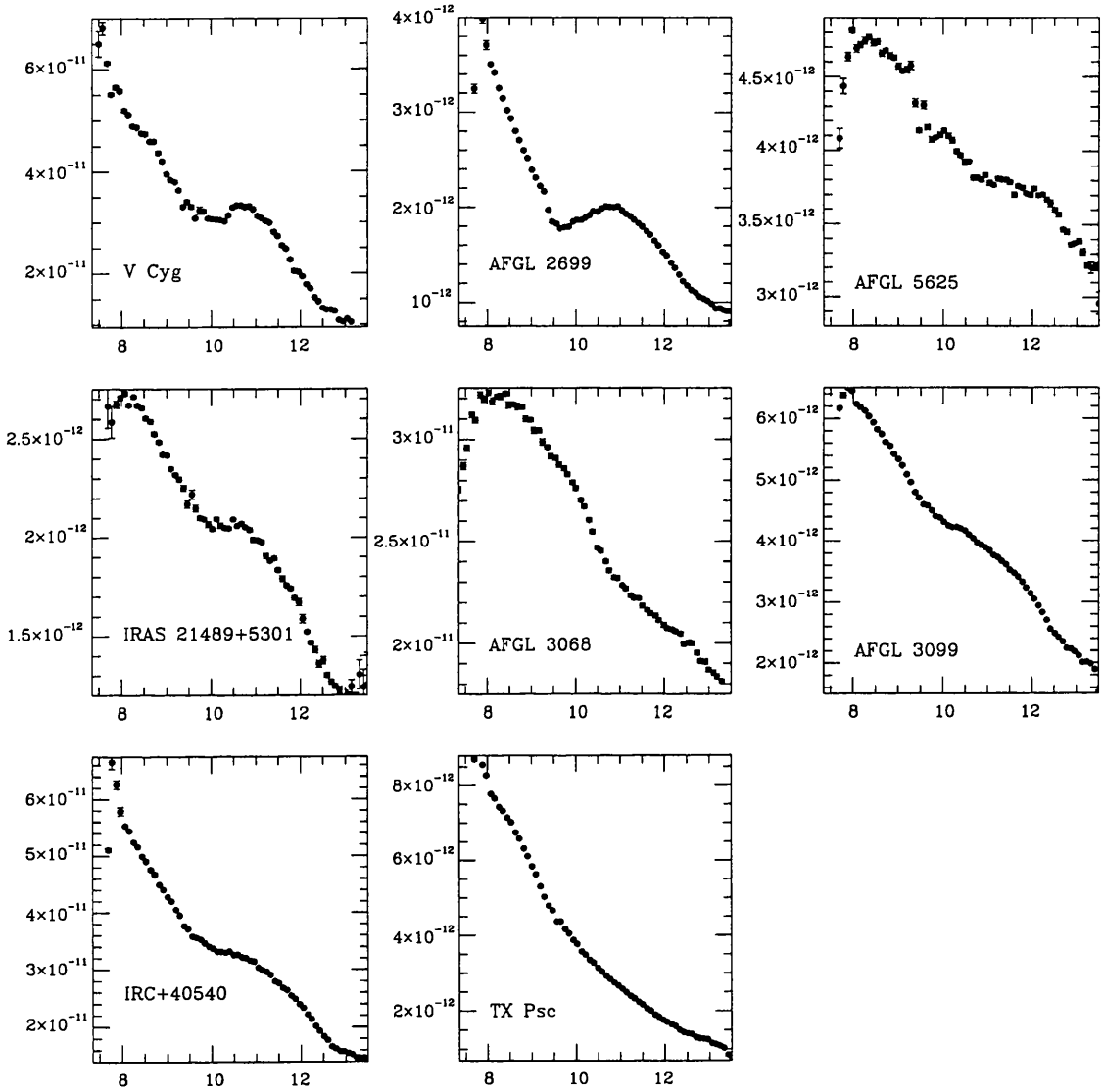

Figure 6.1: (concluded)

In the normalised spectra shown in Fig. 6.2 (see section 6.5), in addition to the obvious SiC feature between 10 and 12.5 μm, a weaker emission feature between 8 and 9.5 μm can be discerned in several of the plots, e.g. those of V Aql and Y CVn. This is presumably the same as the feature found in IRAS LRS spectra of carbon stars by Baron *et al.* (1987) and Skinner and Whitmore (1988b), and attributed by Papoular (1988) and Goebel *et al.* (1995) to amorphous hydrogenated carbon. Note that the uncertainty in the true level of the continuum in the 8 μm region, caused by the presence of the HCN/C_2H_2 absorption band shortwards of 8 μm in about half of the sources, may lead to artificial amplification of some of the 8–9.5 μm features during the normalisation process. Another additional feature that is discernable in the spectra of two stars: TU Tau and UV Aur. This is a narrow peak at $\sim$11.3 μm, superimposed on the SiC feature. This 11.3 μm narrow peak will be discussed further in chapter 7.

6.5 Properties of the spectral features

Each of the flux-calibrated spectra was divided by a suitable blackbody, in order to more easily discern the spectral features against the underlying continuum. The blackbodies were chosen by fitting them to the flux calibrated spectra typically at around 8 μm and around 13 μm. In most cases, the blackbodies used in the normalisation process are of approximately the same temperature as those fitted by the χ^2-minimisation routine described in the next section. Table 6.2 gives temperatures of the blackbodies used to normalise the spectra, together with some properties of the 11 μm feature measured on the normalised spectra. The sources are listed in Table 6.2 in order of increasing 8–13 μm blackbody temperature, which is usually interpreted as a sequence of decreasing mass loss rate, since stars with very low mass loss rates ought to show a photospheric continuum, while stars with high mass loss rates and optically thick dust emission ought to exhibit lower (dust) colour temperatures in the 8–13 μm region. The listed properties of the 11 μm feature are: the feature peak to continuum flux ratio, the wavelength of the peak of the feature (λ_{peak}), its full width at half maximum (FWHM), full width at zero intensity (FWZI), and equivalent width. The peak to continuum ratio is the maximum value of the ratio of the intensity in the feature to the underlying continuum intensity. The peak wavelength of the feature is the wavelength at which this peak to continuum ratio is measured. Some of the flattened spectra have obvious features at about 8-8.5 μm

Table 6.2: Properties of the SiC features measured on the normalised spectra

Source	Peak/Cont.*	T_{BB}†	λ_{peak}	FWHM	FWZI	-EW‡
	Ratio	(K)	(μm)	(μm)	(μm)	(μm)
IRAS 02408+5458	0.87	320	10.87	1.28	3.23	-0.367
AFGL 5625	0.89	337	10.67	1.96	3.42	-0.055
AFGL 2477	0.85	340	10.56	2.05	3.51	-0.279
AFGL 3068	0.93	377	10.81	1.58	2.54	-0.097
AFGL 341	1.12	410	11.88	1.38	2.76	0.163
IRAS 21489+5301	1.17	455	11.28	1.75	2.69	0.299
IRC+10216	1.24	520	11.45	2.08	4.55	0.557
AFGL 5076	1.14	525	11.45	1.93	2.95	0.275
AFGL 2494	1.15	525	11.29	1.93	3.22	0.296
AFGL 2699	1.32	530	11.27	1.75	3.03	0.553
AFGL 3099	1.21	600	11.64	2.13	3.48	0.404
AFGL 5102	1.18	600	11.50	1.74	3.31	0.329
AFGL 2155	1.19	615	11.72	1.87	2.99	0.386
IRAS 02152+2822	1.23	675	11.33	1.44	3.45	0.459
IRC+40540	1.23	680	11.33	1.93	2.93	0.446
AFGL 2368	1.50	800	11.25	1.85	3.48	0.866
V Hya	1.33	865	11.24	1.74	3.48	0.649
IRC+00365	1.39	975	11.38	1.93	3.24	0.713
CIT6	1.47	1100	11.35	1.84	3.48	0.933
TU Tau	1.39	1100	11.50	2.18	3.58	0.597
IRC+50096	1.47	1200	11.20	1.83	3.06	0.869
Y CVn	1.33	1350	11.55	1.64	2.05	0.573
R For	1.43	1400	11.12	1.74	3.43	0.704
R Lep	1.74	1500	11.13	1.75	4.90	1.609
UU Aur	1.42	1500	11.22	1.65	2.97	0.703
UV Aur	1.46	1500	11.23	1.83	3.85	0.917
V Cyg	1.75	1500	11.29	1.76	4.87	1.508
CS 776	1.58	1600	11.15	1.74	3.32	0.857
V414 Per	1.25	1600	11.24	1.74	3.41	0.423
V Aql	1.40	2250	11.29	1.73	3.49	0.725

* Peak/Cont. = the ratio of the feature intensity to the underlying continuum intensity where the feature strength peaks

† T_{BB} = temperature of blackbody which gives best fit to the underlying 8-13 μm continuum

‡ EW = equivalent width

– possibly due to hydrogenated amorphous carbon (Papoular 1988; Goebel *et al.* 1995). Stars displaying this feature are: AFGL 341, TU Tau, Y CVn, V Aql and AFGL 2699. Fig. 6.2 shows all the normalised spectra, excluding TX Psc, AFGL 2333 and the spectra with absorption features, which are dealt with later. The five stars mentioned above can be seen to exhibit prominently the 8-8.5 μm features.

6.6 Fitting the Spectra

We have fitted our observed spectra using a χ^2–minimization routine based on one developed for the 10 μm region by Aitken *et al.* (1979) and Aitken & Roche (1982). The program has been extended by R.J. Sylvester to include the optical constants for six forms of silicon carbide. These are: α-SiC from Friedemann *et al.* (1981); Pég-SiC, a "synthetic" α-SiC from Pégourié (1988); three different forms of α-SiC: SiC-1200, SiC-600 and SiC-N, from Borghesi *et al.* (1985); and β-SiC, also from Borghesi *et al.* (1985). The program is also equipped with the optical constants of silicates from observations of the Orion Trapezium and μ Cep (see Roche & Aitken 1984). The sources of these optical data are discussed in section 6.2.2. Following the findings in chapter 4, some of this data is felt to be erroneous due to the unnecessary application of a KBr correction to the raw laboratory data. In the original fitting of this sample of carbon star spectra we used the KBr corrected laboratory data, the details and results of which can be found in Speck *et al.* (1997a,b). However, following the work on optical constants of solids and the effects of small particles, presented in chapter 4, it was felt that this and previous work was irretrievably flawed and the whole fitting process was repeated using non-KBr corrected laboratory data.

The χ^2-fitting program is equipped with a mechanism which sets minimum errors on the fluxes to be 3% of the flux. For the higher quality spectra used here, all spectra have errors <3% of the flux (except at the extremes of the wavelength window and in the ozone region), and therefore the 1σ errorbars shown in the figures are smaller than the errors used for the χ^2 calculation. Even the noisiest spectra (i.e. those for IRC+00365 and V Hya) have errors of only $\sim$2%, while the lowest errors on any carbon star spectrum are those for IRC+10216, which has errors of $\sim$0.0003%. The fixing of the minimum errors explains why the reduced χ^2 values reported in the results tables do not always correspond to the real flux errors shown on the figures.

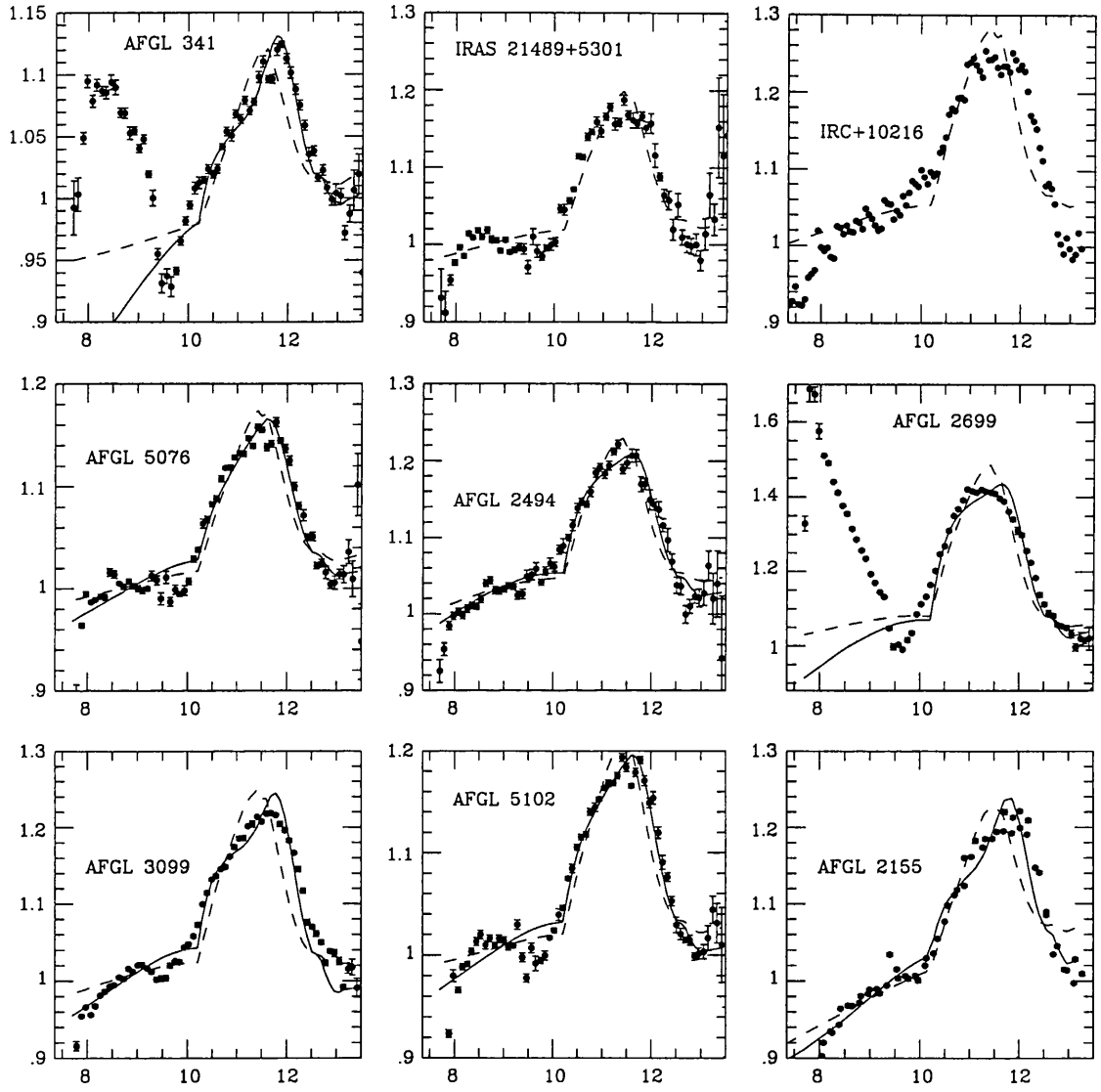

Figure 6.2: 8-13 μm normalised spectra of carbon stars with $\sim$11 μm emission feature with χ^2-fits; pure emission fits as dashed lines, self-absorption fits as solid lines. The errors used to calculate the reduced χ^2 are set to 3% of the flux if the 1σ error on the flux is less than this value. Thus the 1σ error bars shown here are not necessarily the errorbars used by the fitting program. (x-axis: wavelength in μm; y-axis: flux in $\mathrm{Wm^{-2}\mu m^{-1}}$)

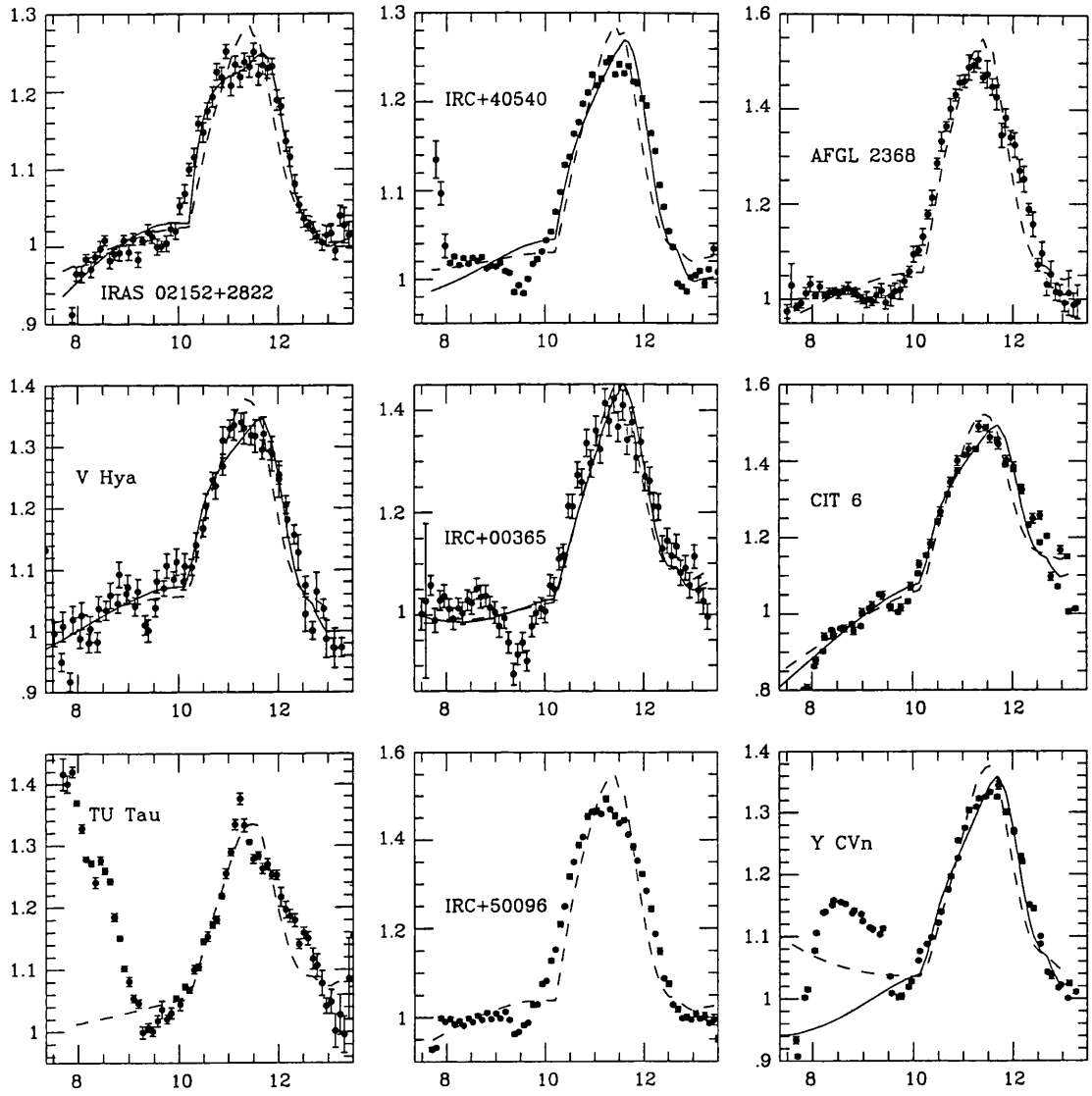

Figure 6.2: (cont.)

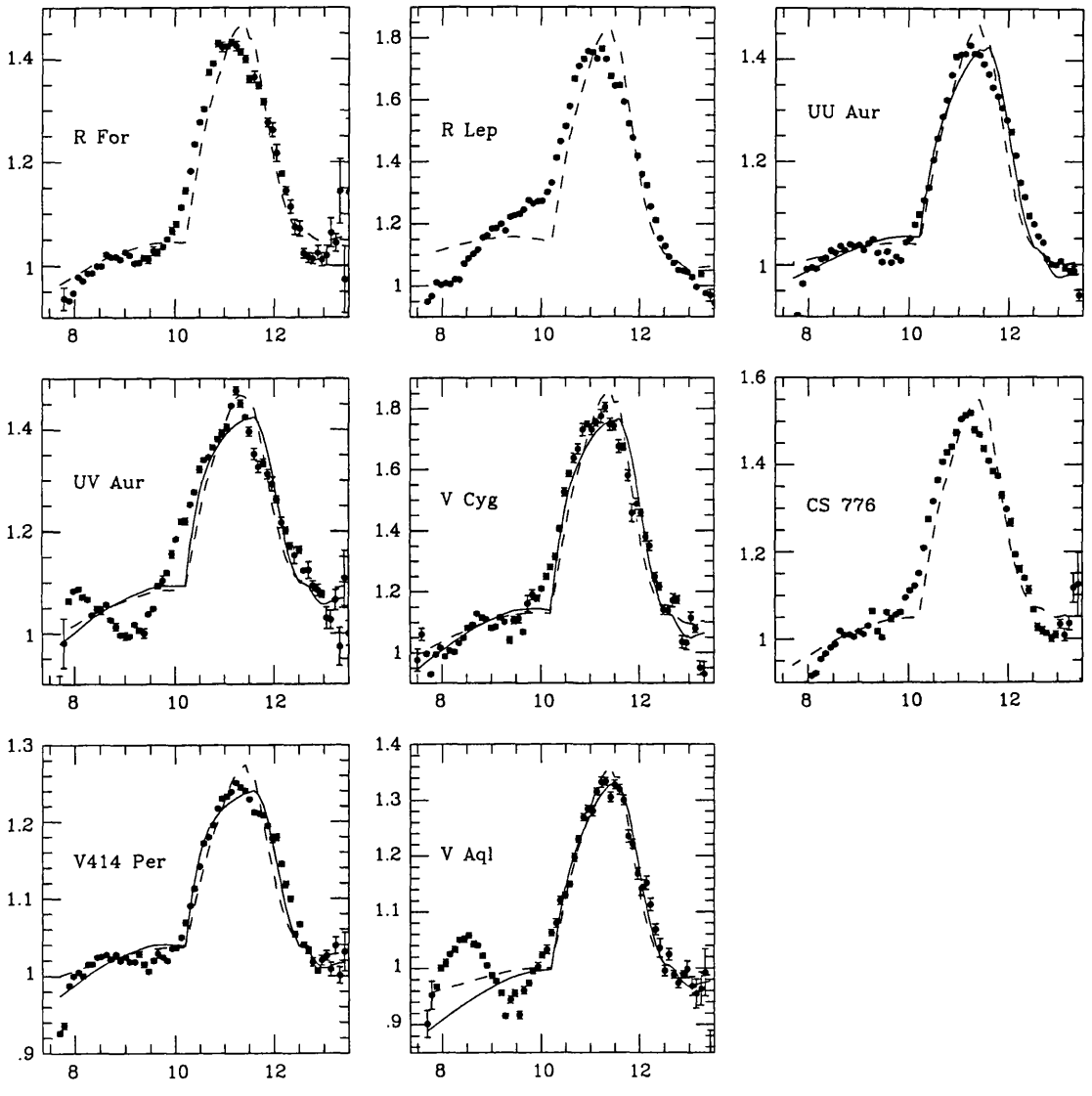

Figure 6.2: (concluded)

Table 6.3: Results of the pure emission χ^2-fitting for the 7.5–13.5 μm region of flux-calibrated spectra.

Source	T_{colour}	SiC type	T_{BB}(K)	$T_{SiC}(K)$	χ^2_R *
AFGL 341	385	—	—	—	—
IRAS 21489+5301	455	β-SiC	449	293	0.515
IRC+10216	520	β-SiC	511	230	1.260
AFGL 5076	525	β-SiC	521	183	0.480
AFGL 2494	525	β-SiC	508	293	0.515
AFGL 2699	530	—	—	—	—
AFGL 3099	600	β-SiC	588	253	2.323
AFGL 5102	600	β-SiC	599	211	0.561
AFGL 2155	615	β-SiC	566	170	1.186
IRAS 02152+2822	675	β-SiC	640	287	1.068
IRC+40540	680	β-SiC	704	216	0.861
AFGL 2368	800	β-SiC	727	321	1.772
V Hya	865	β-SiC	874	275	1.524
IRC+00365	975	β-SiC	1033	164	2.464
CIT 6	1100	β-SiC	760	269	2.229
TU Tau	1100	—	—	—	—
IRC+50096	1200	β-SiC	940	455	2.166
Y CVn	1350	—	—	—	—
R For	1400	β-SiC	906	800	1.237
R Lep	1500	β-SiC	1284	573	5.274
UU Aur	1500	β-SiC	1620	345	1.597
UV Aur	1500	β-SiC	1115	485	2.924
V Cyg	1500	β-SiC	1008	501	3.676
CS 776	1600	β-SiC	993	576	1.879
V414 Per	1600	β-SiC	1508	358	0.810
V Aql	2250	—	—	—	—

* The errors used to calculate the reduced χ^2 are set to 3% of the flux if the 1σ error on the flux is less than this value. The errors shown in Fig 6.2 are 1σ. In all these spectra, the majority of points have errors that are <3% of the flux, the exceptions being for those points at the edges of each spectra and in the ozone region (9.4–9.9μm). Thus the 1σ error bars shown in the fits are not necessarily the errorbars used by the fitting program.

Table 6.4: Results of the emission χ^2-fitting for the 9.5–13.5 μm region of flux-calibrated spectra.

Source	T_{colour}	SiC type	T_{BB}(K)	T_{SiC}(K)	χ^2_R *
AFGL 341	385	β-SiC	405	126	0.788
AFGL 2699	530	β-SiC	469	258	2.568
TU Tau	1100	β-SiC	1095	195	1.245
Y Cvn	1350	β-SiC	2307	149	1.153
V Aql	2250	β-SiC	3467	342	1.283

* The errors used to calculate the reduced χ^2 are set to 3% of the flux if the 1σ error on the flux is less than this value. The errors shown in Fig 6.2 are 1σ. In all these spectra, the majority of points have errors that are <3% of the flux, the exceptions being for those points at the edges of each spectra and in the ozone region (9.4–9.9μm). Thus the 1σ error bars shown in the fits are not necessarily the errorbars used by the fitting program.

We attempted to fit all of the spectra taken. AFGL 3068, IRAS 02408+5458, AFGL 2477 and AFGL 5625 all appear to be sources with SiC in absorption and are dealt with in section 6.7. All attempted fits involved either a pure blackbody or a blackbody with a λ^{-1} emissivity, together with some form of silicon carbide. For some spectra (AFGL 341, AFGL 2699, TU Tau Y CVn and V Aql) the emission fitting routine was unable to provide a satisfactory fit. The spectra cover the 7.5 to 13.5 μm waveband. There are at least two problems with using the fitting routine over this range. (1) There may be problems produced by the atmospheric ozone feature at 9.7 μm. Anomalies at this point may produce erroneous solutions from the fitting program. (2) Goebel *et al.* (1995) have hypothesised that some carbon stars may have amorphous hydrogenated carbon dust in their circumstellar shells, which apparently is the cause of a feature seen in some spectra at about 8.5 μm. At this time the fitting program is not capable of including such a feature in its minimisation routine, due to a lack of suitable laboratory data. Spectra which show this feature can mislead the fitting program into asserting that the spectrum in fact has a higher temperature blackbody part, rather than a feature. Thus, the fitting program was used several times and in several ways for each spectrum in the sample.

First of all, the routine was used on the flux-calibrated spectra, over the whole range (7.5–13.5 μm) with no alterations. The results are listed in Table 6.3. The χ^2_R values are

Table 6.5: Results of the self-absorbed emission χ^2-fitting for the 7.5–13.5 μm region of the flux-calibrated spectra.

Source	T_{colour}	SiC type	T_{BB}(K)	$T_{SiC}(K)$	τ	χ^2_R *
AFGL 341*	385	β-SiC	726	329	0.242	1.370
IRAS 21489+5301	455	-No fits-	—	—	—	—
IRC+10216	520	-No fits-	—	—	—	—
AFGL 5076	525	β-SiC	557	298	0.137	0.369
AFGL 2494	525	β-SiC	516	383	0.167	0.306
AFGL 2699*	530	β-SiC	402	354	0.238	1.334
AFGL 3099	600	β-SiC	726	329	0.242	1.370
AFGL 5102	600	β-SiC	650	355	0.161	0.345
AFGL 2155	615	β-SiC	734	288	0.235	0.418
IRAS 02152+2822	675	β-SiC	548	519	0.223	0.504
IRC+40540	680	β-SiC	859	313	0.173	0.508
AFGL 2368	800	-No fits-	—	—	—	—
V Hya	865	β-SiC	1129	393	0.211	0.761
IRC+00365	975	β-SiC	1788	215	0.114	2.316
CIT 6	1100	β-SiC	960	363	0.217	1.294
TU Tau*	1100	-No fits-	—	—	—	—
IRC+50096	1200	-No fits-	—	—	—	—
Y Cvn*	1350	β-SiC	5239	305	0.200	0.387
R For	1400	-No fits-	—	—	—	—
R Lep	1500	-No fits-	—	—	—	—
UU Aur	1500	β-SiC	2505	446	0.165	1.105
UV Aur	1500	β-SiC	920	745	0.187	2.343
V Cyg	1500	β-SiC	2556	568	0.139	1.014
CS 776	1600	-No fits-	—	—	—	—
V414 Per	1600	β-SiC	1102	920	0.177	0.579
V Aql*	2250	β-SiC	2556	568	0.139	1.014

* These spectra were fitted over the 9.5–13.5 μm wavelength region

* The errors used to calculate the reduced χ^2 are set to 3% of the flux if the 1σ error on the flux is less than this value. The errors shown in Fig 6.2 are 1σ. In all these spectra, the majority of points have errors that are <3% of the flux, the exceptions being for those points at the edges of each spectra and in the ozone region (9.4–9.9μm). Thus the 1σ error bars shown in the fits are not necessarily the errorbars used by the fitting program.

Table 6.6: Summary of the best χ^2-fits for emission features

Source	SiC type	$T_{BB}(K)$	$T_{SiC}(K)$	τ_{SiC}	χ^2_R *
AFGL 341[1]	β-SiC	405	126	—	0.788
IRAS 21489+5301[1]	β-SiC	449	293	—	0.515
IRC+10216[1]	β-SiC	511	230	—	1.260
AFGL 5076[2]	β-SiC	557	298	0.137	0.369
AFGL 2494[2]	β-SiC	516	383	0.167	0.306
AFGL 2699[2]	β-SiC	402	354	0.238	1.334
AFGL 3099[2]	β-SiC	726	329	0.242	1.370
AFGL 5102[2]	β-SiC	650	355	0.161	0.345
AFGL 2155[2]	β-SiC	734	288	0.235	0.418
IRAS 02152+2822[2]	β-SiC	548	519	0.223	0.504
IRC+40540[2]	β-SiC	859	313	0.173	0.508
AFGL 2368[1]	β-SiC	727	321	—	1.772
V Hya[2]	β-SiC	1129	393	0.211	0.761
IRC+00365[2]	β-SiC	1788	215	0.114	2.316
CIT 6[2]	β-SiC	960	363	0.217	1.294
TU Tau[1]	β-SiC	1095	195	—	1.245
IRC+50096[1]	β-SiC	940	455	—	2.166
Y Cvn[2]	β-SiC	5239	305	0.200	0.387
R For[1]	β-SiC	906	800	—	1.237
R Lep[1]	β-SiC	1284	573	—	—
UU Aur[2]	β-SiC	2505	446	0.165	1.105
UV Aur[2]	β-SiC	920	745	0.187	2.343
V Cyg[2]	β-SiC	2556	568	0.139	1.014
CS 776[1]	β-SiC	993	576	—	1.879
V414 Per[2]	β-SiC	1102	920	0.177	0.579
V Aql[2]	β-SiC	2556	568	0.139	1.014

1 Fits with pure emission only

2 Fits with self-absorbed net emission

* The errors used to calculate the reduced χ^2 are set to 3% of the flux if the 1σ error on the flux is less than this value. The errors shown in Fig 6.2 are 1σ. In all these spectra, the majority of points have errors that are <3% of the flux, the exceptions being for those points at the edges of each spectra and in the ozone region (9.4–9.9μm). Thus the 1σ error bars shown in the fits are not necessarily the errorbars used by the fitting program.

the reduced χ^2 values given by dividing the χ^2 value by the number of degrees of freedom. The second attempt at using the fitting routine was restricted to wavelengths longward of 9.5 μm. The reason for this was to minimise the effects of any features shortward of 9.5 μm that might confuse the fitting program (e.g. the 8.5 μm feature). It was not practicable to do the same for the ozone feature at 9.7 μm as this would have resulted in the loss of part of some of the features. This restricted wavelength fitting was only applied to the five spectra for which no fits could be found over the entire wavelength range, all of which appear to have the 8.5 μm feature. The results are listed in Table 6.4 and, for these five stars, these are the fits seen in Fig. 6.2.

Cohen (1984) suggested that the shape of some of the features in carbon stars may arise as a result of different SiC optical depths. With this in mind a third fitting attempt was made, using silicon carbide in both emission and absorption simultaneously, i.e. self-absorbed SiC emission. This self-absorption comprises a warm emitting component and a colder outer component, so that some of the warm 11.3 μm SiC emission is re-absorbed by the cooler dust component. In the case of the five stars with the 8.5 μm feature, the self-absorption fitting only yielded results over the 9.5–13.5 μm range. The results of the self-absorption fitting can be seen in Table 6.5

The results for the overall best fits for emission features are listed together in Table 6.6 and shown in fig. 6.2. Where both the pure emission and self-absorption fits yielded good results, both are shown, with the pure emission fits as dashed lines and the self-absorption fits as solid lines.

6.7 Sources with Absorption Features

There are four carbon star spectra in our sample which exhibit net absorption features. AFGL 3068 and IRAS 02408+5458 both show evidence of a broad absorption band in the 10–12.5 μm region. AFGL 3068 was originally investigated by Jones *et al.* (1978), who concluded that this feature was due to SiC in absorption. IRAS 02408+5458 has a very similar, but much stronger feature than AFGL 3068, as seen from a comparison of Figs. 6.3(a)&(d).

AFGL 2477 and AFGL 5625 also show evidence of absorption features, only this time they

appear to have a double absorption peak (see Figs. 6.3(b)&(c)). The longer wavelength feature is very similar to that seen in the spectra of AFGL 3068 and IRAS 02408+5458. The shorter wavelength feature is centred at about 9.7 μm. Incomplete cancellation of telluric ozone absorption may contribute to this peak but the absorption appears to extend, on both sides, well beyond the 9.3-9.9 μm region affected by ozone. Both these stars had their spectra calibrated using several different standard stars which were observed on the same night and the short wavelength extended absorption was found to persist. For this reason we believe that this feature is real. One possibility is that it is due to interstellar silicate absorption.

We applied the χ^2-minimisation routine to the flux-calibrated spectra in a variety of different ways. In addition to fitting the spectra with a single form of SiC pure absorption, fitting was also attempted using a combination of one silicon carbide variant and an interstellar silicate. Following the success of fitting the emission features using self-absorbed SiC, the absorption features were also fitted using self-absorbed silicon carbide both with and without an interstellar silicate absorption. The results of these fits are listed in Table 6.7. The fits obtained using self-absorbed SiC proved to be very good with plausible optical depths. Fitting using both SiC and interstellar silicate only yields fits for AFGL 2477 and AFGL 5625. We have already mentioned the possibility that the spectra of these two stars are affected by interstellar silicate absorption. Self-absorption fits using SiC only for AFGL 3068 and IRAS 02408+5458 together with fits using self-absorbed SiC and interstellar silicate absorption for AFGL 2477 and AFGL 5625 are shown in Fig. 6.4.

6.8 TX Psc

TX Psc is the only carbon star in the sample for which the χ^2-fitting routine consistently had problems finding fits to the spectrum. For this reason the spectrum of TX Psc needed further investigation. Its flux-calibrated spectrum is shown in Fig. 6.5. The best-fitting 8-13 μm blackbody has a temperature of 3500 K. Dividing by this blackbody yields a normalised spectrum which does not show an obvious 11 μm feature (Fig. 6.5(b)). It does, however, exhibit a prominent feature at 8.8 μm. This could be the usual feature found in this region, attributed to a:C-H. The 3500 K blackbody does not fit perfectly, so that the "normalised" spectrum in Fig. 6.5(b) does not have a flat underlying continuum.

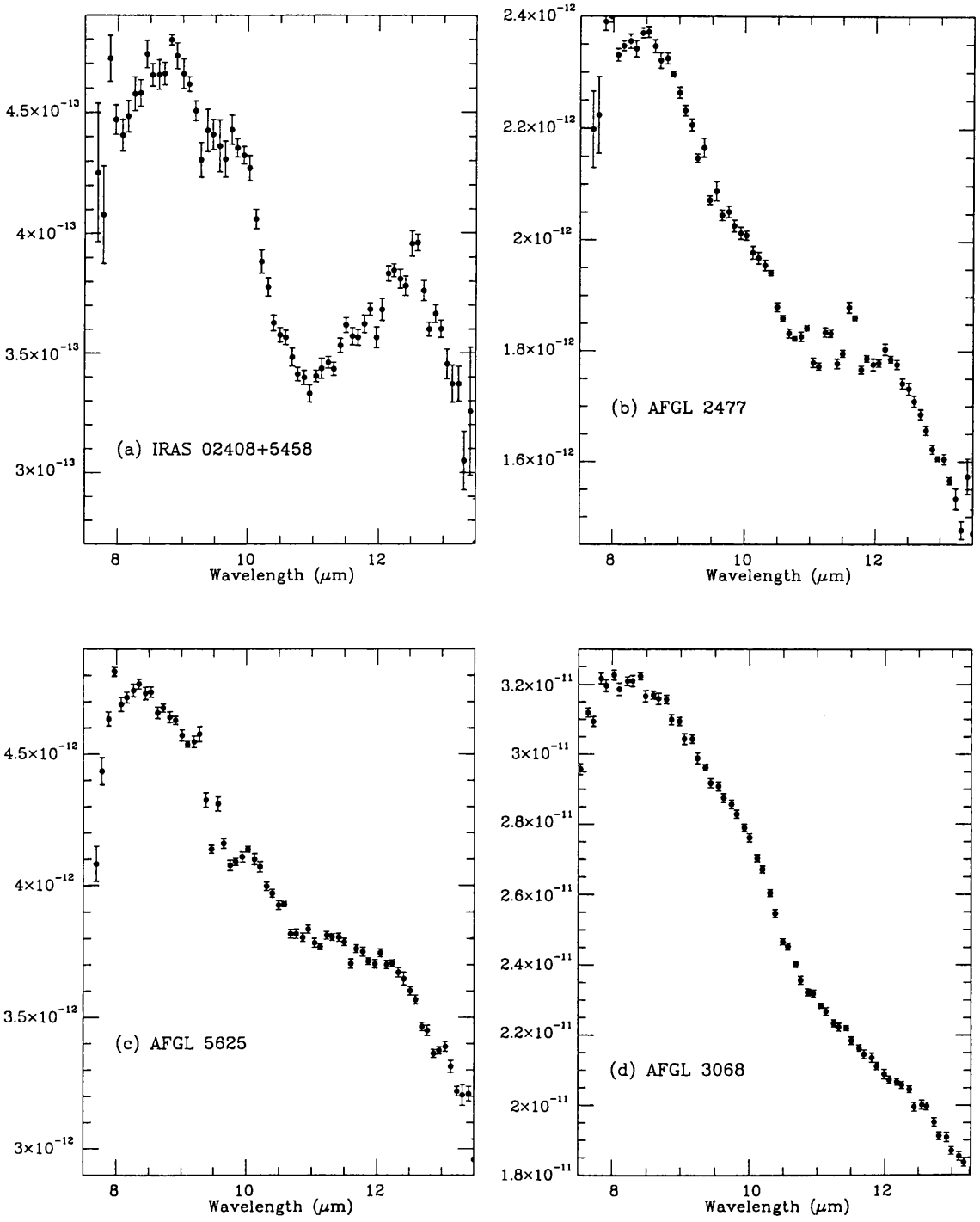

Figure 6.3: 8-13 μm flux-calibrated spectra of carbon stars with $\sim$11 μm absorption features. The errors used to calculate the reduced χ^2 are set to 3% of the flux if the 1σ error on the flux is less than this value. Thus the 1σ error bars shown here are not necessarily the errorbars used by the fitting program

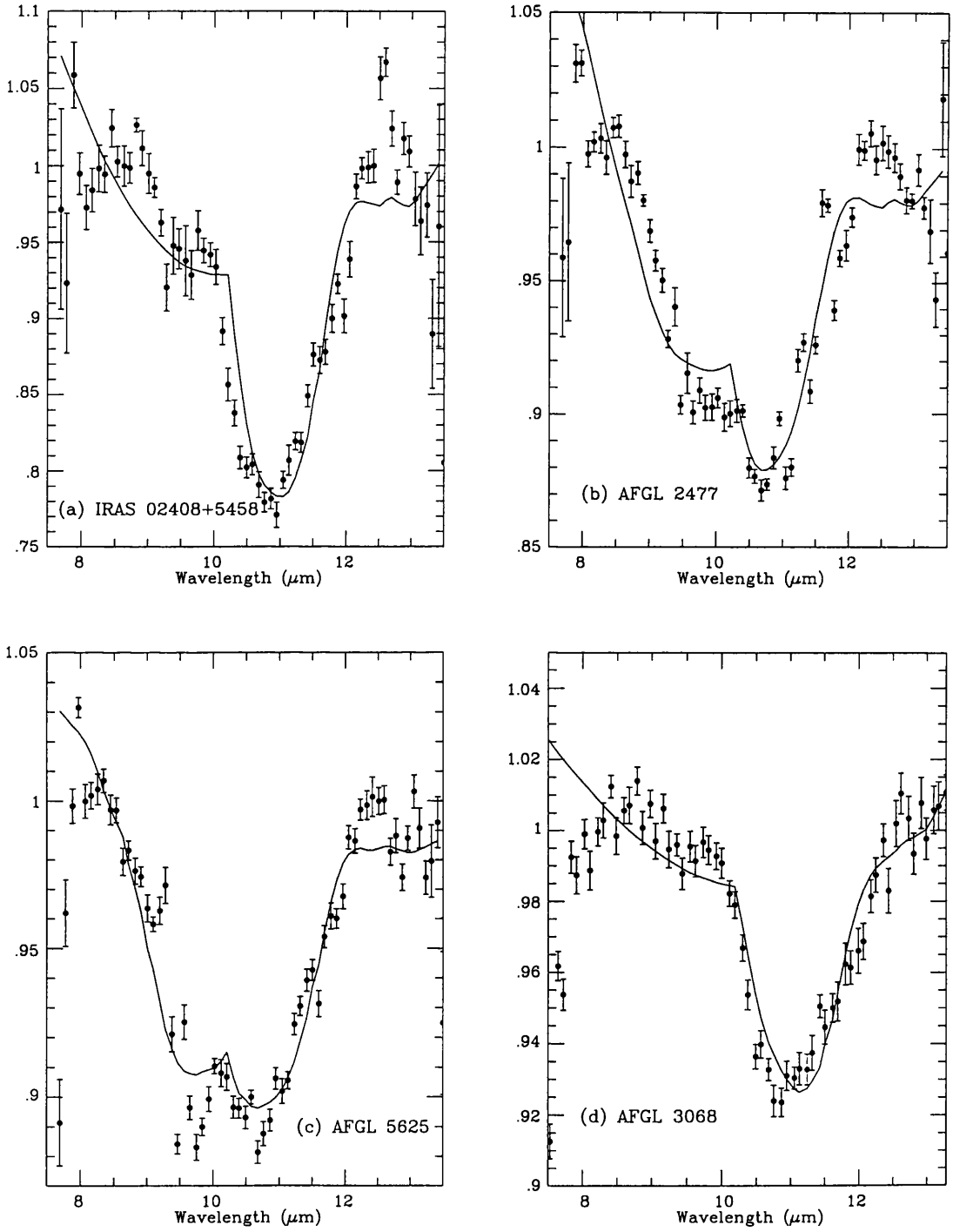

Figure 6.4: 8-13 μm normalised spectra of carbon stars with $\sim$11 μm absorption feature with self absorption fits. The errors used to calculate the reduced χ^2 are set to 3% of the flux if the 1σ error on the flux is less than this value. Thus the 1σ error bars shown here are not necessarily the errorbars used by the fitting program .

Table 6.7: Results of the self-absorption χ^2-fitting for the 7.5–13.5 μm region of flux-calibrated spectra

Source	T_{colour}	SiC type	T_{BB}(K)	T_{SiC}(K)	τ_{SiC}	$\tau_{9.7}$	χ^2_R *
AFGL 3068	377	β-SiC	394	62	0.030	—	0.092
IRAS 02408+5458	320	β-SiC	388	96	0.152	—	1.686
AFGL 2477*	340	β-SiC	377	114	0.073	0.104	0.419
AFGL 5625†	333	β-SiC	358	185	0.097	0.113	0.306

* is fit with Trapezium interstellar silicate

† is fit with μ Cep interstellar silicate

* The errors used to calculate the reduced χ^2 are set to 3% of the flux if the 1σ error on the flux is less than this value. The errors shown in Figs. 6.3 & 6.4 are 1σ. In all these spectra, the majority of points have errors that are <3% of the flux, the exceptions being for those points at the edges of each spectra and in the ozone region (9.4–9.9μm). Thus the 1σ error bars shown in the fits are not necessarily the errorbars used by the fitting program.

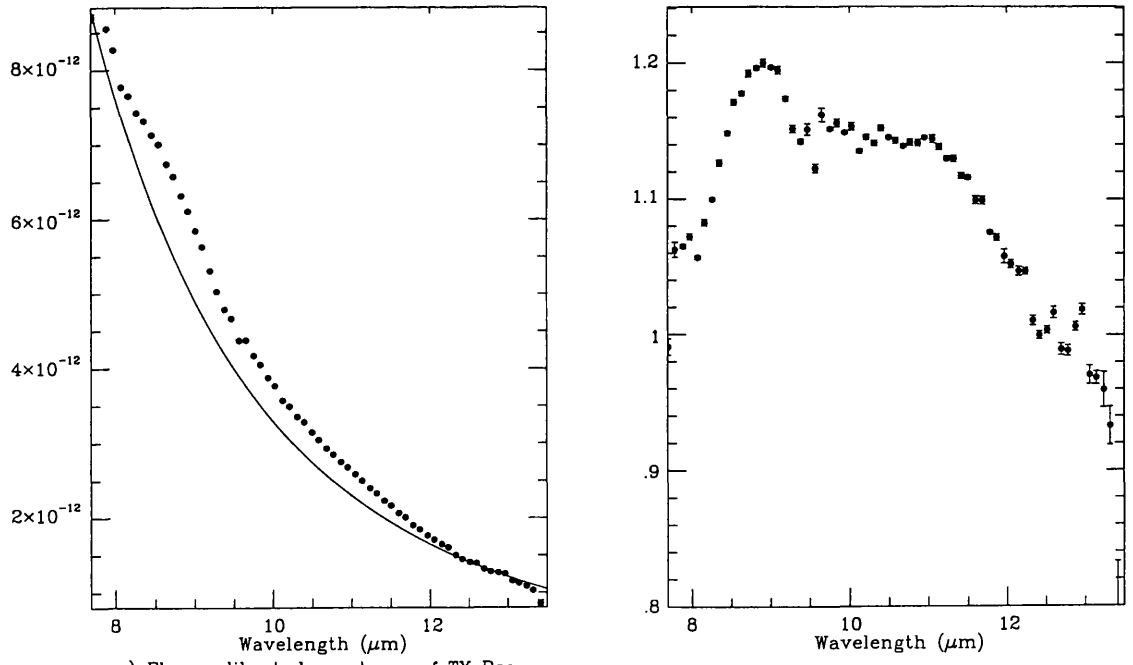

a) Flux-calibrated spectrum of TX Psc with best fitting 3500K blackbody

b) Spectrum of TX Psc after division by a 3500K blackbody

Figure 6.5: 8-13 μm spectrum of unusual carbon stars TX Psc

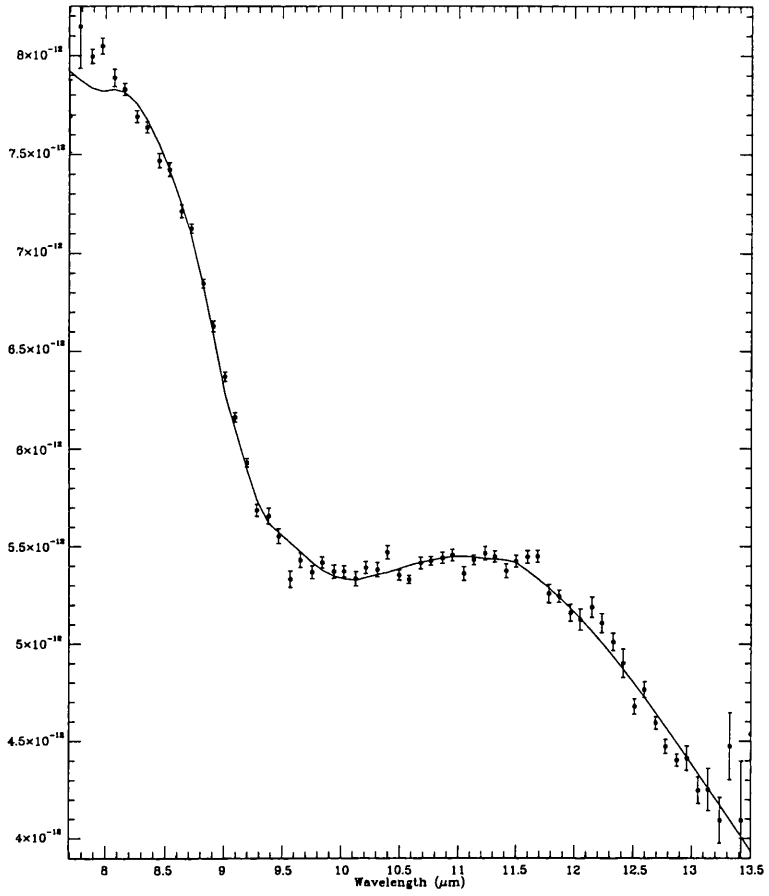

Figure 6.6: The 8-13 μm flux-calibrated spectrum of AFGL 2333, fit by self-absorbed silicate. The errors used to calculate the reduced χ^2 are set to 3% of the flux if the 1σ error on the flux is less than this value. Thus the 1σ error bars shown here are not necessarily the errorbars used by the fitting program.

The resulting spectrum has peaks at 8.8 μm and 11.3 μm (Fig. 6.5(b)). It would appear that the spectrum of TX Psc may have contributions from three sources: 1) a hot 3500K photospheric continuum; 2) a feature at 8.8 μm possibly due to α:C-H; and 3) a weak feature at 11.3 μm possibly due to SiC. Whatever the explanation, it is clear that the mid-IR spectrum of TX Psc is markedly different from those of other carbon stars in our sample.

6.9 AFGL 2333

AFGL 2333 was originally included in our sample as it had been classified as a carbon star based on its IRAS LRS spectrum and HCN emission (Groenewegen *et al.* 1992, Loup *et al.* 1993, Volk, Kwok & Woodsworth 1993, Volk Kwok & Langill 1992). However, on the

basis of its OH maser emission (see David *et al.* 1993, Le Squeren *et al.* 1992), we believe that it is an OH/IR star. The flux-calibrated spectrum of AFGL 2333 is included with those of the rest of the sample in Fig. 6.6 and shows that the spectrum in fact exhibits an absorption feature centred at about 9.6 μm rather than an emission feature at about 11.5 μm. AFGL 2333 can therefore be interpreted as an oxygen rich OH/IR star that exhibits silicate self-absorption. The spectrum of AFGL 2333 can be fitted very well using self-absorbed silicate. The minimisation routine gave a reduced χ^2 value of 0.265 using a Trapezium silicate profile, with an optical depth of 1.51. The fit is shown in Fig. 6.6.

6.10 Discussion

The original fitting of the carbon star spectra was performed using KBr-corrected optical constants. This led to nearly all the sources being best fit by α-SiC. However, as discussed in chapter 4, it is now believed that the KBr-correction is unnecessary and leads to erroneous optical constants. The original results, using corrected optical constants can be found in Speck *et al.* (1997a,b). The current work uses raw (uncorrected) SiC data.

Fig. 6.7 uses some of the SiC feature parameters listed in Table 6.2 with a view to finding trends in the SiC features. In each plot (a-c), the solid line represents a linear regression fit to the plotted data.

We found no correlation between the full width at half maximum (FWHM) of the SiC profile and the 8-13 μm colour temperature (the formal linear correlation coefficient is -0.241) or between the full width at zero intensity (FWZI) of the SiC profile and the colour temperature (the linear correlation coefficient is 0.312) An attempt was made to find correlations between the stellar mass-loss rates and the properties of the 8-13 μm spectra. The mass-loss data were taken from Jura (1986), Jura & Kleinmann (1989), Volk, Kwok and Woodsworth (1993) and Loup *et al.* (1993). Published mass-loss rates were found for 25 of our sources. The only combination of data that yielded any correlation was that of the mass-loss rates of Loup *et al.* (1993) versus the 8-13 μm colour temperature. The plot excludes the mass-loss rates for the four stars whose spectra exhibit absorption features, as well as TX Psc. The resulting correlation can be seen in Fig. 6.7(a). The linear correlation coefficient is -0.605. It can be seen that as the mass-loss rate increases, the underlying continuum colour temperature decreases. This is as expected for dust shells that becomes

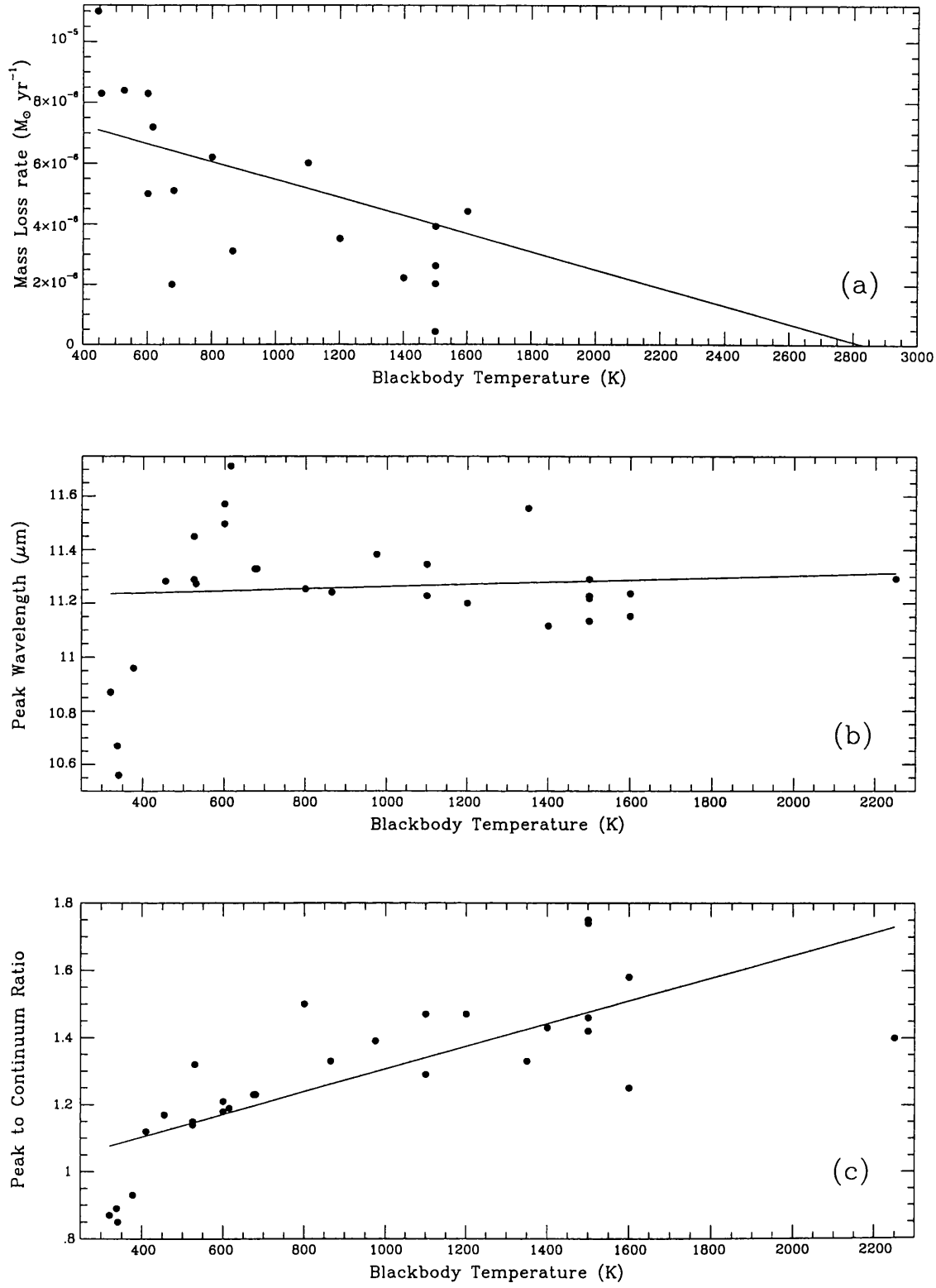

Figure 6.7: Plots of the 8-13μm colour temperature versus various parameters: (a) colour temperature vs. the mass-loss rate (from Loup *et al.* 1993); (b) colour temperature vs. the peak wavelength of the SiC feature; (c) colour temperature vs. the peak to continuum ratio of the SiC feature.

increasingly optically thick as the mass loss rate increases. Fig. 6.7(b). shows the SiC peak wavelength (i.e. the wavelength at which the ratio of the flux of the feature to the flux of the underlying continuum is highest) versus the colour temperature of the underlying 8-13 μm continuum. There is no correlation (the formal linear correlation coefficient for the best straight line fit through the data is 0.11). This lack of correlation between the peak wavelength of the feature and the 8-13 μm colour temperature disagrees with the findings of Willems (1988a,b). Fig. 6.7(c) shows a plot of the SiC peak to continuum ratio versus the underlying 8-13 μm colour temperature. There is an obvious trend, whereby the spectra with the hotter underlying colour temperatures have higher peak to continuum ratios. The linear correlation coefficient is 0.73 This trend is not surprising, since Baron *et al.* (1987) had already found that the SiC feature tends to get stronger as the temperature of the underlying continuum increases. The decrease in the peak to continuum ratio of the SiC feature with decreasing 8-13 μm colour temperature (i.e. increasing mass-loss rates; Fig. 6.7a) can be attributed to two effects: (a) for low mass-loss rates there is no dilution of the SiC feature by dust continuum emission originating in the outflow but as the mass-loss increases the continuum emission produced by an increasingly optically thick dust shell dilutes the SiC emission to an increasing degree; (b) as the mass-loss rate increases (causing the 8-13 μm continuum colour temperature to decrease) the SiC feature itself begins to become optically thick. This causes self-absorption also which reduces the peak to continuum ratio of the SiC emission band and for large enough mass-loss rates, the feature ultimately goes into net absorption. While many of the sources in this sample are best fit by self-absorbed SiC, it is not necessary to use self absorption, as good fits can be achieved using SiC pure emission. There is no tendency for self absorption to become necessary as the colour temperature decreases. Radiative transfer modeling is now desirable, in order to ascertain how much SiC is required for self-absorption to occur. Previous radiative transfer analyses of the SiC feature have neglected self-absorption and have therefore probably underestimated the quantities of SiC in the outflows. The use by previous authors of the KBr-correction for laboratory data will also affect radiative transfer models, which should now be run using uncorrected SiC data.

Chan & Kwok (1990) proposed a scenario for the evolution of SiC dust particles with the evolution of the carbon star that produces them. They suggested that the dust produced when the star has a relatively low mass-loss rate is of the α-SiC variety, since the

high densities needed for grain condensation require grain formation to take place close to the star; at the relatively high temperatures that characterise these regions, only α-SiC would be able to condense. As the mass-loss rate increases and the dust shell becomes denser and more optically thick, β-SiC could begin to condense at the lower temperatures characteristic of the regions further out in the circumstellar envelope. Thus β-SiC might be detected, as the envelope could be highly opaque to the inner α-SiC emission. If this model were correct, we should be able to see a difference between the feature shapes and peak wavelengths observed from optically thick and optically thin envelopes. As discussed above, the correlations found in Fig. 6.7(a)&(c) support the view that those carbon stars which have relatively high 8-13 μm colour temperatures have optically thin circumstellar shells and lower mass loss rates. Likewise those carbon stars with cooler 8-13 μm colour temperatures are likely to have optically thick shells and higher mass loss rates. However, Fig. 6.7(b) shows that the peak wavelength of the SiC feature is not correlated with the 8-13 μm colour temperature, whereas if β-SiC was to become more predominant at higher mass-loss rates we would have expected to see a shortward shift of the peak wavelength with decreasing 8-13 μm colour temperature. Inspection of Tables 6.3, 6.4, 6.5 and 6.6 in which the sources are listed in order of increasing 8-13 μm colour temperature, shows that, for all the sets of results, there is no tendency for the hotter sources to have α-SiC features and the cooler ones to be better fitted by β-SiC features. In fact, for the fitting of the sources with emission features, all sources are fit by β-SiC. There are no fits to α-SiC. This contradicts previous work, however, the KBr-correction factor, discussed in chapter 4, led many previous studies to use erroneous laboratory data. The correction of the data led to the shifting of the α-SiC peak to the position at which uncorrected β-SiC peaks. We find that all circumstellar SiC emission is consistent with being due to the cubic, β- form. This result is reinforced by the fact that all SiC found in meteorites, attributed to formation around C-rich AGB stars, is of the β-SiC form (see chapter 3).

Chapter 7

Carbon Stars II - PAHs, carbon dust and diamonds

"Ours the diamond mines of stars"

Vladimir Mayakovsky (1917)

7.1 UIR bands and the Polycyclic Aromatic Hydrocarbons (PAHs)

7.1.1 Review of the unidentified infrared bands

An unidentified infrared (UIR) band at 11.3 μm was observed by Gillett *et al.* (1973) in the 8-13 μm spectra of two planetary nebulae (PNs). Gillett *et al.* (1973) observed the mid-IR spectra of three PNs, namely NGC 7027, NGC 6572 and BD+30°3639 and found that two of the spectra exhibited a new feature at about 11.3 μm, which could not be attributed to an atomic emission line. Of the three PNs, the two exhibiting the new feature, NGC 7027 and BD+30°3639, are high-excitation and low-excitation objects respectively, whereas the third PN, which did not exhibit the 11.3 μm feature, NGC 6572, is a medium excitation object. Therefore there appears to be no correlation with the excitation of the nebula.

The new feature at 11.3 μm is not compatible with the emission spectrum expected for graphite, and, at that time, had not been seen in the 8-13 μm spectra of late-type stars, e.g. M supergiants, M- and C-variable stars, and other long period variables. Gillett *et al.* (1973) suggested that this new 11.3 μm feature could be due to magnesium and calcium

carbonate, the spectra of which have a strong narrow peak near 11.3 μm. They stated that their own work had too low a resolution and too narrow a wavelength range to be conclusive, and suggested that better resolution observations of these planetary nebulae would be useful, together with spectra over a wider range of wavelengths, so as to encompass the 6.9 μm feature expected if the 11.3 μm feature is indeed due to carbonate. Also continuing on from the work of Gillett *et al.* (1973), Gillett *et al.* (1975) looked for the 11.3 μm feature in other sources. The found it in two extragalactic sources and took this as evidence that the source of the feature is widespread. They also found another narrow feature at 8.7 μm in these sources. This 8.7 μm feature was also seen in HD44179 by Cohen *et al.* (1975). Merrill, Soifer and Russell (1975) investigated the 2-4 μm spectrum of NGC 7027, and found that besides the hydrogen recombination lines in the region there were also three unidentified lines at 2.43, 3.09 and 3.27 μm and also a broad feature centred on 3.4 μm. The strongest of these features were the 3.27 μm line and the 3.4 μm broad feature which were subsequently seen in a variety of other sources (Merrill, Soifer and Russell 1975). These two features were also investigated by Grasdalen and Joyce (1976) who suggested that they were not two distinct features, and that they might be attributable to molecular species, such as CH^+. Russell *et al.* (1977) investigated the 4-8 μm spectrum of one of the planetary nebulae bearing the 11.3 μm band, NGC 7027. They discussed more of these interesting features found at 3.3/3.4, 6.2, 7.7 and 8.6 μm, none of which could be attributed to any blend of atomic lines, but failed to find any feature near 6.9 μm, thus disproving the hypothesis that the 11.3 μm feature was due to carbonates. They interpreted the many sharp features as the structure in the emissivity curve of the dust grains.

The 6.2 and 7.7 μm features were also discovered in the spectrum of NGC 7027 by Russell *et al.* (1977), in which they suggested that these feature, along with all the other UIR bands, could not be attributed to molecular species, as the emissions from molecules are highly temperature dependent, and yet the positions of the UIR bands are remarkably constant.

In 1981, Duley and Williams noted that some of the UIR bands had frequencies that were characteristic of surface functional groups on small carbon particles. They suggested that the UIR bands are in fact due to these surface functional groups. They pointed

out that while all the features (3.3, 3.4, 6.2, 7.7, 8.7, 11.3 μm) are seen in emission, the only band to be seen in absorption is the 3.4 μm feature. Their model attributed the 3.3 and 11.3 μm emission features to resonances in aromatic CH groups, whereas the emission/absorption features at 3.4 μm were associated with aromatic methyl groups (CH_3). The relative strengths of the 3.3 and 3.4 μm features are determined by the balance between CH and CH_3, and that the dominant surface group is determined by the ambient temperature. This means that the 3.3 and 11.3 μm (due to the CH surface group) should be dominant at higher temperatures and the 3.4 μm (due to the CH_3 surface group) should be dominant at lower temperature.

Since then much work has been done on explaining all the UIR bands in terms of emission from polycyclic aromatic hydrocarbons (PAHs) and/or hydrogenated amorphous carbon (HAC) and which specific species are responsible.

Following the attribution of UIR bands to PAHs and/or HACs, it seems prudent to investigate the microstructure of such matter. Dischler *et al.* (1983a) looked at the microstructure of amorphous hydrogenated carbon and found that the bonding between atoms is not of a single form. They found that the bonding was a combination of sp^1 (carbyne or triple bonded carbon), sp^2 (graphite) and sp^3 (diamond). They found the the triple bond was least common, but the relative amounts of sp^2 and sp^3 bonds depended on the temperature. The sp^2 bonds are thought to be responsible for the 3.3 μm feature, while the 3.4 μm feature is attributed to the sp^3 bonds (Dischler *et al.* 1983b). Dischler *et al.* (1983a) found that HAC grown at 50°C gives an infrared feature at 3.4 μm. As this is annealed at higher and higher temperatures the 3.4 μm peak diminishes and a 3.3 μm peak grows, which fits with the Duley & Williams (1981) model. Dischler *et al.* (1983a) do not discuss what would happen if the HACs are formed initially at high temperatures and then cooled.

Barlow (1983) discussed the relationship between the strengths of the 11.3 and 3.3 μm bands, the SiC feature and the C/O ratio in planetary nebulae. He found that PNs with strong SiC features have weak 11.3 μm bands and low C/O ratios (just larger than unity), whereas PNs with strong 11.3 μm bands have high C/O ratios (>2). This is interpreted in terms of the initial mass of the progenitors of the PNs. He suggested that the lowest initial

masses produce the PNs with the lowest C/O ratio, so that for low initial masses, small amounts of carbon are dredged up and the PN remains oxygen-rich. For the more massive progenitors, more carbon is produced so that the PNs become carbon-rich. The relative abundance of carbon over oxygen determines whether the species formed are SiC (C/O>1) or the 11.3 μm band carrier (C/O>2). The correlation of the strengths of the other UIR bands with C/O ratio was investigated by Cohen *et al.* (1986;1989). They found that the C/O ratio correlates with the fractional luminosities of the UIR bands for several PNs, and took this as evidence of a hydrocarbon carrier for the UIR bands. Barlow (1983) proposed that the surface hydrocarbon complexes invoked by Duley & Williams (1981) to explain the UIR bands are formed by the chemical sputtering of carbon by H-atoms as they pass through ionization fronts in PNs.

Sellgren (1984) found 3.3 and 3.4 μm emission bands in the spectra of reflection nebula, together with infrared continuum excess. Sellgren suggested the only explanation for these infrared features involves very small grains ($\sim$10Å/70-90 molecules) being momentarily heated to very high temperatures ($\sim$1000K) by absorption of UV photons. This model fits all her observations, whereas other mechanisms have all been discounted. The small size of the particles is crucial to this model, whereas the model is insensitive to changes in the colour temperature of the source of the UV radiation.

Léger & Puget (1984) considered the transient heating of very small grains (about 50 atoms) by the absorption of a single UV photon and then estimated the infrared emission. They chose to look at graphite as this would not sublime under such conditions. The bulk optical constants cannot be used because the small number of atoms introduce essential differences in the electronic transition of the system. They considered these very small graphite grains to be more like large PAH molecules.

Cohen *et al.* (1985) discussed a new feature associated with the UIR bands in the form of a plateau at 11.3-13.0 μm. This feature is seen in many sources which exhibit the 11.3 μm sharp feature, but not in sources which do not have the 11.3 μm band. This is why the plateau is associated with the UIR bands. In the laboratory, PAHs give rise to infrared features between 11 and 15 μm, whereas interstellar/circumstellar spectra exhibit only a single sharp feature at 11.3 μm. Because the 11.3 μm feature is characteristic of CH

bending modes of H atoms isolated on aromatic hydrocarbons, the predominance of the 11.3 μm band was taken to indicate that the interstellar hydrocarbons were only partially hydrogenated. However, the observations of this 11.3-13.0 μm plateau may force one to reconsider this model. There is also a discrepancy between laboratory spectra and interstellar spectra. The 11.3 μm feature in the laboratory spectra is more intense relative to the 7.7 μm feature than in the IRAS spectra. Cohen *et al.* (1985) noted that this may be due to astronomical PAHs that are either slightly larger or are less hydrogenated than the laboratory samples. They also attribute the 11.3-13.0 μm plateau to large PAHs. This is supported by observations of NGC 7027 and the carbon-rich post-AGB object, HD44179. The B9 exciting star of HD 44179 provides a less hostile environment where partially hydrogenated small ($\leq$ 25 atoms) PAHs could prosper. This would increase the strength of the 11.3 μm feature relative to the plateau, whereas NGC 7027 is more hostile so that the small PAHs would be destroyed. NGC 7027 has the strongest observed emission plateau between 11.3 and 13.0 μm, supporting this hypothesis.

Allamandola *et al.* (1985) derived the properties and the spectra of PAH molecules (as opposed to bulk material), using lab data, statistical mechanics and spectroscopic theory. They suggested that the lack of hydrogenated sites, implied by the existence of only a single band near 11 μm, is due to the intense UV field in the regions where the UIR bands have been observed. They proposed that the presence of PAHs is widespread in the interstellar medium (ISM) and that they are likely to have formed in carbon rich outflows of planetary nebulae. They also showed that PAHs would be relatively resilient in the ISM as they will not easily photo-dissociate since they have other channels for energy relaxation (i.e. redistribution of UV energy to the vibration modes and re-emission as IR features). They suggested that the PAHs are the leftover condensation nuclei from the formation of carbon grains.

Cohen *et al.* (1986) noted that there were two weaker UIR bands at 5.6 μm and 6.9 μm[1] that had been attributed to the UIR family by Bregman *et al.* (1983). They also discussed the class of objects in which the UIR bands are observed. They showed that while the UIR bands are observed in objects which are carbon-rich and have strong UV fields, objects which only exhibit one of these attributes, for example carbon-rich AGB stars,

[1] Perhaps it is ironic that a 6.9 μm was eventually found. If it had been found when the 11.3 μm feature was first discovered, no doubt they would both have been attributed to carbonates

do not exhibit UIR bands. It was, therefore, concluded that the UV radiation was crucial to the processes involved in causing carbon-rich molecules/dust to emit the UIR bands.

More detailed observations of the 3-4 μm region were performed by de Muizon *et al.* (1986). They found that, together with the well known 3.3 μm and 3.4 μm features, there are also weaker features at 3.46, 3.51 and 3.56 μm and a broad, plateau feature at 3.4-3.6 μm. They observed that the appearance of these various features appeared to follow a hierarchy such that: the 3.3 μm feature is always present when any of the others are present; only the 3.3 μm emission need be present for the 3.4 μm feature to be present; both the 3.3 μm and the 3.4 μm features must be present before the 3.4-3.6 μm plateau can be observed; and finally all of the above need to be seen for the weaker 3.46, 3.51 and3.56 μm features to be present. These weaker features were attributed to different molecular subgroups attached to PAHs.

HACs as carriers of the UIR bands were again discussed by Borghesi *et al.* (1987). They found in a laboratory study that amorphous carbon produces a spectrum in which the position of the six emission bands are in "good" agreement with six of the UIR bands. In space, the amorphous carbon grains are expected to have surface functional groups attached. These would be mostly H, CH, CH_2 or CH_3, however other functional groups (e.g. OH, CHO and NH_2) may be present depending on the ambient conditions. The UIR bands are observed in the spectra of planetary nebula, where we expect HACs and PAHs to be formed. Borghesi *et al.* (1987) suggested that the UIR bands could be completely explained by a combination of PAHs and HACs.

The attribution of the UIR bands to Quenched Carbonaceous Composites (QCCs) was discussed by Sakata *et al.* (1987). They had previously found (Sakata 1984) that most of the UIR bands could be fitted using QCCs, however the 7.7 and 8.6 μm features were absent from the QCC spectrum. Sakata *et al.* (1987) showed that a combination of oxidised "film-QCC" (which has ketonic groups) and non-oxidised "granular-QCC" provided good fits to most of the UIR bands (i.e. 3.3, 3.4, 3.5, 6.2, 6.9, 7.7, 8.6 and 11.3 μm).

Papoular *et al.* (1991) investigated various forms of natural coal as carriers of the UIR bands. Apart from the spectral analysis, they also studied the effects of temperature, in-

cluding prolonged heating of samples, and how different surface functional groups affected the spectrum. They looked in detail at the samples and the features they produced, finding that different coal samples could produce spectra that could fit the UIR bands observed in the spectra of a variety of objects. They also attributed specific bands to specific bending and stretching modes. Their suggestion was that the plethora of different objects with different combinations of UIR bands required many different coal samples to fit all the features. Their work supported the hypothesis of surface functional groups on HACs or other similar substance (c.f. Duley & Williams 1981)

Bregman *et al.* (1989) discussed the origin of the UIR bands with respect to PAHs, HACs and QCCs. Both HACs and QCCs are forms of amorphous carbon made up of clusters of PAHs. Therefore, as suggested by Borghesi *et al.* (1987), it is likely that that amorphous carbon particles and the free PAHs co-exist in objects showing UIR bands. Bregman *et al.* (1989) also presented other evidence to support the PAHs as the carriers of the UIR bands. The 3.3 μm and 11.3 μm features are closely correlated, whereas both individually are less well correlated with the 7.7 μm feature. This is consistent with the PAH hypothesis, since the 3.3 and 11.3 μm feature are both associated with C-H bonds and expected to be correlated, whereas the 7.7 μm feature is attributed to C=C bonds. Bregman *et al.* (1989) concluded that there are, in fact, two components contributing to the 3-13 μm emission. These are the PAHs, which produce the narrow emission lines at 3.3, 6.7, 7.7 and 11.3 μm, and HACs or QCCs (or both) responsible for the broad emission plateau. They also suggested that the differences in destruction times of PAHs and HACs/QCCs may be able to explain differences in IR spectra from source to source. As in Cohen *et al.* (1985), Bregman *et al.* (1989) used observations of the planetary nebula NGC 7027 and the Red Rectangle to give support to their hypothesis. NGC 7027 shows strong plateau features with weak narrow features on top, implying that amorphous carbon is dominant here, while the spectrum of the Red Rectangle shows very little plateau emission and is dominated by the narrow emission features. However, counter to this is the fact that the F-G post-AGB objects discussed by Justtanont *et al.* (1996) show very weak 11.3μm bands but strong plateaux.

At this stage, having introduced PAHs, HACs, QCCs and the coal model, it is expedient to discuss the similarities and differences between these species. It has been said

(Duley 1993) that these are all essentially the same materials. This is true in some sense, however the exact size and bonding structures involved vary and it is therefore useful to distinguish between these types of materials. It has been suggested by Tokunaga (1996) that the type of material to which the UIR bands are attributed are in fact too large to be considered molecules (i.e. PAHs) but too small to be considered grains (i.e. HACs, QCCs or coal). This would explain why it is so difficult to attribute the UIR bands to one of these types of material. There is also the theory suggested by Duley & Williams (1981), mentioned earlier, that the UIR bands are produced by PAH molecules stuck on the surface of HAC grains.

Allamandola, Tielens & Barker (1989) presented a comprehensive exposition of the attribution of the UIR bands to PAHs. They suggested that the main narrow UIR bands are due to small PAHs which are very stable, probably symmetrical and fairly ubiquitous. The minor bands are probably due to PAHs that are less stable and therefore not present in all environments that exhibit the major bands. The broad feature is probably due to large PAHs, PAH clusters and/or small amorphous carbon grains. They discussed the formation mechanisms of these particles in the outflows of carbon-rich red giants and concluded that there is a size limiting step to the formation of PAHs in these environments. Large PAHs would have to be formed from destruction of amorphous carbon grains in the ISM. Their discussion of ionised PAHs implies that if these species are responsible for the UIR bands, then the UIR bands can be pumped by visible radiation and would be observable in sources which do not have strong UV field but do have visible radiation. This could be interpreted as evidence that the PAHs responsible for the major UIR bands are indeed neutral.

Furthering the search for the sources of the UIR bands, Cohen *et al.* (1989) discussed the infrared spectra of WC9 stars[2]. They observed the 7.7μm UIR feature, attributed to aromatic C-C stretching modes. The 3.3 and 11.3μm bands were not observed, which is not surprising in a hydrogen-poor environment given that they are attributed to C-H stretching and bending modes respectively. Much more surprising is the non-observation of the 6.2 band attributed to C-C modes and usually associated with the 7.7μm bands (see Table 7.2). However, Cohen *et al.* (1989) reported the results of laboratory experiments

[2]i.e. very luminous, very hot, hydrogen-poor, evolved stars with very high C/O ratios

which showed that the ratio of the band strengths ([6.2]/[7.7]) decreased as the size of the aromatic domain decreases (Friedel & Carson 1972), implying that these late-type WC stars produce either very small PAHs or highly disordered amorphous carbon grains.

Balm & Kroto (1990) suggested that a new type of PAH may be responsible for the UIR bands. They commented that the constancy of the 11.3 μm feature implies that this UIR band is produced by a single species of PAH. This is because in a PAH mixture the exact compositions would vary from source to source and hence the band positions would also vary. As already stated, the 11.3 μm band is attributed to the C-H bending modes of H atoms isolated on aromatic rings (Cohen *et al.* 1985). However the 11-13 μm plateau is attributed to more complicated hydrogen groupings. The extent of the plateau implies that it is produced by paired and triplet hydrogens only, and not by higher order groupings. Since no single PAH had yet given a satisfactory fit to the UIR band spectrum, Balm & Kroto (1990) suggested trying another form of PAH. They proposed a form of PAH with internal hydrogens, for example kekulene ($C_{48}H_{24}$). This is a PAH with an annular structure involving twelve fused aromatic rings. They claimed that the environments where the PAHs are forming are conducive to the formation of such species. Since such particles are expected to form in many astrophysical environments, their model is able to explain both the intensity and the consistency of the 11.3 μm band as well as the widespread observation of the UIR bands.

Another investigation of the broad plateau features versus the narrow features was undertaken by Buss *et al.* (1990). In this work they compared the IR spectra of planetary nebulae (PNs) to the so-called "transition branch" or TB objects. TB objects are objects which are in the evolutionary stages between the asymptotic giant branch and the planetary nebulae. These objects are also known as post-AGB objects. Buss *et al.* (1990) found that the TB objects have strong plateaux and relatively weak narrow features, whereas PNs have stronger narrow features and weaker plateaux. They interpreted this in terms of the radiation available from such objects and the dust present. They suggested that the "dust" around these objects comprises both molecular PAHs and PAH clusters/HAC grains[3]. They attributed the narrow features to the PAH molecules and the broader plateaux to the PAH clusters/HAC grains. The PAH clusters/HAC grains

[3]PAH clusters and HAC grains are virtually the same thing

efficiently absorb visible photons, whereas the molecular PAHs absorb very weakly in the visible. However, molecular PAHs absorb UV photons more efficiently than the PAH clusters/HAC grains. So in the transition-branch objects the predominance of visual radiation leads to dust features due to the PAH clusters/HAC grains, whereas the predominance of UV radiation in PNs yields the features attributed to PAH molecules. Buss *et al.* (1990) do, however, suggest an alternative explanation of the observations in which the HACs "graphitize" during the TB phase, reducing the plateau emission, or the HAC grains are shattered into PAH molecules in the stellar winds, again reducing the plateau emission, and also strengthening the narrow bands. The investigation of the differences between the spectra of TB objects and PNs was continued by Buss *et al.* (1993). They found that the spectra of TB objects vary from source to source, each having at least one unique IR feature, whereas the spectra of PNs are remarkably uniform. These differences in the spectra were interpreted as due to differences in the composition of the matter around the objects observed. Also, a feature at about 8.8μm is seen in the spectra of many TB objects but never in the spectra of PNs. The presence of different material in two successive evolutionary stages (TB objects and PNs) implies that processing of the dust sometimes occurs during the TB phase.

Duley & Jones (1990) discussed the possibility that UIR band emission could be explained by small, simple linear aromatic hydrocarbons (e.g. anthracene, naphthalene and tetracene). In particular they found that the spectrum of anthracene ($C_{14}H_{10}$), a linear, three ring molecule, produced a spectrum with remarkable similarity to the observed UIR band spectrum, thus producing the first evidence that small PAHs could be responsible for the UIR bands. They also suggest that there is evidence that while this and similar species of PAH are probably sputtered from the surface of HACs, the emission of the UIR bands probably takes place before it leaves the HAC surface. They continue by discussing the effect of side-groups on these aromatic molecules and conclude that various substituents may be responsible for the 11-13 μm plateau seen in many objects which exhibit the narrow UIR bands. If this interpretation is correct, UIR bands can be explained in terms of small linear PAHs attached to the surface of HAC grains, without the need for large PAHs or compact PAHs (e.g. coronene, $C_{24}H_{12}$).

Latter (1991) suggested that, rather than forming in the regions around PNs and post-

AGB objects, PAHs in fact form in the circumstellar shells around carbon stars, but that they are hard to detect there due to the lack of UV photons to pump the IR transitions.

Szczepanski & Vala (1993) have found an explanation for the relative intensities of the UIR bands without needing to have the PAHs partially dehydrogenated. They claim that all the observations can be explained in terms of combinations of both neutral and ionised PAHs. If their hypothesis is true, and the diffuse interstellar bands (DIBs) can be attributed to ionised PAHs (Le Bertre 1990), then sources with strong 7.8 and 8.6 μm bands relative to the 11.3 μm band (attributed to more ionised than neutral PAHs) should also exhibit DIBs. Likewise, sources which exhibit DIBs should also show the 7.8 and 8.6 μm bands. This also contradicts the work of Allamandola, Tielens & Barker (1989) who suggested that the PAHs must be neutral.

Sylvester *et al.* (1994) observed UIR bands in the mid-infrared spectra of oxygen-rich supergiants. This was unexpected as carbon-rich molecules/dust are expected to form in carbon-rich regions and oxygen rich regions form oxygen-rich dust. However, where the C/O ratio is greater than about 0.83, sufficient oxygen could be removed from the dust forming gas in to silicates and oxides to yield an excess in the carbon and therefore allow carbon-rich molecules/dust to form. However, the M-supergiants are unlikely to have C/O$\geq$0.83, making this scenario unlikely. Alternatively, UV emission from a warm chromosphere can photo-dissociate CO molecules thereby allowing C-rich molecules or dust to form. These UV photons would also be needed to pump the IR transitions in the PAH molecules.

Joblin *et al.* (1994) discussed the expected physical state of interstellar PAHs with a view to providing laboratory data relevant to the interpretation of astronomical spectra. They argued that the PAHs emitting the UIR bands should be isolated, vibrationally hot (900K) and rotationally cold (100K). They argued that the degree of ionization of the PAHs varies depending on the local environment, however they estimate that PAHs in the diffuse ISM will be about 10% ionised, while PAHs in strongly irradiated regions (e.g. reflection nebulae, planetary nebulae, etc.) will be strongly ionised (about 90%). They also found that the nature of the UIR spectrum is affected by the physical environment from which it is emitted. The relative band intensities of the CH modes compared to the

CC modes change according to the local physical environment, and the position of the band center is sensitive to temperature. However the relative intensities of the different CH modes seem not to be affected by the physical environment. They found that there is a reasonable similarity between the UIR bands and those of neutral, partially dehydrogenated PAHs. This is a problem as recent models have suggested that the PAHs should be at least partially ionised (both positively and negatively; Omont 1986), and laboratory experiments (e.g. Szczepanski& Vala 1993; Robinson *et al* 1997) suggest that the spectra of ionised PAHs are somewhat different from those of neutral PAHs. It does, however, concur with Allamandola, Tielens & Barker (1989).

Joblin *et al.* (1995) continued the discussion of environmental effects on PAHs, this time with the emphasis on the temperature. One of the reasons that the PAH model for the UIR band carriers is popular is that the UIR band emission cannot arise from thermal emission as the grains are far too cold in most of the emitting regions, however PAHs can easily attain a temperature of about 1000K after the absorption of a single UV photon and therefore can emit the UIR bands. The mechanism by which the PAH emits the UIR bands is as follows. The PAH molecule is expected to reach high temperatures after the absorption of a UV photon. A fraction of the absorbed energy is re-emitted in the 3.3 μm band. The exact position at which this emission occurs changes during time as a function of the temperature of the molecule. The observed 3.3 μm band results from the superposition of different bands emitted at different temperatures, during the cooling of the molecule. Joblin *et al.* (1995) concluded that, in the highly irradiated regions, the carriers of the 3.3 μm UIR bands contain about 50 carbon atoms and absorb photon of about 10eV. In the lower radiation fields, smaller PAHs could survive and contribute to the 3.3 μm band.

Goebel *et al.* (1995) investigated the 11 μm spectra of carbon stars. They briefly discussed the 11.3 μm UIR band seen in planetary nebulae, and commented on the lack of this feature in the spectra of carbon stars. In general we do not expect to see the 11.3 μm feature in the spectra of single carbon stars as they do not have a strong enough UV field to excite the PAHs into emitting the UIR bands. However, Goebel *et al.* (1995) suggested that even carbon stars with a hot companion star do not exhibit this feature. As will be seen later this is no longer thought to be the case. They claim that if HACs or PAHs are present

in the atmospheres of carbon stars, they should emit a feature at about 11.9 μm, and not 11.3 μm. Only in environments where there is copious UV radiation (presumably including carbon stars with hot companions), they will emit at 11.3 μm rather than 11.9 μm. They suggested that the evolution of the feature from 11.9 to 11.3 μm reflects the gradual dehydrogenation of the PAHs. They also mention that it is not necessary for PAHs to be formed in the atmospheres of carbon stars, since they can be formed from HACs in the ISM, through destruction in shocks, grain-grain collision, desorption etc. They suggest that it is, in fact, a form of HAC that forms in the regions around carbon stars. The work of Speck *et al.* (1997a,b) found no features at 11.9 μm in the spectra of carbon stars. However they did find possible evidence of the 11.3 μm UIR band in two carbon stars with hot companions. This implies that either the Goebel *et al.* (1995) hypothesis is incorrect and that the UIR bands are not seen in most carbon star spectra due to the lack of UV field, or that the UIR bands are only present in the two sources with hot companions.

Joblin *et al.* (1996a) investigated the variations in the relative intensities of the the 3.3 and 3.4 μm UIR bands in the spectrum of the reflection nebulae NGC 1333. These variations were found to correlate with variations in the UV field intensity and were attributed to photodissociation of aliphatic sub-groups attached to PAH molecules. This interpretation is supported by the work of Dischler *et al.* (1983a & b). Dischler *et al.* found that when HAC films were annealed at higher and higher temperatures a feature at 3.4 μm diminished and a feature at 3.3 μm grows. The variations in the relative strengths of the 3.3 and 3.4 μm bands in NGC 1333 could be interpreted as changes in bonding from sp^2 to sp^3 type bonds depending on the temperature/UV field in that precise region. Following their success in modelling the variations in the relative intensities of the 3.3 and 3.4 μm UIR bands, Joblin *et al.* (1996b) went on to a similar investigation into the variations in the relative intensities of the 8.6 and 11.3 μm bands in the spectrum of NGC 1333. They hypothesised that the variations in the relative intensities of the 8.6 & 11.3 μm bands could be linked to variations in charge. According to Omont (1986) it is expected that such a region will have varying combinations of neutral PAHs and positive and negative PAH ions. In their interpretation, Joblin *et al.* (1996b) suggest that the PAHs are mostly ionised, producing a high [8.6]/[11.3] ratio. Further from the star the PAHs are mostly neutral and therefore the [8.6]/[11.3] ratio is lower. This fits with observation. The relative ionization of PAHs within different regions of the ISM are expected to vary from region

to region, and therefore we expect the [8.6]/[11.3] ratio to show variations with the ISM.

Justtanont *et al.* (1996) investigated the spectra of carbon-rich post-AGB objects. Three of their sources were seen to exhibit new "UIR" features at 7.9, 8.2, 10.6, 11.5 and 12.2 μm. They found that the spectra of these sources could be matched using chrysene ($C_{18}H_{12}$), together with whatever was responsible for the "standard" UIR bands (7.7, 8.6 and 11.3 μm). No other PAH molecule provides a good fit to several UIR features without also producing features that are not seen. They suggest that chrysene is a good candidate for the carrier of the new feature as its predicted disappearance with the evolution of an object towards a the planetary nebula phase agree with observations of UIR bands in various objects.

Beintema *et al.* (1996) looked at the ISO SWS observations of 3 sources which exhibit UIR bands. Rather than trying to attribute these bands to specific PAHs they just stated that the carriers are probably PAHs with about 50 carbon atoms and have attributed the various bands to various combinations of C-H modes, C-C modes etc. Their findings are summarised in Table 7.1. They also observed a plateau in their SWS spectra at 5.5-10 μm attributed to C-C modes in larger PAH cluster ($\simeq$ 300-400 C atoms), and at 11-13 μm due to a blend of various weak out-of-plane deformation modes possibly also connected to the large PAH clusters.

Following on from Beintema *et al.* (1996), Molster *et al.* (1996) used the same observations to investigate the shape and strength of the UIR bands. They compared the observations of the PAH emissions in objects with different physical conditions to help identify the nature of the emission features. They have studied three objects, two planetary nebulae (PNs) and one proto-planetary nebula (PPN) and compared the spectra. They found that the emission bands in the PPN show significant sub-structure and are narrower than those in the two PNs. There is no evidence for a plateau underlying the 7.7-8.6 μm or 11.3 μm bands in the PPN, whereas these plateaus are prominent in the PNs. The 7.7 μm feature is resolved into two components (7.6 & 7.8 μm) in all three sources, but the PPN also seems to have a third component at 8.07 μm. The 11.3 μm band increases in strength dramatically with respect to the 6.2 and 7.7 μm bands in going from the PPN to the PNs. In fact, in one of the PNs the 11.3 μm feature dwarfs the rest of the spectrum. The [7.7]/[11.3] ratio is particularly sensitive to the charge state of the emitting PAHs, and not very sensitive to the degree of excitation. They conclude from their observations

Table 7.1: Summary of UIR bands found in ISO spectra from Beintema *et al.* (1996)

Band position μm	**Relative strength**	**Attribution**
3.248	weak	large less-excited PAHs
3.294	very strong	aromatic C-H stretch
3.342	weak	small more-excited PAHs
3.40		asymmetric stretch in methyl groups attached to PAHs
3.43		"hot-band" C-H stretch
3.43		2-1 overtone (hot-band) of C-H stretch
3.53	weak	C-H stretch in aldehydic groups attached to PAHs
3.55		"hot-band" C-H stretch
3.59	weak	3-2 overtone (hot-band) of C-H stretch
3.64	weak	C-H stretch in aldehydic groups attached to PAHs
5.23	weak	combination band of the out of plane C-H deformation modes
5.65	weak	combination band of the out of plane C-H deformation modes
6.0	weak	may be connected to the 3.248 μm feature
6.2	very strong	aromatic C-C stretching mode
6.9		due to C-C mode OR deformation of CH_3 group
7.7	very strong	aromatic C-C stretching mode
8.6	very strong	aromatic C-H stretching mode
11.0		may be connected to the 3.248 and 6.0 μm features
11.3	very strong	aromatic C-H out-of-plane bending mode
12.1	weak	2 adjacent H-atoms on aromatic ring
12.7		3 adjacent H-atoms on aromatic ring

that the population of PAHs in the PPN seems highly excited, ionized and devoid of large molecules, whereas the PAHs in the two PNs show evidence for the presence of large (300-400 carbon atoms) PAHs and a significant abundance of neutral PAHs. They also state that small PAHs are probably not the carriers of the 2175Å feature in the interstellar extinction curve, but are likely contributors to the far-UV rise. The only problem with this hypothesis is that one expects PNs to have more ionizing environments than PPNs.

Robinson *et al.* (1997) have used laboratory data to characterize the charge state of the PAHs responsible for the UIR bands. There have been objections to the PAH model on the grounds that neutral PAHs have well-known UV absorption bands and yet PAHs are not detected in UV spectra of the source which exhibit the UIR bands. However, Robinson *et al.* found that for ionised PAHs these UV absorption bands disappear. The vibrational modes of the PAHs are much less affected by ionization, and therefore PAHs would still be detected in the IR but not in the UV. Robinson *et al.* have also found that the PAH ions require energies of $\geq$ 7.75 eV in order to pump the UIR band emission. In order for the UIR bands to be emitted, the PAHs must satisfy the condition that UIR emission be favoured over photodissociation upon absorption of a UV photon. This could set important size and structure limitations on which PAH molecules and ions could play a role in the ISM.

A summary of the attributions of the various UIR bands to various vibrational modes is given in Table 7.2. In general, most of the attributions from the works discussed above are consistent. There are, however, some notable exceptions. Firstly Goebel *et al.* (1995) suggest that if PAHs are to be found in the circumstellar regions around carbon stars, we should see another emission band at 11.9 μm in the spectra of those carbon stars where there is no source of UV radiation. This is not mentioned by any other work and has not yet been observed. Robinson *et al.* (1997) have "proved" that all the PAHs must be positively ionised, which disagrees with other work (e.g. Joblin *et al.* 1995, Szczepanski& Vala 1993, Allamandola, Tielens & Barker 1989). The various weak features found by ISO (Beintema *et al.* 1996; Molster *et al.* 1996) due to the higher resolution of the spectra are not included in Table 7.2.

Table 7.2: Summary of attributions for UIR bands compiled from the literature

Band position μm	**Attributed To**
3.3	Aromatic C-H group of PAH with $\approx$ 50 Carbon atoms
	smaller molecules may contribute in lower intensity UV fields
3.4	Methyl group on aromatic ring of PAH with $\approx$ 50 Carbon atoms
	Only survives at low temperatures
5.5-10.0	Large PAH clusters with $\approx$ 300-400 Carbon atoms
6.2	PAH with $\approx$ 50 Carbon atoms - C-C stretching
	possibly part of the 7.7 μm feature
7.7	ionised PAH with $\approx$ 50 Carbon atoms - C-C stretching mode
8.6	ionised PAH with $\approx$ 50 Carbon atoms - C-H stretching mode
11.3	Aromatic C-H group of PAH with $\approx$ 50 Carbon atoms and
	isolated hydrogen atoms (dehydrogenated PAHs)
11.3-13.0	Large neutral PAH clusters with $\approx$ 300-400 Carbon atoms *or* HACs
11.9	PAHs in cool stars (no UV to pump UIR bands)

7.1.2 Meteoritic Evidence

Wdowiak *et al.* (1988) studied the nature of the carbonaceous acid residue from the Orgueil meteorite and found that it contained an extensive component of PAHs. Their work implies that the aromatic species they studied are of a homogeneous nature. Heating in a vacuum to release hydrogen/deuterium produced interesting results. It was found that heating to temperature >500°C released a large amount of deuterium implying that the residue remaining after heating to 500°C has a high deuterium abundance, and it is reasonable to assume that this material may be of interstellar origin. The spectrum of the residue exhibits the 11.3 μm feature associated with the C-H out-of-plane bend, but not the 3.3 μm band associated with the C-H stretch. Their explanation for this invokes large PAH clusters. They claim that the 3.3 μm feature is inherently weaker than the 11.3 μm feature in large PAH clusters, and the PAHs in the residue are formed of aromatic molecules having a large number of aromatic rings (i.e. $\sim$40 to $\sim$90 rings). Given that Duley & Jones (1990) explained the UIR bands in terms of small ($\sim$10 C atoms) PAHs, there is a discrepancy between the size of the PAHs in astronomical environments and those found in meteorites. Those objects that have been hypothesised as having large PAHs in their vicinities do exhibit the 3.3 μm band. If Wdowiak *et al.* (1988) are correct in their arguments this implies that all the PAHs responsible for the main UIR bands are small.

7.2 UIR bands in Carbon Star Spectra

7.2.1 Why Look at Carbon Stars?

As an aging star evolves from a carbon-rich AGB star along the transition branch towards a planetary nebula, the circumstellar dust also evolves. It has been suggested (Jura 1987) that PAHs initially form in the outflow of carbon stars where they are instrumental in the formation of carbon dust. The UIR bands identified with PAHs are commonly seen in the spectra of planetary nebulae and transition branch objects, but rarely in carbon stars. This is because the PAHs need UV radiation to pump the UIR bands. Most carbon stars do not have strong enough UV fields to achieve this. This does not mean that the PAHs are not present, just that they may be invisible to our searches. However, several carbon stars have hot companions which could provide the UV radiation necessary to power the UIR bands. It is these objects that we wish to investigate.

7.2.2 Can PAHs form in C-rich AGB star environments?

Jura (1987) discussed cool red giant stars in the context of a source of interstellar matter. His argument was that PAHs are definitely ejected from carbon-rich PNs, but whether or not they are formed in and ejected from carbon-rich red giants was not certain. There was no direct evidence that these outflows from red giants do in fact contain PAHs. Since then various models have been published for the formation of PAHs in carbon star outflows.

Both Keller (1987) and Gail and Sedlmayr (1987) used classical nucleation theory to model the formation of PAHs. Keller (1987) found that PAHs are unlikely to constitute a significant fraction of the carbon in the circumstellar environment, but that they can be produced. Gail & Sedlmayr (1987) found that PAHs can be produced in carbon-rich stellar winds and that production peaks at 800K.

Frenklach & Feigelson (1989) investigated PAH production in carbon-rich circumstellar envelopes using a kinetic approach rather than relying on classical nucleation theory. They found that PAHs can form in an 1100-900K temperature window, but that the amounts of PAHs formed are very sensitive to the exact nature of the environment in which they are forming. They suggested that most PAHs may come from a few stars with the right conditions in their inner envelopes. Therefore the failure to detect evidence of PAH production on some stars does not rule out PAH production in other stars.

Cherchneff *et al.* (1991) also modelled PAH production in carbon-rich circumstellar envelopes using a kinetic scheme. They claim that the environments used in Frenklach & Feigelson's model are not characteristic of carbon stars. Cherchneff *et al.* (1991) invoke an Inverse Greenhouse Effect (IGE) to create the right environment for PAH formation. The IGE is an important effect because it affects the temperature so dramatically. Other stellar parameters must also be taken into account and not casually adjusted to alter the PAH production. Broadly their findings agreed with those of Frenklach & Feigelson, although they suggested that their (Cherchneff *et al.* 1991) model is missing certain mechanisms which may favour PAH growth.

Cadwell *et al.* (1994) embarked upon an attempt to identify the mechanisms by which carbon grains are formed, and therefore to discover the types of carbonaceous grains forming in various circumstellar environments. Again this study dismisses the classical nucleation theory as incapable of incorporating the necessary complexity. Both Frenklach & Feigelson (1989) and Cherchneff *et al.* (1991) assumed homogeneous nucleation in their models. Cadwell *et al.* (1994) discussed induced nucleation, where the grains are formed by deposition onto a "seed". Their model suggested that PAHs could form a mantle around a seed grain. They then suggested two scenarios for the production of UIR band carriers. Firstly, the aromatic molecules attached to the grains that are ejected into the ISM may be desorbed by various mechanisms, and then the free PAHs give rise to the UIR bands; second, the aromatics near the surface of the depositional grains give rise to the UIR bands without desorption. This scenario fits the hypothesis of Duley & Williams (1981). It is clear that observational evidence of PAHs around carbon-rich AGB stars would aid hypotheses for PAH formation. With this in mind, the 10μm spectra of a number of carbon stars that have external sources of UV photons, that could stimulate UIR-band emission, have been investigated in detail.

7.2.3 Target Selection

Buss *et al.* (1991) examined the IRAS spectra of carbon stars in binaries with hot star companions, with a view to observing UIR bands. Single carbon stars do not have sufficient UV output to excite PAHs and produce UIR bands, therefore, even if the PAHs are there we will not see them. However, carbon stars with hot companions have a source of UV radiation and therefore should show evidence of PAHs if they do indeed form in the outflows of carbon stars. All the stars chosen by Buss *et al.* (1991) have A star companions. One star in their sample, TU Tau, overlaps with the present sample. One star that Buss *et al.* (1991) considered but did not include was UV Aur. It was dismissed as it was classed as a symbiotic star. However, we believe that this classification is incorrect and that UV Aur is, in fact, a binary consisting of a carbon stars with a B star companion. It is therefore included in the present sample.

The third star in our sample is CS 776, a binary with an A star companion. This source was observed by Le Bertre (1990), who detected DIBs in the spectrum of CS 776. It has

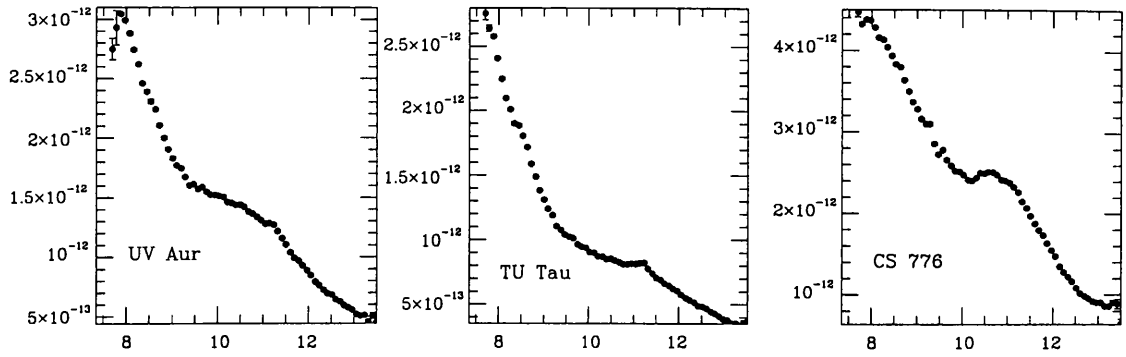

Figure 7.1: Flux-calibrated spectra of candidate UIR-band carbon stars

been suggested (Léger & d'Hendecourt 1985; van der Zwet & Allamandola 1985) that the likely carriers of the DIBs are PAHs. If the DIBs are in fact due to PAHs forming around the carbon star, then it is not unreasonable to assume that there may also be UIR bands evident in the infrared spectrum of CS 776. The flux-calibrated spectra of all three stars can be seen in Fig. 7.1

7.2.4 The Investigation

The three stars in our sample have been investigated in a variety of ways. Firstly, all three of the spectra exhibit a broad silicon carbide feature at about 11.3 μm. In order to discover whether there is also a narrow 11.3 μm feature that can be associated with the UIR band, the profile of the SiC feature must be well characterised. To this end, each of the three spectra were compared to the spectra of the 23 other carbon stars with SiC emission features discussed in Chapter 6 as well as to each other. These comparisons showed that both TU Tau and UV Aur exhibit an additional narrow feature at about 11.3 μm over and above the SiC feature. An example of this is shown in Fig. 7.2, which shows the normalised spectra of TU Tau, UV Aur and CS 776 compared to the normalised spectrum of a typical carbon star. TU Tau may also exhibit a feature at 8.6 μm. As can be seen in Fig. 7.2, CS 776 shows no extra features and therefore the 11.3 μm feature in this spectrum is assumed to be due to SiC alone.

During the fitting of the SiC features (Speck *et al* 1997; Chapter 6) both TU Tau and UV Aur were fitted using spectra which were edited, so that the suspected UIR band did not affect the fitting of the SiC feature. However this had little impact on the results of the χ^2-fitting routine.

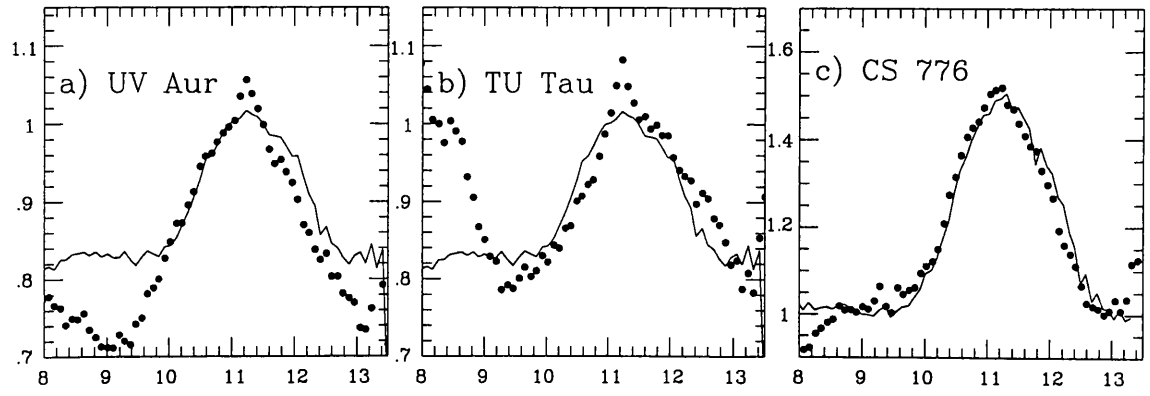

Figure 7.2: Comparison of candidate UIR-band carbon stars (dots) with the spectrum of a typical carbon star (solid line)

The spectrum of TU Tau in Fig. 7.2 shows a clear feature at 11.2 μm over and above that spectrum of V414 Per, together with a steep rise in the continuum shortward of 9 μm and a possible 8.6 μm feature. The spectrum of UV Aur in Fig. 7.2 also shows a clear feature at 11.2 μm. There is only a slight rise in the continuum shortward of 9 μm and no sign of a feature at 8.6 μm.

We then proceeded to fit the 11.3 μm UIR band in these spectra using the chi-squared fitting program described in Chapter 6 which was equipped with the ability to fit a narrow UIR feature at 11.25 μm. The first attempt at fitting was performed using the flux-calibrated spectrum over the entire wavelength range, 7.5-13.5 μm, using a blackbody and an SiC emission feature, as described by Chapter 6, together with the 11.25 μm UIR band. This fitting resulted in no solution for either TU Tau or UV Aur. We then proceeded to attempt the fitting again, this time restricting the fit to the 9.5 to 13.5 μm region. The reason for this restriction of the wavelength range is to minimize the effects of spurious features between 7.5 and 9.5 μm with which the fitting program is not equipped to deal (see Chapter 6). This proved more successful for TU Tau but was still unable to find fits for UV Aur. The results of both these attempts at fits are presented in Table 7.3. Finally, following the success in Chapter 6 in fitting the SiC features using self-absorbed silicon carbide, the fitting of the UIR band was attempted using a blackbody, plus self-absorbed SiC emission and the UIR band. This produced by far the best results for both sources, which are plotted in Fig. 7.3 and Fig. 7.4. The results can be seen in Table 7.3. We also attempted to fit TU Tau using a 8.6 μm UIR feature, and although this was successful for

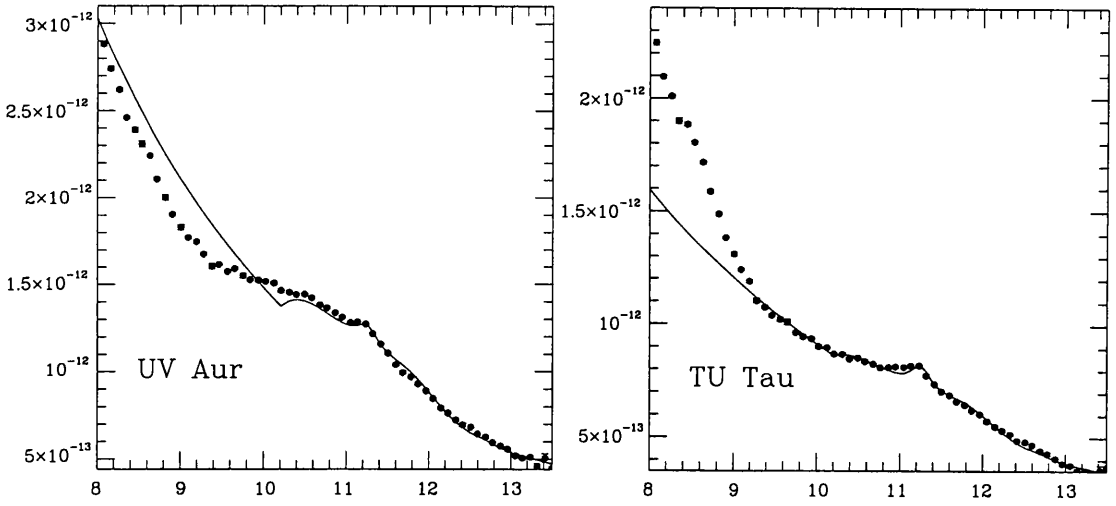

Figure 7.3: UIR band χ^2-fits to TU Tau and UV Aur. The errors used to calculate the reduced χ^2 are set to 3% of the flux if the 1σ error on the flux is less than this value. Thus the 1σ error bars shown here are not necessarily the errorbars used by the fitting program

the SiC self-absorption case, the fit was not very satisfactory

7.2.5 Discussion

As can be seen from the fits to UV Aur and TU Tau in Fig.7.3, we have found convincing evidence for the presence of the 11.3 μm UIR band in the spectra of two carbon stars with A- or B-type companion sources of UV radiation. The lack of a feature in the spectrum of CS 776 is surprising, however the detection of DIBs in the spectrum of its companion star may be the key. It is also surprising that we cannot better fit a 8.6 μm feature to the two spectra which exhibit the 11.3 μm UIR band as these are usually expected together. There is a possible 8.6 μm feature in the spectrum of TU Tau, which has been fitted, but the quality of the fit is poor. This problem may be model based. There is no sign of such a feature, however, in the spectrum of UV Aur. This could be a contrast problem, or it could be due to the nature of the PAHs responsible for each band. In the summary of ascribed origins of the various bands (Section 7.1.1) the 8.6 and 11.3 μm bands are both attributed aromatic C-H bending groups. However it has been suggested that the 8.6 μm band is due to ionised PAHs, whereas the 11.3 μm band is due to neutral PAHs (Szczepanski & Vala 1993). If the 8.6 μm feature is present in the spectrum of TU Tau, this implies that our three carbon stars with hot companions are all different states of ionization, probably due to differences in the companion star.

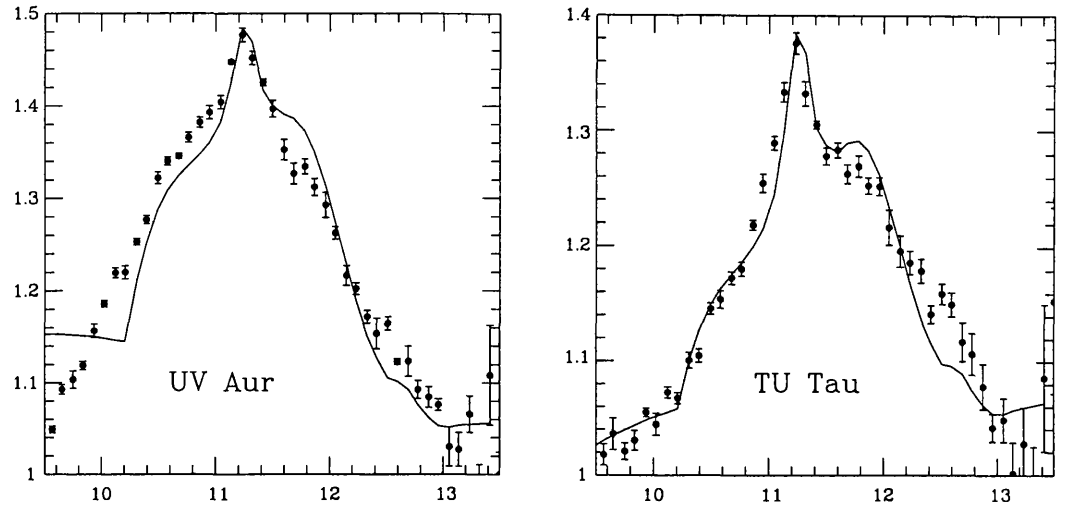

Figure 7.4: UIR band χ^2-fits to normalized 9.5-13.5μm spectra of TU Tau and UV Aur. The errors used to calculate the reduced χ^2 are set to 3% of the flux if the 1σ error on the flux is less than this value. Thus the 1σ error bars shown here are not necessarily the errorbars used by the fitting program

Table 7.3: Results of the 9.5-13.5μm χ^2-fitting the 11.3μm band in the flux-calibrated spectra of TU Tau and UV Aur

Source	$T^{\dagger}_{colour}$	SiC type	T_{BB}(K)	$T_{SiC}(K)$	τ_{SiC}	χ^2_R *
UV Aur	1500	—	—	—		—
TU Tau	1100	β-SiC$^{\diamond}$	1100	190	—	1.257
UV Aur‡	1500	β-SiC	1120	410	0.238	0.691
TU Tau‡	1100	β-SiC	1500	750	0.222	1.345

† The colour temperature is taken from Chapter 6

* The errors used to calculate the reduced χ^2 are set to 3% of the flux if the 1σ error on the flux is less than this value. The errors shown in Fig 7.3&uir4 are 1σ. In all these spectra, the majority of points have errors that are <3% of the flux, the exceptions being for those points at the edges of each spectra and in the ozone region (9.4–9.9μm). Thus the 1σ error bars shown in the fits are not necessarily the errorbars used by the fitting program. ‡ These fits use self-absorbed SiC

$\diamond$ 'β-SiC' data is from Borghesi *et al.* (1985)

Table 7.4: Comparing the binary carbon stars

Source	C-star Sp.type	Hot-Star Sp.type	Simbad description of Primary
TU Tau	C5,4	A2 III	Carbon Star
UV Aur	C6,4	B	Semi-regular pulsating Star
CS 776	C8,1e	A3V-III	Carbon Star

At this point it seems useful to investigate the nature of our three sample stars and their companions. The details are listed in table 7.4.

As stated above, one interpretation of the differences in the spectra may be due to differences in the amount ionization within the circumstellar regions. It may be that UV Aur has the least ionized PAHs and therefore only shows the 11.3 μm bands, while TU Tau is more ionised, which is why it exhibits a weak 8.6 μm band. CS 776 exhibits no UIR bands but does show DIBs. If DIBs are due to very ionised PAHs, then the region around CS 776 may be so ionised that we do not see any UIR bands. Alternatively, the PAH species responsible for the DIBs may be different to those responsible for the UIR bands and something in the physical conditions has caused these to form around CS 776, rather than the UIR band-PAHs. As can be seen above, this sequence of PAH ionization cannot be explained by the spectral types of the hot stars, but may by explained by the distances between the carbon stars and their hot companions. Another possible explanation is suggested by the work of Wdowiak & Flickinger (1988) discussed earlier. They suggest that the reason that the 3.3 μm band is not seen in their meteoritic PAHs is because the PAH molecules they are looking at are very large, which suppresses the 3.3 μm UIR band but enhances the 11.3 μm. If this argument can also be applied to the 8.6 μm feature, the difference between these spectra may be explicable in terms of the size of the species responsible for the UIR bands. However, the non-observance of UIR bands in the spectrum of CS 776 may not be due to UIR bands and DIBS having different carriers at all. Barnbaum & Balm (1995) re-investigated the observations of DIBs in circumstellar shells and found that the strength of the DIBs was correlated with Galactic latitude rather than with the amount of circumstellar material. This implies that the DIBs attributed to the circumstellar shell of CS 776 are actually interstellar and highlights the difficulty in

distinguishing circumstellar from interstellar material through observations.

7.3 An Evolutionary Sequence

As discussed already, it is believed that carbon-rich AGB stars evolve through the transition branch to the planetary nebula phase. One expects the dust to evolve too. It is, therefore, expedient to compare the observations of the UIR bands for carbon stars (C-stars), post-AGB objects and planetary nebulae (PNs).

The nature of PAHs in the regions around C-stars is not well known. However, as discussed above, the only feature definitely recognised in two of our spectra is the 11.3 μm band, attributed to C-H bending modes of mostly neutral PAHs. This is quite weak and there is no sign of the 11-13 μm plateau, although since this feature sits on top of a SiC feature in each of the C-star spectra, it is questionable whether the plateau would be detectable.

The post-AGB objects exhibit all the usual UIR bands (Buss *et al.* 1990). The narrow bands are narrower than those of PNs and show some substructure. Some show the 11-13 μm plateau, and all show the 11.3 μm narrow band, although neither of these features is as strong as in the PNs. The general consensus is that the UIR bands in the post-AGB objects are attributable to small ($\simeq$ 50 carbon atoms), mostly ionised PAHs. There are believed to be very few "large" PAHs around these objects. However, an alternative explanation for the spectra of post-AGB objects is that there are more small PAHs, which disappear when the star gets hotter.

On the other hand, PNs have strong 11-13 μm plateau features and even stronger 11.3 μm features. The spectrum is believed to be contributed to by neutral and ionised small ($\simeq$ 50 carbon atoms) and large ($\simeq$ 300-400 carbon atoms) PAHs.

Assuming that the undetected plateau really is not present in the spectra of C-Stars (rather than being masked by the SiC feature), we can identify an evolutionary trend in the PAHs. PAH molecules found in the C-Stars are predominantly small ($\simeq$ 50 carbon atoms); the PAHs in post-AGB objects are mostly small with a few larger ones (($\simeq$ 300-400 carbon atoms) and many are ionised; the PAHs in the PNs are both large and small, and both neutral and ionised. The only definite trend is that the PAHs tend to grow in

size, as the stars evolve. There may also be a trend in the amount of ionization, but this is more difficult to assess.

A second interpretation for the changes in UIR spectrum with evolution comes from Wdowiak *et al.* (1988). Their interpretation of the spectrum of large meteoritic PAHs was that large PAHs do not exhibit the 3.3 μm UIR bands. Since all the objects along the evolutionary path exhibit the 3.3 μm feature, this implies that the PAHs in the regions around planetary nebulae and post-AGB objects are in fact all small. This may also be supported by the work of Duley & Jones (1990), who suggest that all the UIR features, narrow and broad, can be explained in terms of small PAHs attached to HAC grains. In this case the broad features are attributed to various side-groups substituted onto the PAH molecules. The evolutionary processing of the dust may be in the form of substituting side-groups on the linear aromatic molecules.

Obviously these two solutions to the evolutionary path of the UIR band carriers are mutually exclusive, the first explanation has small grains growing into larger ones, and the second has large grains sputtering out smaller ones.

Higher resolution spectra of carbon-rich AGB stars with hot star companions are needed to get a better picture of the UIR band status of these stars, and of their PAH contributions to the interstellar medium. The situation may be able to be clarified using ISO-SWS spectra of such carbon-rich AGB stars.

7.4 Diamonds in the sky

As discussed earlier in this chapter and in chapter 6, various carbonaceous solids are expected to form around carbon-rich AGB stars. So far, the discussion has centred on silicon carbide, PAHs and various forms of hydrogenated amorphous carbon. Another form of carbon that could be present around these stars is diamond.

Diamonds in the interstellar medium were were first proposed by Saslaw & Gaustad (1969), who argued that, although graphite is the thermodynamically stable form of carbon in dust forming regions and in interstellar space, it was possible that diamond could form as a metastable product(see section 3.2.3). Following this theoretical work, interest in

interstellar diamonds lay dormant until, in 1987, they were found, in meteorites, rather than in interstellar spectra (Lewis *et al.*, 1987).

7.4.1 Diamonds in meteorites

Interstellar diamonds have been found in various carbonaceous chondrites. Their extra-solar origin has been established in various ways. Firstly, objects incorporated into meteorites must predate the meteorite, and chondrites date from the formation of the solar system, therefore the presence of diamonds within chondrites indicates that the diamonds predate the solar system. The presolar diamonds were actually discovered whilst attempting to find the source of an isotopically anomalous noble gas component in carbonaceous chondrites. There was isotopic evidence that Xenon was enriched by up to a factor of 2 in both the lightest and the heaviest isotopes compared to the dominant xenon component in meteorites and xenon in the Earth's atmosphere. This anomalous component is known as the Xe-HL component. This Xe-HL component is only found in diamond inclusions and is not present in any other presolar grain. Furthermore, it is found in *all* presolar diamond inclusions that have been studied. The two parts to the Xe-HL component (the heavy and the light isotopes) have proved to be completely inseparable in the laboratory. It is clear that the anomalous xenon is an indicator that the meteoritic diamond is extra-solar in origin. Physical details of these meteoritic presolar diamonds can be found in section 3.2.3.

7.4.2 Diamonds in the interstellar medium

When meteoritic diamonds were discovered, there had been no observational evidence for diamonds in interstellar space. Then, in 1992, Allamandola *et al.* (1992) found an absorption feature in the spectra of protostars embedded in dense molecular clouds at 3.47 μm (2880 cm^{-1}), which they attributed to sp^3 bonded C-H, i.e. hydrogenated diamond-like particles. Thus, we have evidence of diamonds in space. Their observations suggested that the diamond-like grains seemed to be ubiquitous in dense clouds, while methyl ($-CH_3$) and methylene ($-CH_2$) rich material dominated the diffuse ISM. The diamond signature was only found in dense molecular clouds and not in the diffuse ISM, which was surprising because thorough mixing is expected to occur between the dense and diffuse media. Allamandola *et al.* (1992) suggested that the absence of $-CH_2$ and $-CH_3$ bands, together with appearance of the sp^3 bonded –CH not found in the diffuse ISM, implies that C-rich

materials in the diffuse medium do not become incorporated into, or do not survive incorporation into, dense molecular clouds. Neither destruction by shocks (which are weak in dense clouds) or UV photolysis (mild as a result of dust extinction), or H atom attack (which would make $-CH_2$ and $-CH_3$ groups rather than destroy them) can explain the apparent lack of the carbon-rich diffuse cloud components in dense clouds.

It is my proposal that we need to turn the argument around. I would argue that, without any explanation of how it got there, the sp^3 bonded –CH is stable in the dense molecular clouds where it is protected from the severe environment outside. Only when it leaves the dense cloud is it converted into $-CH_2$ and $-CH_3$ by the harsher environment. If this is the case, we need to seek out a very effective mechanism by which $-CH_2$ and $-CH_3$ groups would be converted into sp^3 bonded –CH inside the dense molecular clouds. However, if this paradigm is correct, the diamonds are formed in dense molecular clouds and are not of interest in a discussion of dust formation around carbon-rich AGB stars. Therefore, let us consider the meteoritic evidence for the origins of interstellar diamonds further.

7.4.3 Sources of meteoritic diamonds

The isotopic complexity of the noble gas component in meteoritic diamonds indicates that it comes from several sources. Other isotopically anomalous elements have also been found, including barium and strontium, which are slightly enriched in *r-process* isotopes. Nitrogen is also anomalous. The most studied aspect of meteoritic diamond isotope anomalies is the noble gas component. The noble gases are released by stepped heating of diamond residues extracted from meteorites. This has revealed three components, each including all five noble gases: 1) the roughly solar system component released between 200 and 900^oC; 2) the HL component (anomalies in all noble gases) released at 1100–1600°C; and 3) a mixture of the first two released at even higher temperatures. Whether the carrier of the first and second components are distinct phases has been the subject of some discussion. It seems that the carrier of the solar system component is a more disordered carbon, with both sp^3 and sp^2 bond C–H, known as a-C:H (amorphous hydrogenated carbon). There are indications that this phase is lost through metamorphism, since the diamonds in the less primitive meteorites do not have this phase. It has been suggested that the carrier of the solar system component is merely the hydrogenated surface of the diamonds, which is supported by EELS (electron energy loss spectroscopy; Bernatowicz *et al.* 1990) data.

However, the isotopic data implies that it formed at a different time or place to the more anomalous diamond. it is possible that in the diffuse interstellar medium, the diamonds acquire a coating of the a-C:H through hydrogenation of their surfaces, rendering the diamonds invisible by changing their spectral properties to those of methyl or methylene groups. Somehow this coating must disappear when the grains enter the dense molecular clouds in order to fit observations. Therefore a mechanism for the loss of the $-CH_2$ and $-CH_3$ coating needs to be established.

The origin of the meteoritic diamonds is still an enigma. The Xe-HL component must have been formed near a supernova, since the enrichment of the lightest and heaviest isotopes of xenon would proceed through the *p-process* and *r-process* respectively, both of which are associated with supernovae. This has led to various hypotheses for the formation of diamonds in space.

7.4.4 Theoretical models of diamond formation in astrophysical environments

Firstly, there is the chemical vapour deposition (CVD) method proposed by Saslaw & Gaustad (1969) and others (e.g. Anders & Zinner 1993 and references therein; Colangeli *et al.* 1994). This is favoured by the size distribution of meteoritic diamonds which is log-normal and is indicative of grain growth rather than fragmentation of larger grains, which tends to give a power law distribution. For this mechanism to be practicable, the diamonds must form in an environment with a carbon-to-oxygen ratio greater than unity. However, the isotope studies imply that a supernova is involved in the process. Carbon stars are not massive enough to become Type II supernovae and the supernova precursors are carbon poor. A possible mechanism, expounded by various authors (e.g. Lewis *et al.* 1987), is that diamond grains form and grow around C-rich AGB stars and then receive the noble gases by implantation in the vicinity of a supernova. I believe this mechanism is somewhat implausible because this scenario would imply that some diamonds would be formed around C-rich AGB stars and not necessarily be exposed to supernovae noble gases. These grains should also have been incorporated into the early solar system, a result which is not substantiated by the isotopic evidence.

Another suggestion for the formation of diamond is the collision of graphitic grains in

supernova shocks (Tielens *et al.* 1987). As the efficiency of this process is estimated to be only ~5%, the diamonds should be accompanied by a twenty-fold excess of unconverted graphitic carbon with the same isotopic composition and the same noble gas components. However, there is no evidence of such unconverted graphitic carbon in meteorites. The lack of graphitic carbon cannot be blamed on preferential destruction in the early solar system, because deuterium-rich, and therefore interstellar, organic carbon survived in the same meteorites, despite greater fragility. Even if the graphitic carbon was converted to organic carbon through reaction with hydrogen in the ISM, this would also produce an unseen twenty-fold increase in the amount of organic carbon. Furthermore, work by Daulton *et al.* (1996) has given persuasive evidence for a low pressure mechanism based on high-resolution TEM studies. Their nanostructural comparison of meteoritic and synthetic diamond crystallites strongly favours a CVD-like process as opposed to one involving high pressure, shock induced metamorphism of pre-existing carbonaceous material.

Jørgensen (1988) tried to solve this problem by invoking a binary carbon star system. Matter flows to the more massive star after it becomes a white dwarf, permitting it to explode as a Type I supernova. Xe-HL ions in the high speed ejecta overtake the diamond dust shell produced during the red giant phase and implant themselves in the diamonds. Clayton (1989), on the other hand, proposed that Xe-HL is made in Type II supernova by neutrino-produced neutrons in the helium shell, and diamonds condense from the expanding shell about a year after the explosion, trapping the ambient Xe-HL. However, this theory only accounts for the heavy xenon component. The heavy and light xenon components have been inseparable in the laboratory, which led Manuel *et al.* (1972) to argue that the *p*- and *r-process* nuclei must have been mixed in the gas phase before Xe-HL was incorporated into the diamonds. There have been several major objections to the theories of both Jørgensen (1988) and Clayton (1989; e.g. Lewis *et al.* 1989), which are beyond the scope of the present work, but which are taken as negating these mechanisms for the formation of meteoritic diamonds.

Nuth & Allen (1992) invoked a supernova for the Xe-HL, but suggested that the diamonds were made from pre-existing carbonaceous dust rather than supernova or red-giant material. They proposed that small ($\leq$100Å) hydrocarbon grains in the vicinity of a supernova are "annealed" to diamond by absorption of several far ultraviolet photons,

lose all their pre-existing gases and then trap heavy ions and neutral atoms from the supernova ejecta. However, this *quantum heating* may be a problem: such "annealing" of carbonaceous grains requires temperatures of over 1000K. Since the energy of the photon is distributed over the entire grain, such temperatures are only achievable by grains of $\leq$ 90 atoms (Anders & Zinner 1993). It is not clear whether this mechanism can yield diamonds larger than 90 atoms, which comprises the bulk of the size distribution of the diamonds in meteorites.

Another proposed mechanism for diamond formation uses photolysis of hydrocarbons (Buerki & Leutwyler 1991). Ethene (C_2H_4) and mixtures of ethene, molecular hydrogen (H_2) and silane (SiH_4) have been decomposed using a laser to obtain spherules of cubic and hexagonal diamonds along with PAHs, organic polymers, graphite and amorphous carbon. The diamond spherules formed had a mean size ranging from 63±24 to 1200±240Å. However, it is not yet known whether this process would work under astrophysically relevant conditions, i.e. lower photon fluxes, lower pressures and higher H/C ratios. If it was a viable formation mechanism, then the range of possible diamond formation sites would be greatly expanded.

At present it seems that the CVD method for producing diamonds is most favoured (Saslaw & Gaustad 1969; Wright 1992; Lewis *et al.* 1989; Daulton *et al.* 1996), although detailed mechanisms by which the diamonds obtain their isotopically anomalous noble gases are yet to be understood. This suggests that diamond production around C-rich AGB stars is not unfeasible, and is possibly expected.

7.4.5 Spectra of meteoritic diamonds

There have been various attempts to get representative spectra from meteoritic diamonds from several different meteorites (Murchison, Allende, Orgeuil; Lewis *et al.* 1989; Koike *et al.* 1995b; Mutschke *et al.* 1995; Hill *et al.* 1997; Andersen *et al.* 1998). A summary of the features seen in these spectra can be seen in Table 7.5. All of these spectra seem to be entirely different from one another. Only one of them shows the 3.47 μm (2880 cm^{-1}) band seen in the spectra of dense molecular clouds (Hill *et al.* 1997). In fact Mutschke *et al.* (1995) have discredited many of these spectra, claiming that many of the features are artifacts of the extractions and spectroscopic techniques.

The most recently published meteoritic diamond spectrum can be seen in Fig. 7.5, which shows the entire spectrum from 2.5 to 25μm, and Fig. 7.6 which show the 7.5–13.5μm region of the spectrum, relevant to our observations. This spectrum comes from Andersen *et al.* (1998), who use their newly measured optical properties of meteoritic diamond in a model of the stellar atmosphere of a carbon star. They suggest that diamonds form in the atmospheres of carbon stars and act as nucleation seeds for other dust grains. Hitherto, PAHs were expected to act as nucleation centres. However, Andersen *et al.* (1998) found that the timescales for PAH formation are too long compared with the dynamical timescales and the gas temperature is too high for PAH formation. The relatively modest opacity and higher condensation temperature of diamond may cause nucleation of diamond grains at relatively high atmospheric temperatures where the velocity field is still negligible.

Given that there are various models for the formation of diamonds around C-rich AGB stars, it would appear that we need to be looking for evidence of diamonds around such stars. The diamond spectrum from Andersen *et al.* (1998), shown in Figs. 7.5 & 7.6, shows various features which may be detectable in the infrared spectra of C-rich AGB stars. It is not yet clear what environmental ingredients are necessary to induce the IR emission in the diamond grains, however, even if they require ultraviolet radiation to emit in this region, we have already shown that C-rich AGB stars in binary systems could fulfil this requirement (see section 7.2). The meteoritic diamond spectrum shown in Fig. 7.5 covers a relatively large wavelength range (2.5-25μm), and the majority of the features are beyond the wavelength range of our observational spectra. However, as seen in Fig. 7.6, there is a prominent feature at $\sim$8.5-9.5μm which may be detectable in the carbon stars in our sample. Unfortunately this is in the same position as the hypothesised a-C:H (see section 6.2.3), making it difficult to conclusively attribute the feature in the observed spectra to diamond grains. It would be interesting to study the high-resolution, wider wavelength range, ISO-SWS spectra of C-rich AGB stars with a view to matching all the features seen in Fig. 7.5 to features in carbon star spectra.

At present our observations have too limited a wavelength range to satisfactorily investigate the possibility of diamond grain formation around carbon stars.

Table 7.5: Spectral features from interstellar diamonds

Lewis *et al.* (1987)		Koike *et al.* (1995b)		Mutschke *et al.* (1995)		Hill *et al.* (1997)		Andersen *et al.* (1998)	
cm^{-1}	μm	cm^{-1}	μm	cm^{-1}	μm	cm^{-1}	μm	cm^{-1}	μm
3402	2.94	3402	2.94	3700-3000	2.70-3.33			3420	2.92
								3236	3.09
		3125-2850	3.2-3.5	3000-2800	3.33-3.57	2961	3.38	2954	3.39
2919	3.43					2935	3.41	2924	3.42
2849	3.51					2875	3.48	2854	3.50
		~2040	~4.9						
1774	5.64	1725-1590	5.8-6.3	1746	5.73	1728	5.79		
1640	6.10							1632	6.13
								1462	6.84
								1456	6.87
1403	7.13	1400	7.14					1402	7.13
								1385	7.22
1361	7.35								
						1282	7.80		
1234	8.10								
1173	8.53	1178	8.49	1175	8.51				
		1144-1138	8.74-8.78						
		1122	8.91			1125	8.89	1122	8.91
1103	9.03	1111-1109	9.00-9.02					1109	9.02
		1090	9.17	1090	9.17			1090	9.17
						1072	9.33		
								1054	9.49
1028	9.73								
		943	10.61						
						744	13.44		
								721	13.86
		637	15.71						
		630	15.88					633	15.80
		626	15.98						
								607	16.5
								471	21.2

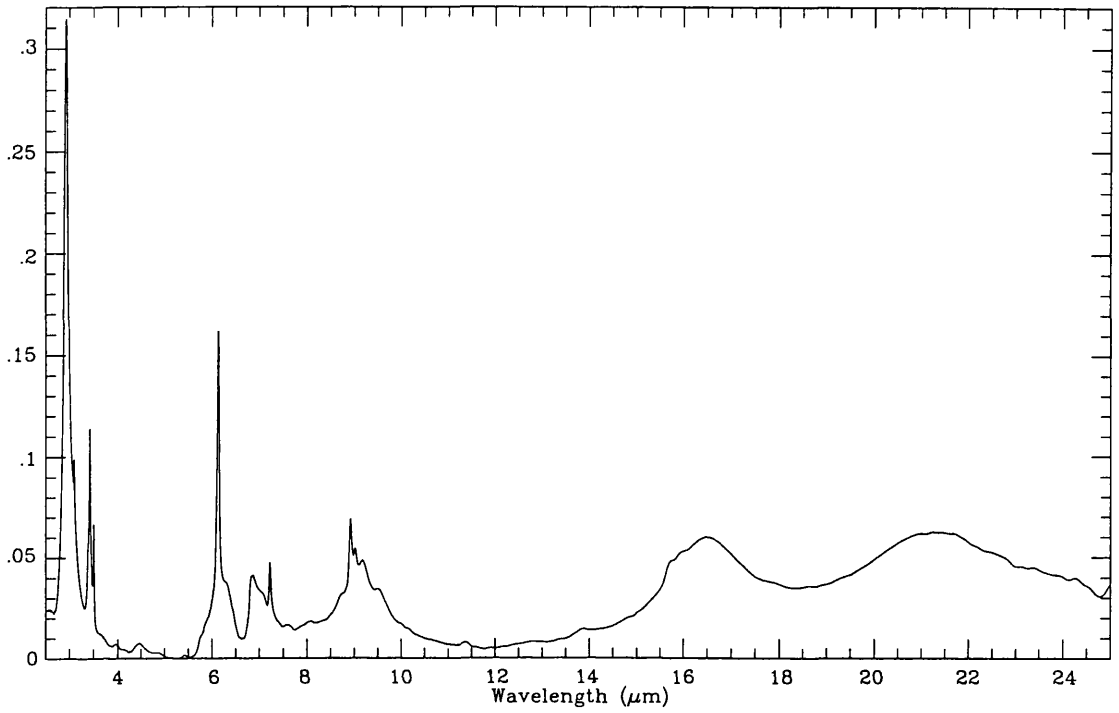

Figure 7.5: Infrared spectrum of meteoritic diamond from Anderson *et al.* (1998)

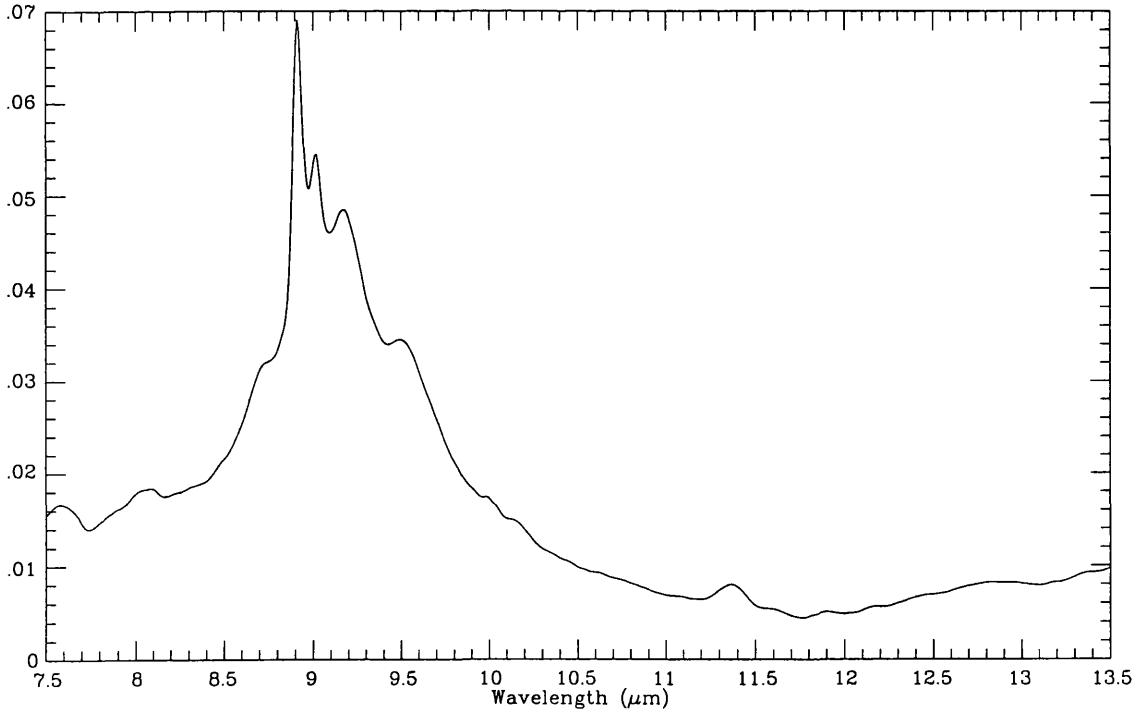

Figure 7.6: 7.5-13.5μm infrared spectrum of meteoritic diamond from Anderson *et al.* (1998)

Chapter 8

Oxygen-rich Stars

"Throbbing dust generation!"

Schizopolis (1996)

8.1 Introduction to O-rich stars

As discussed in chapter 2, most stars whose main sequence masses are in the range $\sim$ 1 - 8 $M_{\odot}$ evolve into a phase known as the Asymptotic Giant Branch (AGB). These AGB stars fit into three broad categories: M, S and C types, where M-type AGB stars have oxygen-rich atmospheres, C-type stars have carbon rich atmospheres and S types stars are somewhat transitional between the two. It is believed that this is an evolutionary series where the M-type stars evolve into S- and then C-type stars. The chemistry around AGB stars is controlled by the C/O ratio (e.g. Woolf 1973). If the C/O ratio is less than unity, all the carbon will be bound into carbon monoxide (CO), which forms very easily and is very stable. The chemistry will be dominated by the remaining oxygen, leading to the formation of oxygen-rich molecules and particles, e.g. silicates and oxides. This is the case for M-type AGB stars. In this chapter, the 8-13μm spectra of M-type AGB stars will be studied with a view to identifying the oxygen-rich dust species forming around such stars.

8.1.1 Background

In the late sixties Gillett, Low & Stein (1968) investigated deviations of stellar spectra from blackbodies. Their observations led to the discovery of an emission peak near 10μm in four late-type, evolved, variable stars. They proposed two explanations for these observations: 1) the effect was due to a combination of stellar opacity and temperature profile;

or, 2) the effect was due to emission by circumstellar matter. This work was followed up by Woolf & Ney (1969), who attributed the emission peak near 10μm (9.7μm) to circumstellar silicate grains around such stars. Since then there has been much interest in the exact nature of the dust around cool evolved stars, how this dust forms and the structure of the dust shells. Hackwell (1972) suggested that the spectra of many M-stars were not consistent with the view that the circumstellar dust was comprised solely of silicate dust. Treffers & Cohen (1974), on the other hand, made high-resolution observations of oxygen rich stars and concurred with Woolf & Ney (1969) on the attribution of the circumstellar dust features to silicates, however they did not preclude the inclusion of other grain types.

The formation of dust grains in the circumstellar shells around oxygen-rich stars was investigated by Salpeter (1974a), who concluded that grain formation proceeded by the nucleation of small refractory seed grains (i.e. oxides) onto which an "onion-layer" mantle of the more abundant silicates could form. Despite this investigation into grain formation Salpeter (1974b) was unable to estimate the size of grains forming in these regions.

The emission from circumstellar grains was investigated further by Forrest, Gillett & Stein (1975), who found the "9.7μm" feature in many evolved M-type stars. However, the feature is not identical in each case (see also Hackwell 1971;1972 and Treffers & Cohen 1974). The variations in feature shape from star to star could not be explained in terms of optical depth or grain temperature effects, which led to the suggestion that grain size is of importance. They also suggested that the features observed in the spectra of AGB stars could be fully explained in terms of blackbody grains, silicate grains and SiC grains. The modelling of circumstellar dust shells includes the introduction of various arbitrary parameters, and so the influence of various model parameters was investigated by Jones & Merrill (1976). They found that using so-called "clean" (i.e. pure magnesium) silicate grains to fit the observed 9.7μm features did not yield a good fit due to the lack of absorption by these grains in the optical and near-IR. They also found that just mixing in more absorbing grains did not solve the problem. This led to the suggestion that the grains responsible for the 9.7μm feature are "dirty" silicates, i.e. Mg-silicates with impurities introduced into the matrix giving more opacity in the optical and near-IR. Following the interest in amorphous silicates as the cause of the 9.7μm feature, Day (1979) produced samples of highly disordered magnesium silicates and produced transmission spectra from them.

The conclusion drawn from this work was that these silicates (an amorphous forsterite and an amorphous enstatite) were very good candidates for the source of the observed 9.7μm feature, however, distinguishing between the different silicates would be difficult. Forrest, McCarthy & Houck (1979) investigated the physical and chemical composition of the dust grains around cool evolved stars and found that the spectral features were smooth indicating that the grains responsible for the features are unlikely to be well ordered like terrestrial silicates and were more likely to be amorphous.

Following the suggestion of Treffers & Cohen (1974), Papoular & Pégourié (1983) explored the effects of grain size on the shape of the 9.7μm feature. They found that grain radii up to 4μm are needed to explain the observed variations in the shapes of the silicate feature. They then went on to discuss the grain-types expected in circumstellar shells (Pégourié & Papoular 1985). Their condensation model shows that the precise nature of the grains formed is determined by the elemental composition and oxidation properties of the parent atmosphere, along with the density structure of the dust shell. They found that: 1) the concentration of iron in silicates is always expected to be low (mole % Fe_2SiO_4(fayalite) $\sim$ 20%; and $FeSiO_3$ $\sim$ 10%); 2) Mg_2SiO_4(forsterite) forms before $MgSiO_3$(enstatite) in a cooling atmosphere, but the forsterite is converted into enstatite by gas-solid reaction. They did not predict the dust to be pure forsterite or even forsterite with some ($\leq$ 20%) fayalite. The disequilibrium calculations showed that the dust shells of M-type stars should also contain SiO_2, solid (metal) Fe, Ca_2SiO_4 and Al_2O_3. Papoular & Pégourié (1985) concurred with Forrest, McCarthy & Houck (1979) on the physical nature of the grains, agreeing that they must be amorphous.

Vardya, de Jong & Willems (1986; hereafter VdJW) examined the possibility that, for a given stellar source, the strength of the 9.7μm feature is related to the mass-loss rate or period of variation of the star. In fact there were no obvious correlations, although they did make an interesting discovery regarding the asymmetry factor (see also Vardya 1989). The asymmetry factor f is defined as the ratio of the number of days between minimum light and the next maximum to the period, so that a symmetric light curve has $f = 0.5$. VdJW found that the silicate emission feature seems to occur only in the spectra of those M-type stars for which $f < 0.43$. The stars with $f \geq 0.5$ show a broader feature centred at about 12μm. They suggested that the 12μm feature is due to more refractory species

(e.g calcium or aluminium silicates) that condense at higher temperatures. As the *f*-value drops the 9.7μm feature appears, due to lower temperature condensates, implying that the change in the *f*-value is an evolutionary trend and important in the nature of circumstellar dust formation.

Gal *et al.* (1987) continued the work on the effects of grains size on circumstellar features. They, again, suggested that the variations in the shapes of the silicate features could be best explained in terms of variations in the size, density and temperature of the circumstellar envelope, the size and physical state of the dust grains and the temperature and distance from the central star, rather than in terms of variations in the dust composition. However, as evidence for this scenario, they stated that the 9.7μm feature is practically always located at the same wavelength. This is not true as can be seen from the work of VdJW and our own work (see section 8.3)

Othman *et al.* (1988) investigated whether there was a correlation between the optical spectral type of stars and the nature of the infrared features. They found that early M-type AGB stars have predominantly featureless spectra, while many late M-type AGB stars do have spectra which exhibit the silicate feature although the correlation is only slight. They also found that simple correlations between silicate emission strength and optical spectral sub-type for both early and late M-type stars are not present. They interpreted this as evidence that the photospheric temperature is not a dominant factor in influencing the emission from oxygen-rich optically thin circumstellar dust shells around M-type AGB stars.

Schutte & Tielens (1989) examined the differences in the shape of the 9.7μm spectral feature from star to star in terms of a model of the circumstellar envelope. Their dust shell model comprised three distinct regions: 1) the regularly pulsating stellar photosphere. Oscillations of the stellar interior propagate shocks into the stellar atmosphere. These shocks transport material to large distances from the stellar surface, where it becomes part of the second distinct region: 2) the (quasi-)stationary layer. The gas temperature is fairly low ($\sim$ 800K) and the dust particles condense in this region; and, 3) an extended, outwardly expanding circumstellar shell or outflow, formed when radiation pressure on the dust particles in the stationary layer accelerates them outwards and drags the gas

along with them. Again the smoothness of the silicate features was taken as evidence of amorphous, rather than crystalline, circumstellar grains.

Onaka, de Jong & Willems (1989; hereafter OdJW) attributed the broad 12μm band (see Hackwell 1972 and VdJW) to corundum (Al_2O_3). They also found that fits to nearly all their M-type star spectra could be improved by the inclusion of Al_2O_3 grains. They suggested that the only way to form silicate grains is for them to grow on pre-existing grains of Al_2O_3, which act as seed nuclei.

Little-Marenin & Little (1990; hereafter LML90) have classified the variation in the spectral features from M-type AGB stars into six categories: featureless, broad, 3 component, sil++ (a "9.7μm" feature with a strong feature on its long wavelength side centred at about 11.3μm), sil+ (a stronger "9.7μm" feature with a weaker long wavelength feature) and sil (a strong "9.7μm" silicate feature). They suggest that there is an evolutionary sequence in the spectral features, starting with a featureless continuum and developing a broad feature, followed by a three component feature, a two component feature and then increasingly strong silicate features. They also tried to find correlations between the emission features and the period, mass-loss rate, maser activity and other physical parameters (c.f. VdJW and Othman *et al.* 1988). The stars with featureless spectra are those with a slightly earlier spectral class than the rest, possibly being less evolved. The most interesting correlation is with the asymmetry factor *f*. Concurring with the finding of VdJW, LML90 found correlations between the feature variations and the asymmetry of the period of the stars. The mean *f* varied from 0.47±0.04 for the broad feature to 0.39±0.03 for the strong silicate feature. If the change in spectral feature shape is an evolutionary process, this implies that the visual light curve becomes slightly more asymmetric with age. The work of LML90 was continued by Stencel *et al.* (1990), who hypothesized some sort of "chaotic silicate" condensation. The chaotic silicate forms from a supersaturated vapour containing metal atoms, SiO, AlO and OH in a hydrogen atmosphere. Inside the chaotic silicate, where both silicon and aluminium are less than fully oxidised, the higher reduction potential of Al would initially act to produce AlO at the expense of SiO. Thus the stretching modes of solid, amorphous Al-O would grow at the expense of the 9.7μm Si-O stretch. However, Al is approximately one tenth as abundant as silicon and therefore once the aluminium is completely oxidised, the Si and SiO components of the grain should

begin to oxidise and thus increase the strength of the 9.7μm Si-O stretching band. Given the overabundance of silicon relative to aluminium, the silicate feature will eventually overwhelm the 12μm aluminium oxide (corundum) feature. The three component, sil++, and sil+ features identified by LML90 are interpreted as intermediate stages between the AlO-dominated broad feature and the strong 9.7μm silicate feature.

The relationship between the 9.7μm feature and the mass-loss rate was re-examined by Hashimoto *et al.* (1990), using spherical dust envelope radiative transfer models and the IRAS LRS spectra. They drew several major conclusion from this work: 1) the strength of the 9.7μm silicate feature is an indicator of the mass-loss rate (c.f. Skinner & Whitmore 1988a); 2) the relationship between the 9.7μm silicate feature and the mass-loss is independent of the outer radius of the dust envelope and, therefore, independent of the duration time of the mass-loss; 3) the mass-loss rate has to be greater than about 7x10$^{-8}M_{\odot}yr^{-1}$ for dust to form; and 4) the characteristic time of steady mass-loss for M-type AGB stars is $<\sim 10^4$ years.

The problems of reconciling theoretical dust formation processes with observations of circumstellar dust are described by Tielens (1990). There are two basic factors which determine the species of dust formed: the thermodynamics and kinetics. According to condensation thermodynamics, the silicate condensation sequence starts with the nucleation of corundum (Al_2O_3) from the circumstellar gas at about 1760K. The first silicate is expected to form by a gas-solid reaction with corundum, to form $Ca_2Al_2SiO_7$. As the temperature drops, further gas-dust reactions occur so that Mg substitutes for Al to form $CaMgSi_2O_6$. The aluminium released and the remaining corundum are converted to spinel ($MgAl_2O_4$). As further cooling occurs the $CaMgSi_2O_6$ and the spinel form a solid-solid reaction, producing anorthite ($CaAl_2Si_2O_8$). At even lower temperatures ($\sim$ 1440K) forsterite (Mg_2SiO_4) starts to condense out. Forsterite continues to form until the temperature has dropped to $\sim$ 1350K when it reacts with gaseous SiO to produce enstatite ($MgSiO_3$). Finally, at $\sim$ 1100K reactions with gaseous iron will convert some enstatite into fayalite (Fe_2SiO_4) and forsterite. Kinetics also plays an important role in determining which silicates form in the outflows of AGB stars. Depending on the density structure of the region circumjacent to the star the condensation sequence will be brought to a halt at different points. Thus, if the density drops rapidly with distance from the

star, the only dust expected to form will be various high temperature oxides (e.g. Al_2O_3, $CaTiO_3$, ZrO_2), which will form very close to the photosphere. If the densities are a little higher further out in the circumstellar shell gas-grain reactions can take place, allowing the formation of calcium-aluminium silicates. If the density is high enough a little further out magnesium silicates may form as rims on the Ca-Al silicates. For magnesium silicates to nucleate, there need to be very high densities a long way out, which is highly unlikely. Feldspars are not expected to form, as the solid-solid reaction requires unrealistically high densities. Finally, Fe can only be incorporated into Mg-silicates if, initially, most of the iron is in gaseous form (rather than solid, metal form) and if the density is high enough at large distances from the star where fayalite can survive. Most laboratory studies of condensation sequences concentrate on very small sub-systems, such as silicate formation in magnesium-iron rich gases. These are obviously not realistic.

The most striking assertion from Tielens (1990) was that observations indicate the presence of crystalline grains. This conflicted with the consensus that the smooth 10μm features are indicative of amorphous, rather than crystalline, grains. The 11.3μm feature attributed to crystalline olivine was taken as evidence of crystallinity. He suggested that the magnesium silicates forming close to the stellar photosphere are crystalline, but the iron silicates are quite amorphous, which may go some way to explaining the variations in the feature.

Waters *et al.* (1996) found features in the ISO-SWS spectra evolved stellar objects (AGB stars, red super giants, post-AGB objects and planetary nebulae) which they have attributed to crystalline silicates. While they acknowledged that some of the features may be attributable to other dust species (e.g. water ice, oxides), they asserted that some of the features can only be explained by using the optical properties of crystalline silicates. These features are mostly longwards of 20μm, where amorphous silicates do not show prominent features. They suggested that a combination of different dust species, both crystalline and amorphous, are needed to explain all the features in the infrared spectra of evolved stars. Unfortunately most of the interesting crystalline silicate features they referred to are found outside the range of our observational spectra.

As discussed earlier, the work of LML90 divided M-type AGB star spectra into six[1] groups,

[1] In fact LML90 used seven categories, however their S-feature category is viewed as separate from the suggested evolutionary track of the dust and is therefore ignored here.

Table 8.1: A classification system for M-type AGB star spectra

Classification	Description of the spectrum
featureless	no features above a blackbody energy distribution
broad	broad, low, fairly smooth feature over the 8.5-12.5μm region
transition	the *broad* with a slight 9.7μm silicate bump
broad+sil	stronger silicate feature, but still a strong *broad* component
sil+broad	silicate feature is stronger still; the *broad* component
	starts the resemble a wing of silicate feature
sil	The 9.7μm silicate feature dominates;
	the *broad* component is no longer visible

the sequence of which was postulated to be evolutionary. However, LML90 seem to have misclassified some of the IRAS LRS spectra (e.g. by seeing broad features where none exist) and their choice of specific classifications seems questionable. The initial and final groups of LML90 are very similar to those set out here, where the spectra exhibit either no feature or a very strong silicate feature, however the intermediate groups are much more ambiguous when it comes to separating them since they tend to merge into one another (as would be expected for an evolutionary sequence) and precise interpretation of these spectra is difficult. We have, therefore, classified 80 CGS3 10μm spectra of oxygen-rich dust shell stars into six groups. These are: featureless, broad, transition, broad+sil, sil+broad, and sil. The basic features of these groups are shown in Table 8.1. Like LML90, we see there is a possible evolutionary progression in the spectra, starting with a *featureless* continuum, building up a broad low feature (*broad*) which develops a slight 9.7μm feature (*broad+sil*). This 9.7μm feature becomes stronger (*sil+broad*) and eventually dominates the mid-IR spectrum (*sil*). The *transition* group is the stage between a dominant broad feature and a dominant silicate feature. We have then compared our classified spectra to the relevant laboratory spectra discussed in chapter 5 and the results are discussed below.

8.2 Observations

Most of the stars in this sample were observed on the nights of October 4 – 7 1992, although twelve stars were observed on the nights of May 21–25 1991. RZ Ari was observed on the night of October 5 1990, and T Cet on November 1 1993. Table 8.2 provides some details of the observations. All observations were made using the 3.8m United Kingdom

Table 8.2: Sources Observed

Source	IRAS names	Other names	Spec. Type†	Observation Date	Calibrator
Y Cas	00007+5524	IRC +60001, HD 225082	M7e	Oct 5 92	ϵCyg
MZ Cas*	00186+5940	IRC +60008	M2Iab	Oct 5 92	ϵCyg
T Cet	00192-2020	IRC -20007, AFGL 53, HD 1760	M5-6S	Nov 1 93	βPeg
T Cas	00205+5530	IRC +60009, AFGL 57, HD 1845	M7e	Oct 5 92	ϵCyg
RW And	00445+3224	IRC +30015, AFGL 109, HD 4489, CIT 2	S6,2e	Oct 5 90	αTau
SAO 37673	01556+4511	IRC +50049, AFGL 278, HD 11979	M7	Oct 4 92	αCet
XX Per*	01597+5459	IRC +50052, HD 12401	MIb	Oct 6 92	βPeg
o Cet	02168-0312	Mira, IRC +00030, AFGL 318, HD 14386	M7IIIe	Oct 6 92	αLyr
AD Per*	02169+5645	IRC +60082, HD14270	M3(I)	Oct 4 92	αTau
R Cet	02234-0024	IRC +00032, AFGL 4195, HD 15105	M4e	Oct 4 92	αCMa
RR Per	02251+5102	IRC +50062, AFGL 335, HD 15186	M6e-M7e	Oct 7 92	αCet
RZ Ari	02530+1807	IRC +20051	M6(III)	Oct 5 90	αTau
IO Per*	03030+5532	IRC +60110	M3(I)	Oct 4 92	αTau
RT Eri	03318-1619	IRC -20043, AFGL 500, HD 22228	M7e	Oct 4 92	αTau
IK Tau	03507+1115	IRC +10050, AFGL 529, NML Tau	M6e	Oct 7 92	αCet
V Eri*	04020-1551	IRC -20049, AFGL 542, HD 25725	M5/M6I	Oct 4 92	αTau
W Eri	04094-2515	IRC -30033, AFGL 552, HD 26601	M7e	Oct 4 92	αCma
BX Eri	04382-1417	IRC -10075, AFGL 615	M3	Oct 4 92	αCMa
R Cae	04387-3819	AFGL 617, HD 29844	M6e	Oct 4 92	αCMa
TX Cam	04566+5606	IRC +60150, AFGL 664	M9	Oct 4 92	αCma
UX Aur	05121+4929	IRC +50138, HD 33877	M4(II)	Oct 4 92	αCet
X Ori	05351-0147	IRC +00080, AFGL 786	M8	Oct 7 92	αAur
RU Aur	05367+3736	IRC +40135, AFGL 794	M8e	Oct 7 92	αAur
SZ Aur	05384+3854	IRC +40136, AFGL 802, HD 37645	M8e	Oct 7 92	αAur
U Aur	05388+3200	IRC +30126, AFGL 822, HD 37724	M7e	Oct 7 92	αAur
RT Lep	05404-2342	IRC -20077, AFGL 8105	M9e	Oct 4 92	αCMa
S Col	05450-3142	IRC -30049	M6e	Oct 4 92	αCMa
CH Pup	06434-3628	AFGL 1008	Me	Oct 7 92	αCet
AZ Mon	06551+0322	IRC +00140,	M6e	Oct 7 92	αCet
GX Mon	06500+0829	AFGL 1028	M9	Oct 7 92	αCet
Y Lyn	07245+4605	IRC +50180, AFGL 1120, HD 58521	M6S	May 24 91	αBoo
Z Pup	07304-2032	IRC -20123, AFGL 1140, HD 60218	M4e	Oct 6 92	αCma
DU Pup	07329-2352	IRC -20134, AFGL 1151	M	Oct 6 92	αCMa
U Pup	07585-1242	IRC -10184, AFGL 1215, HD 65940	M5e-M8e	Oct 6 92	αCma
RS Cnc	09076+3110	IRC +30209, AFGL 1329, HD 78712	M6S	May 25 91	αBoo
R Leo	09448+1139	IRC +10215, AFGL 1380, HD 84748	M8e	May 22 91	αBoo
Z Ant	10436-3459		S5,4	May 25 91	αBoo
R Hya	13296-2301	IRC -20254, AFGL 1627, HD 117287	M7e	May 25 91	αBoo
W Hya	13462-2807	IRC -30207, AFGL 1650, HD 120285	M8e	May 21 91	αBoo
RX Boo	14219+2555	IRC +30257, AFGL 1706, HD 126327	M7.5e	May 24 91	αBoo

Table 8.2: Sources Observed (cont.)

Source	IRAS names	Other names	Spec. Type†	Observation Date	Calibrator
S CrB	15195+3139	AFGL 4990S, HD 136753	M7e	May 24 91	αBoo
RU Her	16081+2511	IRC +30283, AFGL 1832, HD 145459, CIT 8	M7e	May 24 91	αBoo
U Her	16235+1900	IRC +20298, AFGL 1858, HD 148206	M7e	May 24 91	αBoo
BG Her	17072+1844	IRC +20314,	M3	May 24 91	βPeg
VX Sgr*	18050-2213	IRC -20431, AFGL 2071, HD 165674	M5-M6(I)	Oct 4 92	βPeg
V1692 Sgr	18320-1918		M9	Oct 7 92	βPeg
V1111 Oph	18349+1023	IRC +10365, AFGL 2206	M9	Oct 4 92	αLyr
X Oph	18359+0847	IRC +10360, AFGL 2213, HD 172171	M5e-M9e	Oct 4 92	αLyr
V2059 Sgr	18501-2132		M8	Oct 4 92	αLyr
R Aql	19039+0809	IRC +10406, AFGL 2324, HD 177940	M7e	Oct 6 92	αLyr
AG Sgr	19044-2856	IRC -30403, HD177868	M5-M6e	Oct 7 92	βPeg
V342 Sgr	19093-3256	IRC -30404, AFGL 5556	M9	Oct 5 92	βPeg
W Aql	19126-0708	IRC -10497, AFGL 2349	S6,6e	Oct 7 92	βPeg
Z Sgr	19167-2101	IRC -20555, HD 181060	M5e	Oct 5 92	βPeg
V1302 Aql*	19244+1115	IRC +10420, AFGL 2390	F8Ia	Oct 6 92	αLyr
V635 Aql	19343+0912		?	Oct 7 92	βAnd
BG Cyg	19369+2823	IRC +30379, AFGL 2426	M7e	Oct 4 92	αLyr
V462 Cyg	19384+4346	IRC +40355, AFGL 2429	M7e	Oct 4 92	αLyr
RR Sgr	19528-2919	IRC -30419, AFGL 5569, HD 188378	M5e	Oct 7 92	βPeg
Z Cyg	20000+4954	IRC -50314, HD 190163	M5e	Oct 5 92	βPeg
SX Cyg	20135+3055	IRC +30423, HD 192788	M7e	Nov 2 93	αLyr
RU Cap	20296-2151	IRC -20590	M9e	Oct 7 92	βAnd
Y Del	———	IRC +10475	M8e	Oct 7 92	βAnd
Y Aqr	20417-0500	IRC -10546	M6.5e	Oct 7 92	βPeg
W Aqr	20438-0415	IRC +00489	M7	Oct 7 92	βAnd
RZ Cyg	20502+4709	IRC +50347	M7	Oct 5 92	βPeg
UW Cep	20581+5841	IRC +60301	M8	Oct 5 92	βPeg
RU Cyg	21389+5405	IRC +50390, AFGL 2790, HD 206483	M8e	Oct 5 92	βPeg
SAO 145652	21439-0226	IRC +00509, AFGL 2806, HD 207076	M8	Oct 6 92	αLyr
UU Peg	21286+1055	IRC -10498, AFGL 2775	M7e	Oct 7 92	εCyg
YY Cep	22000+5643	IRC +60337	M6	Oct 5 92	βPeg
SV Peg	22035+3506	IRC +40501, AFGL 2845, HD 209872	M7	Oct 7 92	εCyg
CU Cep	22097+5647	IRC +60345, AFGL 2865	M5	Oct 5 92	βPeg
R Peg	23041+1016	IRC +10527, AFGL 3023, HD 218292	M7e	Oct 5 92	βPeg
V Cas	23095+5925	IRC +60389, HD 218997	M5.5e	Oct 5 92	βPeg
BU And	23212+3927	IRC +40536, AFGL 3088	M7e	Oct 6 92	βPeg
R Aqr	23412-1533	IRC -20642, AFGL 3136, HD 222800	M7e	Oct 6 92	αLyr
Z Cas	23420+5618	IRC +60418, AFGL 3141, HD 222914	M7e	Oct 7 92	εCyg
R Cas	23558+5196	IRC +50484, AFGL 3188, HD 224490	M7e	May 21 91	αBoo

* These stars are M-supergiants

† Spectral types taken from Simbad database

Infrared Telescope (UKIRT) with the common-user spectrometer CGS3, a liquid helium cooled, 10- and 20-μm grating spectrometer built at University College London. CGS3 contains an array of 32 discrete As:Si photoconductive detectors, and three interchangeable, permanently mounted gratings covering the 7.5–13.5 and 16.0–24.5μm wavebands. Two settings of a grating give a fully sampled 64-point spectrum of the chosen waveband. We obtained 7.4–13.5μm spectra with a 5.5-arcsec circular beam, and a spectral resolution of 0.17μm. Further details about CGS3 can be found in Cohen & Davies (1995). Eight stars, α Aur, α Cet α CMa, α Tau, α Lyr, β Peg, β And and ϵ Cyg, were use as flux standards. Table 8.2 lists the calibrator used for each source. The spectra of sources taken using α Tau as the standard star were flux-calibrated using the absolutely calibrated spectrum of α Tau constructed by Cohen *et al.* (1992a), whilst several sources were calibrated using a similarly constructed spectrum of β Peg provided by Dr. M. Cohen (see Cohen and Davies 1995). A number of sources were calibrated with respect to the A-type stars α Lyr and α CMa, for which Kurucz model atmosphere calibrations, described by Cohen *et al.* (1992b), were adopted. The deep telluric ozone feature at 9.7μm could not always be completely cancelled, hence in some cases spurious spectral structure could be present in the 9.3–9.8μm region.

8.3 The classification of features

Following the work of LML90, and also the work of Stencel *et al.* (1990), a sample of eighty oxygen rich evolved stars has been divided into six groups by visual inspection of their spectra. Since the changes in the spectral features are believed to be due to the evolution of dust and form a continuum of differing features, categorizing the spectra into specific groups can be difficult as some spectra seem to be between groups. The six groups are: *featureless*, *broad*, *transition*, *broad+sil*, *sil+broad* and *sil.* While these classifications are based on the ideas of LML90, there was no attempt to use or even correspond to their classifications. However, some spectra seem to have naturally fallen into groups very similar to those of LML90: Group O1 (*featureless*) is equivalent to LML90's "no feature" classification; the *broad* groups in each system are similar as are the strong silicate groups (denoted by "sil" in both cases). However, the intermediate groups bear little resemblance to those of the LML90 classifications.

The sequence of classifications of these spectra is expected to show the evolution of the

dust (LML90 and Stencel *et al.* 1990), starting with a featureless spectrum (Group O1 - *featureless*), indicating little or no dust. Next, the spectrum of a star is expected to start showing evidence for dust by developing a broad low feature (Group O2 - *broad*). This is followed by the development of a 9.7μm silicate feature, which begins to appear in Group O3 - *transition*, where it is noticeable but weak. In Group O4 - *broad+sil* the 9.7μm silicate feature is stronger, although there is still a strong broad component. Eventually the 9.7μm silicate feature starts to dominate the spectrum. This can be seen to start in Group O5 - *sil+broad*, until it becomes so strong as to overwhelm any other features, as in the spectra of Group O6 - *sil*.

The shapes of the features in each of these groups are discussed here. In order to understand the attributions of various spectral shapes to the laboratory spectra of minerals expected to form around these stars, Table 8.3 shows the peak positions of the various dust forming minerals, from laboratory measurements. Further details about the minerals expected to form around oxygen-rich stars can be found in chapter 5.

For each group, the flux-calibrated spectrum of each source is shown as well as the continuum-subtracted spectrum (apart from Group O1; see below) produced by subtracting a 3000K blackbody normalised at 8μm.

8.3.1 Group O1 - *featureless* spectra

There are seven stars in this group, all appearing to have featureless spectra. They are: BU And, UX Aur, T Cas, V Cas, R Hya and R Peg. Their flux-calibrated spectra are shown in Fig. 8.1, together with the best fitting blackbody. It can easily be seen that these spectra have little or no emission above a blackbody, with the exception of T Cas which looks like two blackbodies superimposed. The continuum-subtracted spectra, created by subtracting the best-fitting blackbody, can be seen in Fig. 8.2. With the exception of UX Aur, they all show a very small narrow bump at 9.8μm, which is most probably due to incomplete ozone cancellation. They have very slight bumps in the 11.0-11.5μm region, which may be attributable to crystalline olivine or pyroxene. BU And and R Peg also have possible slight bumps in the $\sim$12.5-13.0μm region which may be attributable to corundum or silicon dioxide (see Table 8.3 for attributions). However these minor features are so slight that they may just be the result of noisy spectra. Therefore, there is little or no

Table 8.3: Laboratory spectra of condensation sequence minerals

Mineral name	Chemical composition	Amorphous or Crystalline	Main Peak μm	Minor Peaks μm	Source
Corundum	Al_2O_3	Amorphous	12.1		1
Corundum*	Al_2O_3	Amorphous	11.6		2
Corundum†	Al_2O_3	Amorphous	11.8		2
Corundum	Al_2O_3	Crystalline	11.7	12.4, 13.6, 16.4	1
Rutile	TiO_2	Crystalline	~9	rise longwards of 9.8	3
Rutile	TiO_2	Crystalline	—	rise longwards of 11.5	4
Pyroxene	$Mg_{0.5}Fe_{0.43}Ca_{0.03}Al_{0.04}SiO_3$	Amorphous	9.35		2
Augite	$(Ca,Na)(Mg,Fe,Al,Ti)(Si,Al)_2O_6$	Crystalline	9.4,10.3,11.6		4
Augite	$(Ca,Na)(Mg,Fe,Al,Ti)(Si,Al)_2O_6$	Crystalline	9.4, 10.4, 11.1		4
Diopside	$CaMgSi_2O_6$	Crystalline	9.3, 10.2, 10.9, 11.5		4
Hedenbergite	$CaFe^{2+}Si_2O_6$	Crystalline	9.3, 10.4, 11.6	10.9	4
Spinel	$MgAl_2O_4$	No Data			
Anorthite	$CaAl_2Si_2O_8$	Crystalline	10.8	8.7, 9.1, 9.8, 13.2	4
Forsterite	Mg_2SiO_4	Amorphous	9.8		2
Forsterite	Mg_2SiO_4	Crystalline	11.4	10.2, 12.0	1
Forsterite	Mg_2SiO_4	Powder	9.8	11.1, 11.8	5
Forsterite	Mg_2SiO_4	Amorphous	9.8	10.5, 11.7	6
Enstatite	$MgSiO_3$	Amorphous	9.3		2
Enstatite	$MgSiO_3$	Powder	10.7	9.4, 11.7	5
Enstatite	$MgSiO_3$	Powder	10.5	9.3, 11.6	5
Enstatite	$MgSiO_3$	Amorphous	9.55		7
Enstatite	$MgSiO_3$	Crystalline	10.6	9.3, 11.5	4
Olivine	$MgFeSiO_4$	Amorphous	9.8		2
Olivine	$Mg_{0.8}Fe_{1.2}SiO_4$	Amorphous	9.8		2
Olivine	$Mg_{0.8}Fe_{1.2}SiO_4$	Crystalline	11.5	10.4, 12.1	1
Olivine	$Mg_{1.2}Fe_{0.8}SiO_4$	Crystalline	11.4	10.3, 12.1	1
Olivine	$Mg_{1.6}Fe_{0.4}SiO_4$	Crystalline	11.4	10.2, 12.1	1
Olivine	$Mg_{0.22}Fe_{1.78}SiO_4$	Crystalline	11.3	10.2, 11.9	4
Olivine	$Mg_{0.36}Fe_{1.64}SiO_4$	Crystalline	11.4	10.5, 12.1	4
Olivine	$Mg_{0.58}Fe_{1.42}SiO_4$	Crystalline	11.4	10.5, 12.1	4
Olivine	$Mg_{0.82}Fe_{1.18}SiO_4$	Crystalline	11.4	10.4, 12.0	4
Olivine	$Mg_{1.02}Fe_{0.98}SiO_4$	Crystalline	11.4	10.4, 12.0	4
Olivine	$Mg_{1.2}Fe_{0.8}SiO_4$	Crystalline	11.3	10.3, 12.0	4
Olivine	$Mg_{1.32}Fe_{0.68}SiO_4$	Crystalline	11.3	10.3, 12.0	4
Olivine	$Mg_{1.76}Fe_{0.24}SiO_4$	Crystalline	11.3	10.1, 11.9	4
Olivine	$Mg_{1.76}Fe_{0.24}SiO_4$	Crystalline	11.3	10.1, 11.9	4

1. From Koike *et al.* (1995) 2. From the Jena Group web site 3. From Nyquist
4. From John Salisbury FTP site 5. From Launer (1952) 6. From Kratschmer & Huffman
7. Day (1979) * porous sample † compact sample

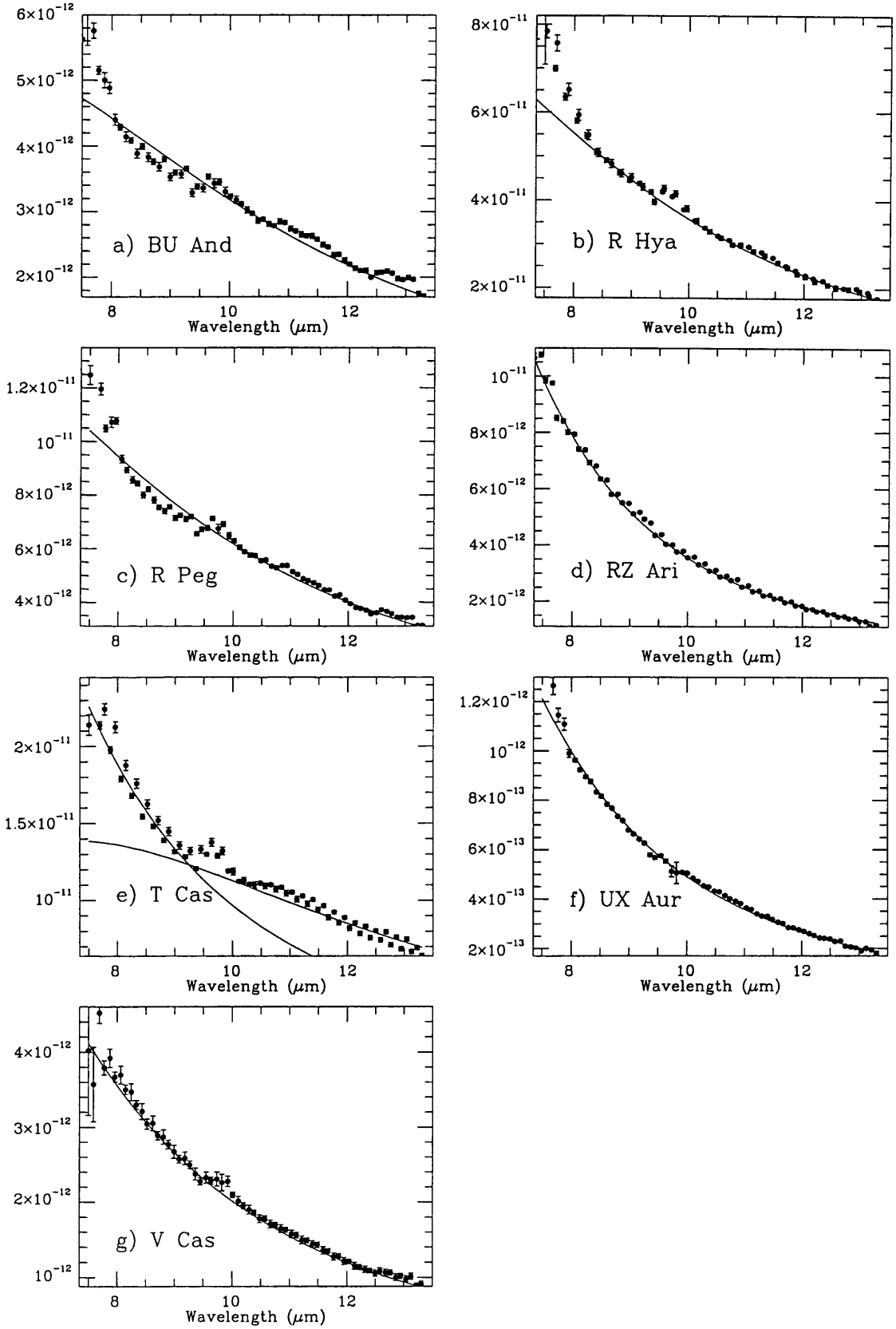

Figure 8.1: Flux-calibrated spectra of Group O1 sources with *featureless* spectra together with the best fitting blackbodies. Fluxes are in $\mathrm{Wm}^{-2}\mu\mathrm{m}^{-1}$

evidence of the minerals expected to form prior to forsterite, e.g. corundum or augite pyroxenes.

8.3.2 Group O2 - *broad* feature

The suggested next stage in the evolution of the sequence from featureless spectra is for them to develop a broad, low, fairly smooth feature over the 8.5-12.5μm region. There are sixteen sources in this category: R Aql, W Aql, R Aur, SZ Aur, MZ Cas, YY Cep, S Col, BG Cyg, RT Eri, W Hya, R Leo, X Oph, AG Sgr, RR Sgr, V1692 Sgr, and Z Sgr, the flux-calibrated spectra of which are shown in Fig. 8.3 and the continuum-subtracted spectra are shown in Fig. 8.4. For this group the spectra exhibit low contrast features which, while fairly smooth, do show a few bumps. The precise positions of these bumps vary from source to source. Four sources (MZ Cas, R Aql, R Aur and V1692 Sgr) exhibit a feature at $\sim$11.0-11.5μm, possibly due to crystalline olivine or pyroxene. However, in three of these cases the feature is so slight as to be dismissed as noise. The remaining source, MZ Cas (Fig. 8.3c), is in fact a supergiant and the 11.3μm feature has previously been identified as a UIR band by Sylvester *et al.* (1994). Some spectra (4/16) have features at $\sim$12.6-13.0μm, possibly due to crystalline silicon dioxide. Several sources exhibit a possible slight spectral features at $\sim$11.9-12.2μm, possibly due to corundum. Many of these spectra exhibit a bump at 9.7μm, however this can be attributed to incomplete ozone cancellation. Overall, these spectra may exhibit features consistent with the formation of a refractory oxide, corundum, silicon dioxide and the first of the silicates in the condensation sequence, the augite pyroxenes. However, with the exception of the 11.3μm band in MZ Cas, all these features are so slight as to be dismissed as noise. The overwhelming feature of all these spectra is the broad, smooth 8.5-12.5μm band which exhibits little to suggest the nature of the dust producing it.

8.3.3 Group O3 - *transition* spectra

Following the broad feature phase, the dust develops the "silicate" feature at 9.7μm, whilst also strengthening the broad underlying feature, so that the spectra appear to have a fairly weak peak at 9.7μm, with a wing out to about 11.5-12.0μm. This group comprises only three sources: Y Aqr, RS Cnc and W Eri, the flux-calibrated spectra of which can be seen in Fig. 8.5 and the continuum-subtracted spectra in Fig. 8.6. In the case of RS Cnc, the broad feature is quite smooth with just the 9.8μm bump showing. This bump is

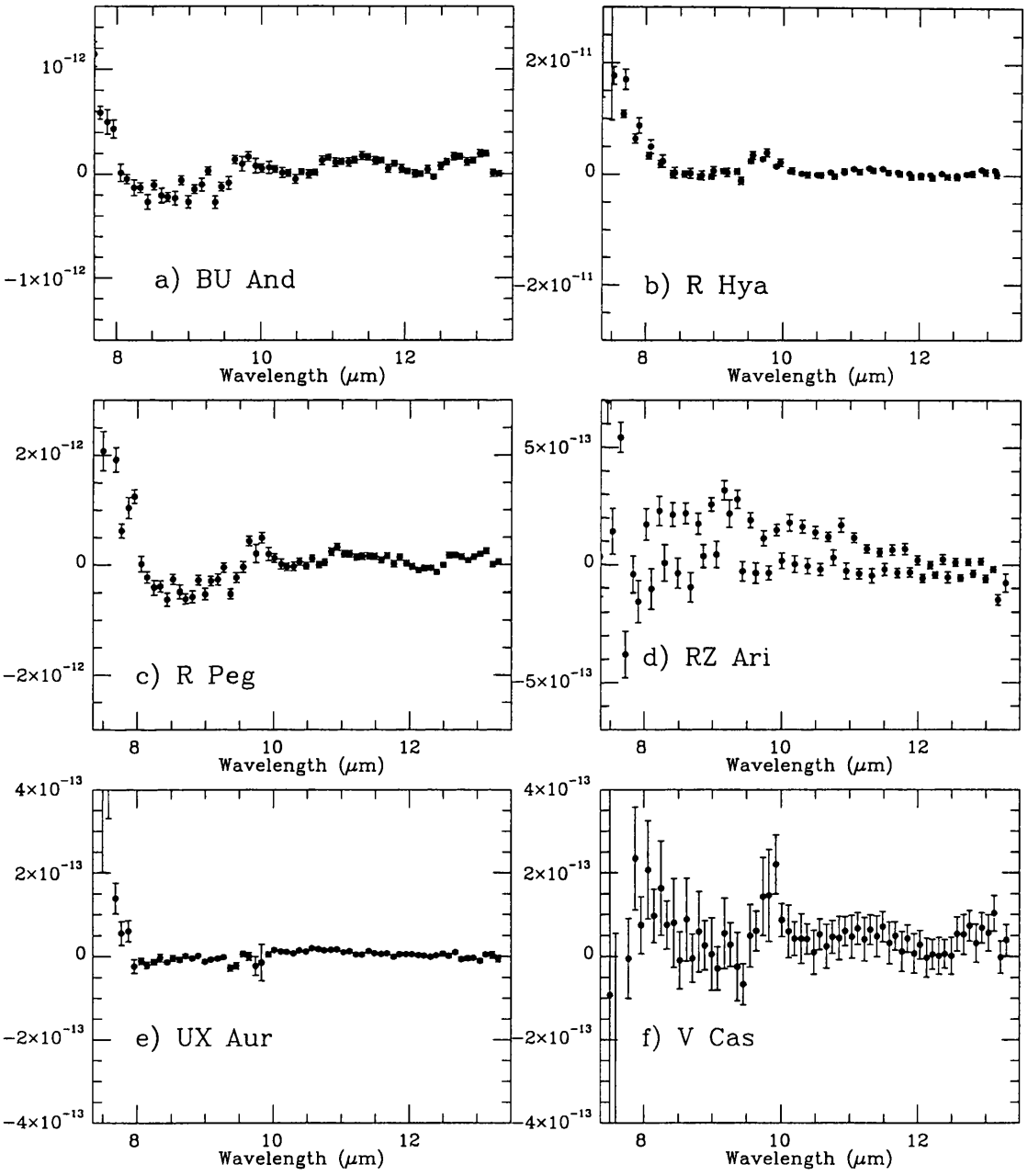

Figure 8.2: Continuum-subtracted spectra of Group O1 (*featureless*) sources. Fluxes are in $\mathrm{Wm}^{-2}\mu\mathrm{m}^{-1}$

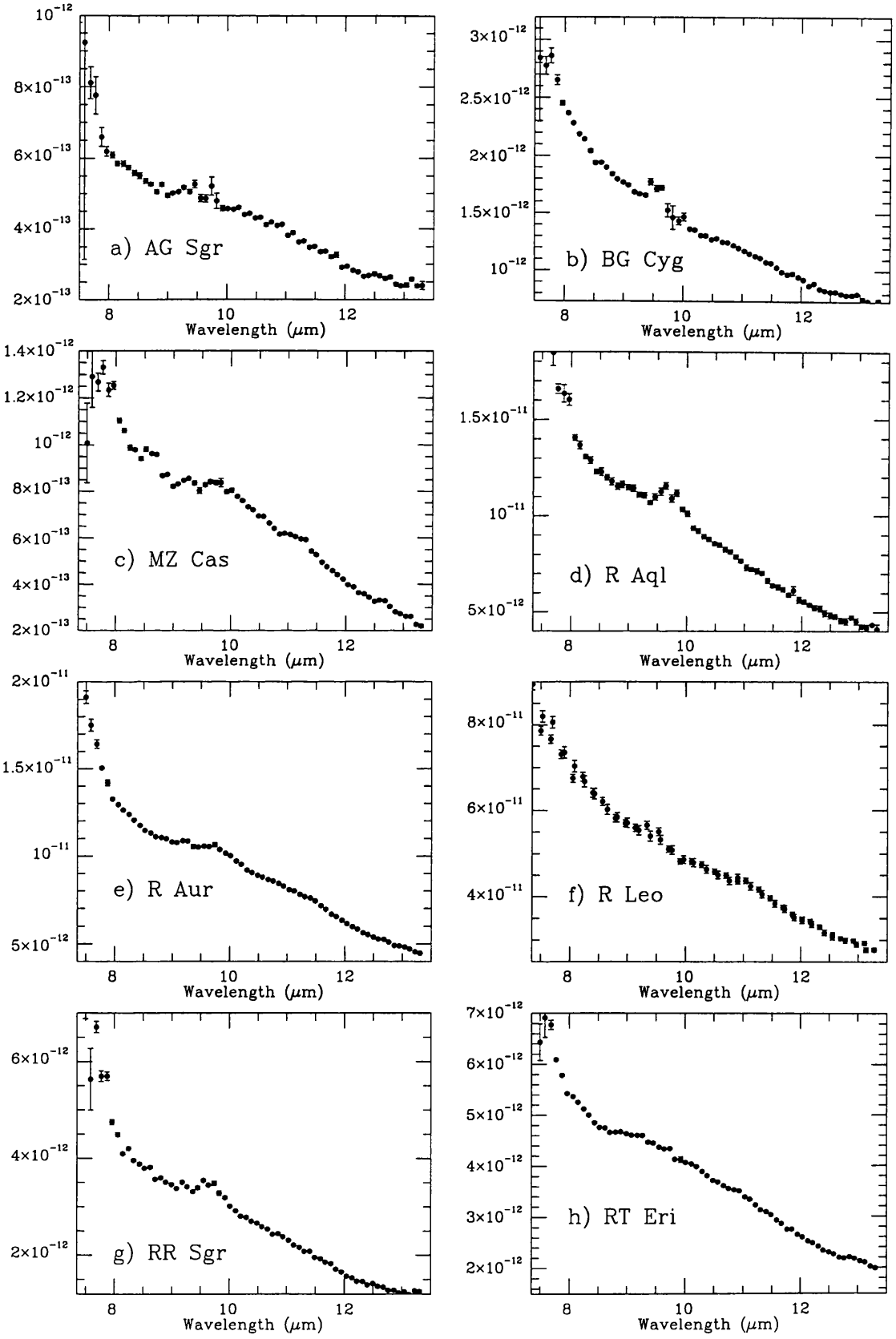

Figure 8.3: Flux-calibrated spectra of Group O2 sources with a *broad* feature. Fluxes are in $\mathrm{Wm}^{-2}\mu\mathrm{m}^{-1}$

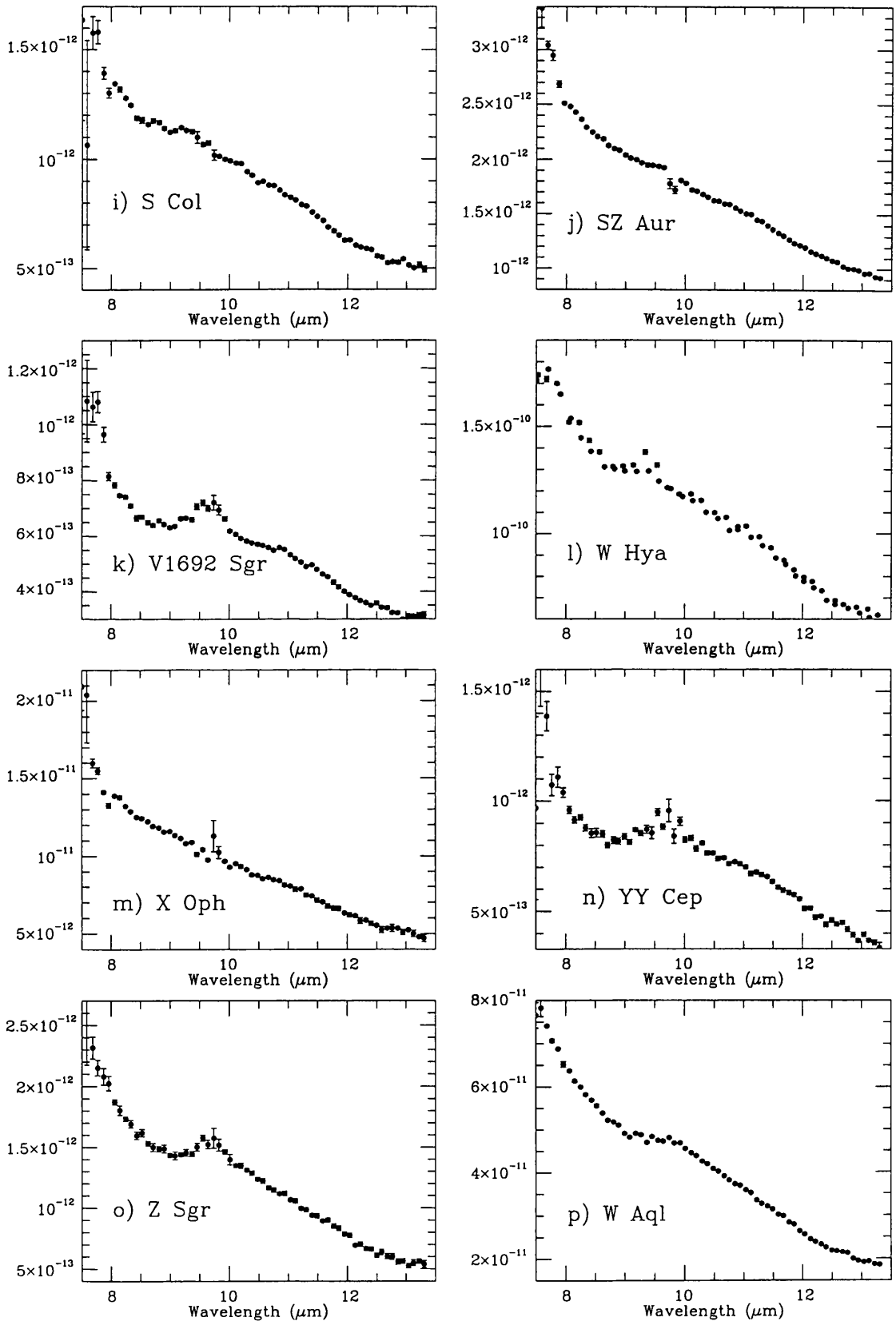

Figure 8.3: (Group O2 cont.)

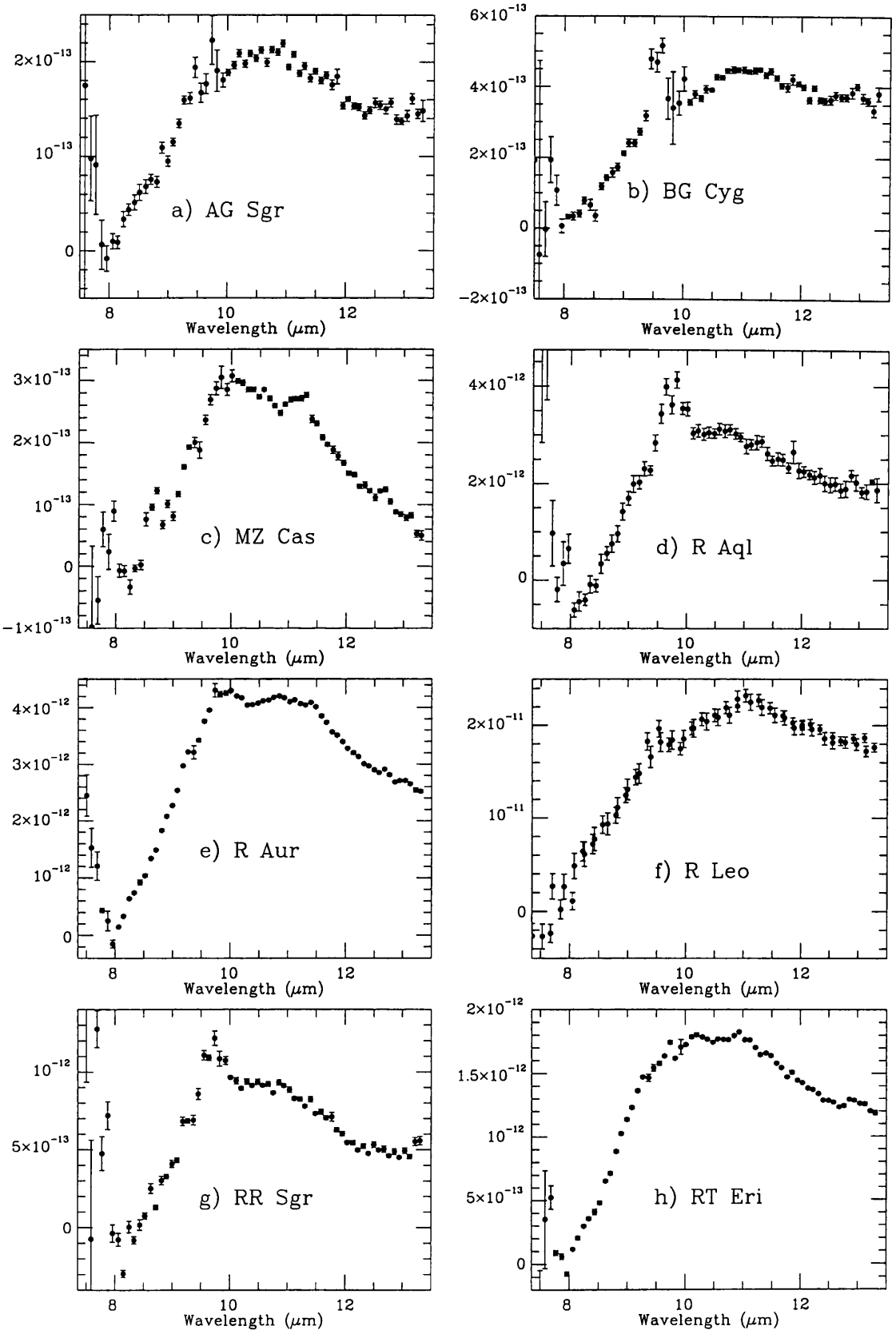

Figure 8.4: Continuum-subtracted spectra of Group O2 sources with a *broad* feature. Fluxes are in $\mathrm{Wm}^{-2}\mu\mathrm{m}^{-1}$

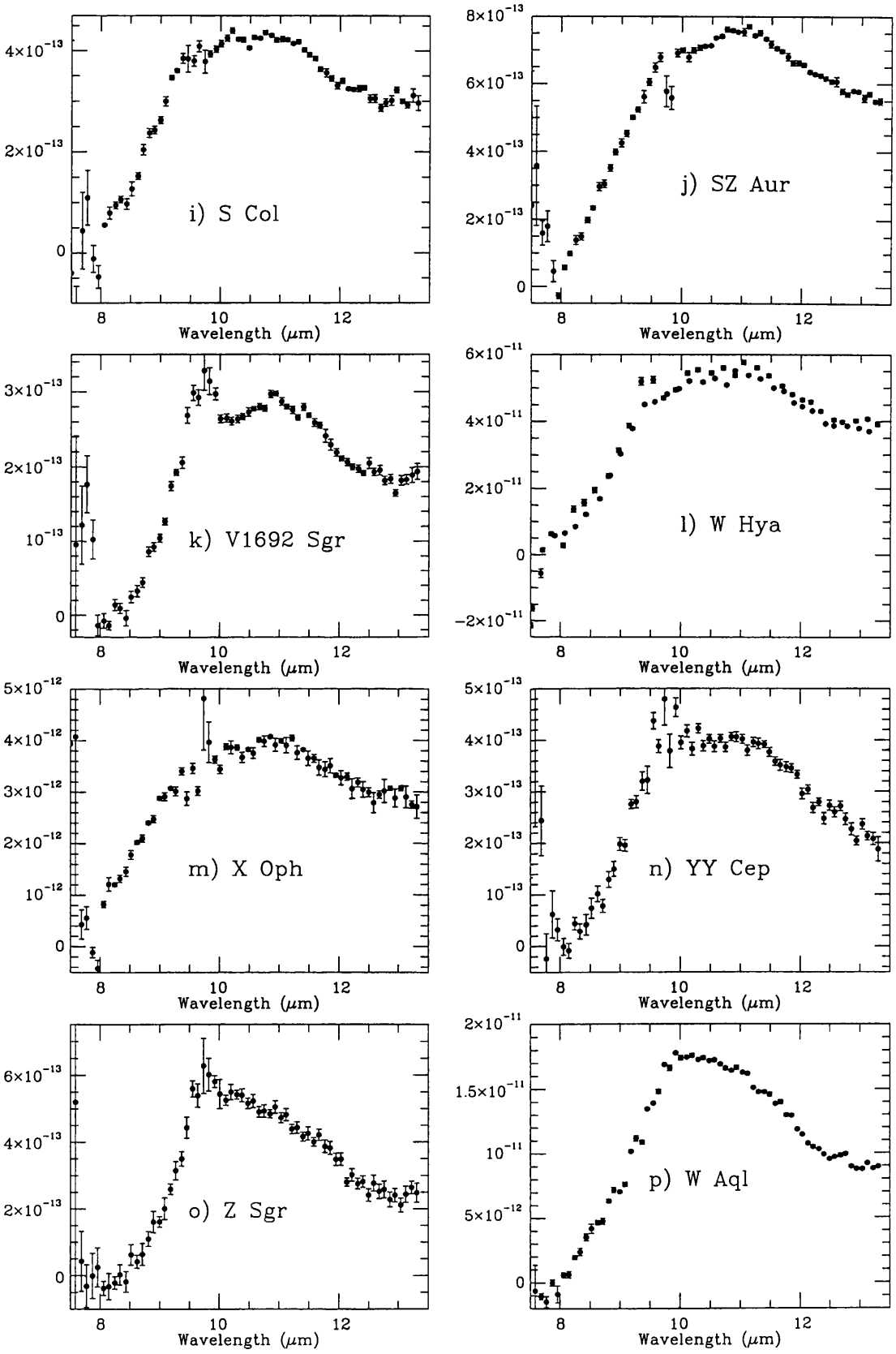

Figure 8.4: (Group O2 cont.)

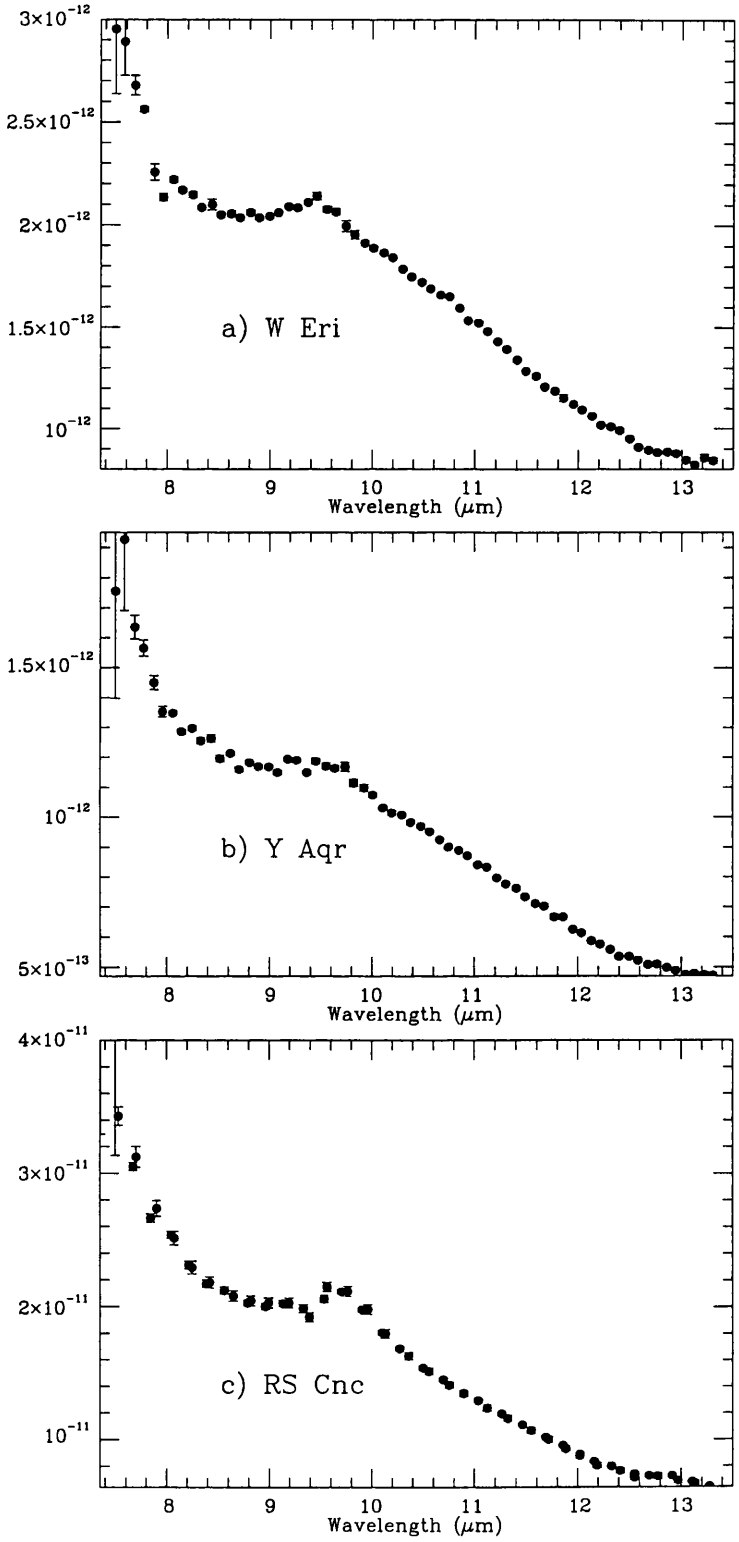

Figure 8.5: Flux-calibrated spectra of Group O3 sources with a *transition* feature. Fluxes are in $\mathrm{Wm}^{-2}\mu\mathrm{m}^{-1}$

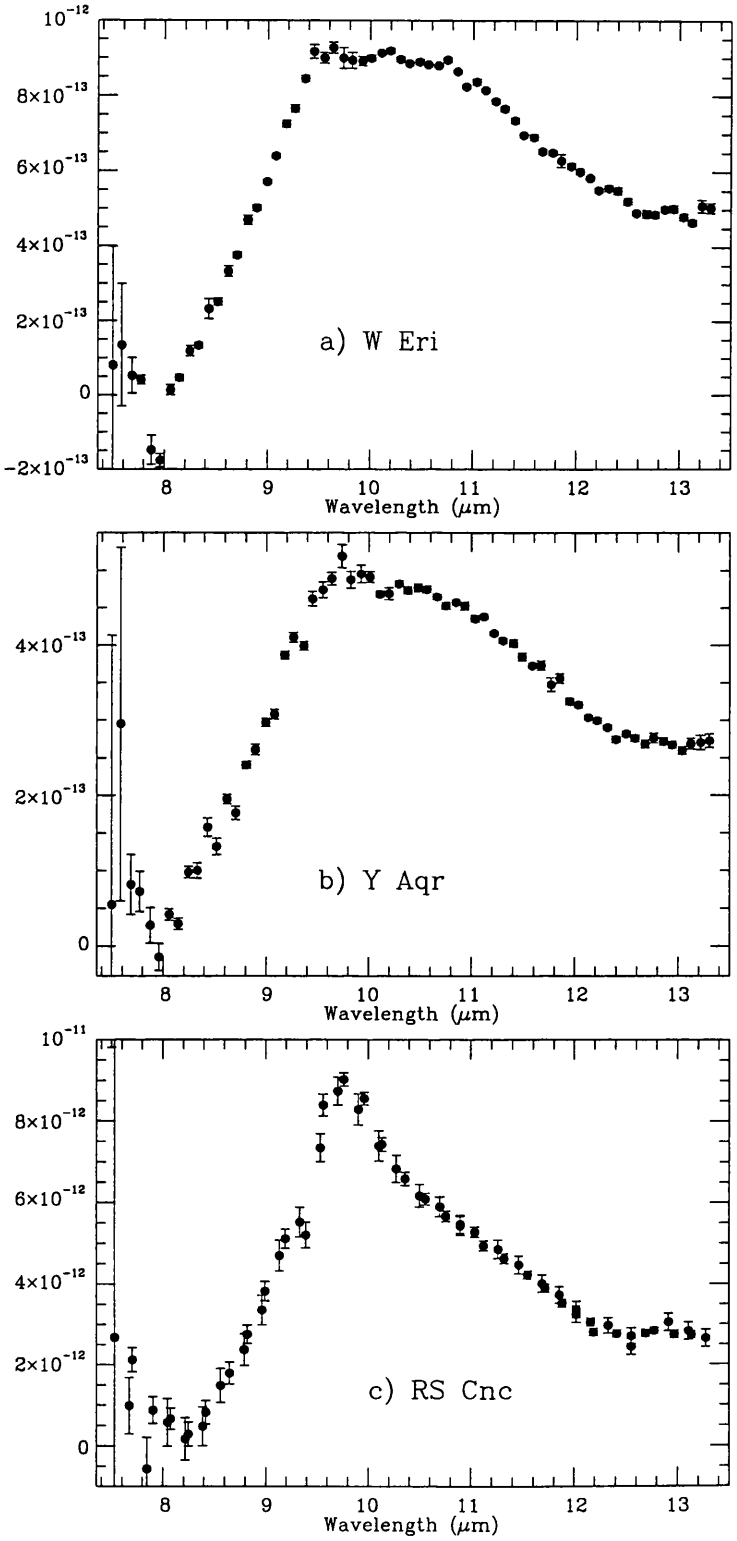

Figure 8.6: Continuum-subtracted spectra of Group O3 sources with a *transition* feature.

too broad to be incomplete ozone cancellation, and is therefore judged to be real and probably due to the onset of magnesium silicate formation. From this we deduce that the dust evolution has progressed at least as far as forsterite formation, and possibly further to ferromagnesian olivines.

8.3.4 The broad feature with a slightly stronger silicate component

Now the silicate component begins to get stronger. This category can be split into two distinct groups: *broad+sil*, in which the broad feature is still very strong relative to the silicate feature; and *sil+broad*, in which the silicate feature is stronger still and the broad feature begins to look more like a wing of the 9.7μm peak than a feature in its own right.

8.3.4.1 Group O4 - *broad+sil*

There are nineteen sources with a definite "silicate" feature on top of a strong broad feature. These are: BG Her, BX Eri, CH Pup, IK Tau, Mira, R Cae, RR Per, RW And, RX Boo, RZ Cyg, SAO 37673, SV Peg, SX Cyg, UW Cep, V462 Cyg, W Aqr, Y Cas, Z Ant and Z Cas, the flux-calibrated spectra of which can be seen in Fig. 8.7 and the continuum-subtracted spectra in Fig. 8.8. These spectra show a major peak at 9.7μm and a minor peak at 10.5-11.5μm, attributable to amorphous olivine and crystalline enstatite respectively. Several stars in this group (BX Eri, RX Boo, RZ Cyg, SAO 37673, SV Peg; Fig. 8.8b, i, j, k & l)) show a feature at 12.5-13.0μm, possibly attributable to silicon dioxide grains. The spectrum which is notably different in the continuum-subtracted illustration is that of Z Ant (Fig. 8.8r), in which the 11.5μm feature is stronger than the 9.7μm silicate feature. However, the components of the spectrum are essentially the same and it remains most naturally in this category.

8.3.4.2 Group O5 - *sil+broad*

This group contains six sources: AZ Mon, R Cas, RU Her, SAO 145652, Y Del and Y Lyn. Their flux-calibrated spectra are shown in Fig. 8.9. In these spectra the "9.7μm" silicate peak is stronger than before, and the broad component is difficult to separate.

8.3.5 Group O6 - *sil* - the silicate feature

For sources in this group, the "9.7μm" silicate feature definitely dominates the spectrum. There are 27 spectra with very strong silicate features: V635 Aql, IRC+10420, R Aqr,

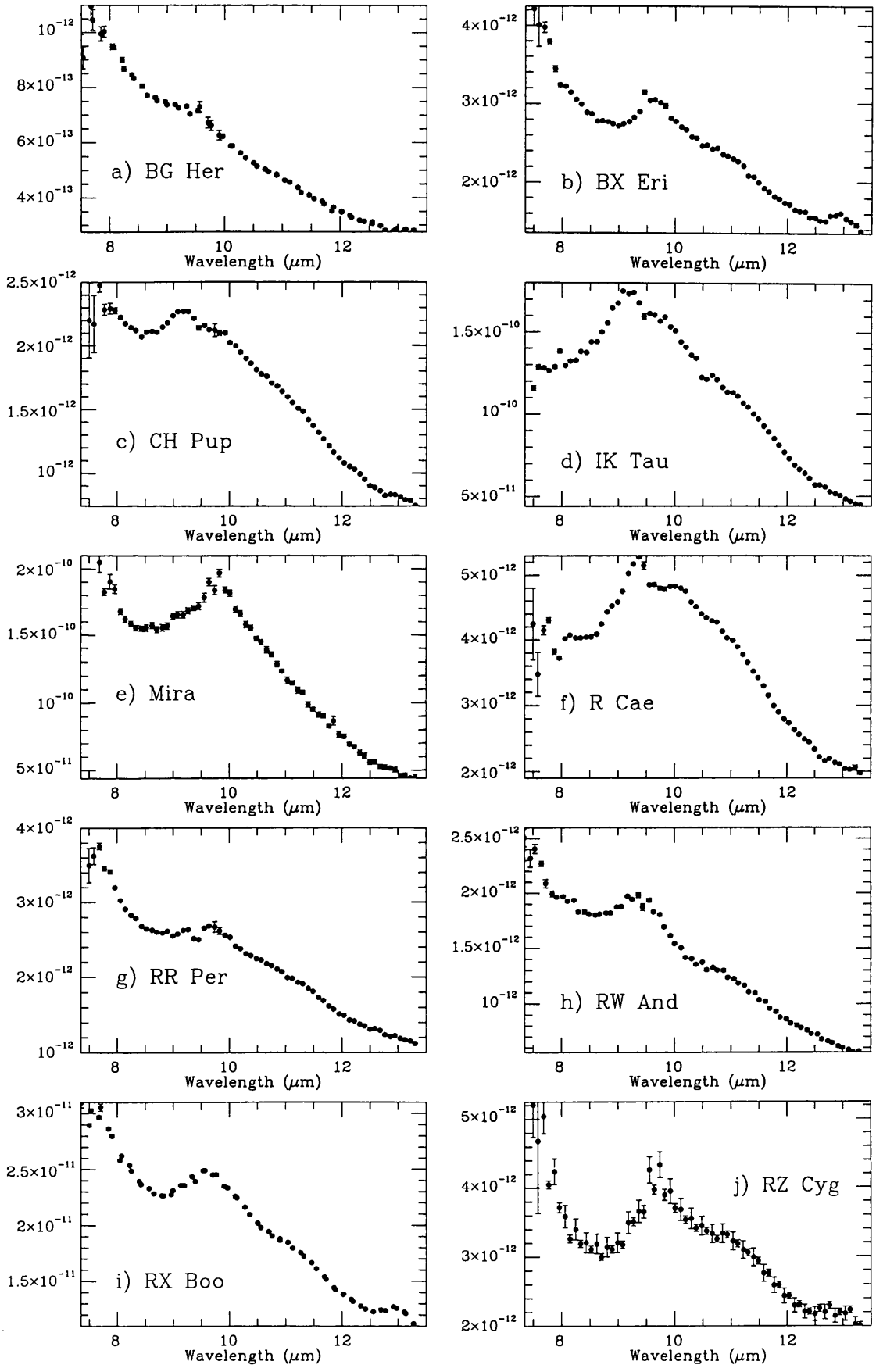

Figure 8.7: Flux-calibrated spectra of Group O4 sources with a *broad+sil* feature. Fluxes are in $\mathrm{Wm^{-2}\mu m^{-1}}$

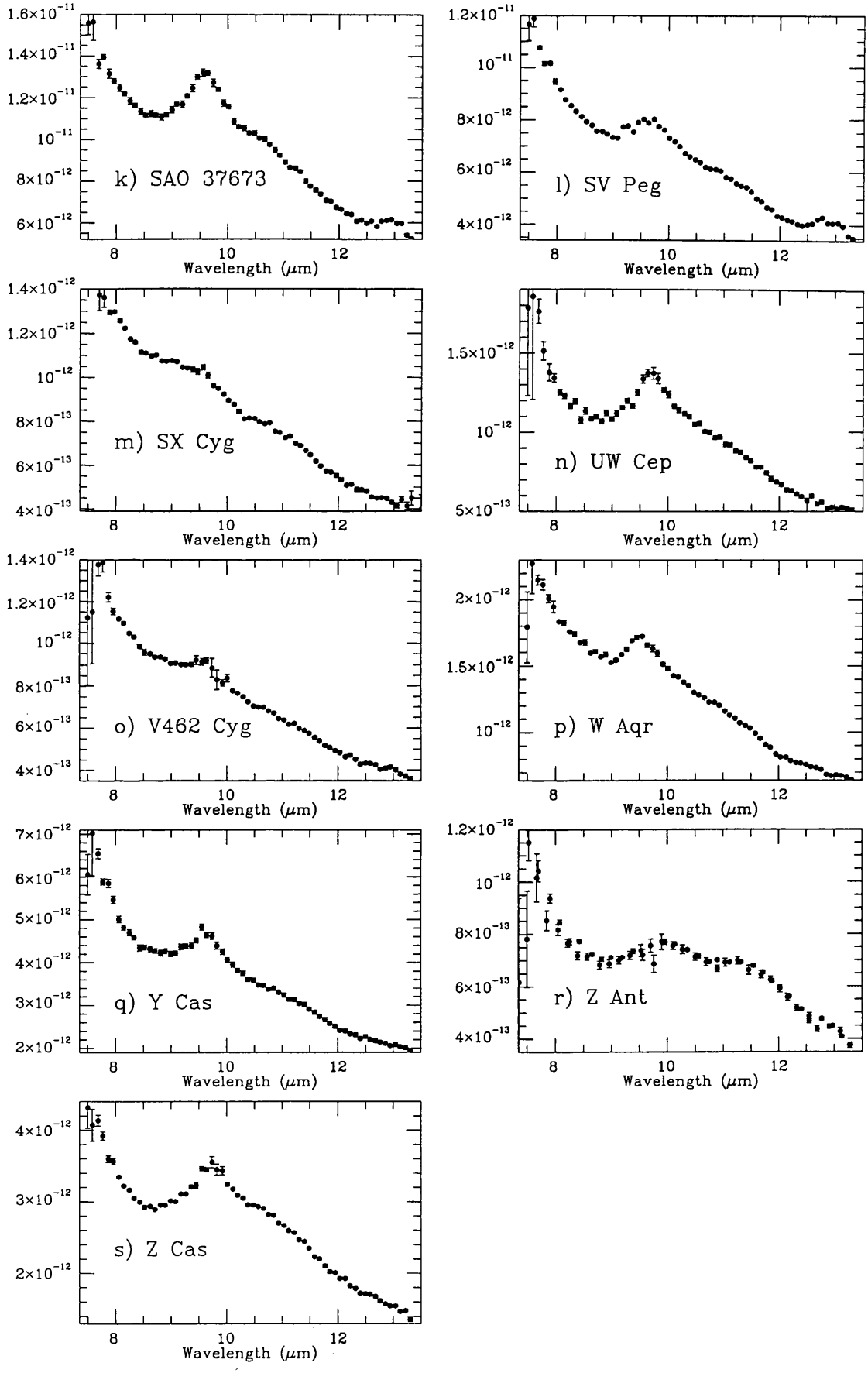

Figure 8.7: (Group O4 cont.)

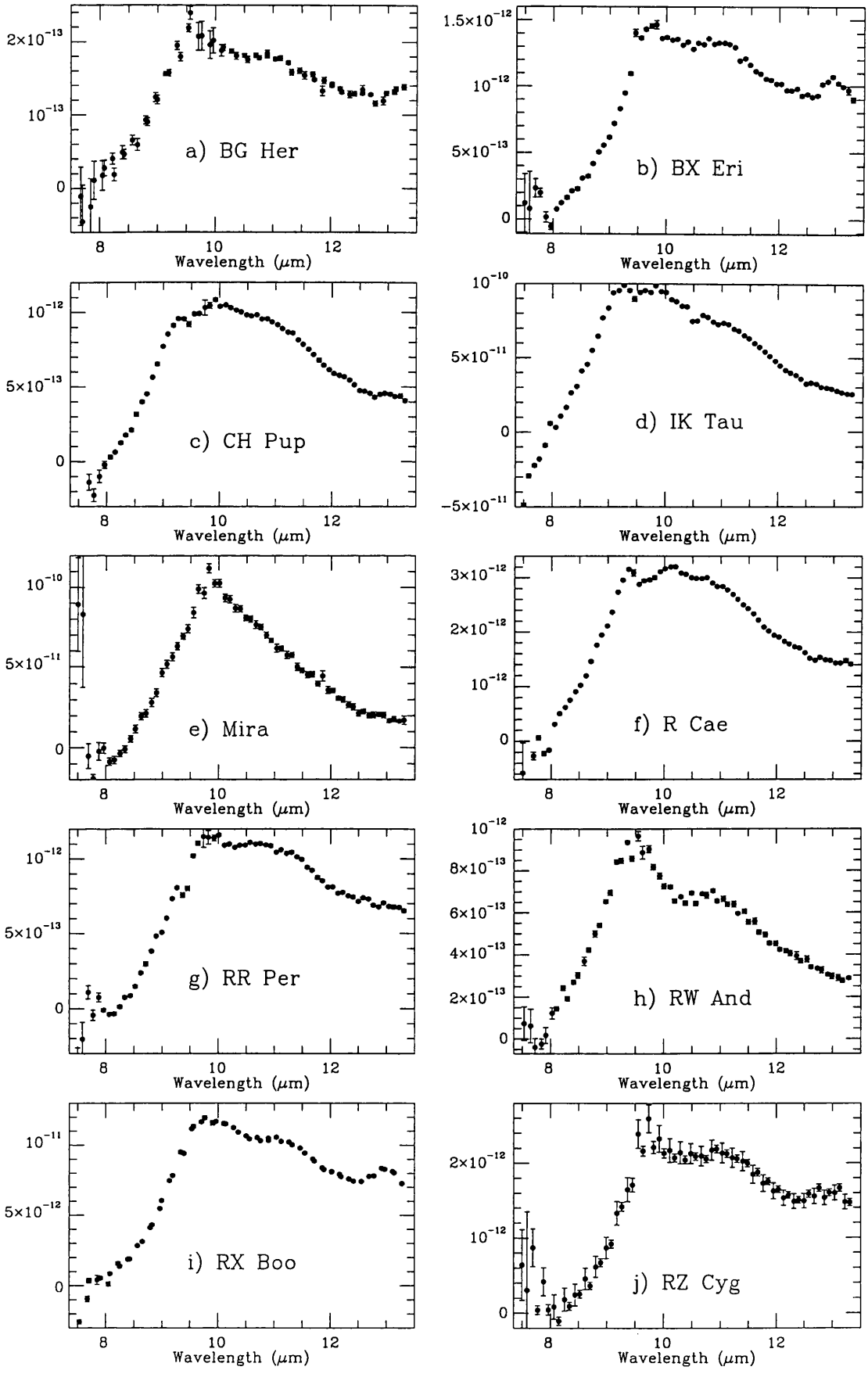

Figure 8.8: Continuum-subtracted spectra of Group O4 sources with a *broad+sil* feature.

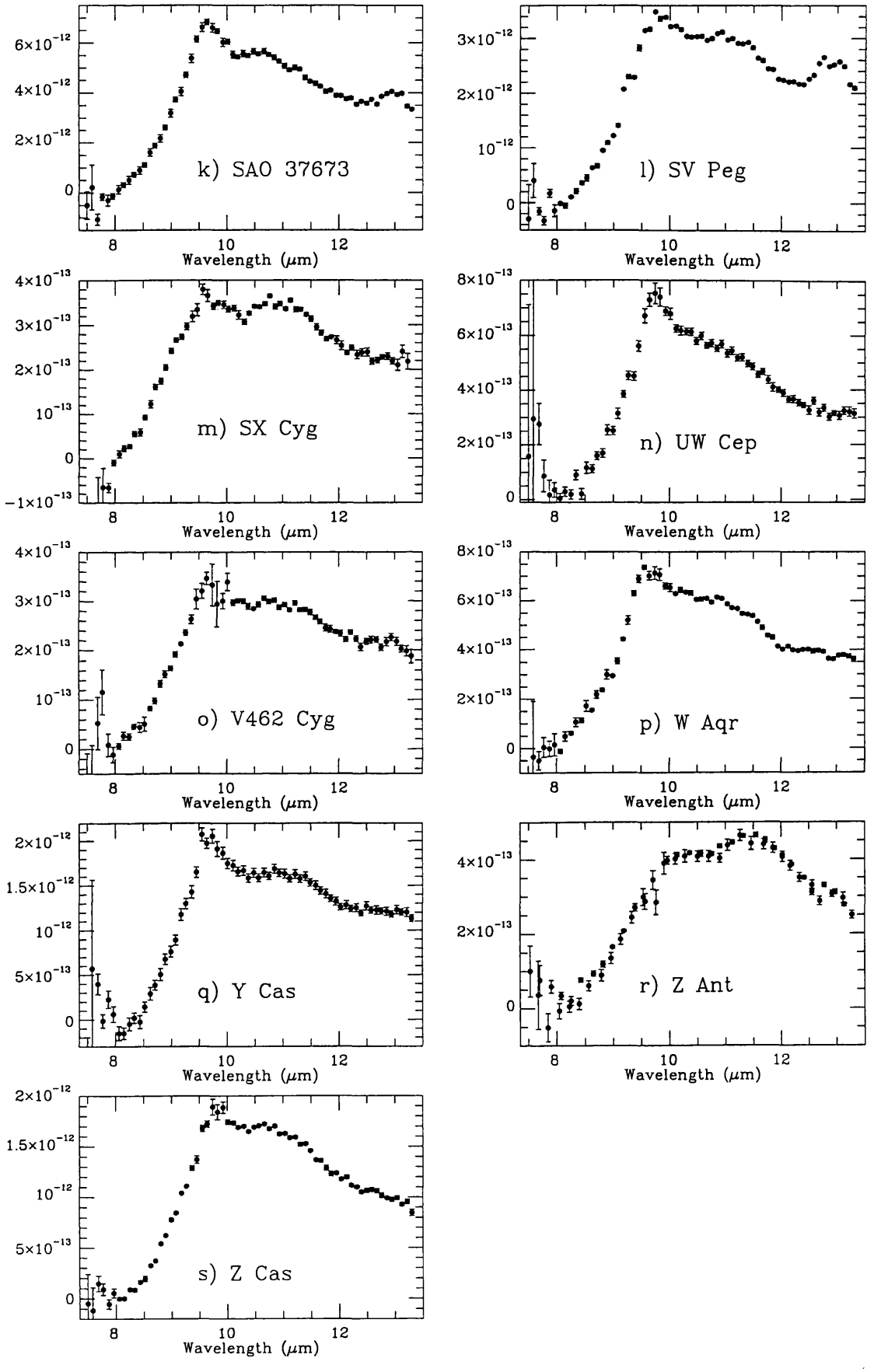

Figure 8.8: (Group O4 cont.)

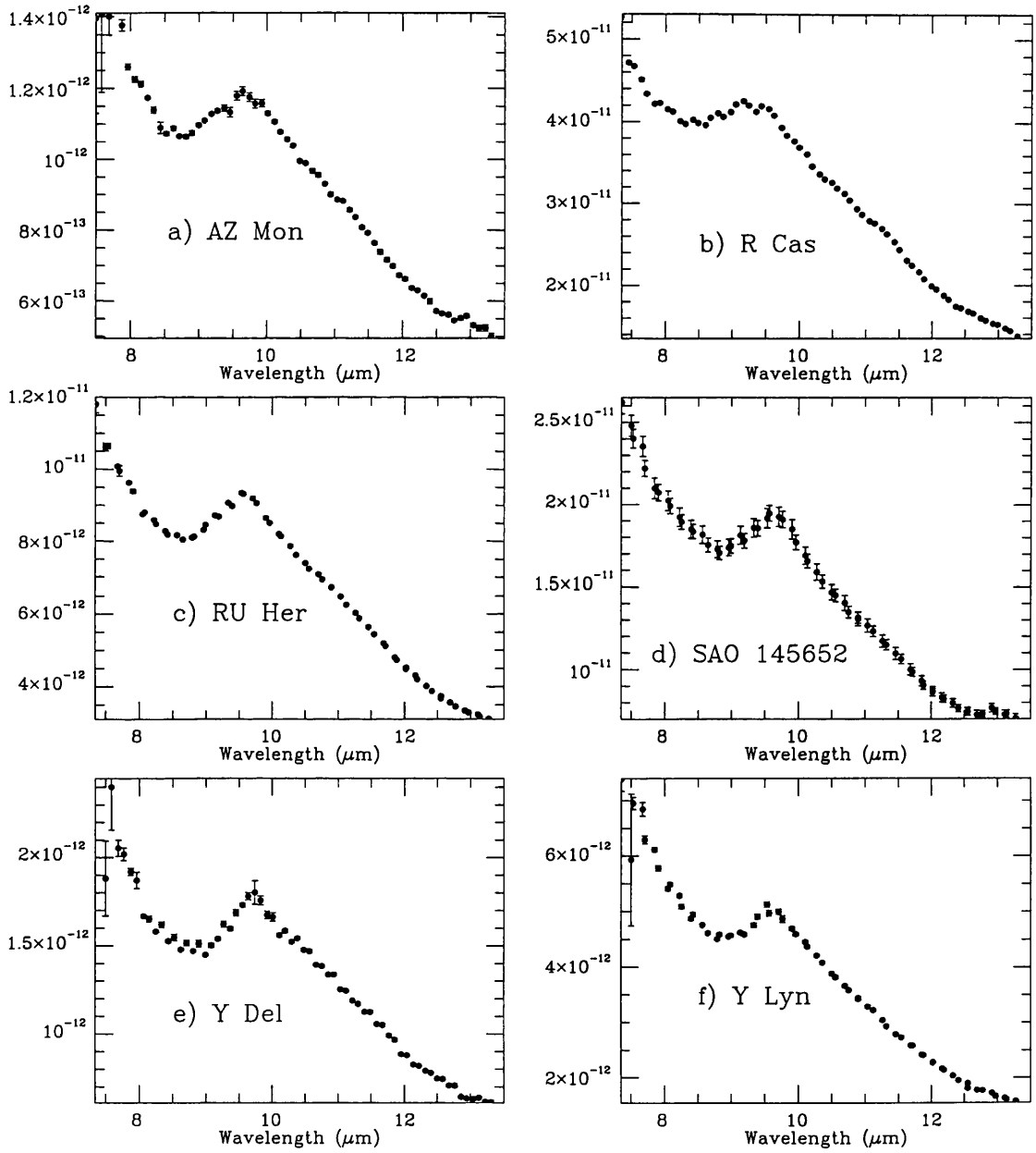

Figure 8.9: Flux-calibrated spectra of Group O5 sources with a *sil+broad* feature. Fluxes are in $\mathrm{Wm^{-2}\mu m^{-1}}$

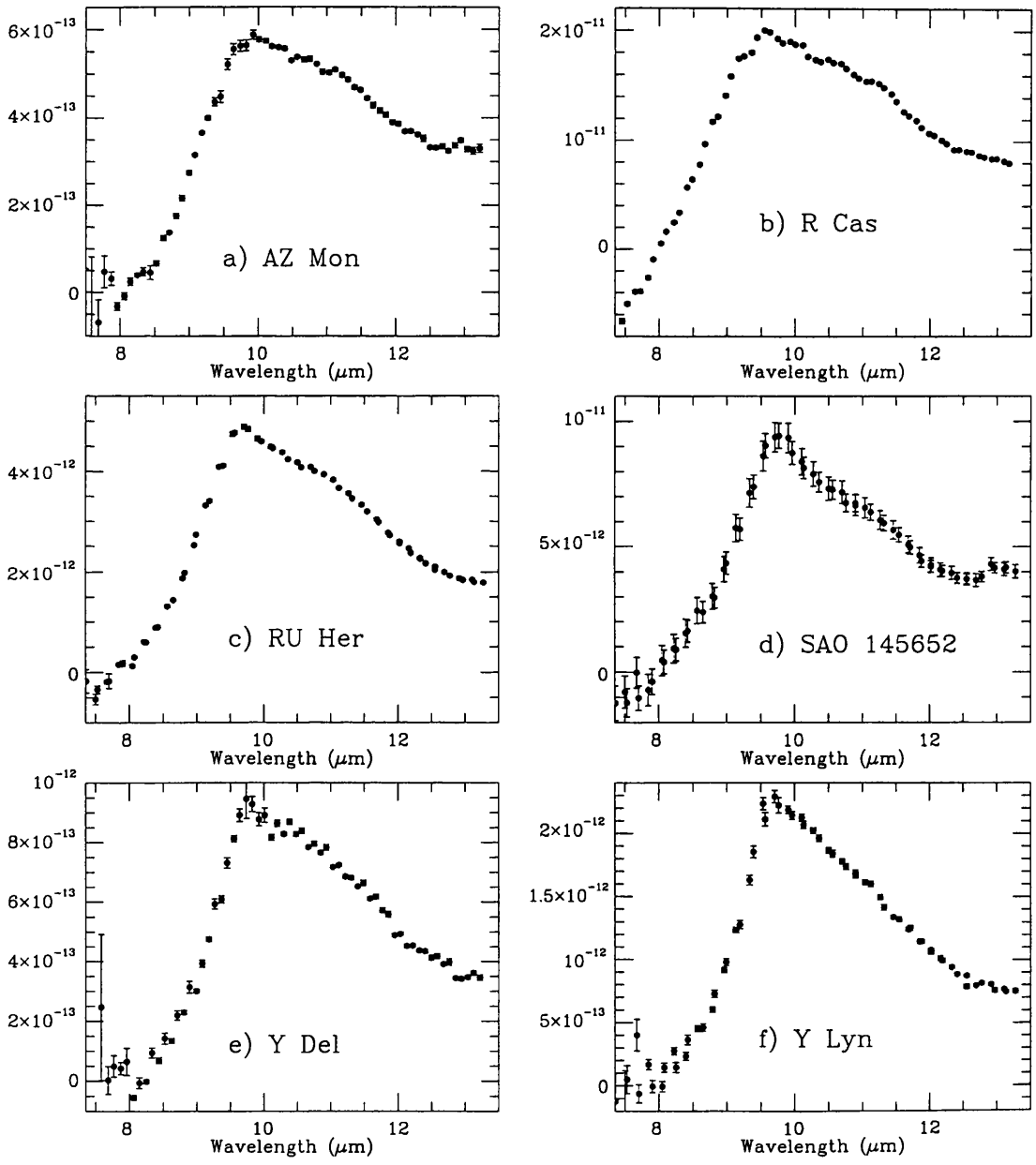

Figure 8.10: Continuum-subtracted spectra of Group 05 sources with a *sil+broad* feature.

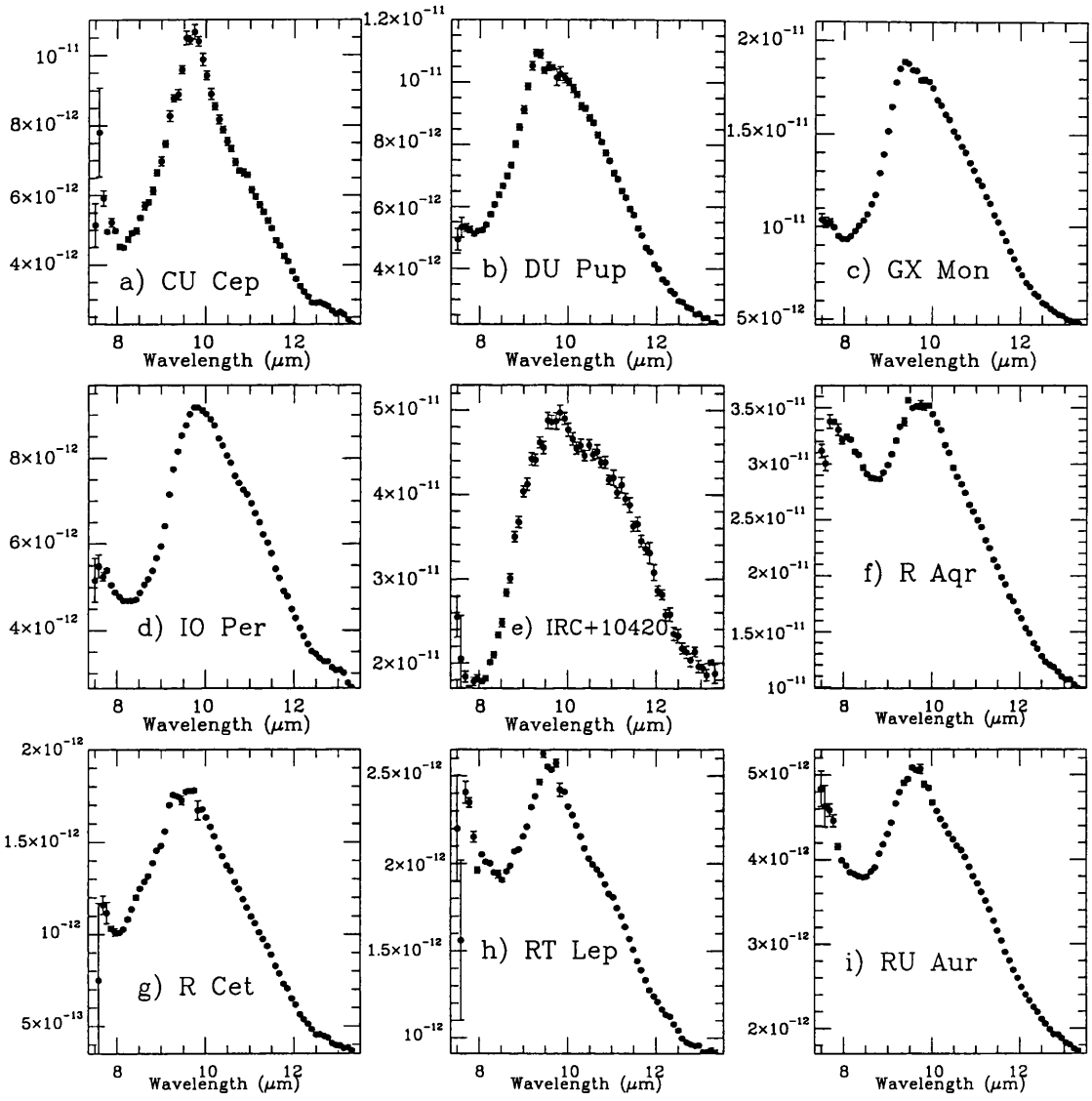

Figure 8.11: Flux-calibrated spectra of Group O6 sources with very strong silicate feature. Fluxes are in $\mathrm{Wm}^{-2}\mu\mathrm{m}^{-1}$

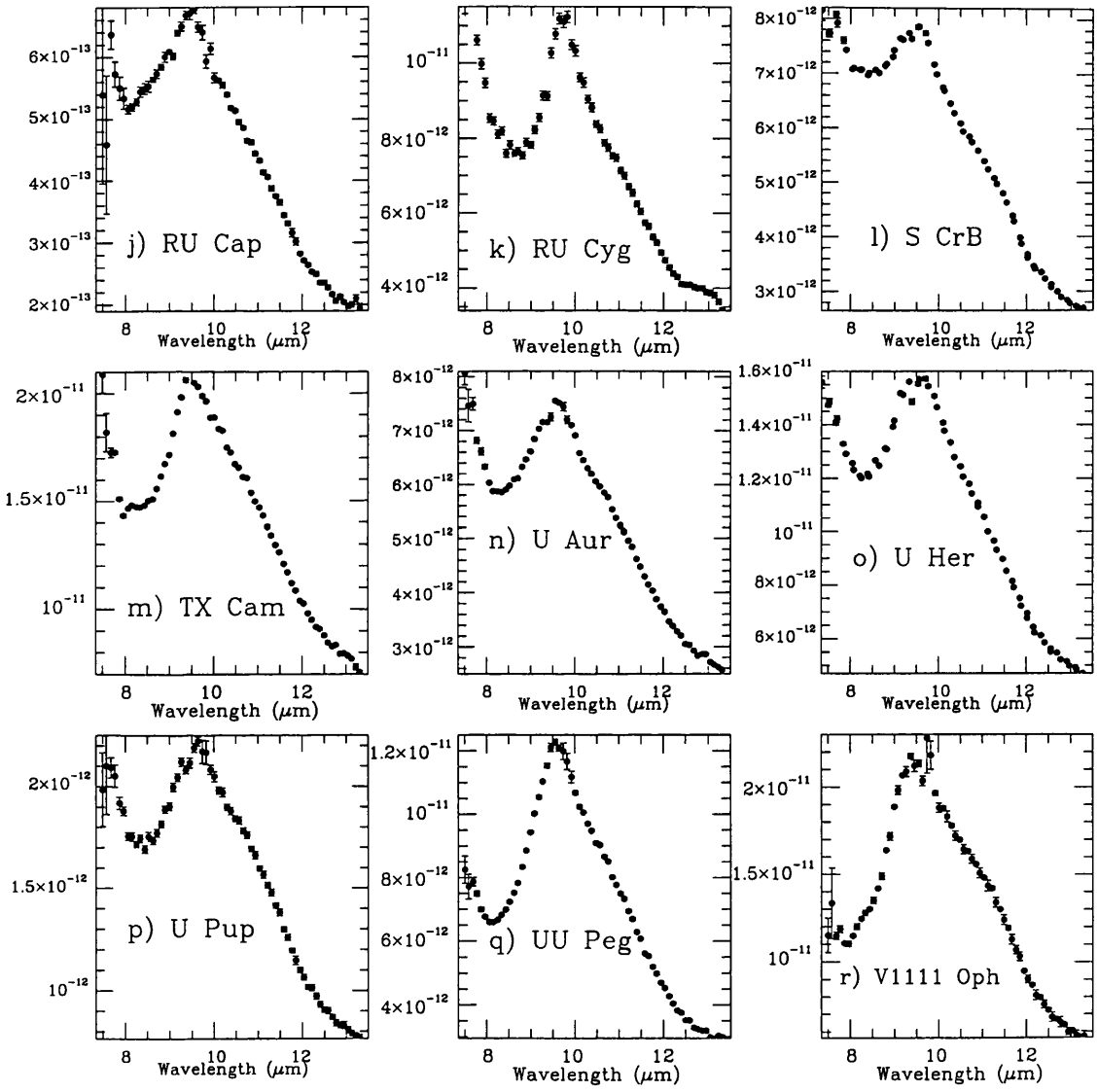

Figure 8.11: (Group O6 cont.)

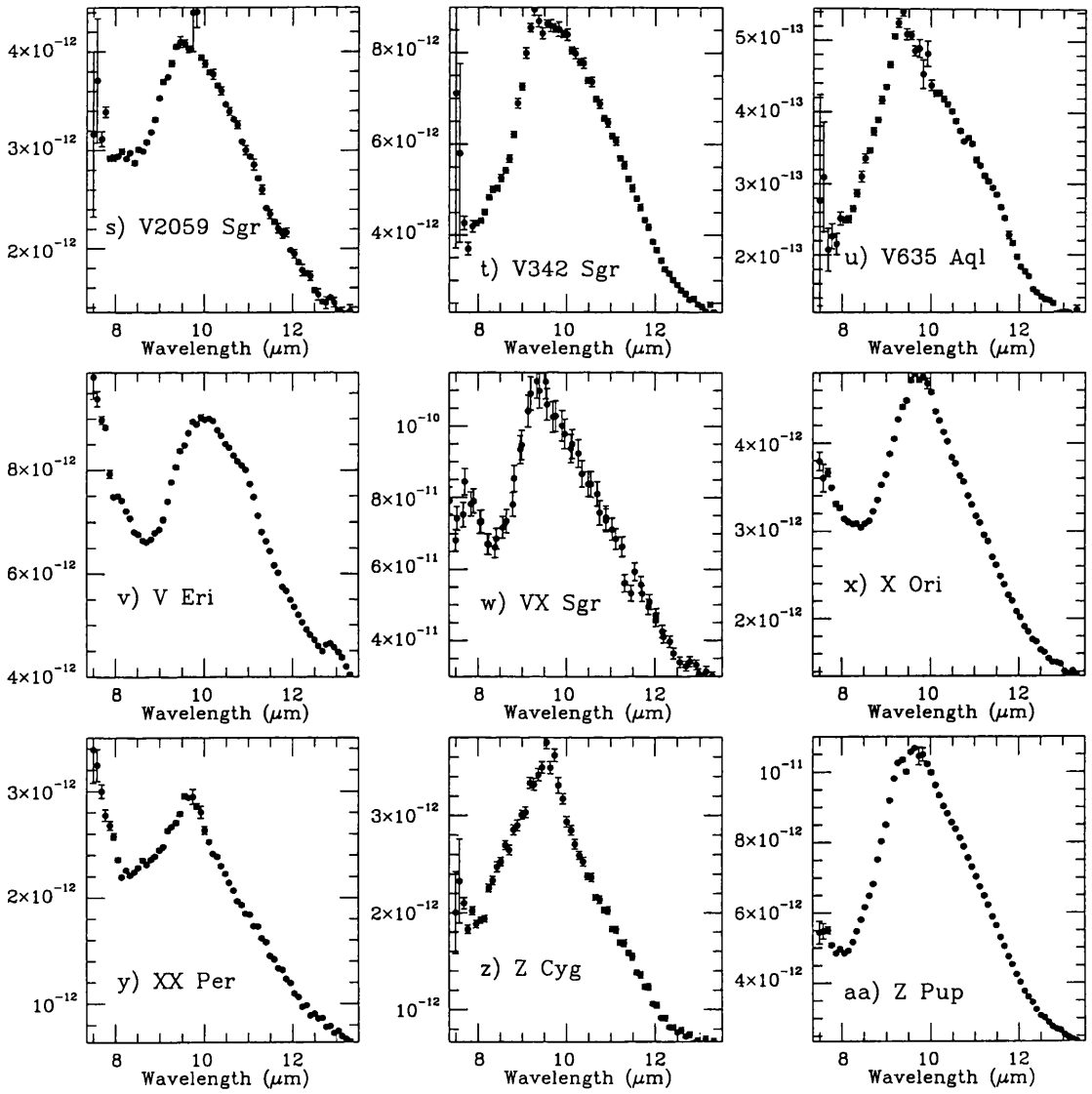

Figure 8.11: (Group O6 concluded)

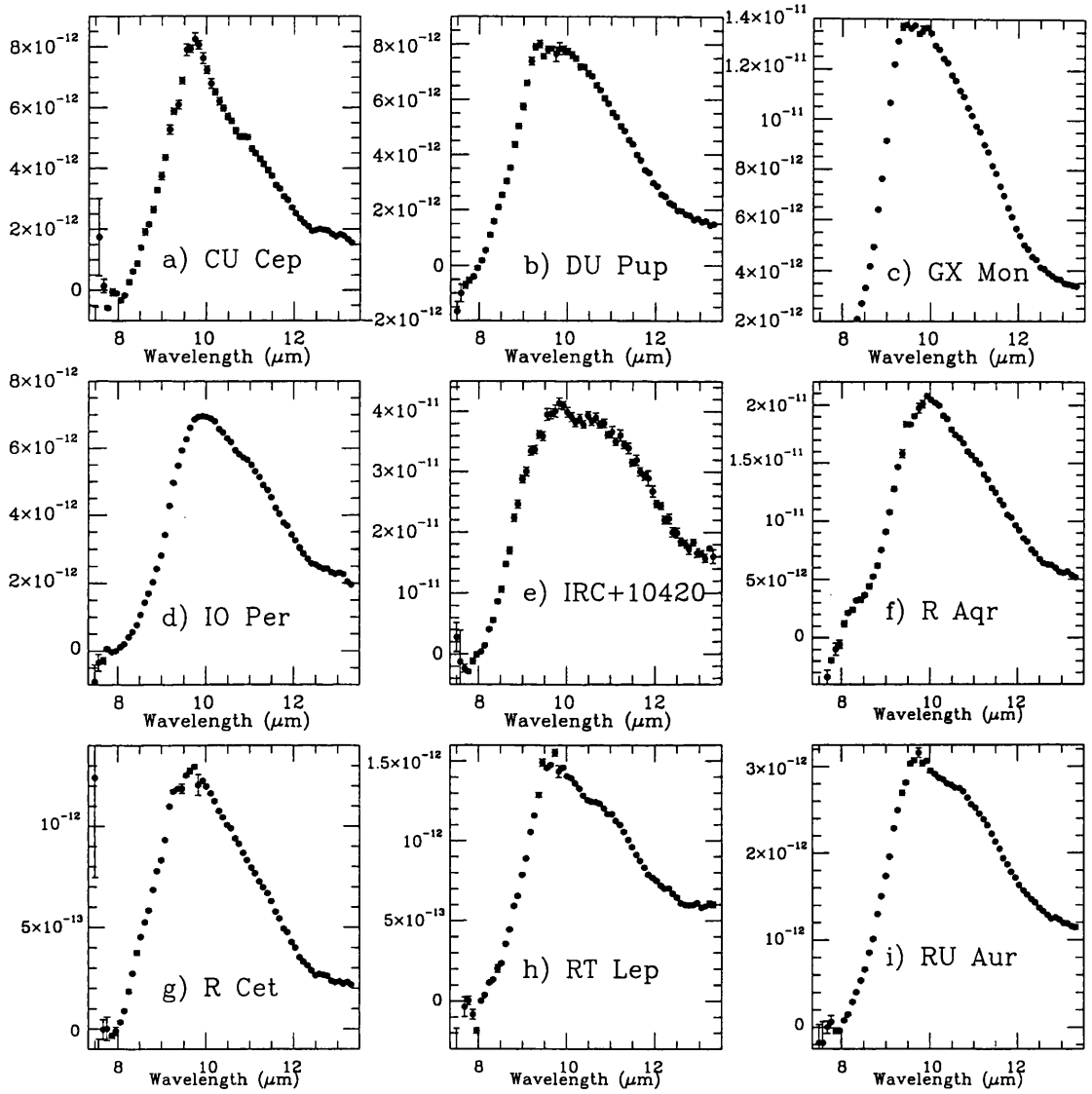

Figure 8.12: Continuum-subtracted spectra of Group O6 sources with very strong silicate feature. Fluxes are in $\mathrm{Wm}^{-2}\mu\mathrm{m}^{-1}$

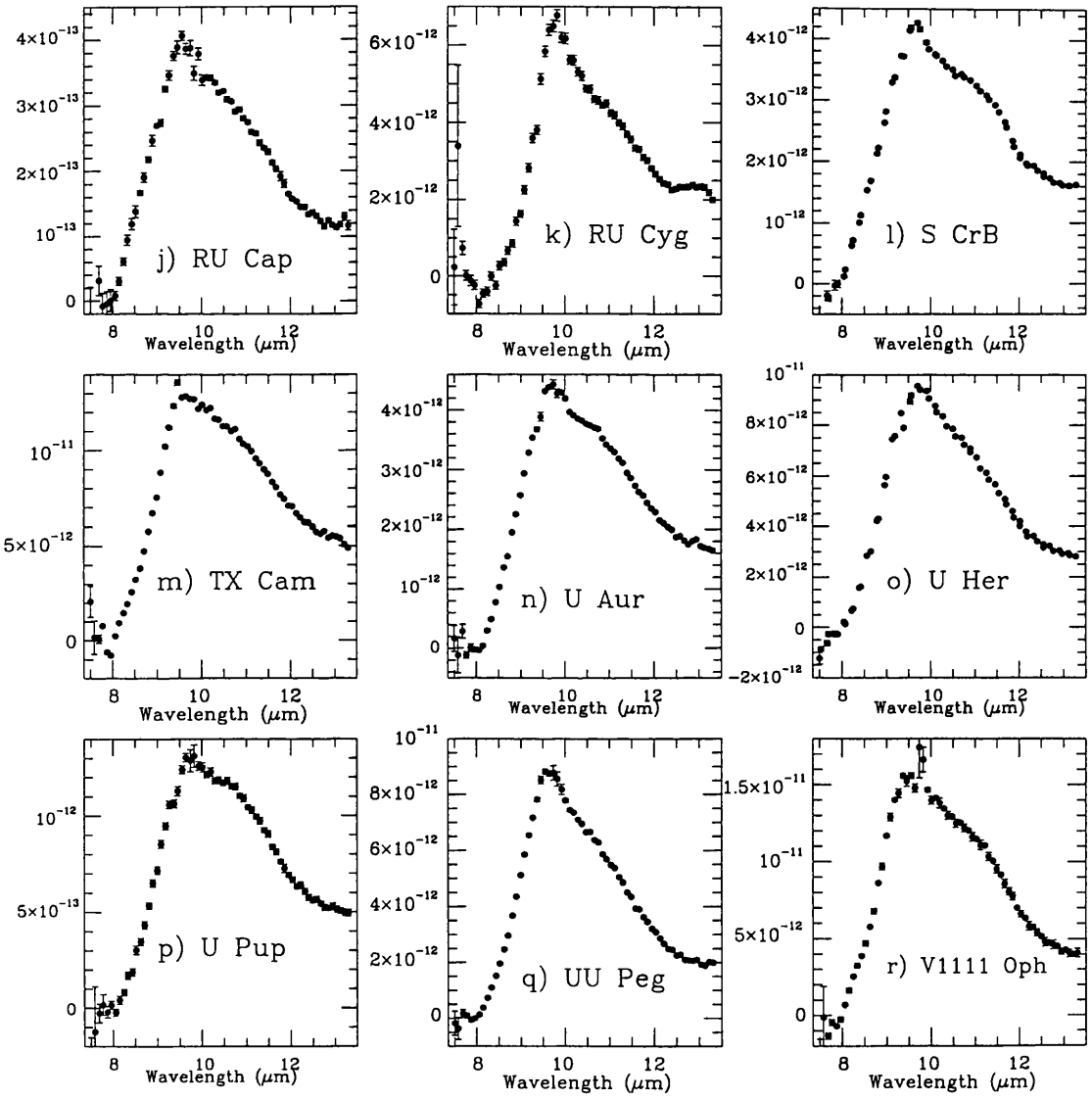

Figure 8.12: (Group O6 cont.)

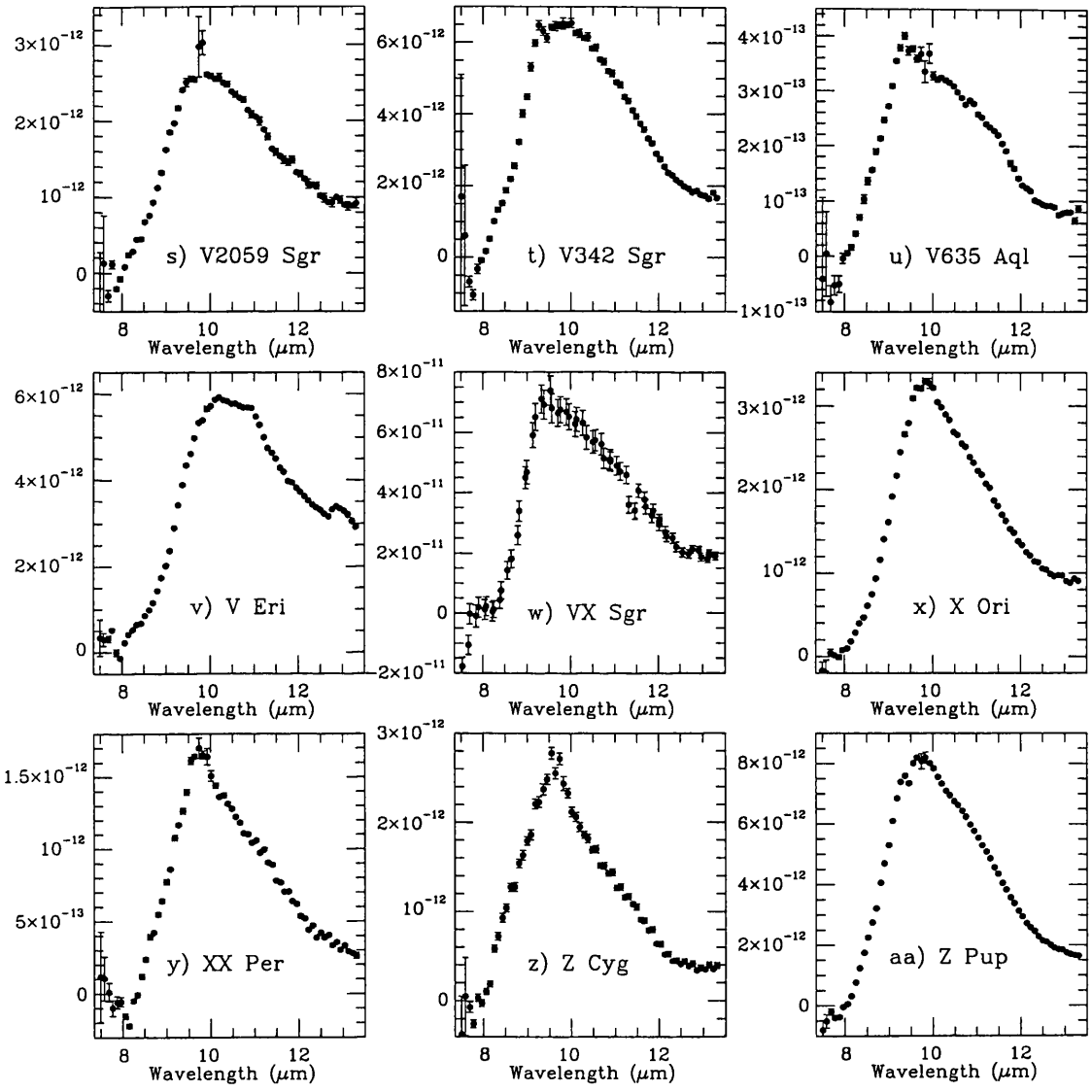

Figure 8.12: (Group O6 concluded)

RU Aur, U Aur, TX Cam, RU Cap, CU Cep, R Cet, S CrB, RU Cyg, Z Cyg, V Eri, U Her, RT Lep, GX Mon, V1111 Oph, X Ori, UU Peg, IO Per, XX Per, DU Pup, U Pup, Z Pup, VX Sgr, V342 Sgr and V2059 Sgr. The flux-calibrated spectra of these stars are shown in Fig. 8.11. All sources show a strong silicate feature which peaks at about 9.6-9.8μm, and no evidence of the broad feature remains. Several sources, DU Pup (Fig. 8.11b), GX Mon (Fig. 8.11c), V1111 Oph (Fig. 8.11r) and VX Sgr (Fig. 8.11w) show a superimposed peak at $\sim$ 9.2-9.35μm. The 9.6-9.8μm peak is attributable to any of a number of amorphous silicates, either pyroxenes or olivines, while the 9.2-9.35μm peak may be due to either some form of silicon dioxide or possibly iron-rich amorphous enstatite. However, according to Pégourié & Papoular (1985), pyroxenes with more than 10% iron are unlikely to be found around these stars. The exact amount of iron present depends on the precise redox conditions in the dust forming region, however, most of the iron content is expected to be in the form of metallic iron. Considerably more than 10% iron is needed to shift the peak of the feature to such a short wavelength. Therefore the 9.2-9.35μm feature is probably due to silicon dioxide.

8.3.6 T Cet

The spectrum of T Cet is an oddity (Fig 8.13). It does not fit into any of the groups described above. It can be better fit by silicate absorption than emission, at about 9.7μm, except for a small feature at about 13μm. Given the unusual nature of this spectrum it will be excluded from the sample, although this will be an interesting star to study in detail in the future.

8.3.7 Trends

Having classified the spectra into these six groups, it seemed desirable to look for trends in the properties of the sources with respect to possible dust evolution. As discussed in section 8.1, this has been attempted before, the only positive correlation being with the asymmetry of the light curve (VdJW; OdJW; LML90). I have compiled data on the spectral types of the sources[2], their mass-loss rates[3] and temperatures of the underlying blackbodies[4] and no correlation could be found. It may be that the data available does

[2] from Simbad

[3] from Skinner & Whitmore (1988a) and Hashimoto *et al.* (1990)

[4] found by fitting a blackbody to the spectrum at 8 & 13μm using Dipso

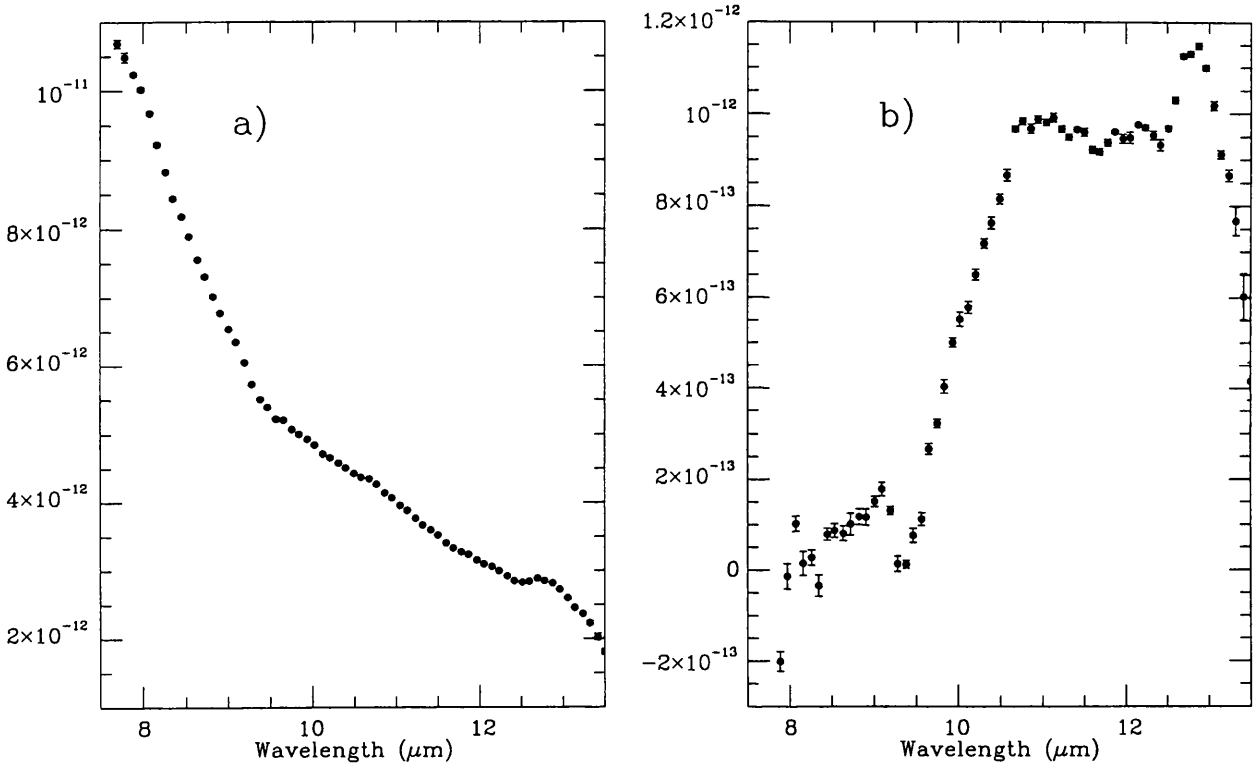

Figure 8.13: a) Flux-calibrated spectrum of T Cet. b) Continuum-subtracted spectrum of T Cet, produced by subtracting a 3000K blackbody from the flux-calibrated spectrum. Fluxes are in $\mathrm{Wm}^{-2}\mu\mathrm{m}^{-1}$

not allow the formation of a statistically meaningful conclusion, however these factors (mass-loss rate, spectral type) do not seem to be indicative of a star's dust evolutionary status. An attempt to follow the work of VdJW and LML90 on the correlation with the asymmetry of the light curve was also made. Information on the light curve asymmetry factor was taken from VdJW, Vardya (1989) and OdJW. Table 8.4 shows the sources for which the information was available on the asymmetry factor, f, and the group to which it has been assigned. There is a general tendency for those stars whose spectra which display no feature or *broad* features to have more symmetric light curves than those which have strong silicate features. The exception to this is Group O4, which contains one star (CH Pup) with a very asymmetric light curve (f=0.19). If this star is removed from the group, the average value of the asymmetry factor decreases with increasing group number, (i.e. increasing silicate feature strength; see Table 8.5). Previous authors (VdJW, LML90) have asserted that the light curve becomes more asymmetric as a star evolves. If the groupings defined here do indeed represent an evolutionary track, these results concur with the previous work.

8.4 Fitting the spectra

We have fitted the observed spectra using a χ^2-minimisation routine similar to that described in section 6.6. This routine has been equipped with the optical constants of the minerals, both crystalline and amorphous, expected to form around oxygen-rich stars. These are discussed and illustrated in the Catalogue of Mineral Spectra in chapter 5.

The χ^2-fitting program is equipped with a mechanism which sets minimum errors on the fluxes to be 3% of the flux. For the higher quality spectra used here, all spectra have errors <3% of the flux (except at the extremes of the wavelength window), and therefore the 1σ errorbars shown in the figures are smaller than the errors used for the χ^2 calculation. Even the noisiest spectra have errors of only ~2%. The fixing of the minimum errors explains why the reduced χ^2 values reported in the results tables do not always correspond to the real flux errors shown on the figures.

Fits were attempted for all observed spectra in the sample. They were undertaken in groups according to the classifications discussed in section 8.3. All attempted fits involved either a pure blackbody or a blackbody modified by a λ^{-1} emissivity, together with a least

Table 8.4: Correlation between the asymmetry of the light curve of a star and the evolution of its dust spectrum

Star	f^*	group	Star	f^*	group
R Peg	0.44	O1	RW And	0.36	O4
R Hya	0.49	O1	SX Cyg	0.41	O4
T Cas	0.56	O1	R Cae	0.41	O4
V Cas	0.48	O1	Y Cas	0.43	O4
			CH Pup	0.19	O4
RR Sgr	0.43	O2	IK Tau	0.50	O4
R Aur	0.51	O2	W Aqr	0.42	O4
X Oph	0.53	O2			
R Aql	0.42	O2	RU Her	0.42	O5
SZ Aur	0.46	O2	R Cas	0.40	O5
S Col	0.46	O2	Y Del	0.43	O5
BG Cyg	0.50	O2			
RT Eri	0.46	O2	Z Cyg	0.45	O6
Z Sgr	0.47	O2	Z Pup	0.38	O6
W Aql	0.36	O2	U Her	0.40	O6
R Aql	0.42	O2	S CrB	0.33	O6
			RU Aur	0.40	O6
W Eri	0.40	O3	U Aur	0.39	O6
Y Aqr	0.43	O3	RU Cap	0.36	O6
			R Cet	0.43	O6
			U Pup	0.41	O6

* The asymmetry factor f is defined as the ratio of the number of days between minimum light and the next maximum to the period in days.

The f-values are taken from VdJW, OdJW and Vardya (1989)

Table 8.5: Correlation between the asymmetry of the light curve of a star and the evolution of its dust spectrum - average f values for each group

Group	Average f-value
O1	0.49±0.07
O2	0.46±0.10
O3	0.42±0.02
O4*	0.42±0.06
O5	0.42±0.02
O6	0.39±0.06

For Group O4, the average f-value was evaluated excluding that for CH Pup

one mineral, although combinations of two, three or four minerals were also attempted.

The first attempted fits used corundum, the refractory oxide expected to form the nucleation seed for further dust species. There was only one source which could be fitted using corundum alone, which was T Cet, however, as mentioned above, T Cet has a spectrum unlike any other star in the sample and a much better fit was obtained using enstatite absorption. This star has been discarded from the sample. Fits were then attempted using corundum, forsterite, olivine, enstatite or pyroxene, or combinations of up to four of these minerals. For each of these minerals there are several sets of optical constant available from different laboratory investigations (see chapter 5 for references), each of which was tried. The differences and similarities between the various laboratory samples are discussed in chapter 5.

8.4.1 Results of the χ^2-fitting

The results of fitting five of the seven group O1 (*featureless*) spectra are shown in Table 8.6 and illustrated in Fig 8.14. The fitting-program was unable to find any fits to T Cas or R Hya. The best fits to RZ Ari, UX Aur and V Cas used only a blackbody, which is as expected for a featureless spectrum. Initially, the spectra of BU And and R Peg both required small amounts of amorphous forsterite emission to obtain fits. Furthermore, R Peg also required amorphous enstatite. However, it is probable that incomplete cancellation of the ozone feature contributed to the minor 9.7μm feature in the spectra of these two stars. Therefore, their spectra have also been fitted with the ozone feature edited out.

Table 8.6: Fits to group O1 (*featureless*) spectra

Source	Blackbody	T_{BB}	χ^2 *
BU And	BB	440	0.945
R Peg	BB	510	0.881
RZ Ari	BB	2496	1.184
UX Aur	BB	1194	1.014
V Cas	BB	740	0.777
T Cas	no fit	1000 & 395*	—
R Hya	no fit	560*	—

* These temperatures come from the fitting of a blackbody to the continuum in Dipso.

* The errors used to calculate the reduced χ^2 are set to 3% of the flux if the 1σ error on the flux is less than this value. The errors shown in Fig 8.14 are 1σ. In all these spectra, the majority of points have errors that are <3% of the flux, the exceptions being for those points at the edges of each spectra and in the ozone region (9.4–9.9μm). Thus the 1σ error bars shown in the fits are not necessarily the errorbars used by the fitting program.

These are the results shown here. With the ozone region omitted, these two spectra can be fitted using only a blackbody. There is no evidence for any refractory oxide dust (e.g. Al_2O_3, SiO_2) expected to be the first dust type to be produced by such stars.

The results of fitting the sixteen group O2 (*broad* feature) spectra, are shown in Table 8.7. In this group, only one source could not be fitted by the χ^2-fitting routine: W Hya (Fig. 8.15l). The fits to the remaining 14 spectra are also shown in Fig. 8.15. SZ Aur, AG Sgr, Z Sgr and V1692 Sgr (Fig. 8.15j, a, o & k) were fitted using a combination of amorphous forsterite and amorphous enstatite; R Aur and R Aql (Fig. 8.15e & d), were fitted with two versions of amorphous forsterite; and X Oph, S Col, RT Eri, R Leo and RR Sgr (Fig. 8.15m, i, h, f & g) were fitted with amorphous enstatite. W Aql, MZ Cas, YY Cep and BG Cyg (Fig. 8.15p, c, n & b) were fitted with single amorphous forsterites. The fit to RT Eri (Fig. 8.15h) was improved by adding obsidian (amorphous SiO_2), and the fit to R Leo (Fig. 8.15f) was improved by adding corundum. The latter two sources provide the only evidence so far of any refractory oxide dust around these stars.

The three group O3 (*transition*) spectra also required amorphous magnesium silicates to

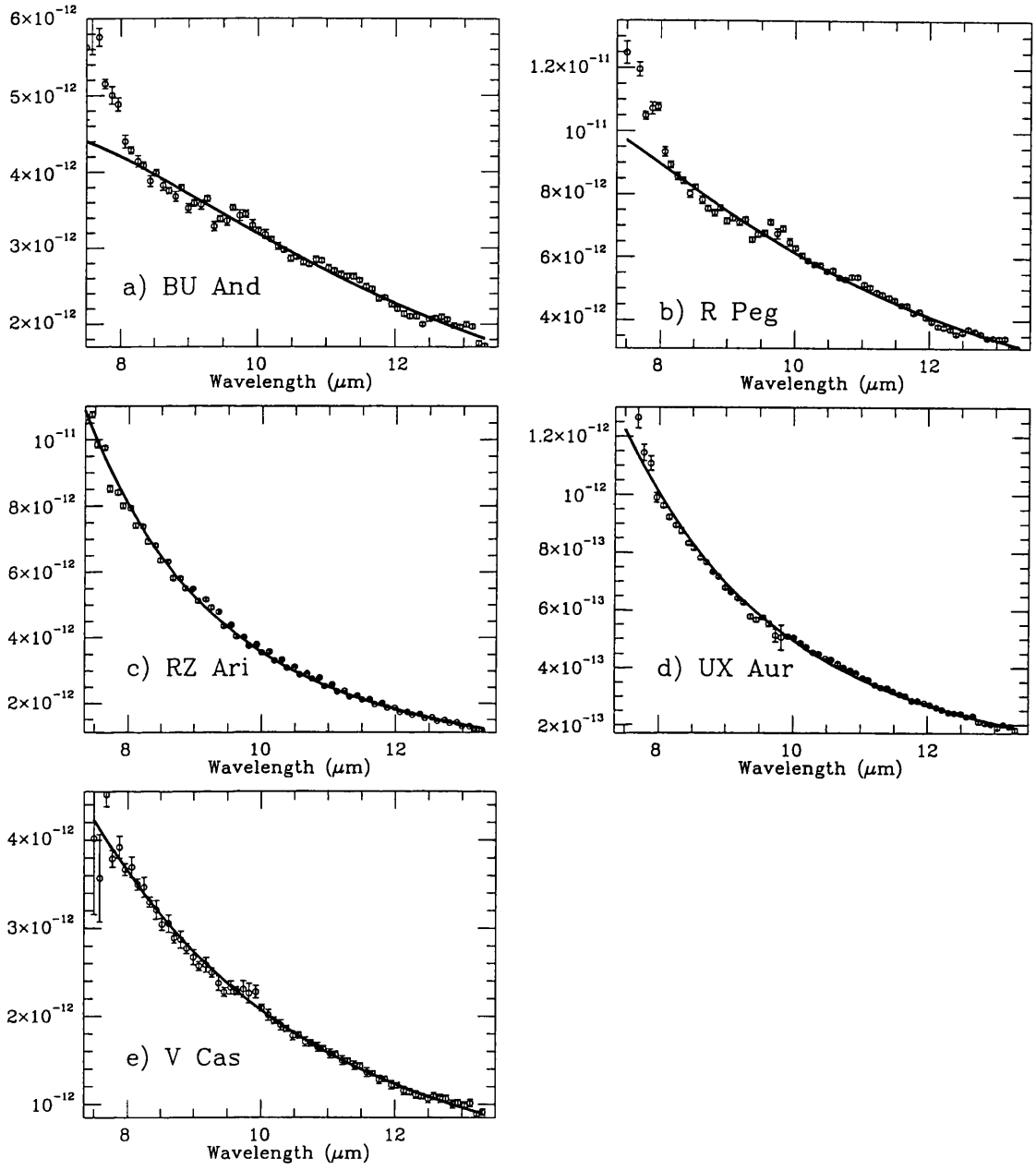

Figure 8.14: Flux-calibrated spectra of Group O1 (*featureless*) sources with best χ^2-fits. The errors used to calculate the reduced χ^2 are set to 3% of the flux if the 1σ error on the flux is less than this value. Thus the 1σ error bars shown here are not necessarily the errorbars used by the fitting program.

Table 8.7: Fits to group O2 (*broad feature*) stars

Source	Blackbody	Silicate Type	T_{BB}	$T_{Sil}1$	$T_{Sil}2$	χ^2 *
W Aql	BB	Fo(K&H)	780	125	—	0.301
BG Cyg	BB*E	Fo(K&H)	2260	90	—	1.158
MZ Cas	BB*E	Fo(Jena)	1295	165	—	1.277
YY Cep	BB*E	Fo(Jena)	1045	160	—	1.715
R Aql	BB*E	Fo(Jena) & Fo(K&H)	3500	255	55	1.232
R Aur	BB*E	Fo(Jena) & Fo(K&H)	2650	65	150	1.377
SZ Aur	BB*E	Fo(Jena) & Enst(Day)	1020	60	120	0.105
AG Sgr	BB*E	Fo(K&H) & Enst(Day)	1195	160	—	0.908
Z Sgr	BB*E	Fo(K&H) & Enst(Day)	3500	280	90	0.796
V1692 Sgr	BB*E	Fo(K&H) & Enst(Day)	2335	80	180	2.774
X Oph	BB*E	Enst(Day)	1090	100	—	0.711
S Col	BB*E	Enst(Day)	950	130	—	0.569
RR Sgr	BB*E	Enst(Day)	3500	150	—	2.751
RT Eri	BB*E	Enst(Day) & Obsid	1200	110	130	0.603
R Leo	BB*E	Enst(Day) & Cor2	1650	175	175	0.328
W Hya	—-	—-	460†	—	—	——

† W Hya could not be fit even with a simple blackbody energy distribution - temp from fitting in Dipso)

* The errors used to calculate the reduced χ^2 are set to 3% of the flux if the 1σ error on the flux is less than this value. The errors shown in Fig 8.15 are 1σ. In all these spectra, the majority of points have errors that are <3% of the flux, the exceptions being for those points at the edges of each spectra and in the ozone region (9.4–9.9μm). Thus the 1σ error bars shown in the fits are not necessarily the errorbars used by the fitting program

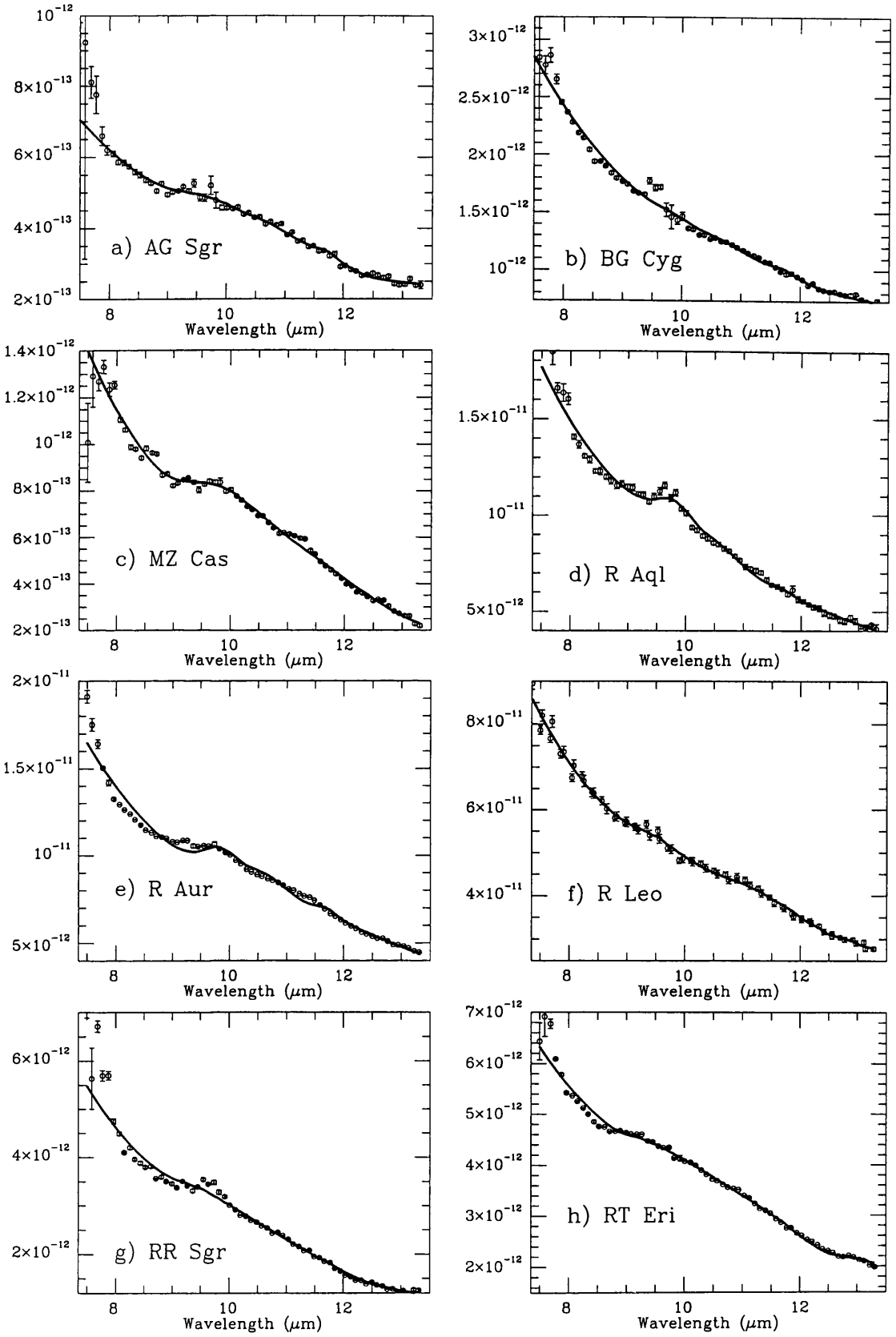

Figure 8.15: Flux-calibrated spectra of Group O2 (*broad feature*) sources with best χ^2-fits. Fluxes are in $\mathrm{Wm^{-2}\mu m^{-1}}$. The errors used to calculate the reduced χ^2 are set to 3% of the flux if the 1σ error on the flux is less than this value. Thus the 1σ error bars shown here are not necessarily the errorbars used by the fitting program.

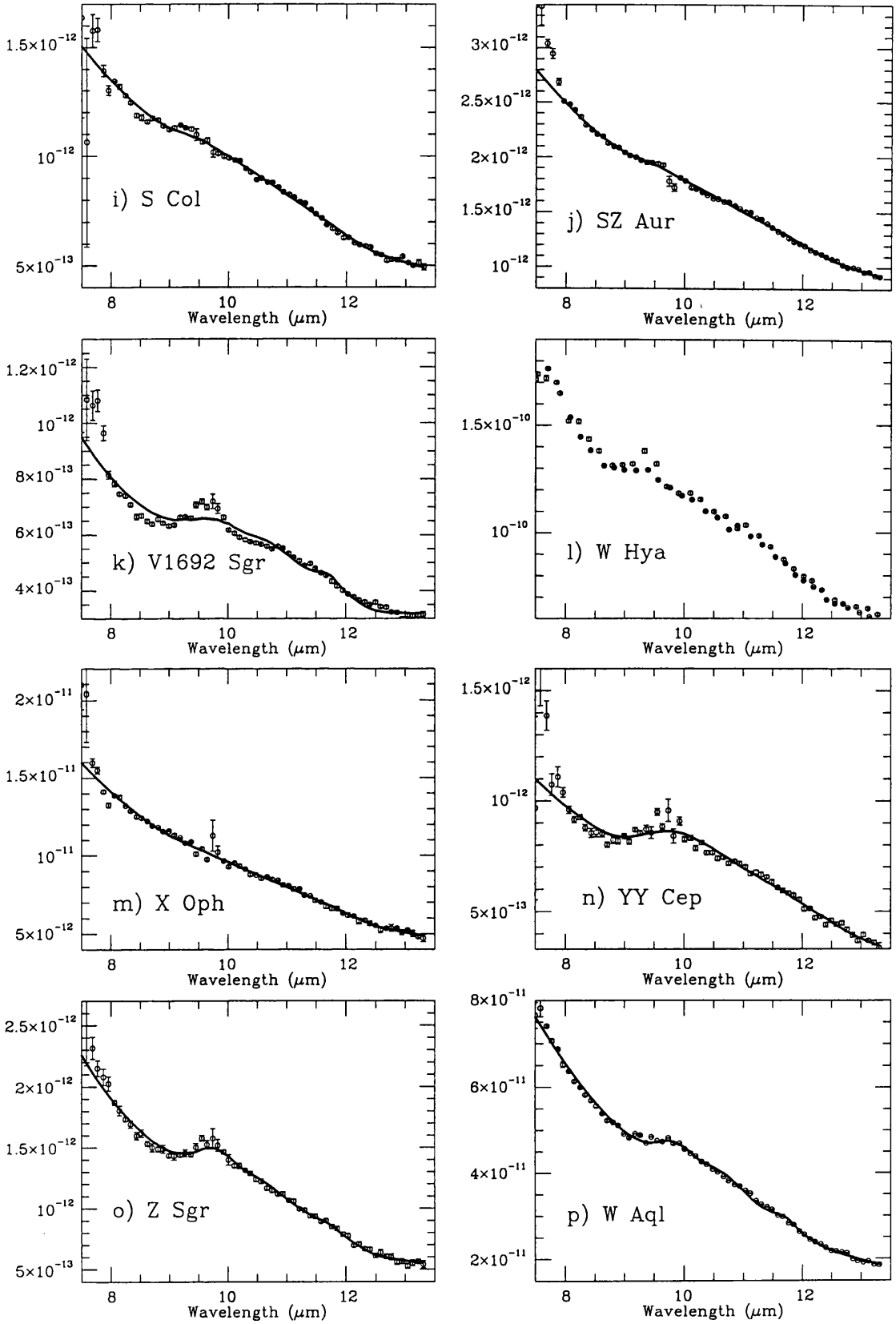

Figure 8.15: (Group O2 cont.)

Table 8.8: Fits to group O3 (*transition* feature) stars

Source	Blackbody	Silicate Type	T_{BB}	$T_{Sil}1$	$T_{Sil}2$	χ^2 *
RS Cnc	BB*E	Fo(K&H)	3500	375	—	1.142
W Eri	BB*E	Enst(Day)	975	165	—	0.708
Y Aqr	BB*E	Enst(Day)	1170	150	—	0.518

* The errors used to calculate the reduced χ^2 are set to 3% of the flux if the 1σ error on the flux is less than this value. The errors shown in Fig 8.16 are 1σ. In all these spectra, the majority of points have errors that are <3% of the flux, the exceptions being for those points at the edges of each spectra and in the ozone region (9.4–9.9μm). Thus the 1σ error bars shown in the fits are not necessarily the errorbars used by the fitting program.

obtain good fits. RS Cnc (Fig 8.16c) was fit using amorphous forsterite, whereas W Eri and Y Aqr (Fig 8.16a & b) were fitted using amorphous enstatite. These fits are shown in Fig 8.16 and the details are given in Table 8.8

The second biggest group in this sample is O4 (*broad+sil*) comprising nineteen spectra. At this stage, fitting the spectra becomes much more complicated. Several spectra could be fitted by several different combinations of minerals. For instance, both RX Boo (Fig. 8.17i) and SX Cyg (Fig. 8.17m) could be equally well fit using a combination of amorphous forsterite and amorphous enstatite *or* two amorphous forsterites *or* two amorphous enstatites. Y Cas (Fig. 8.17q) could be fitted equally well using either an amorphous forsterite with an amorphous enstatite *or* by two amorphous forsterites. V462 Cyg (Fig. 8.17o) could be fitted using either a single amorphous forsterite or a single amorphous enstatite. RZ Cyg (Fig. 8.17j) was fitted equally well by a number of combinations of amorphous forsterites. The other notable result in this group is that four spectra, those of CH Pup, IK Tau, R Cae and RW And (Fig. 8.17c, d, f & h), all had improved fits if obsidian (amorphous SiO_2) was included. All fits to this group require some form of magnesium silicate. The results of the χ^2-fitting of this group can be found in Table 8.9 and the fits are shown in Fig. 8.17. Where there were multiple equally good fits, this is indicated in Table 8.9. In most cases, the fits shown here were, in each case, the fits with the lowest reduced χ^2 value. The one notable exception is SX Cyg. For this source, equally good fits were obtained using various combinations of minerals, however, the only combination that yielded the two distinct bumps seen in the observed spectrum was with

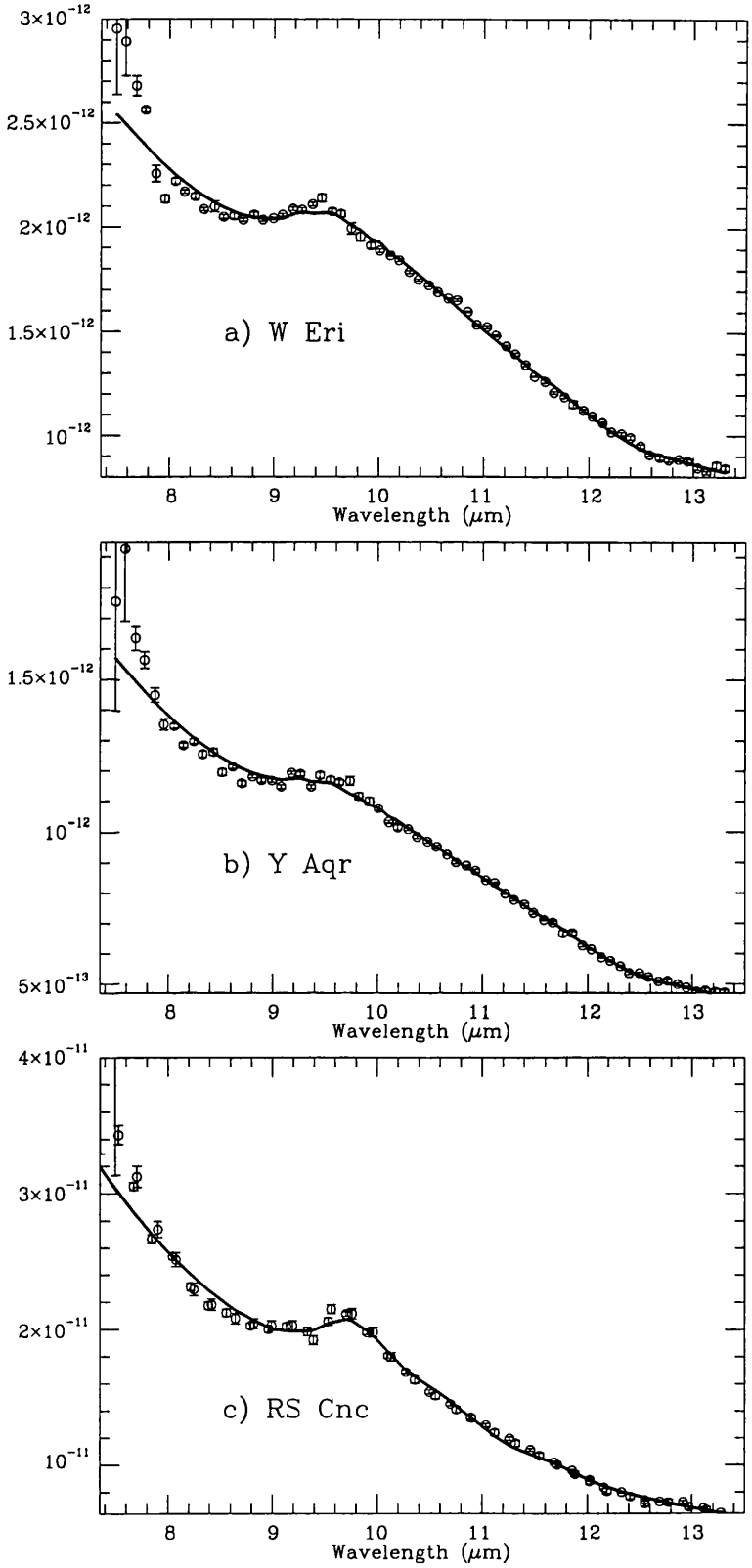

Figure 8.16: Flux-calibrated spectra of Group O3 (*transition*) sources with best χ^2-fits. Fluxes are in $\mathrm{Wm}^{-2}\mu\mathrm{m}^{-1}$. The errors used to calculate the reduced χ^2 are set to 3% of the flux if the 1σ error on the flux is less than this value. Thus the 1σ error bars shown here are not necessarily the errorbars used by the fitting program.

two amorphous forsterites. This is the fit shown in Fig. 8.17m.

The results of fitting the six group O5 (*sil+broad*) spectra can be found in Table 8.10 and the best fits to all six spectra are shown in Fig. 8.18. With the exception of R Cas (Fig. 8.18b), all these spectra could be fitted using a single form of amorphous forsterite. For three sources, better fits were obtained using two forms of amorphous forsterite. R Cas (Fig. 8.18b) was best fitted by a single amorphous enstatite. The fit to RU Her (Fig. 8.18c)was improved by adding amorphous enstatite. Again this group has a spectrum which could be fitted well by more than one combination of minerals: SAO 145652 (Fig. 8.18d) could be fitted equally well by two amorphous forsterites *or* by two amorphous enstatites *or* by an amorphous forsterite plus an amorphous enstatite. The fit shown in Fig. 8.18d has the lowest reduced-χ^2 value.

Group O6 (*sil*) is the largest group in our sample, comprising 27 spectra. Once more there are several ways to achieve good fits to each of these spectra. Moreover, we find that all the spectra could be fitted well using either a single amorphous forsterite, or by a single amorphous enstatite, and some fits were improved by using combinations of both these minerals. For four sources, DU Pup, GX Mon, V342 Sgr and V635 Aql, (Fig. 8.19b, c, t & u) improved fits were obtained by also including obsidian (amorphous SiO_2) and for one source, V Eri Fig. 8.19v), an improved was obtained fit by adding silica glass (another amorphous SiO_2). Details of the fits to group O6 can be found in Table 8.11 and are illustrated in Fig. 8.19.

8.5 Discussion

It is clear from the results of the fitting that it is difficult to discern a definite evolutionary trend in the type of dust found around oxygen-rich stars, since the same minerals give the best fits for all but group O1, for which no dust feature is required. It is also clear that the first detectable minerals to form around these stars are the magnesium-rich silicates. The non-detection of the refractory oxides or of silicates earlier in the condensation sequence (e.g. augite or diopside) may allow one to estimate an upper limit to the amounts of such dust grains around these stars.

There seems to be a distinct lack of evidence for Al_2O_3 grains. Contrary to the iden-

Table 8.9: Fits to Group O4 (*broad+sil* feature) stars.

Source	Blackbody	Silicate Type	T_{BB}	$T_{Sil}1$	$T_{Sil}2$	$T_{Sil}3$	χ^2 *
CH Pup	BB*E	Fo(Jena)+Enst(Day)+Obsid	1670	130	125	305	0.376
IK Tau•	BB*E	Fo(Jena)+Enst(Day)+Obsid	1445	120	135	750	1.896
R Cae	BB	Fo(Jena)+Enst(Day)+Obsid	485	120	125	225	0.701
RW And	BB	Fo(Jena)+Enst(Day)+Obsid	1895	75	120	280	0.845
Z Ant	BB*E	Fo(Jena) & Fo(JWS 92-4)	2700	135	70	—	1.064
Mira•	BB*E	Fo(K&H)+Fo(Jena)+Enst(Day)	1760	230	70	200	0.925
BX Eri	BB*E	Fo(Launer)+Fo(Jena)	1595	70	220	—	1.494
SX Cyg°	BB	Fo(Launer)+Fo(Jena)	625	95	365	—	0.628
Z Cas	BB*E	Fo(Launer)+Fo(Jena)	1630	70	185	—	1.154
RZ Cyg‡	BB*E	Fo(Launer)+Fo(K&H)	745	90	200	—	2.506
SV Peg	BB*E	Fo(Launer)+Fo(K&H)	1375	85	325	—	1.725
UW Cep	BB*E	Fo(Launer)+Fo(K&H)	1045	105	255	—	1.823
W Aqr	BB*E	Fo(K&H)+Fo(Jena)	1835	60	285	—	0.828
RR Per	BB*E	Fo(K&H)+Fo(Jena)	2145	55	185	—	0.706
RX Boo†	BB	Fo(Jena)+Enst(Jena2)	780	85	120	—	0.601
Y Cas•	BB*E	Fo(K&H)+Enst(Jena2)	2275	95	140	—	1.879
SAO 37673	BB*E	Enst(Jena2)+Enst(Day)	1125	125	120	—	1.323
V462 Cyg°	BB*E	Fo(Jena)	1150	240	—	—	1.033
BG Her	BB*E	Enst(Jena2)	705	140	—	—	0.870

* These stars had to be flux-reduced to use fitting program

† RX Boo also has good fits with 2 forsterites or with 2 enstatites

Fo(Jena) & Fo(Launer) → $\chi^2 = 0.719$

Enst (Jena2) & Enst(Day) → $\chi^2 = 0.757$

‡ RZ Cyg also has good fits with other combinations of forsterite

Fo(K+H) & Fo(Launer) → $\chi^2 = 2.632$

Fo(Jena) & Fo(Launer) → $\chi^2 = 2.729$

o SX Cyg also gets good fits to 2 enstatites and 1enst+1for

Enst (Jena2) & Enst(Day) → $\chi^2 = 0.453$

Fo(Launer) & Enst(Day) → $\chi^2 = 0.440$

• Y Cas also gets good fits to 2 forsterites

◇ V462Cyg also gets good fit to enstatite

Enst(Day) → $\chi^2 = 1.053$

* The errors used to calculate the reduced χ^2 are set to 3% of the flux if the 1σ error on the flux is less than this value. The errors shown in Fig 8.17 are 1σ. In all these spectra, the majority of points have errors that are <3% of the flux, the exceptions being for those points at the edges of each spectra and in the ozone region (9.4–9.9μm). Thus the 1σ error bars shown in the fits are not necessarily the errorbars used by the fitting program.

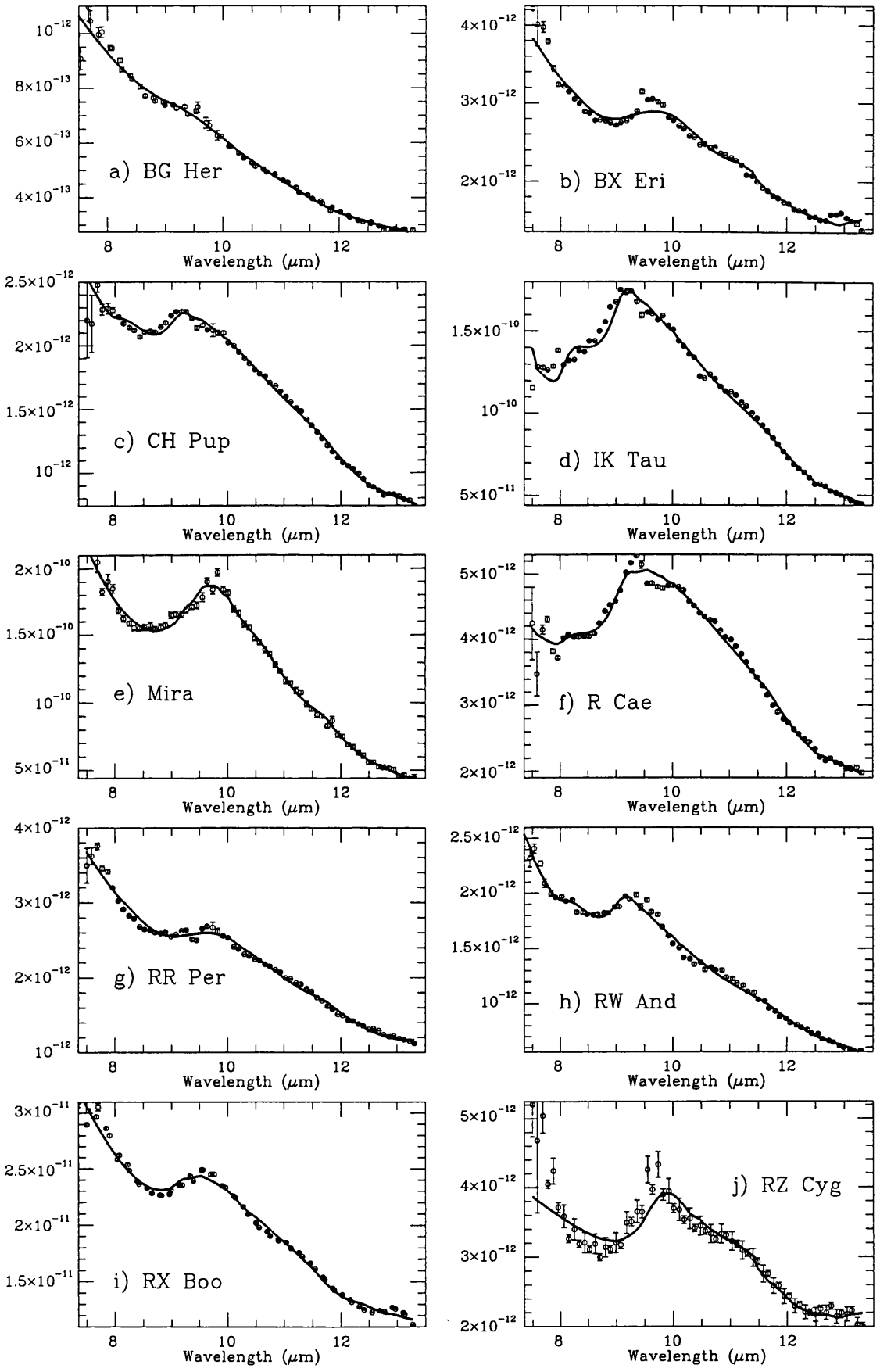

Figure 8.17: Flux-calibrated spectra of Group O4 (*broad+sil*) sources with best χ^2-fits. Fluxes are in $\mathrm{Wm^{-2}\mu m^{-1}}$. The errors used to calculate the reduced χ^2 are set to 3% of the flux if the 1σ error on the flux is less than this value. Thus the 1σ error bars shown here are not necessarily the errorbars used by the fitting program.

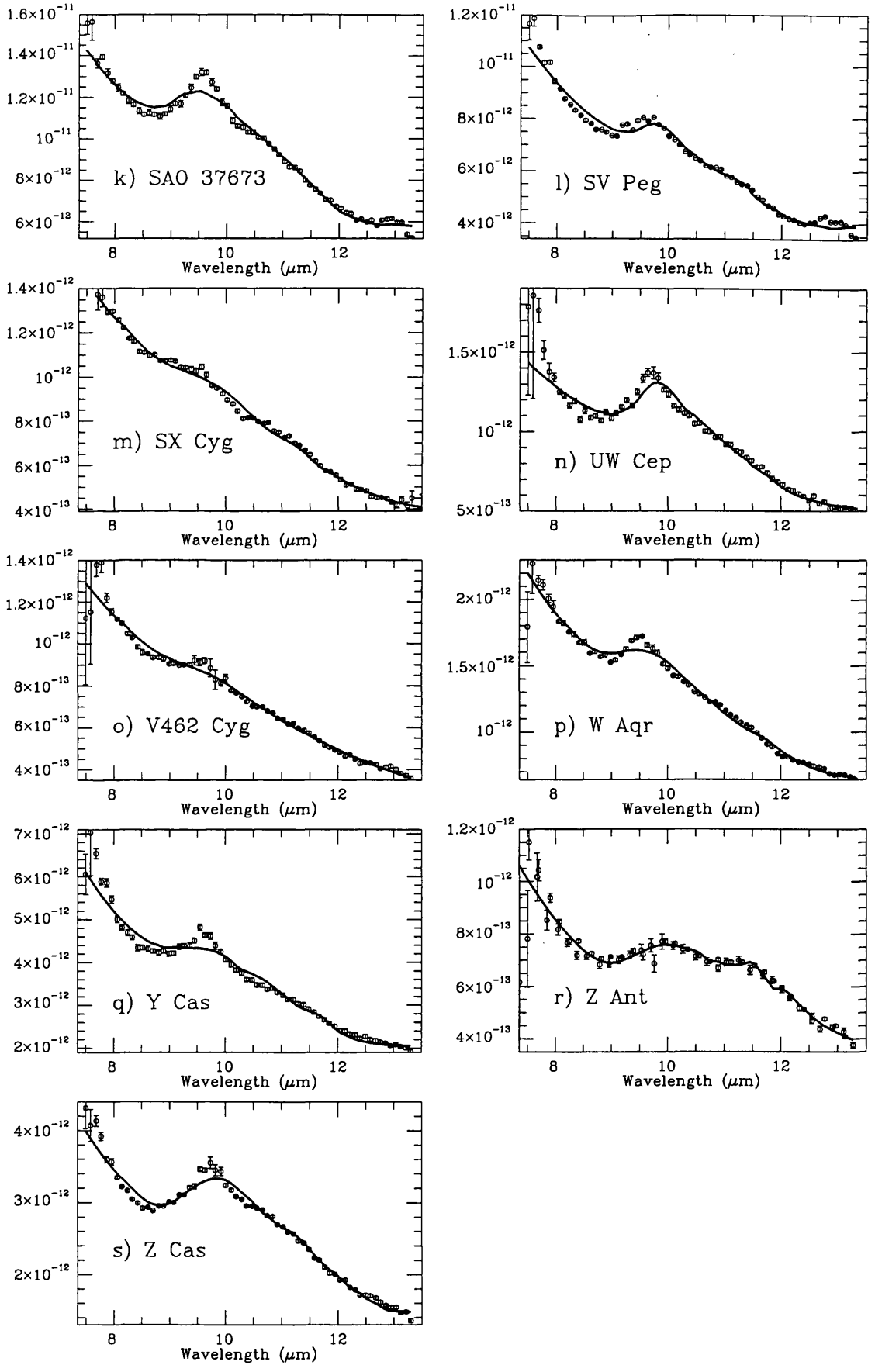

Figure 8.17: (Group O4 cont.)

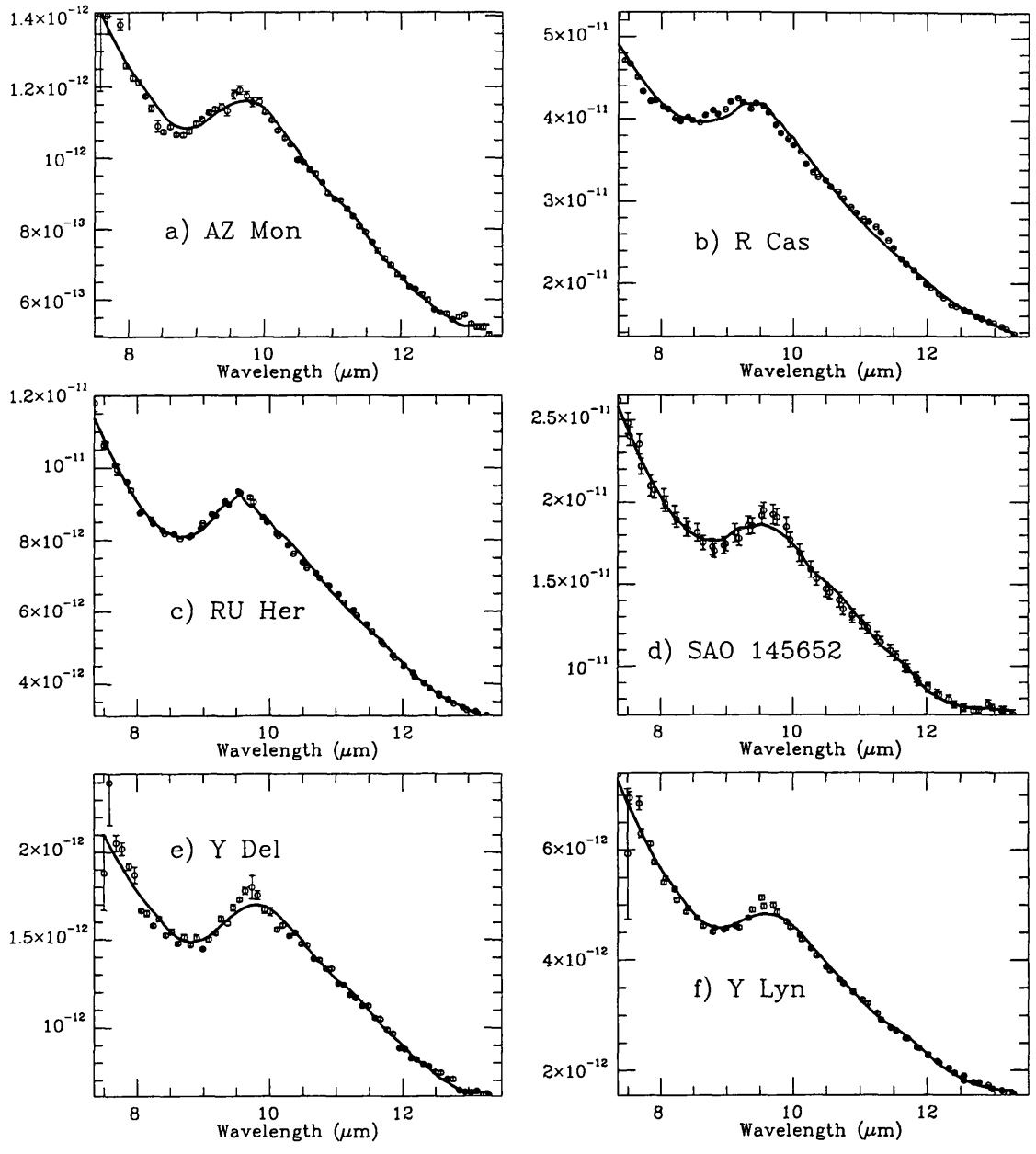

Figure 8.18: Flux-calibrated spectra of Group O5 (*sil+broad*) sources with best χ^2-fits. Fluxes are in $\mathrm{Wm^{-2}\mu m^{-1}}$. The errors used to calculate the reduced χ^2 are set to 3% of the flux if the 1σ error on the flux is less than this value. Thus the 1σ error bars shown here are not necessarily the errorbars used by the fitting program

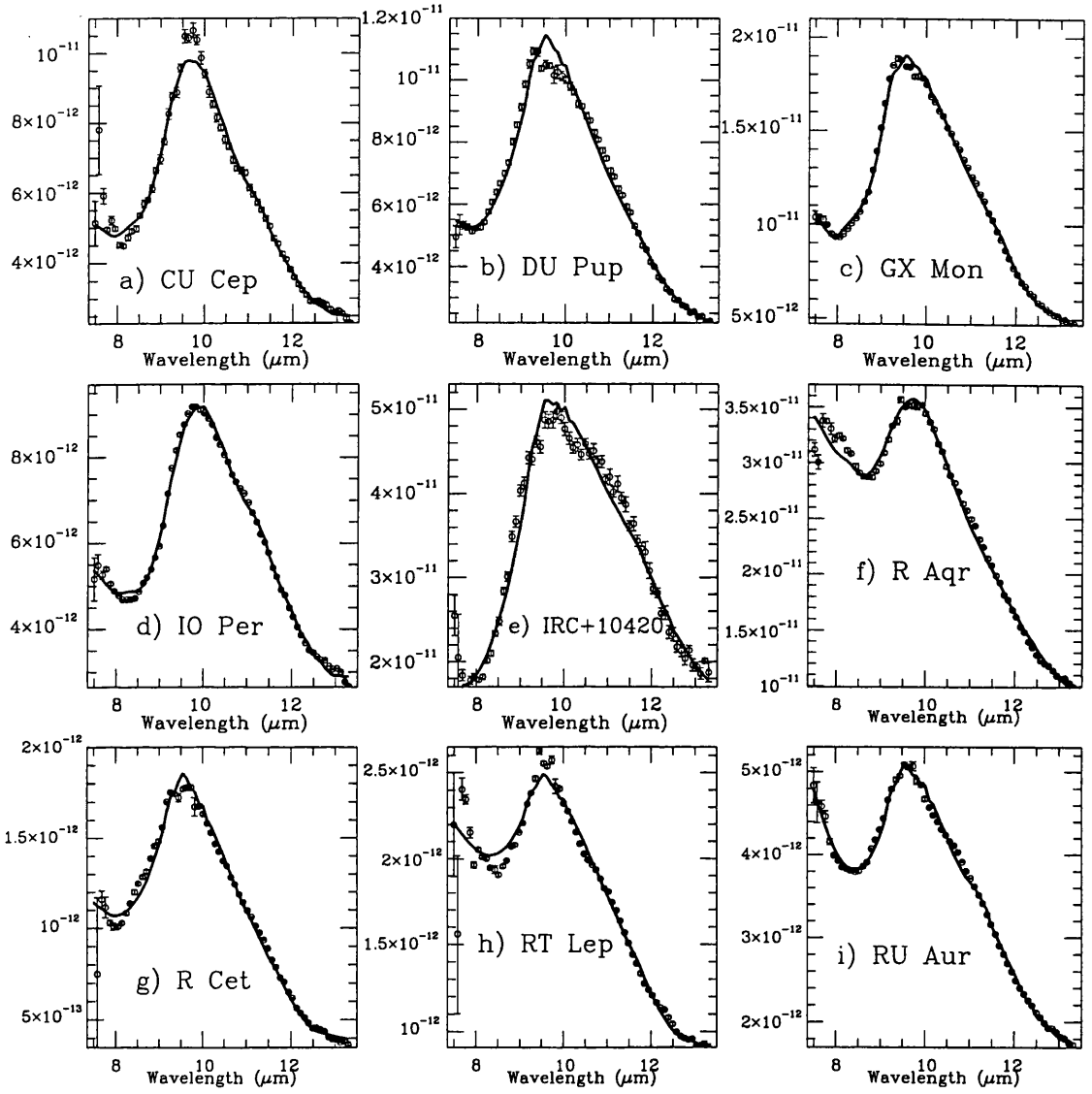

Figure 8.19: Flux-calibrated spectra of Group O6 (*sil*) sources with best χ^2-fits. Fluxes are in $\mathrm{Wm^{-2}\mu m^{-1}}$. The errors used to calculate the reduced χ^2 are set to 3% of the flux if the 1σ error on the flux is less than this value. Thus the 1σ error bars shown here are not necessarily the errorbars used by the fitting program

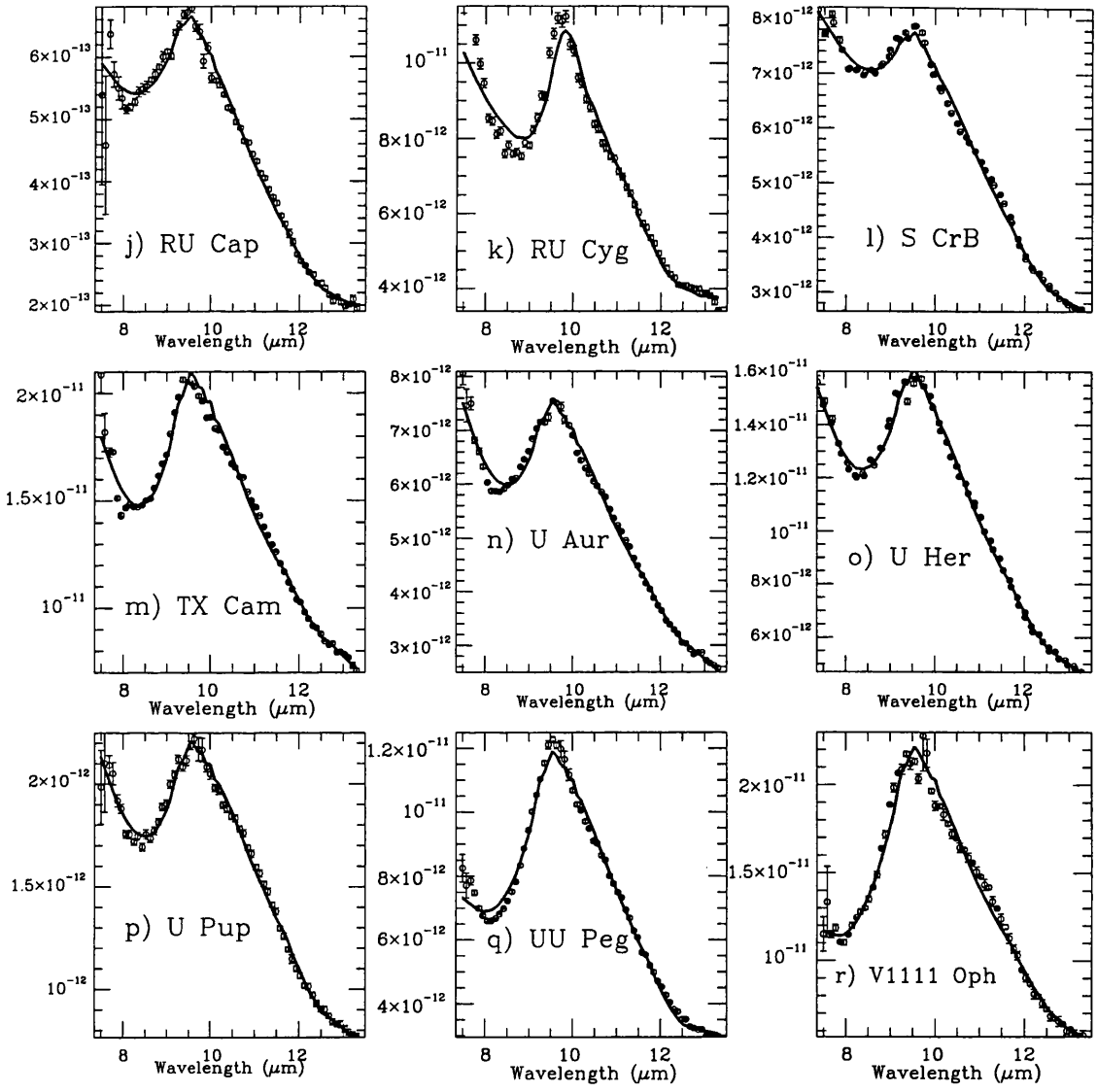

Figure 8.19: (Group O6 cont.)

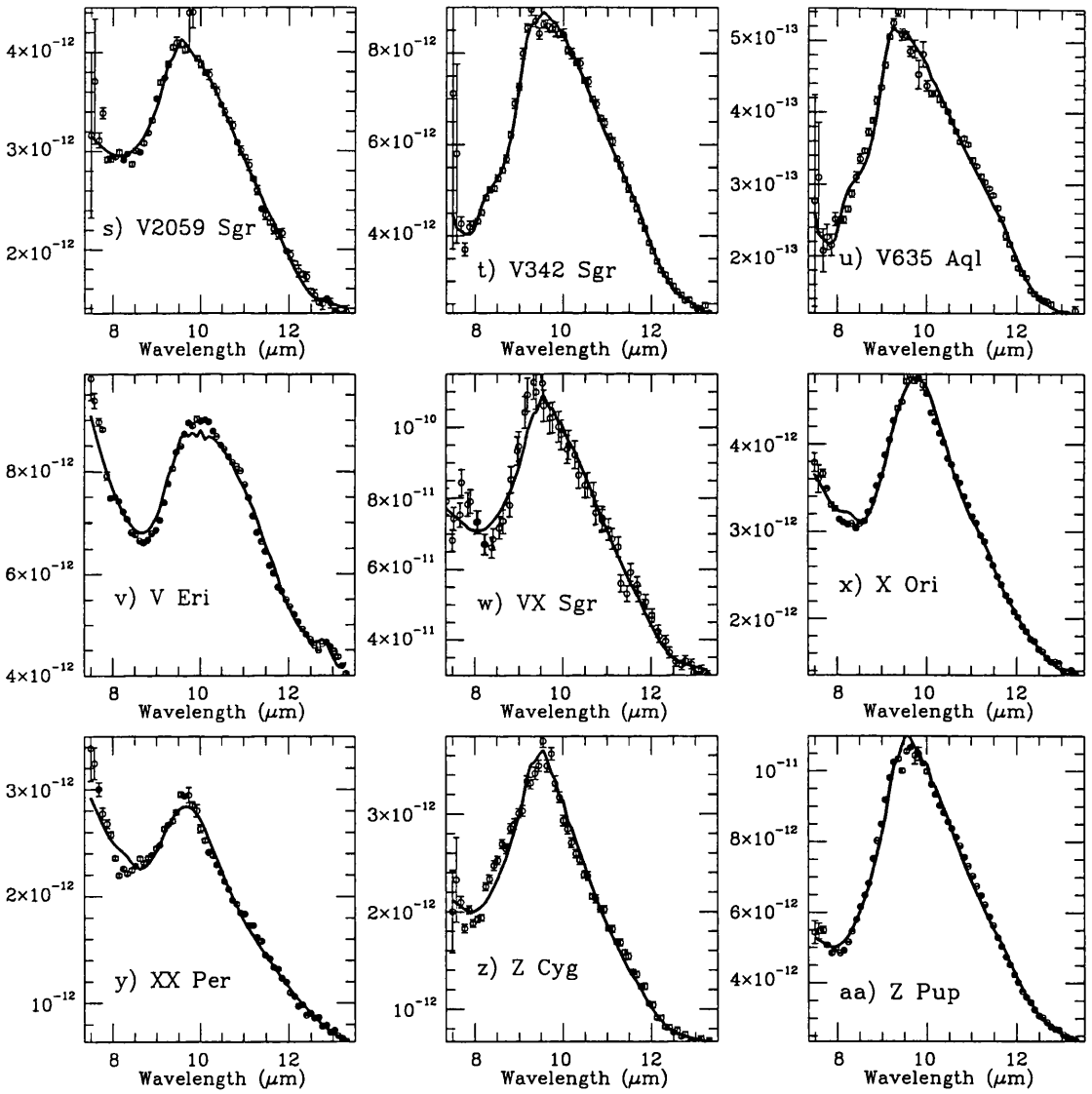

Figure 8.19: (Group O6 concluded)

Table 8.10: Fits to group O5 (*sil+broad* feature) stars.

Source	Blackbody	Silicate Type	T_{BB}	$T_{Sil}1$	$T_{Sil}2$	χ^2 *
Y Del	BB*E	Fo(Jena) & Fo(Launer)	940	190	60	0.861
AZ Mon	BB*E	Fo(Jena) & Fo(Launer)	1445	210	65	0.553
Y Lyn	BB*E	Fo(Jena) & Fo(K&H)	1265	60	255	0.487
RU Her	BB	Fo(Jena) & Enst(Day)	1020	55	170	0.206
SAO 145652*	BB*E	Fo(K&H) & Enst(Jena2)	1090	100	145	0.477
R Cas	BB	Enst(Day)	550	205	—	0.606

* SAO 145652 also has a good fit with Fo(K&H) & Fo(Jena) → χ^2=0.531
SAO 145652 also has a good fit with Enst(Day) & Enst(Jena2) → χ^2=0.579
* The errors used to calculate the reduced χ^2 are set to 3% of the flux if the 1σ error on the flux is less than this value. The errors shown in Fig 8.18 are 1σ. In all these spectra, the majority of points have errors that are <3% of the flux, the exceptions being for those points at the edges of each spectra and in the ozone region (9.4–9.9μm). Thus the 1σ error bars shown in the fits are not necessarily the errorbars used by the fitting program.

tification of this material in ground-based spectra by Hackwell (1972) and in IRAS LRS spectra by VdJW and OdJW, through the presence of the $\sim$ 12μm emission feature, we find here that this feature may be fit by silicon dioxide (SiO_2). Condensation models (Sedlmayr 1989; Tielens 1990) suggest that Al_2O_3 should be the first dust type to condense around O-rich stars. According to some previous research (e.g VdJW; OdJW; and Tielens 1990) Al_2O_3 then forms a nucleation seed on which the silicates can form a mantle. Alternatively, Nuth & Hecht (1990) and Stencel *et al.* (1990) suggested that the condensate is a "chaotic silicate" in which, initially, the emission from Al-O bonds dominates the spectra, but is then overwhelmed by emission from the more abundant Si-O bonds. In both cases, the above authors agreed that the 12-13μm band seen in the spectra of oxygen-rich stars can be attributed to Al-O bonds and that it signifies the presence of some form of aluminium oxide. Moreover, Al_2O_3 grains found in meteorites (Nittler *et al.* 1994a,b; 1997; Huss *et al.* 1995; see section 3.2.3) have isotopic signatures which suggest they were formed around oxygen-rich AGB stars. However, the abundance of such AGB star Al_2O_3 grains is very low (<1ppm; c.f. 6ppm for presolar SiC and 400ppm for presolar diamond). Begemann *et al.* (1997) studied the laboratory spectra of various forms of aluminium oxide, both crystalline and amorphous, with a view to identifying the 12-13μm feature more clearly. They found that amorphous aluminium oxide could not account

Table 8.11: Fits to group O6 (*sil* feature) stars

Source	Blackbody	Silicate Type	T_{BB}	$T_{Sil}1$	$T_{Sil}2$	$T_{Sil}3$	χ^2 *
VX Sgr	BB*E	Enst(Day)	750	205	—	—	1.637
Z Cyg	BB	Enst(Day)	560	310	—	—	2.451
RU Cap	BB	Enst(Day)	525	225	—	—	0.846
S CrB	BB	Enst(Day)	520	190	—	—	0.519
XX Per	BB*E	Fo(Jena)	3075	330	—	—	1.560
TX Cam	BB*E	Fo(Jena) & Enst(Day)	3310	52	185	—	0.940
IRC+10420	BB	Fo(Jena) & Enst(Day)	315	95	255	—	2.777
V1111 Oph	BB	Fo(Jena) & Enst(Day)	455	105	320	—	1.401
U Aur	BB*E	Fo(Jena) & Enst(Day)	3500	52	180	—	0.585
U Her	BB*E	Fo(Jena) & Enst(Day)	1950	57	205	—	0.387
U Pup	BB*E	Fo(Jena) & Enst(Day)	1665	52	165	—	0.455
R Cet*	BB*E	Fo(Jena) & Enst(Day)	1305	115	270	—	1.052
RT Lep*	BB*E	Fo(Jena) & Enst(Day)	745	540	160	—	1.052
UU Peg*	BB*E	Fo(Jena) & Enst(Day)	480	190	225	—	1.229
R Aqr†	BB	Fo(Jena) & Enst(Day)	600	295	135	—	0.794
V2059 Sgr‡	BB*E	Fo(Jena) & Enst(Day)	725	210	215	—	0.669
X Ori	BB*E	Fo(Jena) & Fo(Launer)	1515	320	75	—	0.431
RU Cyg	BB*E	Fo(K&H) & Fo(Launer)	1400	305	105	—	2.560
V Eri	BB*E	Enst(Day) & Silica	3500	120	70	—	0.818
CU Cep	BB*E	Fo(Jena) & Fo(Launer) & Enst(Day)	960	300	85	305	2.007
IO Per†	BB*E	Fo(Jena) & Fo(Launer) & Enst(Day)	1105	205	80	225	0.761
RU Aur	BB	Fo(Jena) & Fo(Launer) & Enst(Day)	1075	65	90	200	0.269
DU Pup	BB*E	Fo(Jena) & Enst(Day) & Obsid	1730	120	180	360	0.931
GX Mon	BB*E	Fo(Jena) & Enst(Day) & Obsid	3500	95	190	200	0.463
V342 Sgr	BB*E	Fo(Jena) & Enst(Day) & Obsid	1365	140	130	300	0.606
V635 Aql	BB*E	Fo(Jena) & Enst(Day) & Obsid	2540	95	145	415	1.855
Z Pup	BB*E	Fo(Jena) & Enst(Day) & Obsid	1405	100	220	225	0.709

All these stars can be fit quite well with either Fo(Jena) or Enst(Day)

The fits shown are the best fits with the lowest value of χ^2

* The fits to these spectra were slightly improved by adding a very small amount of forsterite, the amount added and the improvement achieved was so small that the fit to enstatite is equally good, with only slightly higher χ^2 values

† The fits to these spectra were slightly improved by adding a very small amount of enstatite, the amount added and the improvement achieved was so small that the fit to forsterite is equally good, with only slightly higher χ^2 values

‡ This spectrum could be fit very well by a single forsterite (χ^2=0.976) or a single enstatite (χ^2=0.924), however the improvement to the fit on using both (χ^2=0.669) justified their use.

* The errors used to calculate the reduced χ^2 are set to 3% of the flux if the 1σ error on the flux is less than this value. The errors shown in Fig 8.19 are 1σ. In all these spectra, the majority of points have errors that are <3% of the flux, the exceptions being for those points at the edges of each spectra and in the ozone region (9.4–9.9μm). Thus the 1σ error bars shown in the fits are not necessarily the errorbars used by the fitting program.

for the observations, and that, while one crystalline form of Al_2O_3 could account for the 12-13μm feature, a second feature seen at 21μm in laboratory spectra was not observed in astronomical spectra. They suggested that the 12-13μm feature may come from a form of silicate rather than aluminium oxide. This is confirmed by the results in this thesis which uses optical data of silicon dioxide to fit the 12-13μm feature rather than Al_2O_3, as discussed below and in chapter 5. In fact the spectra showing the 12-13μm feature could not be fit using any of the laboratory optical constants of Al_2O_3. The non-detection of aluminium oxide may allow one to constrain the amount of such material present around oxygen-rich stars using radiative transfer models. Furthermore, this may explain the low abundance of such grains in meteorites relative to other pre-solar grain types.

From the results obtained here it is not possible to be more specific about the dust species detected other than to say that they are various forms of amorphous magnesium silicates. On this point we concur with Day (1979) that the exact nature of the magnesium silicate cannot be determined from the 10μm spectra. In order to get a more unambiguous mineralogy for the dust, observational spectra with a broader wavelength range coverage, together with a better understanding of the nature of the laboratory samples, would be required. This is beyond the scope of the present work, but will hopefully be addressed by the study of ISO spectra (see e.g. Waters *et al.* 1996). While this sort of ambiguous result is not what had been hoped for, the use of the χ^2-fitting technique has confirmed that the mineralogy cannot be determined from the 10μm spectra alone. It may also be possible to use these results to constrain the amount of crystalline silicates present around oxygen-rich stars. It is clear from the fitting results that there is little evidence of crystalline silicates in the 10μm region. In particular, we have not observed the 11.3μm crystalline olivine feature. Non-observance of this feature (and others) may constrain the relative quantities of crystalline and amorphous silicates around these stars, since the crystalline silicates have been observed at longer wavelengths in the ISO-SWS spectra (Waters *et al.* 1996).

One of the interesting results is the necessity to use SiO_2 to explain the narrow $\sim$9.25μm peak seen in some of the spectra. As elaborated in chapter 5 and section 8.1.1, one of the molecules/minerals that is likely to be involved in the formation of silicates around O-rich stars is silicon dioxide (SiO_2; Pégourié & Papoular 1985). However, the spectral features/optical constants of SiO_2 have never been included in investigations of the fea-

Table 8.12: Silicon dioxide stability temperatures

SiO_2 type	stable/formation temperature in K	Crystal Structure	Main Peak of Spectral feature	2nd peak
α-quartz	$\leq$846	trigonal trapezoidal	9.20	12.5&12.8
β-quartz	846–1143	hexagonal trapezoidal	9.20	12.5&12.8
tridymite	1143–1743	hexagonal holohedral	9.15	12.6
cristobalite	1743–1986	cubic	9.25	12.65
silica glass	$\leq\sim$ 1300	amorphous	9.25	12.5
obsidian	$\leq\sim$ 1300	amorphous	9.20	—
lechatelierite	$\leq\sim$ 1300	amorphous	9.20	12.7

tures in the spectra of such stars. The forms of SiO_2 found on Earth are diverse and are discussed in more detail in chapter 5, and a summary is given here, in Table 8.12.

Given the temperatures of stability of each form of SiO_2, it is not unreasonable to assume that all these forms could be constituents of the circumstellar dust around oxygen-rich stars. The spectra of six samples of SiO_2, used in the χ^2-fitting routine, are presented in section 5.4. Three of these samples are crystalline SiO_2: quartz, tridymite and cristobalite; and three samples are amorphous: silica glass, obsidian and amorphous SiO_2. All these spectra have a strong features peaking at about 9.2μm and all but obsidian show a minor peak at $\sim$12.5μm.

The inclusion of silicon dioxide in models of circumstellar dust is reasonable. Those sources whose "silicate" features actually peak at 9.25μm are possibly best explained in this way. The 12.5μm feature seen in some O-rich circumstellar spectra (see Hackwell 1972; VdJW; OdJW) may also be attributable to SiO_2, rather than Al_2O_3 as has previously been asserted. The only problem with this hypothesis is that the 12.5μm feature and the 9.25μm feature seem to be mutually exclusive in the observed astronomical spectra whereas they appear together in the laboratory spectra (Fig. 5.13 and Table 8.12), with the exception of obsidian which exhibits only the 9.25μm feature. Therefore, obsidian can be used to explain those spectra which exhibit the 9.25μm only, but this does not resolve the problem of those spectra which exhibit the 12.5-13μm feature without a 9.25μm feature. The variations in the relative strengths of the two features from polytype to polytype may be

the key. The attribution of the 12.5-13.0μm feature to SiO_2 would not be a problem if the 12.5μm were strong enough, as the 9.25μm feature would be masked by other features in that region. Indeed, the *broad* feature, most closely associated with the appearance of the of the 12.5-13.0μm feature, extends from 8.5-12μm. This is a wide enough range to obscure the 9.2μm feature, and allow the 12.5-13.0μm feature to be observed. The nature of the dust responsible for the *broad* feature is very ambiguous and may well be contributed to by some form of SiO_2. It may be possible to use the lack of 9.2μm feature in these cases to constrain the SiO_2 polytype. For instance, the ratio of the strengths of the features is much more in favour of the 12.5-13.0μm feature for the quartz polytypes than for the other polytypes. It should be possible to calculate how much of a given polytype is needed to produce the 12.5-13.0μm feature without the 9.2μm feature protruding above the *broad* feature. The formation of various types of SiO_2 will be dependent on the ambient conditions. A closer look at the optical properties of the different SiO_2 polytypes may be expedient if more precise identifications are to be made. It may be that different polytypes of silicon dioxide form in the differing conditions around different stars, or that all the SiO_2 polytypes are formed in different regions around a single star.

The stars in group O6 which exhibit a 9.25μm peak (DU Pup, GX Mon, V342 Sgr and V635 Aql) do not show the 12.5μm feature. Although this may be too small a sample to be statistically significant, this could imply that the 9.25μm feature in these stars is due to an amorphous silicon dioxide which does not exhibit the 12.5μm feature. This is substantiated by the χ^2-fitting by obsidian, the only form of SiO_2 in our laboratory sample that does not exhibit the 12.5μm feature. If the 12.5μm feature is attributable to crystalline silicon dioxide, then this implies that the earlier groups contain crystalline SiO_2, while the later groups contains amorphous SiO_2 (which may represent a dust evolutionary process). The diminution of the 12.5μm feature in the supposed evolution of circumstellar dust spectra (see Little-Marenin & Little 1990; Stencel *et al* 1990) could be explained in terms of the types of silicon dioxide grains being formed. Since the inclusion of SiO_2 into the fitting program has produced reasonable results and there is no theoretical reason for excluding silicon dioxide dust, it is obviously desirable to include the optical constants for various SiO_2 types in radiative transfer models of oxygen-rich stars. The strict temperature ranges of some of the different crystalline SiO_2 types and their (slightly) differing optical constants may be useful in constraining models of dust formation around such

stars.

Chapter 9

Summary & future work

" Well, I don't really think that the end can be assessed as of itself as being the end because what does the end feel like? It's like saying when you try to extrapolate the end of the universe, you say, if the universe is indeed infinite, then how - what does that mean? How far is all the way, and then if it stops, what's stopping it, and what's behind what's stopping it? So, what's the end, you know, is my question to you."
This Is Spinal Tap (1984)

9.1 The beginning of the end

As was discussed in the introduction, this work is split into two distinct sections, one dealing with carbon-rich evolved stars (chapters 6 & 7) and one dealing with oxygen-rich evolved stars (chapter 8). The aim has been to identify dust forming around these stars. Several interesting new results have been found. In the next section there is a précis of the outcome of studying the optical properties of solids (see Chapter 4). The discovery of an error in previous laboratory-produced spectra (Dorschner *et al* 1978, Friedemann *et al* 1981, Pégourié 1988) has had some interesting implications for work in later chapters. The results of the work on carbon stars are summarised in section 9.3, and then in the following section the results of the work on oxygen-rich stars is discussed. Finally, the future work arising from these studies is discussed in section 9.5.

In chapter 2, the basics of stellar evolution and nucleosynthesis were discussed so that the origins of the building blocks of dust grains could be recognized and the evolution of dust type with the evolution of the star could be understood. This chapter also had implications for the meteoritic work discussed in chapter 3. The work on meteoritic data was

intended to help the reader to understand how the isotopic study of the meteoritic samples leads to the identification of the sources of the samples by comparison with nucleosynthesis models. The physical nature of circumstellar grains was also discussed, along with the discrepancies between the results from the studies of these samples and the astronomical models (i.e. dust species formed, grain formation and growth models, radiative transfer models) for such grains.

9.2 Optical properties of solids

In order to interpret the observed astronomical spectra it is necessary to have a good understanding of the way in which electromagnetic radiation interacts with solids. This was the aim of chapter 4. A simple explanation of how the physical properties of a solid determine its spectrum was discussed in section 4.2, followed by a brief discussion of the special case of very small particles of solids in section 4.3. The difference between the spectral properties of bulk medium and those of a medium consisting of particles whose diameter is small compared with the wavelength of light incident on it was explained. One of the major findings of this work was the discovery of an error in many of the published spectra of silicon carbide and some other dust types. This error was exposed whilst trying to reconcile meteoritic SiC data with the numerous astronomical observations which had, until now, presented a discrepancy between the type of SiC carbide believed to form around carbon-rich AGB stars and that found in meteorites, also believed to form around such stars. Meteoritic SiC grains are all of the β-SiC type, while astronomical observations seemed to be best explained by the presence of α-SiC. The probability of a grain forming as α-SiC and then somehow transforming into β-SiC is very low, and therefore this discrepancy could not be easily explained. This problem actually arose through a misunderstanding of the optical properties of solids, which lead to the imposition of a matrix-correction factor applied to those spectra taken using a dispersion matrix. Having discovered this problem, uncorrected SiC spectra were used and have had a profound effect on the fitting of the 11.3μm feature seen in the spectra of carbon stars (see next section and chapter 6). The work on optical properties was followed, in chapter 5, by a catalogue of spectra of minerals which may constitute some of the dust around evolved stars. The differences and similarities between the various spectra were discussed, and the possible condensation sequence of such minerals in the circumstellar environment around evolved stars was outlined.

9.3 Carbon-rich dust

9.3.1 Silicon carbide

The work on carbon-rich stars was split into two section based on the specific dust/molecular species of interest, i.e. silicon carbide (SiC; chapter 6) and PAHs/HACs/interstellar diamonds (chapter 7). In chapter 6, we discussed the presence of an 11.3μm feature in the infrared spectra of carbon stars which has been attributed to silicon carbide (Hackwell 1972; Treffers & Cohen 1974). Circumstellar SiC is particularly interesting because it is found in meteorites and the meteoritic grains appear to have suffered very little alteration during their travels through the interstellar medium (see Chapter 3). Since the discovery of the 11.3μm feature, there has been considerable of curiosity about the exact nature of the silicon carbide dust around these stars, and to this end, many astronomers have used laboratory spectra to try to constrain the properties of the dust (Friedemann *et al.* 1981; Borghesi *et al.* 1985, Pégourié 1998; Groenewegen 1995, Speck *et al.* 1997a,b). As mentioned above, until now there has been a discrepancy between the meteoritic and astronomical work of silicon carbide grains. This discrepancy seems to have arisen through the use of an erroneous correction factor applied to the laboratory data used for fitting spectral features. Having eliminated the problem with the laboratory data, it was found that the 11.3μm feature was fitted using β-SiC, rather than α-SiC as was previously found (e.g. Speck *et al.* 1997 a,b; Groenewegen 1995). This removes the discrepancy between meteoritic and astronomical results at least as far as the grain type is concerned. It does however introduce other questions which were successfully avoided by astronomers while the meteoritic dust was not seen as representative of the dust around C-rich AGB stars. For instance, the SiC grains found in meteorites are relatively large (up to 26μm in diameter), whereas the grains expected to cause the 11.3μm feature are $\leq\sim$0.1μm in size (see section 3.2.2). Isotopic studies of the grains found in meteorites show that even the noble gases trapped in them have signatures of AGB-star formation, and therefore the large grains were also formed in these regions. While we cannot observe these grains due to their large diameters[1], that does not mean they do not exist. At present, there are no grain growth mechanisms that can produce such large grains and radiative transfer models have consistently ignored large grain sizes (e.g. Bagnulo *et al.* 1995). This needs to be addressed. It was also found that many of the observed 11.3μm features could be best fit

[1] λ must be $> 2\pi a$ for the infrared features to be observable, where a is the effective radius of the grain. Therefore, in the 10μm region the radius of the grains must be $<\sim$1μm

using self-absorbed SiC[2], rather than SiC in pure emission.

The second interesting result arising from the work of the SiC feature in the spectra of carbon stars was the discovery of three sources with SiC absorption features, a phenomenon previously observed in only one stellar spectrum (AFGL 3068; Jones *et al.* 1978). Observations of all four sources exhibiting the SiC absorption feature are shown in chapter 6. Furthermore, two of these spectra also showed evidence for interstellar silicate absorption. The best fits to the spectra of these stars was found to use self-absorbed silicon carbide. These observations show that carbon stars can produce enough SiC to eventually develop optically thick dust shells. These may also be the sources where the dust shell is dense enough to be able to produce large SiC grains needed to explain meteoritic data.

9.3.2 UIR bands in carbon star spectra

A discussion of the nature and origin of the so-called unidentified infrared (UIR)[3] bands was presented in chapter 7. The origin of these bands is believed to be some sort of carbonaceous grain(s) or molecule(s) interacting with ultraviolet light. There have been many suggestions for the origin of these grains/molecules, including the formation around carbon stars. Unfortunately, carbon stars do not produce UV radiation to excite to UIR bands and so even if the grains/molecules do form in these regions they would not be detectable in infrared spectra. This suggests that, if the UIR band carriers do form around carbon stars, we just need to find carbon stars with a source of UV radiation in order to detect them. To this end, the spectra of three stars with hot-star companions were studied. The results in chapter 7 showed that UIR bands were indeed detected in the spectra of two of these stars, and thus at least some form of UIR band carrier must form in the circumstellar shells around carbon stars. Unfortunately, many of the UIR bands observed in other objects are outside the range of our 8-13μm observations. In order to investigate the UIR bands in carbon star spectra, we need to have observations with a wider wavelength range. This avenue can be explored through the ISO-SWS spectra of such sources (see section 9.5).

[2]i.e., the 11.3μm SiC feature in both emission an absorption simultaneously.

[3]recently and ironically renamed over-identified infrared bands, due to the many different dust/molecular species that have been postulated to be the cause of the bands

9.4 Oxygen-rich dust

Dust around oxygen-rich AGB stars was discussed in chapter 8. The problem with oxygen-rich stars, as opposed to the carbon-rich stars already discussed, is that the number of different dust species that are expected to form is much larger, and the spectra of many such species are quite similar (see chapter 5). There has been a suggestion that the dust around oxygen-rich stars evolves, and thus their infrared spectra evolve. With this in mind, the spectra of 80 oxygen-rich AGB/supergiant stars were divided into six groups based of their spectral features. It was assumes that the sequence of groups represented some sort of dust evolution, and hence various correlations of spectral features with physical parameters of the stars were sought (e.g. mass-loss rate, spectral type etc.). As in previous work (Hashimoto *et al* 1990, Little-Marenin & Little 1990), no correlations were found except with the asymmetry function (see Chapter 8), which implies that the light curve of an O-rich star becomes more asymmetric as the star evolves. In addition, the spectral features for each of the stars in this sample were identified. The results of this were as follows:

1) There is little or no evidence of corundum (Al_2O_3) in these circumstellar shells. This was unexpected, since this is the first dust-type expected to form and is postulated to become a nucleation site for further dust species to form. Many dust formation and radiative transfer models have been found to improve with the addition of corundum. However, a feature that has previously been attributed to some form of Al_2O_3, can be better explained as due to silicon dioxide. The non-detection of Al_2O_3 has certain implications. Either this particular grain type does not form, or it forms in such small quantities that it remains undetectable. If the latter is true, radiative transfer models could be used to determine an upper limit to the amount of Al_2O_3 that forms around O-rich stars. If the former is true, the proposed condensation sequence of O-rich grains around these stars need to be re-evaluated

2) Silicon dioxide (SiO_2) is the best explanation for both the 12.5-13μm feature, previously attributed to Al_2O_3, and the peak seen in several spectra in this sample at 9.2-9.35μm. This feature has not been mentioned before, possibly due to the lower resolution of previous observations (e.g. IRAS). The detection of the "SiO_2"-feature implies that such grains should be included into grain growth/formation mechanisms and radiative transfer models. Such work has already been started by Morioka *et al.* (1998).

3) The spectral differences between the various silicates, particularly the magnesium silicates, are too subtle for a more exact identification of the major 9.7μm feature in the observed 10μm spectra than "silicates" or possible "magnesium silicates". The only possible way to identify the minerals present in these spectra more accurately, would be using much longer wavelength observations, where slight differences in the mineralogical composition of the dust has a much greater effect on the positions of the spectral features (see next section).

9.5 Future work

The research presented in this thesis seems to have raised more questions that it has answered. There are several lines of research arising from this work which should be pursued.

Firstly, the work on the optical properties of silicon carbide came about through a collaboration with Anne Hofmeister at Washington University in St. Louis. It is our intention to investigate thoroughly the optical properties of silicon carbide, with a view to explaining how different physical parameters (e.g. grain size, shape, crystal structure) affect the shape of the infrared feature. This will hopefully eliminate any misunderstanding of the published spectra used for astronomical interpretations and allow better identifications of the existing infrared spectra of carbon stars. When this is done, the understanding of the nature of SiC grains forming around carbon stars should be greatly improved and can be incorporated into grain formation/growth models and radiative transfer models for such stars. Furthermore, we plan to investigate the optical properties of more minerals of astronomical interest, with a view to producing a definitive database of such materials. The spectra will cover large wavelength ranges, and explanations of the differences between similar samples will be produced. This should allow better interpretation of spectra of astronomical objects which are associated with dust and remove any ambiguity caused by differences between the various laboratory techniques used in producing mineral spectra.

Having reconciled the differences between astronomical observations and meteoritic laboratory data, at least as far as the type of silicon carbide forming is concerned, we now have several further discrepancies to resolve. The most important of these is the grain size problem. The grains found in meteorites can be as large as $\sim$25μm, and although as

mentioned above observing these grains would be a problem, that does not mean they do not exist[4]. It is therefore desirable to discover the mechanism by which these large grains could be produced. Since these grains obviously do exist, they should also be included into radiative transfer models. It would be interesting to see how the need to grow large grains affects models for mass-loss from these stars. As mentioned above, the carbon stars which exhibit absorption features may be the ideal place to start when incorporating large grain sizes into the models. Most of the radiative transfer models produced previously (e.g. Bagnulo *et al.* 1995) have used the flawed α-SiC optical properties (e.g. Pégourié 1988), and therefore need to be re-evaluated using the optical properties of β-SiC. Previous radiative transfer models have also neglected to include self-absorption. As shown in chapter 6, self-absorbed SiC produced good fits to many SiC features in carbon star spectra. This also needs to be addressed.

A second line of research, which follows from chapter 7, is to investigate the UIR bands in carbon star spectra further. The ISO-SWS spectrum of one of the stars which has already been shown to exhibit at least one UIR band (TU Tau), will allow a more detailed look at the UIR bands, and a comparison with the UIR bands observed in other objects.

Also following from chapter 7 is the possibility of finding a way to detect diamonds in carbon star spectra, if they do indeed form there. As discussed in chapter 7, the problem with the 8-13μ spectra is that the features seen in the meteoritic diamond spectra coincide with those of amorphous hydrogenated carbon. However, it may be possible to look for diamond features in the ISO-SWS spectra. It is not clear whether, in order to see diamond infrared spectra, source of UV must be present (c.f. PAHs). However, even if this is the case, observations of carbon stars with hot star companions may provide the right environment for such features to be produced. Furthermore, diamonds have an interesting ultraviolet spectrum of their own (Andersen *et al.* 1998), and it may be possible to use carbon stars in binaries systems to look for diamonds in the UV.

Thus far, the study of the 10- and 20-μm spectra of oxygen-rich stars has produced disappointingly vague results (chapter 8). The spectra produced by ISO may permit a more accurate identification of the minerals comprising the dust around oxygen-rich stars. It

[4]in fact it has been suggested that someone should tell the large meteoritic SiC grains that they do not exist, because no grain growth mechanism exists to produce them

can be expected that combining the high resolution, large wavelength range observations of ISO with a new comprehensive database of laboratory spectra will permit circumstellar dust around these objects (and others) to be better understood. The observations of crystalline silicates in ISO-SWS AGB-star spectra (Water *et al* 1996) are fascinating. The results here (chapter 8) have provided no evidence for crystalline silicates around such stars. The non-observance of crystalline silicate features in the 10-μm spectra, together with the observation of features for such species at longer wavelength requires further investigation. It may be possible to use these results to constrain the quantity of crystalline dust formed, or to provide insight into the possible different formation sites of the amorphous and crystalline species.

The sample of oxygen-rich stars presented in chapter 8 includes several Red Supergiants (RSGs). The spectra of these stars seem to fit nicely into the same categories as the oxygen-rich AGB stars. Further investigation into the similarities and differences between the dust features of the two groups (RSGs and AGB stars) should be undertaken.

There is a "new" dust species discussed in chapter 8 - silicon dioxide (SiO_2). Although SiO_2 has been mentioned by previous authors (e.g. Pégourié & Papoular 1985), it has never been seriously considered as a major constituent of circumstellar dust. Having shown, in chapter 8, that SiO_2 likely to be present in the circumstellar dust around oxygen-rich AGB stars, further investigations need to take place. For instance, as mentioned in section 8.5, the observations of the 9.25μm and 12.5-13μm features may constrain the polytype and relative quantity of SiO_2 forming in these regions. Again, we have a dust type which has previously been excluded from radiative transfer models and grain formation mechanisms. This needs to be addressed.

Finally, there are two stars, one carbon-rich (TX Psc) and one oxygen-rich (T Cet), which were excluded from the two samples (chapter 6 and chapter 8 respectively) due to their bizarre spectra. These stars need to be further investigated and explanations for their unusual spectra need to be found.

The End?

References

ABDULLAH, A.H., Sherman, W.F., 1997, *Vibrational Spectroscopy*, **13**, 133.

ABELÈS, F. (Ed.), 1972, *Optical Properties of Solids*, Elsevier:New York.

AITKEN, D.K., Roche, P.F., 1982, *Mon. Not. R. Astron. Soc.* **200**, 217.

AITKEN, D.K., Roche, P.F., Spenser, P.M., Jones, B., 1979, *Astrophysical Journal*, **233**, 925.

ALEXANDER, C.M.O'D., 1997, in *Astrophysical Implications of the Laboratory Study of Presolar Materials (AIP Conference Proceeding 402)*, eds T.J. Bernatowicz and E.K. Zinner, American Institute of Physics:New York, p567.

ALEXANDER, C.M.O'D., 1993, *Geochim. Cosmochim. Acta*, **57**, 2869.

ALLAMANDOLA, L.J., Sandford, S.A., Tielens, A.G.G.M., Herbst, T.M., 1992, *Astrophysical Journal*,**399**, 134

ALLAMANDOLA, L.J., Tielens, A.G.G.M., Barker, J.R., 1989, *Astrophysical Journal Supp. Ser,*. **71**, 733

ALLAMANDOLA, L.J., Tielens, A.G.G.M., Barker, J.R., 1985, *Astrophysical Journal*, **290**, L25

AMARI, S., Lewis, R.S., Anders, E., 1994, *Geochimica et Cosmochimica Acta*, **58**, 459

AMARI, S., Hoppe, P., Zinner, E.K., Lewis, R.S., 1992, *Astrophysical Journal*, **394**, L43

ANDERS, E., Zinner, E.K., 1993, *Meteoritics*, **28**, 490

ANDERSEN, A.C., Jorgensen, U.G., Nicolaisen, F.M., Sorensen, O.G., Glejbol, K., 1998, *Astronomy & Astrophysics*, **330**, 1080-1090

BAGNULO, S., Doyle, J.G., Griffin, I.P., 1995, *Astronomy & Astrophysics*, **301**, 501

BALM, S.P., Kroto, H.W., 1990, *Mon. Not. R. Astron. Soc.*, **245**, 193

BARLOW, M.J., 1983, in *Planetary Nebulae*, eds David R. Flower , Reidel:Dordrecht, 105

BARNBAUM, C., Balm, S., 1995, *American Astronomical Society Meeting*, **187**, 45.01

BARON, Y., de Muizon, M., Papoular, R., Pegourie, B., 1987, *Astronomy & Astrophysics*, **186**, 271

BECHSTEDT, F., Kaeckell, P., Zywietz, A., Karch, K., Adolp, B., Tenelsen, K., Furthmueller, J., 1997, *Physica Status Solidi B*, **202**, 35-62

BEGEMANN, B., Dorschner, J., Henning, T., Mutschke, H., 1997, *Astrophysical Journal*, **476**, 199

BEINTEMA, D.A., van den Ancker, M.E., Molster, F.J., Waters, L.B.F.M., Tielens, A.G.G.M., Waelkens, C., de Jong, T., de Graaw, Th., Justannont, K., Yamamura, I., Heras, A.,

Lahuis, F., Salama, A., 1996, *Astronomy & Astrophysics*, **315**, 369

BERNATOWICZ, T.J., 1997, *ASP Conference Series - From Stardust to Planetessimals*, **122**, 227

BERNATOWICZ, T.J., Amari, S., Zinner, E.K., Lewis, R.S., 1991, *Astrophysical Journal*, **373**, L73

BERNATOWICZ, T.J., Gibbons, P.C., Lewis, R.S., 1990, *Astrophysical Journal* **359**, 246

BERNATOWICZ, T.J., Fraundorf, G., Tang, M., Anders, E., Wopenka, B., Zinner, E.K., Fraundorf, P., 1987, *Nature* , **330**, 728

BERREMAN, D.W., 1963, *Physical Review.* **130**, 2193

BLANCO, A., Borghesi, A., Fonti, S., Orofino, V., 1994, *Astronomy & Astrophysics*, **283**, 561

BLOMMAERT, J.A.D.L., van der Veen, W.E.C.J., Habing, H.J., 1993, *Astronomy & Astrophysics*, **267**, 39

BODE, M.F., 1988, *Dust in the Universe*, eds M.E. Bailey & D.A. Williams, Cambridge University Press:Cambridge, 73

BOHREN, C.F., Huffman, D.R., 1983, *Absorption and Scattering of Light by Small Particles*, John Wiley & Sons:New York

BOOTHROYD, A.I., Sackmann, I.-J. Ahern, S.C., 1993, *Astrophysical Journal*, **418**, 457

BORGHESI, A., Bussoletti, E., Colangeli, L., 1987, *Astrophysical Journal*, **314**, 422

BORGHESI, A., Bussoletti, E., Colangeli, L., De Blasi, C., 1985, *Astronomy & Astrophysics*, **153**, 1

BREGMAN, J.D., Allamandola, L.J., Tielens, A.G.G.M., Geballe, T.R., Witteborn, F.C., 1989, *Astrophysical Journal*, **344**, 791

BREGMAN, J.D., Dinerstein, H.L., Goebel, J.H., Lester, D.F., Witteborn, F.C., Rank, D.M., 1983, *Astrophysical Journal*, **274**, 666

BUERKI, P.R., Leutwyler, S., 1991, J. Appl. Phys., **69**, 3739

BUSS, R.H. Jr., Tielens, A.G.G.M., Cohen, M., Werner, M.W., Bregman, J.D., Witteborn, F.C., 1993, *Astrophysical Journal*, **415**, 250

BUSS, R.H. Jr., Tielens, A.G.G.M., Snow, T.P., 1991, *Astrophysical Journal*, **372**, 281

BUSS, R.H. Jr., Cohen, M., Tielens, A.G.G.M., Werner, M.W., Bregman, J.D., Witteborn, F.C., Rank, D.M., Sandford, S.A., 1990, *Astrophysical Journal*, **365**, L23

CADWELL, B.J., Wang, H., Feigelson, E.D., Frenklach, M., 1994, *Astrophysical Journal*, **429**, 285

CHAN, S.J., Kwok, S., 1990, *Astronomy & Astrophysics*, **237**, 354

CHERCHNEFF, I., Barker, J.R., 1991 , *Astrophysical Journal*, **377**, 541

CHOPELAS, A., Hofmeister, A.M., 1991, *Phys. Chem. Mineral*, **17**, 503-526

CLAYTON, D.D., 1989, *Astrophysical Journal*, **340**, 613

CLAYTON, D.D., 1978, *Moon and the Planets*, **19**, 109

CLAYTON, D.D., 1977, *Astrophysical Journal*, **214**. 300

CLAYTON, R.N., Onuma, N., Grossman, L., Mayeda, T.K., *E&PSL*, **34**, 209, 1977

COHEN, M., Davies, J.K., 1995, *Mon. Not. R. Astron. Soc.*, **276**, 715

COHEN, M., Walker, R.G., Witteborn, F.C., 1992a, *Astronomical Journal*, **104**, 2030

COHEN, M., Walker, R.G., Barlow, M.J., Deacon, J.R., 1992b, *Astronomical Journal*, **104**, 1650

COHEN, M., Tielens, A.G.G.M., Bregman, J.D., 1989, *Astrophysical Journal*, **344**, L13

COHEN, M., Allamandola, L.J., Tielens, A.G.G.M., Bregman, J.D., Simpson, J.P., Witteborn, F.C., Wooden, D.H., Rank, D.M., 1986, *Astrophysical Journal*, **302**, 737

COHEN, M., Tielens, A.G.G.M., Allamandola, L.J., 1985, *Astrophysical Journal*, **299**, L93

COHEN, M., 1984, *Mon. Not. R. Astron. Soc.*, **206**, 137

COHEN, M., 1979, *Mon. Not. R. Astron. Soc.*, **186**, 837

COHEN, M., Anderson, C.M., Cowley, A., Coyne, G.V., Fawley, W.M., Gull, T.R., Harlan, E.A., Herbig, G.H., Holden, F., Hudson, H.S., Jakoubek, R.O., Johnson, H.M., Merrill, K.M., Schiffer, F.H., Soifer, B.T., Zuckerman, B., 1975, *Astrophysical Journal*, **196**, 179

COLANGELI, L., Mennella, V., Di Marino, C., Rotundi, A., Bussoletti, E., 1995, *Astronomy & Astrophysics*, **293**, 927

COLANGELI, L., Mennella, V., Stephens, J.R., Bussoletti, E., 1994, *Astronomy & Astrophysics*, **289**, 604

COLANGELI, L., Mennella, V., Bussoletti, E., Merluzzi, P., Rotundi, A., Palumbo, P., Di Marino, C., 1993, *Meteoritics*, **28**, 338

CYNN, H., Hofmeister, A.M., 1994, *Journal of Geophysical Research*, **99**, 17712

DAULTON, T.L., Eisenhour, D.D., Bernatowicz, T.J., Lewis, R.S., Buseck, P.R., 1996, *Geochim. Cosmochim. Acta*, **60**, 4853

DAVID, P., Le Squeren, A.M., Sivagnanm, P., Braz, M.A., 1993, *Astronomy & Astrophysics Supp. Ser.*, **98**, 245

DAY, K.L., 1979, *Astrophysical Journal*, **234**, 158

DEER, W.A., Howie, R.A., Zussman, J., 1966, *An Introduction to the Rock Forming Min-*

erals, Longman Scientific & Technical:London

DISCHLER, B., Bubenzer, A., Koidl, P., 1983, *Soild State Communications*, **48**, 105

DISCHLER, B., Bubenzer, A., Koidl, P., 1983, *Applied Physics Letters*, **42**, 636

DORSCHNER, J., Friedemann, C., Gurtler, J., 1978, *Astronomische Nachrichten*, **299**, 269

DULEY, W.W., 1994, *Astrophysical Journal*, **430**, L133

DULEY, W.W., Jones, A.P., 1990, *Astrophysical Journal*, **351**, L49

DULEY, W.W., Williams, D.A., 1981, *Mon. Not. R. Astron. Soc.*, **196**, 269

EL EID, M.F., 1994, *Astronomy & Astrophysics*, **285**, 915

EVANS, A., 1994, *The Dusty Universe*, John Wiley & Sons:New York.

FORREST, W.J., McCarthy, J.F., Houck, J.R., 1979, *Astrophysical Journal*, **233**, 611

FORREST, W.J., Gillett, F.C., Stein, W.A., 1975, *Astrophysical Journal*, **195**, 423

FRENKLACH, M., Feigelson, E.D., 1989, *Astrophysical Journal*, **341**, 372

FRIEDEMANN, C., Gürtler, J., Schmidt, R., Dorschner, J., 1981, *Astrophysics & Space Science*, **79**, 405

FRIEDEL, R.A., Carson, G.L., 1972, *Fuel*, **51**, 194

FRIEDEMANN, C., 1969, *Physica*, **41**, 139

FROST, C.A., Lattanzio, J.R., 1992, *Proceedings of the Astronomical Society of Australia*, **10**, 125

GAIL, H-.P., Sedlmayr, E., 1987, in *Physical processes in interstellar clouds*, eds. G.E. Morfill, M. Scholer, Reidel:Dordrecht, 275

GAL, O., de Muizon, M.J., Papoular, R., Pegourie, B., 1987, *Astronomy & Astrophysics*, **183**, 29

GALLINO, R., Raiteri, C.M., Busso, M., 1993, *Astrophysical Journal*, **410**, 400

GALLINO, R., Raiteri, C.M., Busso, M., Matteucci, F., 1994, *Astrophysical Journal*, **430**, 858

GILLETT, F.C., Kleinmann, D.E., Wright, E.L., Capps, R.W., 1975, *Astrophysical Journal*, **198**, L65

GILLETT, F.C., Forrest, W.J., Merrill, K.M., 1973, *Astrophysical Journal*, **183**, 87

GILLETT, F.C., Low, F.J., Stein, W.A., 1968, *Astrophysical Journal*, **154**, 677

GILMAN, R.C., 1969, *Astrophysical Journal*, **155**, L185

GILRA, D.P., 1972, *Proceedings NASA SP-310*, 295

GILRA, D.P., 1971, *Nature*, **229**, 237

GILRA, D.P., Code, A.D., 1971, *Bulletin of the American Astonomical Society*, **3**, 379

GOEBEL, J.H., Cheeseman, P., Gerbault, F., 1995, *Astrophysical Journal*, **449**, 246

GOEBEL, J.H., Bregman, J.D., Witteborn, F.C., 1994, *Astrophysical Journal*, **430**, 317

GOEBEL, J.H., Bregman, J.D., Witteborn, F.C., Taylor, B.J., Willner, S.P., 1981, *Astrophysical Journal*, **246**, 455

GRASDALEN, G.L., Joyce, R.R., 1976, *Astrophysical Journal*, **205**, L11

GRIFFIN, I.P., 1990, *Mon. Not. R. Astron. Soc.*, **247**, 591

GROENEWEGEN, M.A.T., 1997, *Astronomy & Astrophysics*, **317**, 503

GROENEWEGEN, M.A.T., 1995, *Astronomy & Astrophysics*, **293**, 463

GROENEWEGEN, M.A.T., 1994, *Astronomy & Astrophysics*, **290**, 207

GROENEWEGEN, M.A.T., de Jong, T., van der Bliek, N.S., Slijkhuis, S., Willems, F.J., 1992, *Astronomy & Astrophysics*, **253**, 150

GROSSMAN, L., 1972, *Geochim. Cosmochim. Acta*, **36**, 597.

HACKWELL, J.A., 1971, Ph.D. Thesis

HACKWELL, J.A., 1972, *Astronomy & Astrophysics*, **21**, 239

HAPKE, B., 1993, *Theory of reflectance and emittance spectroscopy* Cambridge University Press:Cambridge

HASHIMOTO, O., Nakada, Y., Onaka, T., Tanabe, T., Kamijo, F., 1990, *Astronomy & Astrophysics*, **227**, 465

HILL, H.G.M., d'Hendecourt, L.B., Perron, C., Jones, A.P., 1997, *Meteoritics & Planetary Science*, **32**, 713

HOFMEISTER, A.M., 1995, in *Practical Guide to Infrared Microspectroscopy*, ed. H. Humicki, Marcel Dekker Inc:New York, 377

HOFMEISTER, A.M., 1997, *Physics & Chemistry of Minerals*, **24**, 535

HOFMEISTER, A.M., Xu, J., Mao, H-K., Bell, P.M., Hoering, T.C., 1989, *American Mineralogist*, **14**, 281

HOPPE, P., Ott, U., 1997, in *Astrophysical Implications of the Laboratory Study of Presolar Materials (AIP Conference Proceeding 402)*, eds T.J. Bernatowicz and E.K. Zinner, American Institute of Physics:New York, p27

HOPPE, P., Amari, S., Zinner, E.K., Ireland, T., Lewis, R.S., 1994, *Astrophysical Journal*, **430**, 870

HUSS, G.R., Fahey, A.J., Gallino, R., Wasserburg, G.J., 1995, *Astrophysical Journal*, **430**, L81

IBEN, I. Jr., Renzini, A., 1983, *Annual Review of Astronomy & Astrophysics*, **21**, 271

JOBLIN, C., Tielens, A.G.G.M., Allamandola, L.J., Geballe, T.R., 1996, *Astrophysical Journal*, **458**, 610

JOBLIN, C., Tielens, A.G.G.M., Allamandola, L.J., Geballe, T.R., Wooden, D.H., 1996, *Astrophysical Journal*, **460**, L119

JOBLIN, C., Boissel, P., Leger, A., d'Hendecourt, L.B., Defourneau, D., 1995, *Astronomy & Astrophysics*, **299**, 835

JOBLIN, C., d'Hendecourt, L.B., Leger, A., Defourneau, D., 1994, *Astronomy & Astrophysics*, **281**, 923

JONES, T.W., Merrill, K.M., Puetter, R.C., Willner, S.P., 1978, *Astronomical Journal*, **83**, 1437

JONES, T.W., Merrill, K.M., 1976, *Astrophysical Journal*, **209**, 509

JØRGENSEN, U.G., 1988, *Nature.* **332**, 702

JURA, M., 1990, in *Dusty Objects in the Universe*, eds. E. Bussoletti & A.A. Vittone, Kluwer:Dordrecht, 27

JURA, M., Turner, J., Balm, S.P., 1997, *Astrophysical Journal*, **474**, 741

JURA, M., Kleinmann, S.G., 1990, *Astrophysical Journal*, **364**, 663

JURA, M., Kleinmann, S.G., 1989, *Astrophysical Journal*, **341**, 359

JURA, M., 1987, in *Proceedings of the IAU Symposium, Astrochemistry*, eds M.S. Vardya & S.P. Tarafdar, Reidel Publishing Co.:Dordrecht, 547

JURA, M., 1986, *Astrophysical Journal*, **303**, 327

JUSTANNONT, K., Barlow, M.J., Skinner, C.J., Roche, P.F., Aitken, D.K., Smith, C.H., 1996, *Astronomy & Astrophysics*, **309**, 612

KELLER, R., 1987, in *Polycyclic aromatic hydrocarbons and astrophysics*, eds. A. Leger, L. D'Hendecourt, N. Boccara, Reidel:Dordrecht, 387

KINGSBURGH, R.L., Barlow, M.J., 1994, *Mon. Not. R. Astron. Soc.*, **271**, 257

KNACKE R F, 1960 , in *Protostars and planets: Studies of star formation and of the origin of the solar system*, ed T. Gehrels, University of Arizona Press:Tucson, 112

KOIKE, C., Kaito, C., Yamamoto, T., Shibai, H., Kimura, S., Suto, H., 1995a, *Icarus*, **114**, 203

KOIKE, C., Wickramasinghe, N.C., Kano, N., Yamakoshi, K., Yamamoto, T., Kaito, C., Kimura, S., Okuda, H., 1995b, *Mon. Not. R. Astron. Soc.*, **277**, 986

KOIKE, C., Shibai, H., Tuchiyama, A., 1993, *Mon. Not. R. Astron. Soc.*, **264**, 654

KOZASA, T., Dorschner, J., Henning, T., Stognienko, R., 1996, *Astronomy & Astrophysics*,

307, 551

KRAMERS, H.A., 1956, *Collected Scientific Papers*, North-Holland:Amsterdam.

KRATSCHMER, W., Huffman, D.R., 1979, *Astrophysics & Space Science*, **61**, 195

KRONIG, R. de L., 1928, *J. Opt. Soc. Am.*, **12**, 542

1612

LARIMER, J.W., 1979, *Astrophys. Sp. Sci.*, **65**, 351

LATTANZIO, J.C., Frost, C.A., 1998, in *Proceedings of IAU Symposium 189 on Fundamental Stellar Properties: The Interaction between Observation and Theory*, eds. T.R. Bedding, A.J. Booth & J. Davis, Kluwer:Dordrecht, 373

LATTER, W.B., 1991, *Astrophysical Journal*, **377**, 187

LATTIMER, J.M., 1982, in *Formation of Planetary Systems*, ed. A. Brahic, CNES:France, 191.

LAUNER, P.J., 1952, *American Mineralogist*, **37**, 764

LE BERTRE, T., 1997, *Astronomy & Astrophysics*, **324**, 1059

LE BERTRE, T., 1990, *Astronomy & Astrophysics*, **236**, 472

LE SQUEREN, A.M., Sivagnanam, P., Dennefield, M., David, P., 1992, *Astronomy & Astrophysics*, **254**, 133

LEBOFSKY, L.A., Rieke, G.H., 1977, *Astronomical Journal*, **82**, 646

LEE, T., Papanastassiou, D.A., Wasserburg, G.J., *Astrophysical Journal*, **220**, 21, 1978

Léger, A., d'Hendecourt, L.B., 1985, *Astronomy & Astrophysics*, **146**, 81

LÉGER, A., Puget, J.L., 1984, *Astronomy & Astrophysics*, **137**, L5

LEISING, M.D., Clayton, D.D., 1987, *Astrophysical Journal* **323**, 159

LEWIS, R.S., Ming, T., Wacker, J.F., Anders, E., Steel, E., 1987, *Nature*, **326**, 160

LITTLE-MARENIN, I.R., Little, S.J., (LML90), 1990, *Astronomical Journal*, **99**, 1173

LORENZ-MARTINS, S., 1996, *Astronomy & Astrophysics*, **314**, 209

LORENZ-MARTINS, S., Lefèvre, J., 1994, *Astronomy & Astrophysics*, **291**, 831

LORENZ-MARTINS, S., Lefèvre, J., 1993, *Astronomy & Astrophysics*, **280**, 567

LORIN, J.C., Michel-Levy, M.C., 1978, *Lunar & Planetary Abstracts*, **9**, 660

LOUP, C., Forveille, T., Omont, A., Paul, J.F., 1993, *Astronomy & Astrophysics Supp.*, **99**, 29

LUKASIAK, A., Ferrando, P., McDonald, F.B., Webber, W.R., (1994), *Astrophysical Journal*, **426**, 366

MANUEL, O., Hennecke, E.W., Sabu, D.D., 1972, *Nature*, **240**, 99

MARTIN, P.G., Rogers, C., 1987, *Astrophysical Journal*, **322**, 374

MATHIS J S, 1990, *Annual Review of Astronomy & Astrophysics*, **28**, 37

MCALOON, B.P., Hofmeister, A.M., 1993, *American Mineralogist*, **78**, 957-967

MCCULLOCH, M.T., Wasserburg, G.J., 1978 *Astrophysical Journal*, **220**, 15

MERRILL, K.M., Stein, W.A., 1976, *Publ. of the Astronomical Soc. of the Pacific*, **88**, 285

MERRILL, K.M., Soifer, B.T., Russell, R.W., 1975, *Astrophysical Journal*, **200**, L37

MOLSTER, F.J., van den Ancker, M.E., Tielens, A.G.G.M., Waters, L.B.F.M., Beintema, D.A., Waelkens, C., de Jong, T., de Graaw, T., Justtanont, K., Yamamura, I., Vandenbussche, B., Heras, A., 1996, *Astronomy & Astrophysics*, **315**, 373

MORIOKA, T., Kimura, S., Tsuda, N., Kaito, C., Saito, Y., Koike, C., 1998, *Mon. Not. R. Astron. Soc.*, **299**, 78.

MOWLAVI, N., 1998a, in *Tours Symposium on Nuclear Physics III*, eds. M. Arnould, M. Lewitowicz, Y.T. Oganessian, M. Ohta, H. Utsunomiya, T. Wada, AIP Conf. Proc. **425**, 507

MOWLAVI, N., 1998b, in *Cosmic Chemical Evolution, IAU Symposium 187*, in press

DE MUIZON, M.J., Geballe, T.R., d'Hendecourt, L.B., Baas, F., 1986, *Astrophysical Journal*, **306**, L105

MUKAI, T., Koike, C., 1990, *Icarus*, **87**, 180

MUTSCHKE, H., Dorschner, J., Henning, T., Jäger, C., Ott, U., 1995, *Astrophysical Journal*, **454**, 157

NITTLER, L.R., Alexander, C.M.O'D., Gao, X., Walker, R.M., Zinner, E.K., 1997, *Astrophysical Journal*, **483**, 475

NITTLER, L.R., Lewis, R.S., Walker, R.M., Zinner, E.K., 1995a, *Meteoritics & Planet. Sci.*, **31**, 6

NITTLER, L.R., Hoppe, P., Alexander, C.M.O'D., Amari, S., Eberhardt, P., Gao, X., Lewis, R.S., Strebel, R., Walker, R.M., Zinner, E.K., 1995b, *Astrophysical Journal*, **453**, L25

NITTLER, L.R., Alexander, C.M.O'D., Gao, X., Walker, R.M., Zinner, E.K., 1994a, *Nature*, **370**, 443

NITTLER, L.R., Alexander, C.M.O'D., Gao, X., Walker, R.M., Zinner, E.K., 1994b, *Meteoritics & Planet. Sci.*, **29**, 512

O-rich NUTH, J.A., Allen, J.E., 1992, *Astrophysics & Space Science*, **196**, 117

NUTH, J.A., Hecht, J.H., 1990, *Astrophysics & Space Science*, **163**, 79

NYQUIST, R.A., 1971, *Infrared Spectra of Inorganic Molecules*, Academic Press:New York

OMONT, A., Loup, C., Forveille, T., Lintel Hekkert, P., Sivagnanam, P., Habing, H.J., 1993, *Astronomy & Astrophysics*, **267**, 515

OMONT, A., 1986, *Astronomy & Astrophysics*, **164**, 159

ONAKA, T., de Jong, T., Willems, F.J., (OdJW), 1989, *Astronomy & Astrophysics Supp. Ser.*, **81**, 261

OTHMAN, M., Ishida, K., Okamura, S., Nishimura, S., 1988, *Astrophysics & Space Science*, **148**, 191

OTT, U., 1993, *Nature*, **364**, 25

PAPOULAR, R., Reynaud, C., Nenner, I., 1991, *Astronomy & Astrophysics*, **247**, 215

PAPOULAR, R., Cauchetier, M., Begin, S., LeCaer, G., 1998, *Astronomy & Astrophysics*, **329**, 1035-1044

PAPOULAR, R., 1988, *Astronomy & Astrophysics*, **204**, 138

PAPOULAR, R., Pegourie, B., 1983, *Astronomy & Astrophysics*, **128**, 335

PARKER, S.P., 1988, *Optics source book*, McGraw-Hill:New York

PATZER, A.B.C., Gauger, A., Sedlmayr, E., 1998, *Astronomy & Astrophysics*, **337**, 847

PEGOURIE, B., 1988 , *Astronomy & Astrophysics*, **194**, 335

PEGOURIE, B., Papoular, R., 1985, *Astronomy & Astrophysics*, **142**, 451

PREUDHOMME, J., Tarte, P., 1971, *Spectrochimica Acta*, **27A**, 1817

PUGET, J.L., Léger, A., Boulanger, F., 1985, *Astronomy & Astrophysics*, **142**, 19

729

ROBINSON, M.S., Beegle, L.W., Wdowiak, T.J., 1997, *Astrophysical Journal*, **474**, 474

ROCHE, P.F., Aitken, D.K., 1984, *Mon. Not. R. Astron. Soc.*, **208**, 481

RUSSELL, R.W., Soifer, B.T., Willner, S.P., 1977, *Astrophysical Journal*, **217**, L149

SAKATA, A., Wada, S., Onaka, T., Tokunaga, A.T., 1987, *Astrophysical Journal*, **320**, L63

SAKATA, A., Wada, S., Tanabe, T., Onaka, T., 1984, *Astrophysical Journal*, **287**, L51

SALPETER, E.E., 1974, *Astrophysical Journal*, **193**, 585

SALPETER, E.E., 1974, *Astrophysical Journal*, **193**, 579

SALPETER, E.E., 1977, *Annual Review of Astronomy & Astrophysics*, **15**, 267

SANDFORD, S.A., 1996, *Meteoritics & Planetary Science*, **31**, 449

SASLAW, W.C. Gaustad, J.E., 1969, *Nature*, **221**, 160

SAXENA, S.K., Eriksson, G., 1983, *Earth & Planetary Sci. Lett.*, **65**, 7

SCHUTTE, W.A., Tielens, A.G.G.M., 1989, *Astrophysical Journal*, **343**, 369

SEDLMAYR, E., 1998, in *Proceedings of the Faraday Discussion no. 109: Chemistry and Physic of Molecules and Grains in Space*, in press

SEDLMAYR, E., 1989, *Interstellar Dust*, eds L.J. Allamandola & A.G.G.M. Tielens, Kluwer Academic Publishers:Dordrecht, 467

SELLGREN, K., 1984, *Astrophysical Journal*, **277**, 623

SKINNER, C.J., Whitmore, B., 1988b, *Mon. Not. R. Astron. Soc.*, **234**, 79

SKINNER, C.J., Whitmore, B., 1988a, *Mon. Not. R. Astron. Soc.*, **231**, 169

SKINNER, C.J., Whitmore, B., 1988, *Mon. Not. R. Astron. Soc.*, **235**, 603

SPECK, A.K., Barlow, M.J., Skinner, C.J., 1997, *Mon. Not. R. Astron. Soc.*, **288**, 431

SPECK, A.K., Barlow, M.J., Skinner, C.J., 1997, *Meteoritics & Planetary Science*, **32**, 702

SPITZER, W.G., Kleinman, D.A., Walsh, D., 1959, *Physical Review*, **113**, 127

SPITZER, W.G., Kleinman, D.A., Frosch, C.J., 1959, *Physical Review*, **113**, 133

STENCEL, R.E., Nuth, J.A., Little-Marenin, I.R., Little, S.J., 1990, *Astrophysical Journal*, **350**, L45

STEPHENS, J.R., 1980, *Astrophysical Journal*, **237**, 450

220, 406

SYLVESTER, R.J., Barlow, M.J., Skinner, C.J., 1994, *Mon. Not. R. Astron. Soc.*, **266**, 640

SZCZEPANSKI, J., Vala, M., 1993, *Nature*, **363**, 646

TANG, M., Anders, E., Hoppe, P., Zinner, E.K., 1989, *Nature*, **339**, 351

TAYLOR, A., Jones, R.M., 1960, in Silicon Carbide: A High Temperature Semiconductor, ed J. O'Conner, Franklin:Boston, 147

TIELENS, A.G.G.M., 1990, *From Miras to Planetary Nebulae: Which Path for Stellar Evolution*, Editions Frontieres:Gif-sur-Yvette, France, 186

TIELENS, A.G.G.M., Seab, C.G., Hollenbach, D.J., McKee, C.F., 1987, *Astrophysical Journal*, **319**, L109

TIMMES, F.X., Clayton, D.D., 1996, *Astrophysical Journal*, **472**, 723

TOKUNAGA, A.T., 1996, paper presented at *Diffuse Infrared Radiation and the IRTS.*

TREFFERS, R., Cohen, M., 1974, *Astrophysical Journal*, **188**, 545

VAN DE HULST, H.C., 1957, *Light Scattering by Small Particles*, Wiley:New York

VAN DER ZWET, G.P., Allamandola, L.J., 1985, *Astronomy & Astrophysics*, **146**, 76

VARDYA, M.S., 1989, *Astronomy & Astrophysics*, **209**, 165

VARDYA, M.S., de Jong, T., Willems, F.J., (VdJW), 1986, *Astrophysical Journal*, **304**,

L29

VIRAG, A., Wopenka, B., Amari, S., Zinner, E.K., Anders, E., Lewis, R.S., 1992, *Geochim. Cosmochim. Acta*, **56**, 1715

VOLK, K., Kwok, S., Woodsworth, A.W., 1993, *Astrophysical Journal*, **402**, 292

VOLK, K., Kwok, S., Langill, P.P., 1992, *Astrophysical Journal*, **391**, 285

WAELKENS, C., Waters, L.B.F.M., de Graauw, T., Huygen, R., Malfait, K., Plets, H., Vandenbussche, B., Beintema, D.A., Boxhoorn, D.R., Habing, H.J., Heras, A.M., Kester, D.J.M., Lahuis, F., Morris, P.W., Roelfsema, P.R., Salama, A., Siebenmorgen, R., Trams, N.R., van der Bliek, N.R., Valentijn, E.A., Wesselius, P.R., 1996, *Astronomy & Astrophysics*, **315**, L245

WATERS, L.B.F.M., Molster, F.J., de Jong, T., Beintema, D.A., Waelkens, C., Boogert, A.C.A., Boxhoorn, D.R., de Graauw, T., Drapatz, S., Feuchtgruber, H., Genzel, R., Helmich, F.P., Heras, A.M., Huygen, R., Izumiura, H., Justtanont, K., Kester, D.J.M., Kunze, D., Lahuis, F., Lamers, H.J.G.L.M, Leech, K.J., Loup, C., Lutz, D., Morris, P.W., Price, S.D., Roelfsema, P.R., Salama, A., Schaeidt, S.G., Tielens, A.G.G.M., Trams, N.R., Valentijn, E.A., Vandenbussche, B., van den Ancker, M.E., van Dishoeck, E.F., van Winckel, H., Wesselius, P.R., Young, E.T., 1996, *Astronomy & Astrophysics*, **315**, L361

WDOWIAK, T.J., Flickinger, G.C., Cronin, J.R., 1988, , **328**, L75

WHITE, W.B., DeAngelis, B.A., 1967, *Spectrochimica Acta*, **23A**, 985-995

WHITTET, D.C.B., Duley, W.W., Martin, P.G., 1990, *Mon. Not. R. Astron. Soc.*, **244**, 427

WILLEMS, F.J., de Jong, T., 1988, *Astronomy & Astrophysics*, **196**, 173

WILLEMS, F.J., 1988, *Astronomy & Astrophysics*, **203**, 51

WILLEMS, F.J., 1988, *Astronomy & Astrophysics*, **203**, 65

WOOLF, N., 1973, in *IAU Proceedings - Interstellar Dust & Related Topics*, eds J. Mayo Greenberg & H. C. van de Hulst, Reidel:Dordrecht, 485

WOOLF, N., Ney, E.P., 1969, *Astrophysical Journal*, **155**, L181

WOOTEN, F., 1972, *Optical Properties of Solids*, Academic:New York

WOUTERLOOT, J.G.A., Brand, J., Fiegle, K., 1993, *Astronomy & Astrophysics Supp.*, **98**, 589

WRIGHT, I.P., 1992, *Nature*, **360**, 20

ZEILEK, M., Smith, E.v.P., 1987, *Introductory Astronomy & Astrophysics*, Suanders:New York

ZINNER, E.K., 1991, in *Space Science Reviews* , **56**, 147